AEROELASTIC LIMIT-CYCLE OSCILLATIONS RESULTING FROM AERODYNAMIC NON-LINEARITIES

AEROELASTIC LIMIT-CYCLE OSCILLATIONS RESULTING FROM AERODYNAMIC NON-LINEARITIES

Proefschrift

ter verkrijging van de graad van doctor
aan de Technische Universiteit Delft,
op gezag van de Rector Magnificus prof. ir. K.C.A.M. Luyben,
voorzitter van het College voor Promoties,
in het openbaar te verdedigen op woensdag 12 april 2017 om 10:00 uur

door

Anna Catharina Leonarda Maria VAN ROOIJ

ingenieur luchtvaart- en ruimtevaarttechniek,
geboren te Berkel-Enschot.

Dit proefschrift is goedgekeurd door de

promotor: Prof. dr. ir. drs. H. Bijl
copromotor: Dr. R.P. Dwight

Samenstelling promotiecommissie:

Rector Magnificus	voorzitter
Prof. dr. ir. drs. H. Bijl	Technische Universiteit Delft, promotor
Dr. R.P. Dwight	Technische Universiteit Delft, copromotor
Onafhankelijke leden:	
Prof. dr. K.J. Badcock	University of Liverpool, Verenigd Koninkrijk
Prof. dr. G. Dimitriadis	Université de Liège, België
Prof. dr. S. Hickel	Technische Universiteit Delft
Dr. D.E. Raveh	Technion, Israël
Prof. dr. L. Tichy	Deutsches Zentrum für Luft- und Raumfahrt, Duitsland
Prof. dr. F. Scarano	Technische Universiteit Delft, reservelid

This research was supported by the Institute of Aeroelasiticy of the German Aerospace Center (DLR).

Keywords: Aeroelasticity, limit-cycle oscillations, unsteady aerodynamics, bifurcation behaviour, structural parameter variations

Printed by: Sieca Repro Delft

Front & Back: A.C.L.M. van Rooij

ISBN 978-94-6186-794-0

An electronic version of this dissertation is available at
http://repository.tudelft.nl/.

CONTENTS

SUMMARY

Aeroelasticity is the discipline that studies the interaction between structures and the fluid flow around them. Flexible structures can easily be deformed by the fluid flow. The resulting aerodynamic forces in turn affect the structural deformation. Typical aeroelastic problems include a gust encounter and flutter. A disturbance in the air, for example turbulence, might cause oscillations of the aircraft's wing. At certain air speeds the amplitude of these oscillations grows unbounded, i.e. flutter occurs. The flutter boundary, beyond which the oscillation amplitude grows unbounded, should never be surpassed in flight. In contrast, during so-called limit-cycle oscillations (LCOs) the oscillation amplitude stays constant. Limit-cycle oscillations are caused by non-linearities in either the structure or the fluid flow around the aeroelastic system or by a combination of both. Structural non-linearities can be for example freeplay or non-linear damping. Aerodynamic non-linearities include shock wave dynamics, boundary-layer separation and boundary-layer transition. This thesis only considers aerodynamic non-linearities.

Flutter onset is normally computed using a linearised method. However, since a certain minimum disturbance level is necessary for flutter to occur, flutter is, in reality, always non-linear. This means that a linearised method might not predict flutter onset correctly. Hence, it might be possible that non-linear flutter, i.e. an LCO, already occurs below the flutter boundary predicted from linearised theory. Whether limit-cycle oscillations caused by aerodynamic non-linearities can occur below the linear flutter speed has not yet been investigated systematically. Therefore, the main research question of this thesis is whether LCOs caused by aerodynamic non-linearities can already occur below the flutter boundary predicted from linearised theory.

Theoretically, there are two types of LCOs that might exist when considering aerodynamic non-linearities only. LCOs that occur beyond the flutter boundary are so-called benign LCOs. These benign LCOs are stable. In other words, when the system is disturbed, it will return to its LCO state. In contrast, so-called detrimental LCOs might occur already below the flutter boundary. They are stable and they are accompanied by an unstable LCO of smaller amplitude that occurs at the same freestream velocity. The amplitude of this unstable LCO marks the boundary between two stable states; a stable LCO and a steady state (without oscillations). When a detrimental LCO would occur in reality, the linearised flutter onset computation would not be correct, since non-linear flutter, i.e. a stable LCO, would exist below the flutter boundary. The variation of the LCO's amplitude with for example the freestream velocity or the dynamic pressure is mathematically called the bifurcation behaviour. Benign LCOs cause so-called supercritical bifurcations and detrimental LCOs cause so-called subcritical bifurcations.

In this thesis limit-cycle oscillations of a two degree-of-freedom airfoil system caused by aerodynamic non-linearities were studied. In order to do so fully coupled fluid-structure interaction (FSI) simulations as well as forced motion oscillation simulations were performed. The supercritical NLR7301 airfoil has been used for all analyses in this thesis.

The degrees of freedom of the airfoil are pitch and plunge.

First, the energy budget of the LCOs was analysed. The mean power components computed from FSI simulations showed that the mean total power (sum of the mean power of the aerodynamic lift, aerodynamic moment and structural damping) is zero at the LCO amplitude, as expected. Furthermore, a defect in the mean power of the aerodynamic lift was found to be responsible for the amplitude limitation. This defect originates from the impact of small variations of the phase of the lift with oscillation amplitude. The small variations of the magnitude and phase of the aerodynamic moment do not have the same impact on the mean aerodynamic power (sum of the mean power of the lift and mean power of the moment) as those of the lift. Therefore, the defect in the mean power of the moment is much smaller than that in the mean power of the lift. Due to the complicated flow behaviour, no local features were found to be responsible for the defect in the mean power of the lift.

To study the bifurcation behaviour of the LCOs of the two degree-of-freedom airfoil system, an extension to the well-known p-k method used in classical linear flutter analysis has been developed in this thesis. This method is called the amplitude-dependent p-k method (ADePK), since it takes into account the amplitude of the (forced) motion (in contrast to the standard p-k method). ADePK solves the equations of motion in the frequency domain. In order to do so, a so-called response surface is first set up from forced motion oscillation simulations at several amplitudes, frequencies and complex-valued amplitude ratios between the two degrees of freedom. The response of the lift and moment to these forced motion oscillation simulations is then transferred into the frequency domain via a Fourier transformation. During the iterations of ADePK the first harmonic of the aerodynamic force and moment is obtained from interpolation on the response surface. The LCO amplitude and mode shape are found iteratively from ADePK. In order to verify ADePK the van der Pol-oscillator has been used. After verification, the method has been validated against time domain results for the two degree-of-freedom airfoil system. The bifurcation behaviour of the LCO amplitude and mode shape obtained from ADePK showed good agreement with the results of the FSI simulations in the time domain.

After validation of ADePK, it has been used for systematic studies of the bifurcation behaviour of the LCO amplitude of the two degree-of-freedom airfoil system. Several response surfaces were built in order to study various aerodynamic non-linearities. A bifurcation behaviour analysis using these response surfaces showed that the strongest non-linearity occurs in transonic flow with trailing-edge separation. For the other test cases, transonic inviscid flow, subsonic flow with trailing-edge separation and subsonic flow with free boundary-layer transition, limit-cycle oscillations only occurred very close to the flutter boundary, hence the non-linearity was observed to be relatively weak. In case of transonic inviscid flow multiple nested LCOs (of different amplitude) occurred at one freestream velocity, i.e. a detrimental LCO occurred.

To study the effect of LCOs close to the flutter boundary, the Mach number was varied in inviscid flow. The linear flutter boundary, shows, as expected, a so-called transonic dip, i.e. a minimum in the flutter boundary at transonic flow speeds. Contours of constant LCO amplitude showed that at subsonic Mach numbers the LCO amplitude increases much faster than at transonic speeds. Furthermore, these contours showed

that the transonic dip could be significantly less deep when a certain LCO amplitude is considered.

A variation of the structural frequency ratio of the two degree-of-freedom airfoil system showed a significant influence on the bifurcation behaviour for all four aerodynamic non-linearities. In subsonic flow with trailing-edge separation, increasing the structural frequency ratio resulted in detrimental LCOs or unstable LCOs only (up to an amplitude of 5°). For the viscous transonic flow test case, the bifurcation behaviour was supercritical at all structural frequency ratios studied in this thesis, except for the largest structural frequency ratio at which only unstable LCOS (up to an amplitude of 5°) were obtained. In inviscid transonic flow, both detrimental and benign LCOs were observed as well. In subsonic flow with free boundary-layer transition slightly subcritical bifurcations and supercritical bifurcations of the LCO solutions were observed when the structural frequency ratio was varied. Furthermore, for all aerodynamic non-linearities, the LCO mode shape changes from plunge dominated to pitch dominated when the structural frequency ratio increases, as expected. The non-dimensional mass ratio was also changed for all test cases, however, no significant changes in the bifurcation behaviour were observed, unless the non-linearity was already very weak. In that case a change from a benign to a detrimental LCO is possible when the mass ratio is changed. However, the strength of the non-linearity is influenced by a mass ratio change. The same holds for the addition of structural damping to the two degree-of-freedom system. For all sources of aerodynamic non-linearity, variation of the elastic axis location was found to significantly influence the strength of the non-linearity and in case of a weak non-linearity, the bifurcation type can easily change from supercritical to subcritical (or the other way around) when the elastic axis is moved. It was observed that a subcritical bifurcation of the LCO solution occurs, in viscous transonic flow, when the elastic axis is moved aft at the second largest structural frequency ratio tested.

The response surface necessary to apply the ADePK method has been studied to investigate whether it revealed any clues on the bifurcation type. Using one-at-a-time linearised aerodynamic forces it was found that, at the nominal structural parameter values, the phase of the lift has the largest influence on the bifurcation behaviour. Keeping the phase of the lift at its linearised value and performing a bifurcation behaviour computation with ADePK resulted in a completely different bifurcation behaviour than when the amplitude-dependence of the phase of the lift is taken into account (for all aerodynamic non-linearities). Therefore, the phase of the lift-slices of the response surface versus amplitude (at the flutter- and 5°-LCO amplitude mode shapes) were studied. A comparison of the sine of these slices (i.e. the sine of the phase of the lift versus the oscillation amplitude) to the bifurcation diagram revealed a very similar shape. However, for other structural frequency ratios then the nominal one, the shape of the sine of the lift and that of bifurcation diagram were not always similar. Hence, further investigations are needed to clarify why for other structural parameters these two curves do no longer exhibit a similar shape or to identify a parameter that has the same shape as the bifurcation diagram for all structural parameter values.

Using the flutter mode shape to compute the phase of the lift from forced motion oscillation simulations, the local features responsible for the behaviour of the phase of the lift and hence for the LCO behaviour have been studied. For both transonic test

cases, the shock motion on the lower surface of the airfoil was found to be responsible for the changes in the phase of the lift.

In this thesis fundamental investigations into the bifurcation behaviour of a two-degree-of-freedom airfoil system with aerodynamic non-linearities have been performed. A first step has been made in identifying the effect of various structural parameter changes, in identifying the relation between the aerodynamic forces and the LCO bifurcation behaviour and in identifying possible ways to predict the LCO bifurcation behaviour from the flutter onset behaviour. These investigations with ADePK serve as the basis for larger degree-of-freedom systems.

SAMENVATTING

Aero-elasticiteit is de discipline die de interactie tussen constructies en de stroming om deze constructies bestudeert. Flexibele constructies kunnen gemakkelijk gedeformeerd worden door de stroming. De resulterende aerodynamische krachten beïnvloeden dan op hun beurt de deformatie van de constructie. Typische aero-elastische problemen zijn bijvoorbeeld een windvlaag-confrontatie en fladderen. Storingen in de lucht, zoals turbulentie, kunnen oscillaties van de vleugel van het vliegtuig veroorzaken. Op bepaalde luchtsnelheden kan de amplitude van deze oscillaties ongelimiteerd groeien, dan treedt "fladderen" op. De fladdergrens, boven welke de oscillatie amplitude ongelimiteerd groeit, mag tijdens een vlucht nooit worden overschreden. In tegenstelling tot fladderen blijft bij zogenaamde limietcycli de oscillatie amplitude constant. Limietcykli worden veroorzaakt door niet-lineariteiten in de constructie of in de stroming om de aero-elastische constructie of door een combinatie van beide. Niet-lineariteiten in de constructie zijn bijvoorbeeld "freeplay" of niet-lineaire demping. Aerodynamische niet-lineariteiten zijn de dynamica van schokgolven, grenslaag loslating en grenslaag transitie. Dit proefschrift neemt alleen aerodynamische niet-lineariteiten in beschouwing.

Het optreden van fladderen wordt normaal gesproken berekend door middel van linearisatie. Echter, fladderen is in werkelijkheid altijd niet-lineair, omdat een bepaald storingsniveau nodig is voordat fladderen optreedt. Dit betekent dat een gelineariseerde methode het optreden van fladderen mogelijk niet correct zal voorspellen. Daarom zou het mogelijk kunnen zijn dat niet-lineair fladderen, m.a.w. een limietcyclus, al onder de, door gelineariseerde theorie voorspelde, fladdergrens optreedt. Of limietcycli veroorzaakt door aerodynamische niet-lineariteiten al onder de lineaire fladder snelheid kunnen optreden is nog niet systematisch onderzocht. Daarom is de hoofdonderzoeksvraag van deze dissertatie of limietcycli die veroorzaakt worden door aerodynamische niet-lineariteiten al onder de, door gelineariseerde theorie voorspelde, fladdergrens op kunnen treden.

Theoretisch zijn er twee typen limietcycli die zouden kunnen optreden als alleen aerodynamische niet-lineariteiten worden beschouwd. Limietcykli die boven de fladdergrens optreden zijn de zogenaamde goedaardige limietcycli. Deze goedaardige limietcycli zijn stabiel. Met andere woorden, als het systeem wordt verstoord, zal het naar zijn limietcyclus-toestand terugkeren. In tegenstelling tot goedaardige limietcycli, zouden kwaadaardige limietcycli al onder de fladdegrens kunnen optreden. Zij zijn stabiel en worden vergezelt door een instabiele limietcyclus met een kleinere amplitude die op dezelfde luchtsnelheid optreedt. De amplitude van deze instabiele limitcyclus markeert de grens tussen twee stabiele toestanden; een stabiele limietcyclus en een stationaire toestand (zonder oscillaties). Als een kwaadaardige limietcyclus in werkelijkheid zou optreden, dan zou de de linearisatie om het optreden van fladderen te voorspellen eigenlijk niet correct zijn, omdat niet-lineair fladderen, d.w.z. een stabiele limietcyclus, al onder de fladdergrens zou optreden. De variatie van de limietcyclus amplitude met bijvoor-

beeld de luchtsnelheid of de dynamische druk wordt bifurcatie gedrag genoemd in de wiskunde. Goedaardige limietcycli veroorzaken zogenaamde superkritische bifurcaties en kwaadaardige limietcycli veroorzaken zogenaamde subkritische bifurcaties.

In dit proefschrift worden limietcycli van een twee vrijheidsgraad vleugelprofiel systeem veroorzaakt door aerodynamische niet-lineariteiten bestudeerd. Om dat te doen worden zowel fluïdum-constructie interactie simulaties als simulaties waar een oscilleerende beweging wordt gesimuleerd, uitgevoerd. Het superkritische NLR7301 vleugelprofiel is gebruikt voor alle analyses in dit proefschrift. Het vleugelprofiel heeft als vrijheidsgraden stampen en dompen.

Als eerste wordt de energiehuishouding van de limietcycli bestudeerd. De gemiddelde vermogenscomponenten, berekent door middel van de fluïdum-constructie interactie simulaties, toonden aan dat het gemiddelde totale vermogen (som van het gemiddelde vermogen van de aerodynamische liftkracht, het aerodynamische moment en de structurele constructie), zoals verwacht, nul is op de limietcyclus amplitude. Een defect in het gemiddelde vermogen van de liftkracht veroorzaakt deze begrenzing van de amplitude. Dit defect komt voort uit de impact van kleine variaties in de fase van de liftkracht die optreden zodra de oscillatie amplitude verandert. De kleine variaties in de amplitude en de fase van het aerodynamische moment hebben niet dezelfde impact op het gemiddelde aerodynamische vermogen (som van het gemiddelde vermogen van de liftkracht en van het moment) als die van de liftkracht. Daarom is het defect in het gemiddelde vermogen van het moment veel kleiner dan dat in het gemiddelde vermogen van de lift. Door het gecompliceerde stromingsgedrag was het niet mogelijk om lokale fenomenen te vinden die verantwoordelijk zijn voor het defect in het vermogen van de liftkracht.

Om het bifurcatie gedrag van limietcycli van een twee vrijheidsgraad vleugelprofiel systeem te bestuderen is er een uitbreiding van de gerenommeerde p-k methode, die wordt gebruikt in een lineaire fladder analyse, ontwikkeld in dit proefschrift. Deze nieuwe methode wordt de amplitude-afhankelijke p-k methode (ADePK) genoemd, omdat rekening gehouden wordt met de amplitude van de (geforceerde) beweging (in tegenstelling tot de standaard p-k methode). De ADePK methode lost de bewegingvergelijkingen in het frequentie-bereik op. Om dat te doen, moet eerst een zogenaamd response oppervlak gegenereerd worden uit de resultaten van simulaties van geforceerde harmonische bewegingen met verschillende amplitudes, frequenties en complex-waardige amplitude verhouding tussen de twee vrijheidsgraden. De response van de liftkracht en het moment op deze geforceerde bewegingen wordt dan in het frequentie-bereik getransformeerd via een Fourier transformatie. Tijdens de iteraties van ADePK wordt de eerste harmonische component van de aerodynamische kracht en die van het moment berekend via interpolatie op het response oppervlak. De limietcyclus amplitude en -trilvorm kunnen dan iteratief worden gevonden in de ADePK methode. De van der Pol-oscillator is gebruikt om de ADePK methode te verifiëren. Na deze verificatie is de methode gevalideerd met tijdsbereik resultaten voor het twee vrijheidsgraad vleugelprofiel systeem. Het bifurcatie gedrag van de limietcyclus amplitude en de limietcyclus trilvorm berekend met ADePK komt goed overeen met de resultaten van fluïdum-constructie interactie simulaties in het tijdsbereik.

Nadat ADePK gevalideerd is, is de methode gebruikt voor systematische studies van

het bifurcatie gedrag van de limietcyclus amplitude van het twee vrijheidsgraad vleugelprofiel systeem. Er zijn verschillende response oppervlakken geconstrueerd om verschillende aerodynamische niet-lineariteiten te kunnen bestuderen. Een analyse van het bifurcatie gedrag, gebruikmakende van deze response oppervlakken, toonde aan dat de sterkste niet-lineariteit optreedt in een transsonische stroming met achterkant-loslating. Voor de andere testgevallen, transsonische invisceuze stroming, subsonische stroming met achterkant-loslating en subsonische stroming met vrije grenslaagtransitie, traden limietcycli alleen heel dichtbij de fladdergrens op. De niet-lineariteit is daarom relatief zwak in deze testgevallen. In transsonische invisceuze stroming treden op één luchtstroomsnelheid meerdere limietcycli (van verschillende amplitude) tegelijk op, dat willen zeggen, er treden kwaadaardige limietcycli op.

Om het effect van limietcycli dichtbij de fladdergrens te bestuderen, is het Machgetal gevarieërd. De lineaire fladdergrens laat, zoals verwacht, een zogenaamde "transsonische dip" zien, dat wil zeggen, een minimum in de fladdergrens op transsonische luchtsnelheden. Het berekenen van contouren van constante limietcyclus amplitude toont aan dat de limietcyclus amplitude bij subsonische Machgetallen veel sneller toeneemt dan bij transsonische Machgetallen. Verder lieten deze contouren zien dat, als limietcycli van een bepaalde amplitude beschouwd worden, het transsonische minimum in de fladdergrens significant minder diep kan zijn.

Een variatie van de verhouding van de structurele eigenfrequenties van het twee vrijheidsgraad vleugelprofiel systeem laat een significante invloed op het bifurcatie gedrag zien voor alle vier de aerodynamische niet-lineariteiten. Het verhogen van de verhouding van structurele eigenfrequenties zorgt in subsonische stroming met achterkant-loslating voor kwaadaardige limietcycli of alleen instabiele limietcycli (tot een amplitude van 5°). Voor het visceuze transsonische testgeval treedt superkritisch bifurcatie gedrag op voor alle verhoudingen van de structurele eigenfrequenties die onderzocht zijn in deze dissertatie, behalve voor de grootste verhouding, voor deze verhouding treden alleen instabiele limietcycli op (tot een amplitude van 5°). In invisceuze transsonische stroming treden ook zowel kwaadaardige en goedaardige limietcycli op. In subsonische stroming met vrije grenslaagtransitie treden minieme subkritische bifurcaties en superkritische bifurcaties van de limietcyclus oplossingen op als de verhouding van structurele eigenfrequenties gevarieërd wordt. Verder verandert de trilvorm, zoals verwacht, voor alle aerodynamische niet-lineariteiten van dompen-gedomineerd naar stampen-gedomineerd als de verhouding van structurele eigenfrequenties wordt vergroot. De dimensieloze massaverhouding is ook gevarieërd voor alle testgevallen. Dit resulteert echter niet in significante veranderingen in het bifurcatie gedrag, behalve als de niet-lineariteit al heel zwak was. In dat geval kan een limietcyclus van goedaardig naar kwaadaardig veranderen als de massaverhouding wordt veranderd. Echter, de sterkte van de niet-lineariteit wordt beïnvloed door een verandering van de massaverhouding. Hetzelfde geldt voor het toevoegen van structurele demping aan het twee vrijheidsgraad systeem. De variatie van de locatie van de elastische as heeft voor alle aerodynamische niet-lineariteiten een significante invloed op het bifurcatie gedrag en in als de niet-lineariteit zwak is, kan het bifurcatie gedrag gemakkelijk veranderen van superkritisch naar subkritisch (of andersom) als de elastische as wordt verplaatst. Voor de op een na grootste verhouding van structurele eigenfrequenties onderzocht in deze dis-

sertatie, treedt, in visceuze transsonsiche stroming, een subkritische bifurcatie van de limietcyclus oplossing op wanneer de elastische as naar achter worden verplaatst.

Het response oppervlak dat nodig is om berekeningen te kunnen doen met ADePK is bestudeerd om te onderzoeken of het aanwijzingen over het bifurcatie gedrag bevat. Door middel van het een-voor-een lineariseren van de aerodynamische krachten, is vastgesteld dat, op de nominale structurele parameterwaardes, de fase van de liftkracht de grootste invloed op het bifurcatie gedrag heeft. Als de fase van de liftkracht constant gehouden wordt op zijn gelineariseerde waarde, resulteert een compleet ander bifurcatie gedrag dan wanneer er rekening gehouden wordt met de amplitude-afhankelijkheid van de fase van de liftkracht (voor alle aerodynamische niet-lineariteiten). Daarom zijn doorsnedes van het response oppervlak waarop de fase van de liftkracht versus de limietcyclus amplitude (op de fladder- and de 5°-limietcyclus-trilvorm) te zien is, bestudeerd. Uit een vergelijking van de sinus van deze doorsnedes (d.w.z. de sinus van de liftkracht versus de oscillatie amplitude) met het bifurcatie diagram blijkt dat de vorm van deze twee grafieken ongeveer hetzelfde is. Echter, voor andere verhoudingen van de structurele eigenfrequenties dan de nominale verhouding, zijn de vorm van de sinus van de liftkracht en die van het bifurcatie diagram niet altijd ongeveer hetzelfde. Daarom is verder onderzoek nodig om uit te vinden waarom deze twee curves voor andere structurele parameters niet meerdere ongeveer dezelfde vorm hebben of om een parameter te identificeren die voor alle structurele parameterwaardes dezelfde vorm heeft als het bifurcatie diagram.

De fase van de liftkracht is berekend met stromingssimulaties met een geforceerde harmonische beweging op de fladder trilvorm om lokale fenomenen verantwoordelijk voor het gedrag van de fase van de liftkracht, en dus ook voor het bifurcatie gedrag, te vinden. De schokgolf beweging op de onderkant van het vleugelprofiel wordt verantwoordelijk gehouden voor de veranderingen in de fase van de liftkracht voor de twee transsonische testgevallen.

In dit proefschrift zijn fundamentele analyses gedaan die het bifurcatie gedrag van een twee vrijheidsgraad vleugelprofiel systeem met aerodynamische niet-lineariteiten onderzoeken. Een eerste stap is gezet in het identificeren van het effect van verschillende structurele parameter variaties, in het identificeren van de relatie tussen de aerodynamische krachten en het bifurcatie gedrag en in het identificeren van manieren om het limietcyclus bifurcatie gedrag te voorspellen met behulp van het lineaire fladder gedrag. Deze studies met de ADePK methode vormen de basis voor onderzoeken naar systemen met meer vrijheidsgraden.

PREFACE

The research presented in this thesis has been conducted at the Institute of Aeroelasticity of the German Aerospace Center (DLR) from May 2012 till present. The first three years I've worked there as a "Doktorandin" and after that as a "wissentschaftliche Mitarbeiterin" with a part time contract. Working at the German Aerospace Center is truly inspiring. The center's reputation is large, even in the Netherlands. Being a part of the Institute of Aeroelasticity has taught me a lot about topics outside of my field of expertise and has enriched my professional life. I would like to thank a few people here for making this experience possible.

First of all I would like to thank Prof. Tichy and Prof. Krüger for letting me continuing the next step in my career at the Institute of Aeroelasticity. Then I would like to continue my thanksgiving with my department leader, Dr. Holger Hennings for allowing me to continue the work on my thesis as a "wissenschaftliche Mitarbeiterin" after the funding for the "Doktorandenstelle" was out. Second, I would like to thank Prof. Bijl from TU Delft for agreeing to be my promotor and allowing me to pursue my PhD research at the German Aerospace Center. Being an external PhD candidate was not always easy, our the teleconferences and personal meetings helped me with this step in my career. Furthermore, a large thanks to Dr. Richard Dwight from the TU Delft Aerodynamics Chair for being my supervisor and copromotor. Although the topic of my PhD is not exactly your field of research, you were always willing to help me out and explain me things on the phone. In a way it was good that you were not directly working in the field of aeroelasticity, so I got the feeling how to explain my research to non-experts in the field.

Moreover, a very large thank you goes to Jens Nitzsche, my team leader at DLR. Your ideas and the discussions we had helped me shape my research. A further thanks goes to all the members of the unsteady aerodynamics team. Especially to Reik Thormann, my former office colleague, for the discussions about my research when I was stuck and for helping me finding the focus of my research. Also thanks to my team colleague Christoph Kaiser for helping me with programming/cluster issues and being an ear to my problems, the same goes for Diliana Friedewald. I would like to thank Michael Fehrs for answering my questions about simulations with boundary layer transition. Next to my group members I would like to thank my office colleagues, Reik, Oliver and later on Thomas for providing a nice office atmosphere and Reik and Oliver for helping me with software and programming issues.

Besides my thesis work I was involved in a lot of social activities with a large group of colleagues. Thanks to all members of the "swimming group", Gabriel, Stefan, Christoph, Michael and Reik for enjoying swimming with me and for the occasional swimming group dinner. Also thanks to the distractions and nice socialising provided by some other colleagues on the occasional birthday party or dinner. Or the occasional hike with my hiking colleagues Reik and Virginie. Although, the Harz mountain area are not the Alps,

hiking with you was a nice way to spend my time. Next to playing sports with colleagues I also discovered the sport “floorball” in Göttingen and this is really one of the best discoveries of my life. Not only playing floorball, but playing it with friends is what makes it a great way to spend your time. I enjoyed all the trainings, competition games and tournaments with you guys. Additionally, thanks for all the game nights we spent together, where I could pursue one of my other hobbies, playing board games. A special thanks to Anne, Henriette, Garrett and Miquel from the floorball group for all the other nameless activities (“Stammtisch”, swimming, running, cross-country skiing, etc.). I feel delighted to have such a nice group of friends!

Last but not least I would like to thank my family; my parents and my sisters. You have always encouraged me to do the things I like. It must be very hard for you, mam and dad, to have your daughter live so far away. However, you did not let this distance stand in the way to help me where ever and whenever you could and to pay me an occasional visit with the caravan. Thank you very much to my sisters Milou and Britt as well, for always being there for me although we live so far apart and for listing to me going on and on about my research on the phone. And for all the camping holidays and other activities we enjoy together. I’m very proud of your adventures in the US and Canada and visiting you there was a great experience. Especially the trip to Canada were we all went together.

Anouk van Rooij
Göttingen, November 2016

1

INTRODUCTION

The field of aeroelasticity studies the interaction between structures and a surrounding fluid flow. The fluid flow around, for example, a bridge pillar or an aircraft wing, exerts forces on the structure and when this structure is flexible enough, it will deform. This elastic deformation of the structure will in turn perturb the fluid flow surrounding the structure. When the structure interacts with a steady flow one speaks of static aeroelasticity. Two examples of static aeroelastic phenomena are divergence of aircraft wings and tailplanes and control reversal (which make the aircraft's control surfaces ineffective). In contrast, the interaction between structure and fluid flow will become dynamic, when an external disturbance for example (e.g. turbulence) causes oscillations of e.g. the wing of the aircraft. Normally, these oscillations will be damped. However, above certain airspeeds, the interaction of the structure and the aerodynamic forces is such that the oscillations of the wing will be amplified and the oscillation amplitude grows. This is called flutter. Flutter can lead to structural failure and must never occur in flight. Hence, for certification of an aircraft, the aircraft has to be proven flutter-free inside its flight envelope [1]. The boundary beyond which arbitrarily small disturbances in the flow will lead to unbounded growth of the wing's oscillation amplitude is called the flutter boundary. Close to this flutter boundary so-called limit-cycle oscillations (LCOs) may occur. During these LCOs the oscillation will grow to a constant (and bounded) amplitude due to the presence of a non-linearity in the structure or in the fluid flow. These limit-cycle oscillations can be observed e.g. in the F-16 fighter aircraft with external stores [2–5].

Non-linearities that lead to limit-cycle oscillations in the field of aeroelasticity can be either structural or aerodynamic in nature. Structural non-linearities include non-linear stiffeners (e.g. freeplay), geometric non-linearities and non-linear damping. Aerodynamic sources of non-linearity might be shock waves or flow separation. Combinations of these sources of non-linearity also lead to limit-cycle oscillations, see e.g. [6–11]. LCOs due to structural non-linearities are relatively easy to study both experimentally and numerically, as is represented by the large amount of literature available on the subject, see e.g. [12–20]. Lee et al. [21] present a detailed overview of LCOs caused by structural non-linearities.

In contrast, non-linearities in the flow are more difficult to investigate both experimentally and numerically. Experiments require expensive wind-tunnel tests and numerical investigations require a computationally expensive flow solver that is capable of representing the sources of aerodynamic non-linearity. Numerical investigations in this area have only gained interest due to the increased computer power over the last few decades. Hence, investigations that study limit-cycle oscillations caused by aerodynamic non-linearities are limited and therefore this thesis focusses on limit-cycle oscillations due to these non-linearities.

In this chapter first the motivation of this thesis is presented. Then, the types of limit-cycle oscillations will be discussed in Section 1.2. Section 1.3 provides an overview of the investigations performed by previous researchers. At the end of this section the unanswered questions in the field of flow-induced limit-cycle oscillations will be addressed. The objectives of this thesis following from these research questions will be presented in Section 1.4. Finally an outline of the thesis is given in Section 1.5.

1.1. MOTIVATION OF THIS THESIS

The aviation authorities see limit-cycle oscillations as a type of flutter, i.e. they are not allowed for certificated aircraft. The proof that an aircraft is flutter-free inside its flight envelope has to be delivered by flight tests and one or two other methods [1]. Generally, a numerical prediction method, validated by (wind-tunnel) tests, is used. This flutter-prediction method comprises a linearised method, which assumes flutter to be a linear phenomenon. However, flutter is, in reality, always non-linear, i.e. a certain minimum excitation level is needed in order for flutter to occur. Hence, linearised methods that predict flutter onset will fail to predict actual, non-linear, flutter. That is, limit-cycle oscillations of finite amplitude might already occur below the flutter boundary,

Therefore, it is necessary to investigate whether a linearised flutter analysis predicts the correct flutter speed, or whether stable limit-cycle oscillations do already occur below the flutter boundary. Hence, the main research question of this thesis is:

Can limit-cycle oscillations caused by aerodynamic non-linearities occur below the (linear) flutter boundary?

And if so, at what flow conditions do they occur? And what structural properties are needed for them to occur?

In order to investigate whether limit-cycle oscillations can occur below the flutter boundary, numerical flow simulations are used in this thesis. The most direct, and commonly used, method to study limit-cycle oscillations caused by aerodynamic non-linearities is fluid-structure coupling, in which a computational fluid dynamics (CFD) code is coupled to a structural solver. This approach has been used by [22–30]. However, such a coupling method is computationally expensive and hence not suitable to study the limit-cycle oscillation amplitude as a function of, for example, the freestream velocity. Therefore, computationally efficient methods that predict limit-cycle oscillations with sufficient accuracy, i.e. non-linear reduced-order models (ROMs), are needed for a faster

prediction and evaluation of the aircraft's non-linear aeroelastic behaviour. In this thesis such a ROM will be developed and then it will be used to investigate the possibility of non-linear flutter below the flutter boundary.

1.2. LIMIT-CYCLE OSCILLATIONS

Limit-cycle oscillations (LCOs) are the simplest form of non-linear aeroelastic oscillations. In these oscillations the oscillation amplitude first grows (or decreases) and then stays constant, i.e. the oscillation amplitude remains limited, due to the presence of a non-linearity. Other, more complicated, non-linear aeroelastic responses include higher harmonic and sub-harmonic resonances, jump-resonances, entrainment, beating and period doubling [31]. Limit-cycle oscillations are often used as a prototype of a non-linear aeroelastic response. Figure 1.1 shows an example of a time signal of an LCO and a phase plane view of an LCO.

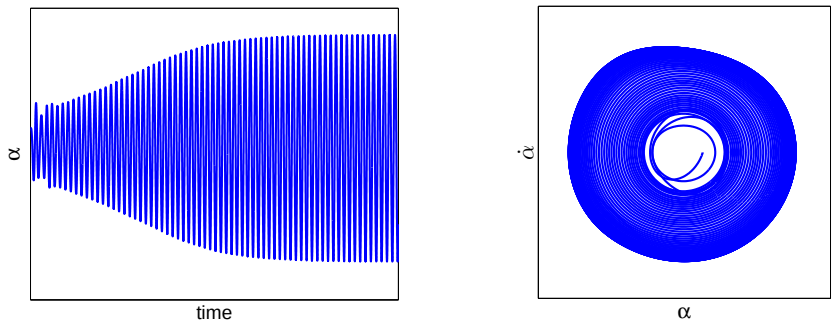

(a) Oscillation amplitude versus time

(b) Phase plane

Figure 1.1: A limit-cycle oscillation

For systems with aerodynamic non-linearities there exist two types of LCOs depending on the strength of non-linearity, i.e. LCOs can be either benign or detrimental. Figure 1.2 depicts these two types of LCOs. The variation of the LCO amplitude (or LCO mode shape) with, for example, the freestream velocity, as shown in Figure 1.2, is called the bifurcation behaviour. The dynamic pressure is another possible bifurcation parameter. In the case of flutter, i.e. when no non-linearities are present, the oscillation amplitude would increase unboudedly and hence this is represented in the bifurcation diagram by a vertical line at the flutter speed, see Figure 1.2. Benign LCOs occur beyond the flutter boundary. For a benign LCO, or more precisely, a supercritical Hopf bifurcation, the LCO amplitude increases with an increasing value of the bifurcation parameter. If the benign non-linearity is weak, the LCO amplitude will quickly grow when the airspeed or dynamic pressure is increased, i.e. the deviation from the linear case is small. If the non-linearity is strong, a smaller LCO amplitude will result and the deviation from the flutter case is large. These benign LCOs are always stable, i.e. they are attractors. If a disturbance causes a sudden oscillation amplitude increase or decrease then the system

will always return to the LCO state.

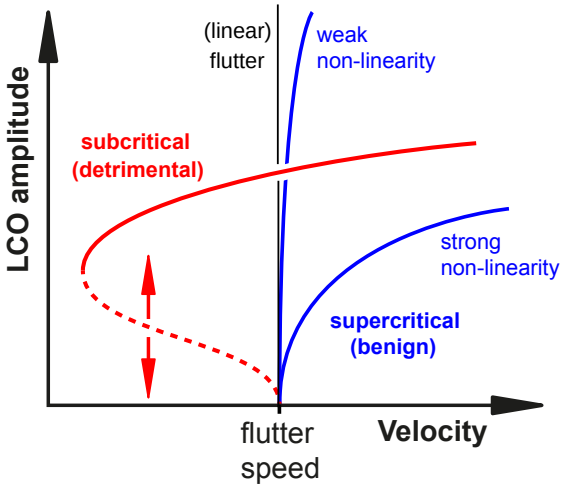

Figure 1.2: Two types of LCO as described by Dowell et al. [32]

The second LCO type that might occur is a detrimental LCO. Detrimental LCOs are those that would occur at airspeeds or dynamic pressures below the flutter boundary. Two LCOs would then exist below the flutter boundary, a stable and an unstable LCO. The unstable LCO is a so-called repeller, which separates two stable conditions (fixed points or LCOs). If a disturbance causes an amplitude increase such that the oscillation amplitude of the system is smaller than the unstable LCO amplitude, then the oscillation amplitude will decay to zero. If the oscillation amplitude after the disturbance is larger than the unstable LCO amplitude, a stable LCO results. For oscillations with initial amplitudes above the stable LCO amplitude, the amplitude will decay to the stable LCO amplitude, since the stable LCO is an attractor. In this manner LCOs might exist below the flutter boundary. In Figure 1.2 unstable LCOs are indicated by a dashed line. The red line indicates the so-called subcritical Hopf bifurcation, which exhibits hysteresis. When the freestream velocity is increased up to the flutter speed, and there is no disturbance larger than the unstable LCO amplitude, at the flutter speed any disturbance will cause a sudden amplitude increase up to the stable LCO amplitude. Then the LCO amplitude increases with freestream velocity. When the freestream velocity is decreased from a velocity above the flutter speed, the stable LCO amplitude decreases, until the point below which no LCOs exist (which is called a saddle-node bifurcation of limit cycles [33]) is reached. At this point the LCO amplitude will drop to zero, i.e. the LCO will disappear. If there is a disturbance larger than the unstable LCO amplitude at a velocity lower than the flutter speed but larger than the velocity at which the saddle-node bifurcation of LCOs occurs, then a stable LCO would occur below the flutter boundary.

1.3. PREVIOUS INVESTIGATIONS ON LIMIT-CYCLE OSCILLATIONS

Several reduced-order models (ROMs) for limit-cycle oscillations caused by aerodynamic non-linearities have been developed. An overview is given in Section 1.3.1. Section 1.3.2 then describes the bifurcation behaviour of limit-cycle oscillations obtained from previous investigations with aerodynamic non-linearities. Finally, the remaining open questions are discussed in Section 1.3.3.

1.3.1. COMPUTATIONAL METHODS

To circumvent computationally expensive fluid-structure interaction (FSI) simulations, various researchers have developed alternative methods. This section presents an overview.

A first alternative method is the aeroelastic harmonic balance (HB) method [34, 35]. This is a frequency domain method which uses an aerodynamic harmonic balance method to solve the governing fluid dynamic equations. In this aerodynamic HB method, the state variables of the flow are described using a Fourier series and then the governing fluid dynamic equations are solved in the frequency domain. Greco et al. [34] developed a frequency-domain transonic small-disturbance equations solver and Hall et al. [36] applied this procedure for the Euler equations. The frequency-domain fluid dynamic equations can easily be coupled to the equations of motion of an aeroelastic system. These equations of motion are then solved iteratively in the frequency domain. The aerodynamic forces are obtained from the HB flow solver at each iteration. Thomas et al. [35, 37–39] and Greco et al. [34] have demonstrated the prediction of limit-cycle oscillations caused by aerodynamic non-linearities by the harmonic balance method. Thomas et al. [37–39] used a RANS-based HB flow solver derived from Hall et al.'s Euler-based flow solver, whereas Thomas et al. [35] used the Euler-based HB solver [36]. Ekici and Hall [40] and Yao et al. [41] have suggested improvements for the coupling of the aerodynamic HB method and the aeroelastic equations of motion. Yao et al. [41] have shown that the results obtained with their aeroelastic harmonic balance method are in good agreement with those obtained from FSI simulations. The harmonic balance method allows for taking into account multiple harmonics in the structural motion and in the aerodynamic response. However, all investigations addressed above have only considered the first harmonic of the structural motion. For the aerodynamic response, in some cases, multiple harmonics were used. Application of the aeroelastic harmonic balance method significantly reduces the computational work compared to coupled time domain simulations, due to the harmonic balance CFD solver.

Another method that can be used to investigate limit-cycle oscillations is to make use of neural networks. In that case a neural network is set up using a certain data set for training. The input to this network is the airfoil's motion and the output are the aerodynamic forces. The network represents the relation between the applied airfoil motion and the aerodynamic forces. The equations of motion are then solved in the time domain with the aerodynamic forces predicted from the neural network. The LCO amplitude is predicted by applying a certain disturbance to the system and identifying the system's response in time, similar as for fluid-structure interaction simulations. This approach has been demonstrated in [42–44]. Balajewicz and Dowell [42] found a good agreement with the bifurcation behaviour obtained from the harmonic balance method when the LCO amplitude was smaller than 3°. For larger amplitudes, no agreement was obtained

with the HB method results. Zhang et al. [44] and Mannarino and Mantegazza [43] compared their results with FSI simulations and observed good agreement when the neural network was sufficiently trained.

A final approach is to use an extended version of a linearised frequency domain method that was actually developed to predict (linear) flutter, such as the p-k method or the k-method. The idea for this extended p-k method was first given by Ueda et al. [45], who used the transonic small disturbance equations as flow solver. The main idea is to take into account the amplitude-dependence of the aerodynamic forces instead of the frequency-dependence only (as in a linearised flutter analysis). Ueda et al. [45] did this using superposition of the aerodynamic forces for a two degree-of-freedom (DoF) airfoil system. To compute the aerodynamic forces a quasi-steady flow assumption was made, which in only valid for low reduced frequencies (< 0.3). Nevertheless, the method of Ueda et al. was found to be successful for stable LCOs of small amplitude (i.e. smaller than 0.5°), in comparison to the results of time domain simulations. The validity of Ueda et al.'s method for larger amplitudes could not be proven, because of numerical instabilities of the flow solver during the reference time domain simulations. Recently, the extended version of the p-k method of Ueda et al. [45] has been used by He et al. [46]. He et al. [46] have dropped the quasi-steady flow assumption and instead used CFD simulations to compute the aerodynamic forces. They also applied superposition of the aerodynamic forces obtained from forced motions of each degree of freedom to obtain the total aerodynamic forces due to the motion of both degrees of freedom simultaneously. He et al. [46] have demonstrated their extended p-k method for different test cases using CFD simulations to compute the aerodynamic forces. Good agreement with other methods (harmonic balance method, direct time integration) was obtained when the non-linearity is weak. For stronger non-linearities deviations compared to the reference time-domain solution (and the harmonic balance solution) are present. Somieski [47] also applied superposition of non-linear forces in an eigenvalue method for the computation of limit-cycle oscillations of an aircraft nose landing gear. He used linear dynamic relations to relate one non-linearity to the other in case of multiple non-linearities in the aeroelastic system. In other words, a certain amplitude relation is chosen, dependent on the frequency, to represent the amplitudes of the other non-linearities as a function of that of the first non-linearity. The results of Somieski [47] were in excellent agreement with direct time domain computations.

1.3.2. LIMIT-CYCLE OSCILLATION BIFURCATION BEHAVIOUR

The main sources of aerodynamic non-linearity of interest for (civil) transport aircraft are moving shock waves and unsteady interactions of these shock waves with the boundary layer. Therefore, most of the previous investigations into the bifurcation behaviour of limit-cycle oscillations have been performed in the transonic flow regime. This flow regime is also the main focus of this thesis. However, limit-cycle oscillations have also been observed in subsonic flows with boundary-layer transition and flow separation. Since, the motivation of this thesis is whether and at which flow conditions subcritical bifurcations occur, a short overview of these limit-cycle oscillations is also presented here.

Numerous investigations have been performed in transonic flow in which various

airfoils have been studied. Schewe et al. [48] and Dietz et al. [49, 50] performed wind-tunnel experiments with the NLR7301 airfoil. Therefore, this airfoil is often used for numerical studies of limit-cycle oscillations. Several researchers [22, 23, 25, 26, 28–30, 37, 51–53] investigated LCOs of the NLR7301 airfoil using either fluid-structure coupling or the harmonic balance method. However, few have considered the bifurcation behaviour of the LCOs found for this airfoil. Thomas et al. [37] studied the bifurcation behaviour of the LCO (pitch) amplitude with the HB method using both viscous and inviscid modelling of the aerodynamics. When the flow was inviscid a large LCO amplitude was found, i.e. the non-linearity is apparently very weak. However, for the viscous case a supercritical bifurcation was observed with smaller amplitudes. Hence, from this study it was concluded that viscous effects are important when studying LCOs caused by aerodynamic non-linearities.

The bifurcation behaviour of the NACA64A010A airfoil was studied by various researchers [43, 44, 54–56] using the same linear structural model. Benign LCOs were found at $M_\infty = 0.8$ and $\alpha_0 = 0°$ in inviscid flow [43, 44, 56]. Kholodar et al. [54, 55] have performed an extensive study on the LCO behaviour of the NACA64A010A airfoil under the variation of two structural parameters (mass ratio and uncoupled natural frequency ratio) using the harmonic balance method in combination with a flow solver for the Euler equations. They found that the mass ratio does not significantly influence the type of LCO behaviour unless the non-linearity is weak. The uncoupled natural frequency ratio was found to influence the stability and the eigenform of the LCOs. When this ratio is increased from 0.5 to 1.8, the LCOs are first stable (supercritical), then become weak and finally unstable (subcritical). The eigenform changes from plunge dominated to a complex pitch/plunge motion to pitch dominated when the frequency ratio is increased. The Mach number was observed to influence the strength of the non-linearity significantly. Small LCO amplitudes, caused by strong non-linearities, were only found in a very limited Mach number range [54, 55].

Kousen and Bendiksen [57] have studied the NACA64A006 airfoil using fluid-structure coupling of the Euler equations with a linear structural model. They found supercritical bifurcation behaviour of the LCO amplitude at several transonic Mach numbers in range from 0.85 to 0.92. At $M = 0.25$ and $M = 0.6$, the oscillations were still growing in amplitude after sixty oscillation cycles.

Balajewicz and Dowell [42] and Zhang et al. [44] have studied the NACA0012 airfoil in inviscid flow numerically using neural networks and found supercritical LCOs (each using a slightly different linear structural model though). In addition, Balajewicz and Dowell [42] also used the HB method for the NACA0012 airfoil in inviscid flow. From this method unstable LCOs were observed at $M = 0.7$ and $M = 0.8$. At $M = 0.95$ both methods predicted a supercritical bifurcation. Raveh and Dowell [58] have also used the NACA0012 airfoil in their study of transonic aerodynamic buffet. They observed LCOs at dynamic pressures below the linearly predicted flutter dynamic pressure when the natural frequencies of their two degree-of-freedom system are close to the buffet frequency.

All of the studies mentioned above considered limit-cycle oscillations in transonic flow. However, limit-cycle oscillations can also occur in subsonic flow, even incompressible flow at low Reynolds numbers. Poirel et al. [24, 59–61] and Yuan et al. [62] studied

the NACA0012 airfoil at Reynolds numbers ranging from $4.5 \cdot 10^4$ to $1.3 \cdot 10^5$, both experimentally and numerically. The airfoil was assigned either one (pitch) or two degrees of freedom (pitch, plunge). Limit-cycle oscillations of small amplitude ($<\sim 6°$) were observed in this Reynolds number range. These small-scale LCOs are attributed to the dynamics of the laminar separation bubble [59]. They were also found from aeroelastic numerical simulations in the time domain [60]. In addition, for the two degree-of-freedom system large-amplitude LCOs occurred ($\gtrsim 10°$). These are probably caused by flow separation at large angles of attack [61]. The large-amplitude LCOs do also occur when a trip wire at 18% of the chord length is applied on the airfoil's surface [61] (in order to trigger transition). On the other hand, the small-scale LCOs disappear when the trip wire is applied [61]. These investigations demonstrate that a laminar separation bubble (LSB) and laminar trailing-edge separation might be another source of aerodynamic non-linearity. Poirel and Mendes [61] have also varied the uncoupled natural frequency ratio by a variation of the plunge stiffness for the two degree-of-freedom airfoil system. It was observed that for an increase of this ratio from 0.74 to 1.2, the LCO amplitude of both the small-amplitude and the large-scale LCOs increased and the range of Reynolds number for which the small-amplitude LCOs were observed decreased. For a natural frequency ratio of 1.63 the Reynolds number range for which small-amplitude LCOs exist has increased compared to a frequency ratio of 1.2, but is still smaller than at a frequency ratio of 0.74.

1.3.3. CONCLUSIONS AND OPEN QUESTIONS

The central question of this thesis, as stated in Section 1.1, is whether aerodynamic non-linearities might cause limit-cycle oscillations already below the flutter boundary predicted from linearised theory. The literature overview given in this section showed that several researchers have studied limit-cycle oscillations caused by aerodynamic non-linearities. Furthermore, limit-cycle oscillations were found, from numerical simulations or wind-tunnel measurements, in both subsonic and transonic flow, i.e. caused by various sources of non-linearity. The bifurcation behaviour of these limit-cycle oscillations was also studied by a few researchers, especially in transonic flow. However, most of these studies have found supercritical bifurcation behaviour of the LCO amplitude. Only two studies, who considered transonic inviscid flow, have observed subcritical bifurcations (predicted by the harmonic balance method).

Hence, the question whether a subcritical bifurcation of the LCO amplitude can occur and at what flow conditions and with which structure, has not been systematically addressed by the research community. Especially for realistic flight conditions, i.e. for viscous transonic flows, almost no systematic investigations into LCO bifurcation behaviour were performed and those researchers that studied LCOs at these flow conditions, did not observe subcritical bifurcations of the LCO amplitude [37]. The main focus of this thesis will therefore be on subcritical bifurcations caused by aerodynamic non-linearities occurring in the transonic flow regime, i.e. shock wave motion and unsteady shock-wave boundary-layer interaction. Non-linearities occurring in subsonic flow will be addressed as well. Their detailed analysis is however out of the scope of this thesis.

Furthermore, the effect of variations of the structural model and of the aerodynamic flow conditions on the bifurcation behaviour has only been addressed briefly by two re-

search groups, in inviscid transonic flow [54, 55] and in subsonic flow with free boundary-layer transition [61]. However, since the structural model might be epistemically uncertain, it is very important to know what happens to the LCO behaviour when the structural model changes. Hence, another open question is whether a change in the structural model can result in a change in the bifurcation behaviour in viscous transonic flow.

In addition, no studies into the relation between the aerodynamic forces and the bifurcation behaviour of the limit-cycle oscillations have been performed. However, such studies are thought to be essential in order to find the sources of amplitude limitation and to possibly avoid the occurrence of LCOs. Concretely, the following questions regarding the type of bifurcation of limit-cycle oscillations have not been answered satisfactory by the research community:

- Can stable limit-cycle oscillations occur below the (linear) flutter boundary, i.e. can the bifurcation behaviour be subcritical, in the presence of aerodynamic non-linearities only or are structural non-linearities necessary?
- Is it possible to have unstable LCOs only without stable LCOs in the presence of aerodynamic non-linearities?
- Is it possible to deduce the bifurcation behaviour of an LCO solution from the (linear) flutter behaviour?
- What is the influence of uncertain parameters of the structural model on the bifurcation behaviour?
- Which types of bifurcations are possible in subsonic laminar/transitional flow?
- How are the aerodynamic forces, and the occuring type of bifurcation, related?

In order to be able to study limit-cycle oscillation bifurcation behaviour and thus answer the questions stated above, a computationally efficient method is necessary. Therefore, as suggested by the computational methods outlined in Section 1.3.1, a frequency-domain based non-linear reduced-order model is developed in this thesis. This ROM will be an adapted version of the p-k method which will take into account the amplitude-dependence of the aerodynamic forces via an aerodynamic response surface. This response surface is set up using harmonic forced motion oscillations at several amplitudes, frequencies and complex-valued amplitude ratios between the degrees of freedom. This leads to an improvement in accuracy compared to the extended p-k methods of Ueda et al. [45], He et al. [46] and Somieski [47], since no superposition of the aerodynamic forces is applied. The aerodynamic forces will be computed in a similar way as for the aerodynamic harmonic balance method [34, 35], which does not apply superposition of the aerodynamic forces either. However, in the aeroelastic HB method, a HB flow solver is used to obtain the aerodynamic forces during the solution procedure of the aeroelastic equations of motion. In the ROM developed in this thesis work, on the other hand, the aerodynamic forces are interpolated on the aerodynamic response surface (which is obtained a-priori from harmonic forced motion oscillations) during the iterations of the equations of motion-solver. Since the ROM will be a frequency domain method, it will be possible to separate the aerodynamics and the structure, such that structural parameter

variations can be easily studied once an aerodynamic response is available. Furthermore, using the ROM it might be possible to relate certain features in the aerodynamic response surface to a certain type of bifurcation behaviour of the limit-cycle oscillations. When this is possible, can certain aerodynamic features (reversed shock motion, shock-induced separation, etc.) even be linked to a certain response surface shape? And hence to a certain bifurcation type? To the knowledge of the author, these questions have not been answered yet by other investigators who studied limit-cycle oscillations caused by aerodynamic non-linearities.

1.4. OBJECTIVES

From the open questions stated in Section 1.3.3, the objectives of this thesis are derived. The main objective of this thesis is to study the bifurcation behaviour of LCOs caused by aerodynamic non-linearities. In doing so, the main research questions of this thesis will be answered. To be able to find out whether a subcritical bifurcation of the LCO amplitude can occur due to aerodynamic non-linearities only, several sub-objectives are defined. Concretely, these objectives are to:

- Identify the sources of the amplitude limitation in a limit-cycle oscillation caused by an aerodynamic non-linearity. An energy budget analysis of a limit-cycle oscillation is performed, in order to identify why the LCO establishes itself and what global features are responsible for this amplitude limitation. The results of this analysis can be used to find out if there is a relation between the aerodynamic forces and the bifurcation behaviour.
- Develop and validate a frequency domain ROM for estimating the LCO amplitude. This method is necessary in order to study the bifurcation behaviour of the limit-cycle oscillations in a computationally efficient way. The working principle of the developed non-linear ROM is first verified using analytical test cases, because for these test cases exact solutions are available and no expensive CFD simulations are necessary. Once the working principle has been established, the non-linear ROM is validated using coupled FSI simulation results, to assure that the developed non-linear ROM is sufficiently accurate.
- Study the bifurcation behaviour of limit-cycle oscillations caused by various sources of aerodynamic non-linearity using the developed ROM. In this way, it can be established whether stable limit-cycle oscillations can already occur below the flutter boundary and for aerodynamic non-linearities these subcritical bifurcations occur.
- Investigate the effect of a change in the structural model on the bifurcation behaviour of the limit-cycle oscillation amplitude. The nominal structural model may result in a supercritical bifurcation, but a change in bifurcation behaviour of the limit-cycle oscillation amplitude might occur when the structural model changes.
- Find a relation between the aerodynamic features and the type of bifurcation that occurs. When it is possible to relate the behaviour of the aerodynamic forces or the

local pressure distributions to the bifurcation behaviour, then this relation might be used to quickly establish the type of bifurcation that will occur based on a few forced motion oscillation simulations.

It should be noted here that the ROM developed in this thesis is only a means to study the bifurcation behaviour of the limit-cycle oscillations at reduced computational costs and therefore no optimisation in terms of the efficiency of the ROM is attempted in this thesis. Furthermore, to study the (subcritical) bifurcation behaviour of limit-cycle oscillations caused by aerodynamic non-linearities, this thesis will consider a two-dimensional aeroelastic problem, i.e. an airfoil system with two degrees of freedom; bending and torsion. As these two degrees of freedom usually couple during flutter of three-dimensional wings as well, this is thought to be a good first step.

1.5. OUTLINE OF THE THESIS

Chapter 2 of this thesis describes the aeroelastic problems considered in this thesis and discusses the methods that are used to solve them. Chapter 3 considers the energy budget of limit-cycle oscillations. Time-consuming fluid-structure interaction simulations are used together with simulations in which the airfoil is forced to perform a sinusoidal motion to analyse the energy budget during LCO development. This gives insight into the factors responsible for the amplitude limitation. The frequency domain method used for computing the LCO amplitude and mode shape is verified and validated in Chapter 4. Furthermore, the first applications of the amplitude-dependent p-k method ADePK are shown in Chapter 4. In Chapter 5 ADePK is applied to study the LCO bifurcation behaviour of several aerodynamic non-linearities (e.g. shock waves, trailing-edge separation, boundary layer transition). In addition, the influence of several structural model parameters on the bifurcation behaviour is studied (in both viscous and inviscid flow). Also, the effect of a change in Mach number is analysed in inviscid flow. The final part of Chapter 5 considers the response surface necessary for the frequency domain method. The response surface is analysed and related to the bifurcation behaviour. The aerodynamic non-linearities responsible for the response surface curvature are identified. Finally, Chapter 6 presents the conclusions of this thesis and an outlook to future work.

REFERENCES

[1] R. Kimberlin, *Flight testing of fixed-wing aircraft* (American Institute of Aeronautics and Astronautics, Inc, 2003).

[2] C. Dreyer and D. Shoch, *F-16 flutter testing at eglin air force base,* (Las Vegas, NV, USA, 1986) 3rd Flight Testing Conference.

[3] P. Chen, D. Sarhaddi, and D. Liu, *Limit-cycle-oscillation studies of a fighter with external stores,* (1998) AIAA Paper 98-1727.

[4] C. Denegri, *Limit cycle oscillation flight test results of a fighter with external stores,* Journal of Aircraft **37**, 761 (2000).

[5] R. Bunton and C. Denegri, *Limit cycle oscillation characteristics of fighter aircraft,* Journal of Aircraft **37**, 916 (2000).

[6] D. Tang and E. Dowell, *Flutter and stall response of a helicopter blade with structural nonlinearity,* Journal of Aircraft **29**, 953 (1992).

[7] K. Kousen and O. Bendiksen, *Limit cycle phenomena in computational transonic aeroelasticity,* Journal of Aircraft **31**, 1257 (1994).

[8] D. Qian and W. Dong-Li, *The flutter of an airfoil with cubic structural and aerodynamic non-linearities,* Aerospace Science and Technology **10**, 427 (2006).

[9] E. Camilo, F. Marques, and J. Azevedo, *Hopf bifurcation analysis of typical sections with structural nonlinearities in transonic flow,* Aerospace Science and Technology **30**, 163 (2013).

[10] Z. Yang, S. He, and Y. Gu, *Transonic limit cycle oscillation behavior of an aeroelastic airfoil with free-play,* Journal of Fluids and Structures **66**, 1 (2016).

[11] N. Razak and G. Dimitriadis, *Aeroelastic response of a 2-dof wing with structural and aerodynamic non-linearity,* (Bristol, UK, 2013) internation Forum on Aeroelasticity and Structural Dynamics.

[12] Z. Yang and L. Zhao, *Analysis of limit cycle flutter of an airfoil in incompressible flow,* Journal of Sound and Vibration **123**, 1 (1988).

[13] M. Conner, D. Tang, E. Dowell, and L. Virgin, *Nonlinear behavior of a typical airfoil section with control surface freeplay: A numerical and experimental study,* Journal of Fluids and Structures **11**, 89 (1997).

[14] B. Lee and P. LeBlanc, *Flutter Analysis of a Two-Dimensional Airfoil with Cubic Non-linear Restoring Force,* Tech. Rep. NRC No. 25438 (National Research Council Canada, 1986) aeronautical Note NAE-AN-36.

[15] S. Price, H. Alighanbari, and B. Lee, *The aeroelastic response of a two-dimensional airfoil with bilinear and cubic structural nonlinearities,* Journal of Fluids and Structures **9**, 175 (1995).

[16] B. Lee, L. Gong, and Y. Wong, *Analysis and computation of nonlinear dynamic response of a two-degree-of-freedom system and its application in aeroelascitity,* Journal of Fluids and Structures **11**, 225 (1997).

[17] L. Liu and E. Dowell, *Harmonic balance approach for an airfoil with a freeplay control surface,* AIAA Journal **43**, 802 (2005).

[18] B. Ghadari and M. Razi, *Limit cycle oscillations of rectangular cantilever wings containing cubic nonlinearity in an incompressible flow,* Journal of Fluids and Structures **23**, 665 (2007).

[19] G. Gai and S. Timme, *Nonlinear reduced-order modelling for limit-cycle oscillation analysis,* Nonlinear Dynamics **84**, 991 (2016).

[20] A. Ghadami and B. Epureanu, *Bifurcation forecasting for large dimensional oscillatory systems: Forecasting flutter using gust responses,* Journal of Computational and Nonlinear Dynamics **11** (2016).

[21] B. Lee, S. Price, and Y. Wong, *Nonlinear aeroelastic analysis of airfoils: bifurcation and choas,* Progress in Aerospace Sciences **35**, 205 (1999).

[22] O. Bendiksen, *Transonic limit cycle flutter/lco,* (Univerisity of California, Los Angelos, Palm Springs, California, 2004) 45th AIAA/ASME/ASCE/AHS/ASC Structures, Structural Dynamics, and Materials Conference.

[23] S. Weber, K. Jones, J. Ekaterinaris, and M. Platzer, *Transonic flutter computations for a 2d supercritical wing,* (Naval Postgraduate School, Monterey, CA, Reno, NV, 1999) 37th AIAA/ASME/ASCE/AHS/ASC Structures, Structural Dynamics, and Materials Conference and Exhibit.

[24] D. Poirel, Y. Harris, and A. Benaissa, *Self-sustained aeroelastic oscillations of a naca0012 airfoil at low-to-moderate reynolds numbers,* Journal of Fluids and Structures **24**, 700 (2008).

[25] L. Tang, R. Bartels, P. Chen, and D. Liu, *Numerical investigation of transonic limit cycle oscillations of a two-dimensional supercritical wing,* Journal of Fluids and Structures **17**, 29 (2003).

[26] L. Tang, R. Bartels, P. Chen, and D. Liu, *Simulation of transonic limit cycle oscillations using a CFD time-marching method,* (Seattle, WA, 2001) 42nd AIAA/ASME/ASCE/AHS/ASC Structures, Structural Dynamics, and Materials Conference and Exhibit.

[27] R. Voss, *Numerical simulations of limit cycle oscillations in transonic airfoil flow with mild separation,* (Deutsches Zentrum für Luft- und Raumfahrt, Institut für Aeroelastik, Madrid, Spain, 2001) international Forum on Structural Dynamics and Aeroelasticity (IFASD).

[28] B. Wang and G.-C. Zha, *Numerical simulation of transonic limit cycle oscillations using high-order low-diffusion schemes,* Journal of Fluids and Structures **26**, 579 (2010).

[29] S. Weber, K. Jones, J. Ekaterinaris, and M. Platzer, *Transonic flutter computations for the NLR 7301 supercritical airfoil,* Aerosp. Sci. Technology **5**, 293 (2001).

[30] K. Saitoh and H. Kheirandish, *Numerical simulation of small amplitude lco for NLR-7301 profile,* (Stockholm, Sweden, 2007) international Forum on Structural Dynamics and Aeroelasticity (IFASD).

[31] E. Dowell, *A Modern Course in Aeroelasticity* (Kluwer Academic Publishers, 2004).

[32] E. Dowell, J. Edwards, and T. Strganac, *Nonlinear aeroelasticity,* Journal of Aircraft **40**, 857 (2003).

[33] C. Gros, *Bifurcations and Choas in Dynamical Systems*, Tech. Rep. (Goethe Universität Frankfurt am Main, 2014) lecture notes course Self-Organization: Theory and Simulation.

[34] P. Greco, C. Lan, and T. Lim, *Frequency domain unsteady transonic aerodynamics for flutter and limit cycle oscillation prediction,* (Reno, NV, USA, 1997) 35th AIAA Aerospace Sciences Meeting & Exhibit.

[35] J. Thomas, E. Dowell, and K. Hall, *Nonlinear inviscid aerodynamic effects on transonic divergence, flutter and limit-cycle oscillations,* AIAA Journal **40**, 638 (2002).

[36] K. Hall, J. Thomas, and W. Clark, *Computation of unsteady nonlinear flows in cascades using a harmonic balance technique,* AIAA Journal **40** (2002).

[37] J. Thomas, E. Dowell, and K. Hall, *Modeling viscous transonic limit cycle oscillation behavior using a harmonic balance approach,* (Duke University, Durham, NC, Denver, CO, 2002) 43rd AIAA/ASME/ASCE/AHS/ASC Structures, Structural Dynamics, and Materials Conference and Exhibit.

[38] J. Thomas, E. Dowell, K. Hall, and C. Denegri, *Modeling limit cycle oscillation behaviour of the f-16 fighter using a harmonic balance approach,* (Palm Springs, CA, USA, 2004) 45th AIAA/ASME/ASCE/AHS/ASC Structures, Structural Dynamics, and Materials Conference and Exhibit.

[39] J. Thomas, E. Dowell, K. Hall, and C. Denegri, *Further investigation of modeling limit cycle oscillation behaviour of the f-16 fighter using a harmonic balance approach,* (2005) 46th AIAA/ASME/ASCE/AHS/ASC Structures, Structural Dynamics, and Materials Conference and Exhibit.

[40] K. Ekici and K. Hall, *Harmonic balance analysis of limit cycle oscillations in turbomachinery,* AIAA Journal **49** (2011).

[41] W. Yao and S. Marques, *Prediction of transonic limit-cycle oscillations using an aeroelastic harmonic balance method,* AIAA Journal **53** (2015).

[42] M. Balajewicz and E. Dowell, *Reduced-order modeling of flutter and limit-cycle oscillations using the sparse volterra series,* Journal of Aircraft **49** (2012).

[43] A. Mannarino and P. Mantegazza, *Nonlinear aeroelastic reduced order modeling by recurrent neural networks,* Journal of Fluids and Structures **48**, 103 (2014).

[44] W. Zhang, B. Wang, Z. Ye, and J. Quan, *Efficient method for limit cycle flutter analysis by nonlinear aerodynamic reduced-order models,* AIAA Journal **50** (2012).

[45] T. Ueda and E. Dowell, *Flutter analysis using nonlinear aerodynamic forces,* Journal of Aircraft **21** (1984).

[46] S. He, Z. Yang, and Y. Gu, *Transonic limit cycle oscillation analysis using aerodynamic describing functions and superposition principle,* AIAA Journal **52** (2014).

[47] G. Somieski, *An eigenvalue method for calculation of stability and limit cycles in nonlinear systems,* Nonlinear Dynamics **26**, 3 (2001).

[48] G. Schewe, H. Mai, and G. Dietz, *Nonlinear effects in transonic flutter with emphasis on manifestations of limit cycle oscillations,* Journal of Fluids and Structures **18**, 3 (2003).

[49] G. Dietz, G. Schewe, and H. Mai, *Experiments on heave/pitch limit-cycle oscillations of a supercritical airfoil close to the transonic dip,* Journal of Fluids and Structures **19**, 1 (2004).

[50] G. Dietz, G. Schewe, and H. Mai, *Amplification and amplitude limitation of heave/pitch limit-cycle oscillations close to the transonic dip,* Journal of Fluids and Structures **22**, 505 (2006).

[51] B. Castro, K. Jones, J. Ekaterinaris, and M. Platzer, *Analysis of the effect of porous wall interference on transonic airfoil flutter,* (Naval Postgraduate School, Monterey, CA, Anaheim, CA, 2001) 31st AIAA Fluid Dynamics Conference & Exhibit.

[52] J. Thomas, E. Dowell, and K. Hall, *Modeling limit cycle oscillations for an NLR 7301 airfoil aeroelastic configuration including correlation with experiment,* (Duke University, Durham, NC, Norfolk, VA, 2003) 44th AIAA/ASME/ASCE/AHS/ASC Structures, Structural Dynamics, and Materials Conference and Exhibit.

[53] K. Saitoh, R. Voss, and H. Kheirandish, *Numerical study of nonlinearity of unsteady aerodynamics for NLR7301 profile,* (Munich, Germany, 2005) international Forum on Structural Dynamics and Aeroelasticity (IFASD).

[54] D. Kholodar, J. Thomas, and E. Dowell, *A parameter study of transonic airfoil flutter and limit cycle oscillation behaviour,* (Denver, CO, 2002) 43rd AIAA/ASME/ASCE/AHS/ASC Structures, Structural Dynamics, and Materials Conference and Exhibit.

[55] D. Kholodar, E. Dowell, J. Thomas, and K. Hall, *Limit-cycle oscillations of a typical airfoil in transonic flow,* Journal of Aircraft **41** (2004).

[56] E. Dowell and D. Tang, *Nonlinear aeroelasticity and unsteady aerodynamics,* AIAA Journal **40**, 1697 (2002).

[57] K. Kousen and O. Bendiksen, *Nonlinear aspects of the transonic aeroelastic stability problem,* (1988) AIAA/ASME/ASCE/AHS 29th Structures, Structural Dynamics and Materials Conference.

[58] D. Raveh and E. Dowell, *Aeroelastic responses of elastically suspended airfoil systems in transonic buffeting flows,* AIAA Journal **52**, 926 (2014).

[59] D. Poirel and W. Yuan, *Aerodynamics of laminar separation flutter at a transitional reynolds number,* Journal of Fluids and Structures **26**, 1174 (2010).

[60] D. Poirel, V. Métivier, and G. Dumas, *Computational aeroelastic simulations of self-sustained pitch oscillations of a naca0012 at transitional reynolds numbers,* Journal of Fluids and Structures **27**, 1262 (2011).

[61] D. Poirel and F. Mendes, *Experimental small-amplitude self-sustained pitch-heave oscillations at transitional reynolds numbers,* AIAA Journal **52**, 1581 (2014).

[62] W. Yuan, D. Poirel, and B. Wang, *Simulations of pitch-heave limit-cycle oscillations at a transitional reynolds number,* AIAA Journal **51**, 1716 (2013).

2

AEROELASTIC PROBLEM DESCRIPTION AND SOLUTION STRATEGIES

2.1. INTRODUCTION

This chapter describes the aeroelastic problem that has been studied in this thesis, a two DoF airfoil system and the solution strategies to solve this problem. The airfoil, the structural model and the fluid model are presented first. Then, the solution strategies used to solve the aeroelastic problem are addressed. Both time and frequency domain methods have been applied. In the time domain, fluid-structure coupling is applied. The details of this coupling are shortly described in Section 2.3. The frequency domain method used for linear flutter prediction is presented in Section 2.4. Section 2.5 describes the frequency domain-based non-linear ROM developed in this thesis for the prediction of LCOs, the amplitude-dependent p-k method ADePK.

2.2. AEROELASTIC PROBLEM DESCRIPTION

To solve an aeroelastic problem, a model of the system is needed. In the structural model the stiffness is modelled by linear springs which are proportional to the displacement. Structural damping, if present, is modelled by viscous damping proportional to the velocity. Additionally, aerodynamic forces are present when the system is placed in a fluid flow. The aerodynamic forces are in general non-linear functions of the displacement, velocity and acceleration. Newton's second law is used to derive the equations of motion of an aeroelastic system. In matrix form the equations of motion for a general aeroelastic problem of n degrees of freedom are given by:

Parts of this chapter have been published in van Rooij et al., Prediction of aeroelastic limit-cycle oscillations based on harmonic forced motion oscillations, AIAA journal (submitted).

$$\mathbf{M}\ddot{\vec{x}} + \mathbf{D}\dot{\vec{x}} + \mathbf{K}\vec{x} = \vec{f}\left(\vec{x}, \dot{\vec{x}}, \ddot{\vec{x}}\right), \tag{2.1}$$

where **M** is the mass matrix, containing the masses, mass moments of inertia and the static moments, **D** is the structural damping matrix, **K** contains the structural stiffnesses and $\vec{f}$ the aerodynamic forces. $\vec{x}$ is the displacement vector containing the displacements of all degrees of freedom (DoFs). The mass, damping and stiffness are nxn-matrices. The displacement vector $\vec{x}$ and the force vector $\vec{f}$ are n-dimensional vectors.

The aeroelastic problems considered in this thesis will be restricted to a maximum of two degrees of freedom. The general equations of motion for such a system are given by (2.1). To study the behaviour of limit-cycle oscillations based on aerodynamic non-linearities only, a two degree of freedom airfoil system without structural non-linearities will be considered. This two DoF aeroelastic system is allowed to pitch (i.e. rotate) and plunge (i.e. translate vertically). Figure 2.1 shows an example of an airfoil system with two degrees of freedom. It consists of two springs and two dampers.

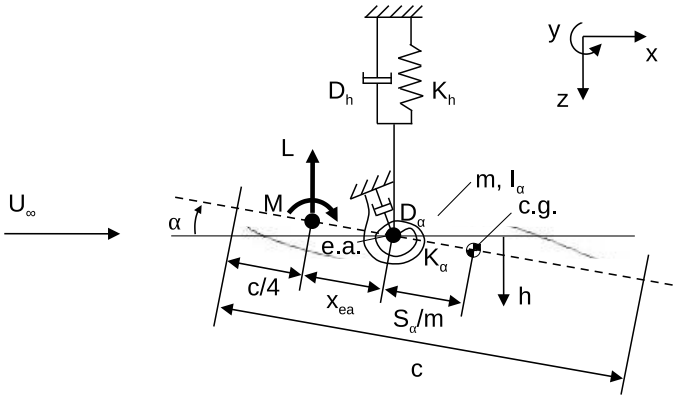

Figure 2.1: Sketch of the model with two degrees of freedom

The equations of motion of this two DoF system are derived using conservation of linear and angular impulse. Linear and angular impulse, denoted by $\vec{G}$ and $\vec{H}$, respectively, are defined as:

$$\dot{\vec{G}} = m\vec{a} = \sum \vec{F} \tag{2.2}$$

$$\dot{\vec{H}} = m\vec{r} \times \vec{a} = \sum \vec{M}_{\text{ea}}, \tag{2.3}$$

where m is the mass, $\vec{a}$ the accerelation vector and $\vec{r}$ the displacement vector of the system. $\vec{F}$ is the vector containing the external forces in x, y and z-direction and $\vec{M}_{\text{ea}}$ is the vector containing the moments about all three axis. For the two DoF system depicted in Figure 2.1, the conservation of linear impulse in z-direction and the conservation of angular impulse about the y-axis are needed to derive the equations of motion. In order to do so the displacement vector $\vec{r}$ of the system is needed. This vector is defined as:

$$\vec{r} = \begin{bmatrix} \frac{S_\alpha}{m}\cos(\alpha) \\ h + \frac{S_\alpha}{m}\sin(\alpha) \\ 0 \end{bmatrix}, \tag{2.4}$$

where S_α the static mass moment around the elastic axis. The plunge displacement is denoted by h and the rotation around the elastic axis by α. Now it is assumed that α is small such that $\sin(\alpha) \approx \alpha$ and $\cos(\alpha) \approx 1$, hence $\vec{r}$ becomes:

$$\vec{r} = \begin{bmatrix} \frac{S_\alpha}{m} \\ h + \frac{S_\alpha}{m}\alpha \\ 0 \end{bmatrix}. \tag{2.5}$$

The acceleration vector a is then given by:

$$\ddot{\vec{r}} = \vec{a} = \begin{bmatrix} 0 \\ \ddot{h} + \frac{S_\alpha}{m}\ddot{\alpha} \\ 0 \end{bmatrix}. \tag{2.6}$$

The linearised equations of motion are now obtained using (2.2), (2.3), (2.5) and (2.6):

$$\underbrace{\begin{bmatrix} m & S_\alpha \\ S_\alpha & I_\alpha \end{bmatrix}}_{\mathbf{M}} \underbrace{\begin{bmatrix} \ddot{h} \\ \ddot{\alpha} \end{bmatrix}}_{\ddot{\vec{x}}} + \underbrace{\begin{bmatrix} D_h & 0 \\ 0 & D_\alpha \end{bmatrix}}_{\mathbf{D}} \underbrace{\begin{bmatrix} \dot{h} \\ \dot{\alpha} \end{bmatrix}}_{\dot{\vec{x}}} + \underbrace{\begin{bmatrix} K_h & 0 \\ 0 & K_\alpha \end{bmatrix}}_{\mathbf{K}} \underbrace{\begin{bmatrix} h \\ \alpha \end{bmatrix}}_{\vec{x}} = \underbrace{\begin{bmatrix} -L \\ M + x_{\text{ea}} \cdot L \end{bmatrix}}_{\vec{f}}, \tag{2.7}$$

where I_α the mass moment of inertia, K_h the plunge stiffness, K_α the torsional stiffness, D_h is the plunge damping and D_α is the torsional damping. The aerodynamic force vector $\vec{f}$ consists of the aerodynamic lift L and the moment around the elastic axis $M + x_{\text{ea}} L$, where M is the moment about the quarter-chord point and x_{ea} the distance between the quarter-chord point and the elastic axis, which is positive when the elastic axis is located aft of the quarter-chord point. Note that in the definition of the moment around the elastic axis, the small-angle assumption has again been used.

2.2.1. NLR7301 AIRFOIL

The airfoil used in this thesis is the NLR7301 airfoil. This airfoil has been used for various wind tunnel tests [1–9] and numerical investigations e.g. [10–20]. The airfoil, originally designated as the NLR HT 7310810 airfoil, has been designed by the holograph method [21] developed at the National Aerospace Laboratory (NLR). It is a supercritical airfoil with a design Mach number of 0.721 and a design lift coefficient of 0.595. For the wind-tunnel measurements performed by Zwaaneveld [1], the airfoil was manufactured having a 1% thick trailing-edge, instead of the sharp trailing-edge the theoretical NLR HT 7310810 airfoil had. Therefore the wind-tunnel model was renamed to NLR7301 airfoil. Experimentally the shock-free design pressure distribution was established to occur at $M = 0.747$ and at a lift coefficient c_l of 0.455 (in case of free boundary layer transition) [1]. The theoretically and experimentally obtained shock-free pressure distributions as well as the airfoil itself are depicted in Figure 2.2 (which has been taken from [1]). The

theoretical pressure distribution shown in this figure has been obtained from potential theory by Boerstoel and van Egmond [22]. The NLR7301 airfoil is relatively thick, with a maximum thickness of 16.5%. The nose radius of the airfoil is 5% of the chord length. Since the cut-off trailing-edge NLR7301 airfoil has been used in various experiments and numerical studies (as mentioned above), this airfoil, with the coordinates of Zwaaneveld [2], has also been used in this thesis. Although it should be noted here that the purpose of this thesis is not to directly compare the results obtained in this work to those obtained from the wind-tunnel experiments mentioned above. Nevertheless, a small validation has been performed for two steady test cases of Dietz et al. [8], see Appendix A.

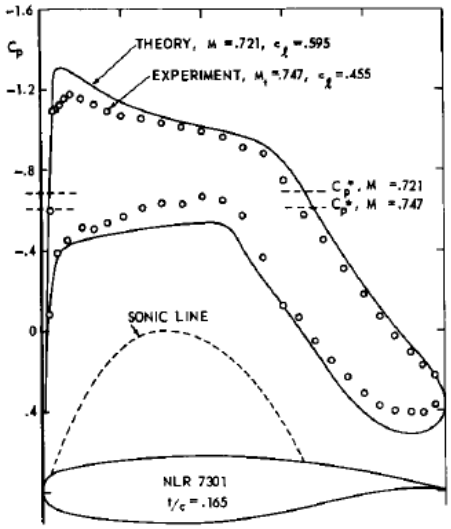

Figure 2.2: Design pressure distribution of the NLR7301 airfoil [1]

2.2.2. STRUCTURAL MODEL

The structural model consists of a set of mass, stiffness and damping properties of the airfoil structure. These are constant when the structural model is linear, as is the case throughout this thesis. Schewe et al. [5, 6] and Dietz et al. [7–9] have tested the NLR7301 airfoil in the Transonic Wind Tunnel Göttingen (TWG). The structural properties of this airfoil model were used as a starting point in this thesis. Table 2.1 provides these properties, which were taken from [8]. Note that in comparison to the classical two DoF system, the elastic axis is located at the quarter-chord point, i.e. $x_{ea} = 0$ m. Other elastic axis locations will be studied in Chapter 5. The chord length c and the structural properties m, I_α, K_α, K_h and S_α were determined from direct measurements. In addition, a ground vibration test has been carried out in order to correct the measured values obtained for the mass moment of inertia, the static mass moment and the plunge spring stiffness [8]. The pitch and plunge damping constants were obtained from the ground vibration test as well. More details can be found in [8].

Structural parameter	Value
Wing span b	1.0 m
Chord length c	0.3 m
Mass m	26.268 kg
Mass moment of inertia (about the elastic axis) I_α	0.079 kgm^2
Torsional spring stiffness K_α	$6.646 \cdot 10^3$ Nm/rad
Plunge spring stiffness K_h	$1.078 \cdot 10^6$ N/m
Static moment related to EA S_α	0.331 kgm
Pitch damping D_α	0.0687 kgm^2/s/rad
Plunge Damping D_h	45.764 kg/s
Distance between quarter-chord point and elastic axis x_{ea}	0 m

Table 2.1: Structural parameters for the two DoF NLR7301 airfoil system (taken from Dietz et al. [8])

2.2.3. FLUID MODEL

The fluid is modelled using the Computational Fluid Dynamics (CFD). In this thesis either the Euler equations or the Reynolds-Averaged Navier-Stokes (RANS) equations (or Favre-Averaged Navier-Stokes equations when the flow is compressible) are solved. The CFD code used is the TAU code [23], which was developed by the German Aerospace Center. The compressible RANS equations are derived from the Navier-Stokes (NS) equations. The conservative form of the NS-equations is:

$$\frac{\partial \rho}{\partial t} + \nabla \cdot \left(\rho \vec{u}\right) = 0, \tag{2.8}$$

$$\frac{\partial \left(\rho \vec{u}\right)}{\partial t} + \nabla \cdot \left(\rho \vec{u} \otimes \vec{u}\right) = -\nabla p + \nabla \cdot \bar{\bar{\tau}}, \tag{2.9}$$

$$\frac{\partial \left(\rho E\right)}{\partial t} + \nabla \cdot \left(\rho E \vec{u}\right) = -\nabla \cdot \left(p \vec{u}\right) + \nabla \cdot \left(\vec{u} \cdot \bar{\bar{\tau}}\right) + \nabla \cdot \vec{q}, \tag{2.10}$$

where in ρ is the density, $\vec{u} = [u, v, w]^T$ is the velocity vector, p is the pressure, T is the temperature, $E = e + \frac{1}{2}\left(u^2 + v^2 + w^2\right)$ is the total specific energy (here e is the internal energy) and $\vec{q} = -k\nabla T$ is the heat flux vector, where k is the thermal conductivity. In (2.9), $\vec{u} \otimes \vec{u}$ represents the tensor product of the velocity vector with itself. In (2.10), $\bar{\bar{\tau}}$ is the stress tensor, whose components are given by:

$$\tau_{ij} = \mu\left(\frac{\partial u_i}{\partial x_j} + \frac{\partial u_j}{\partial x_i}\right) + \lambda \delta_{ij} \frac{\partial u_k}{\partial x_k}, \tag{2.11}$$

where μ is the dynamic viscosity, λ the Lamé coefficient and δ_{ij} the Kronecker delta. The Lamé coefficient is usually taken as: $\lambda = -\frac{2\mu}{3}$ [24].

In order to have the same number of equations as there are unknowns, an equation of state is needed to complete the system. For a perfect gas in terms of the internal energy this is:

$$p = (\kappa - 1)\,\rho e = (\kappa - 1)\,\rho\left(E - \frac{1}{2}\left(u^2 + v^2 + w^2\right)\right), \tag{2.12}$$

2

where κ is the ratio of specific heats.

In the Reynolds-/Favre-Averaged Navier-Stokes approach it is assumed that the flow quantities can be decomposed into an average and a fluctuation around this average. In the compressible case, i.e. in order to derive the Favre-Averaged Navier-Stokes equations, two decompositions are used. The first decomposition, which is also used for incompressible flows, is known as the Reynolds' average. The Reynolds' average, which is a time-average, is given by:

$$\phi(x,t) = \bar{\phi}(x,t) + \phi'(x,t), \tag{2.13}$$

where ϕ represents a flow quantity. The mean is indicated by a bar and the fluctuation of the flow quantity is indicated by an accent. The second decomposition is the Favre average [25, 26] (also known as the mass average). This decomposition is used for compressible flows, since in that case it is impractical to use only the Reynolds' decomposition, because extra unknowns will result. The Favre average [25, 26] is defined as [27]:

$$\phi = \frac{\overline{\rho\phi}}{\bar{\rho}} + \phi'' = \tilde{\phi} + \phi'', \tag{2.14}$$

where the fluctuation of a flow quantity is now indicated by a double accent and the Favre average is indicated by a tilde. To derive the Favre-averaged Navier-Stokes equations for a compressible flow, the Reynolds' average is used for the pressure and the density, whereas the Favre average is used for the other flow quantities (such as the velocity components). When these decompositions are substituted in (2.8), (2.9) and (2.10) and when the time average (i.e. the Reynolds' average) is taken of the resulting equations, the following Favre-Averaged Navier-Stokes equations result [27]:

$$\frac{\partial \bar{\rho}}{\partial t} + \frac{\partial(\bar{\rho}\tilde{u}_j)}{\partial x_j} = 0, \tag{2.15}$$

$$\frac{\partial(\bar{\rho}\tilde{u}_i)}{\partial t} + \frac{(\bar{\rho}\tilde{u}_i\tilde{u}_j)}{\partial x_j} = -\frac{\partial \bar{p}}{\partial x_i} + \frac{\partial}{\partial x_j}\left(\overline{\tau_{ij}} - \overline{\rho u_i'' u_j''}\right), \tag{2.16}$$

$$\begin{aligned}\frac{\partial}{\partial t}(\bar{\rho}\tilde{E}) + \frac{\partial}{\partial x_j}(\bar{\rho}\tilde{u}_j\tilde{H}) = &-\frac{\partial}{\partial x_j}\left(\overline{q_j} - \overline{\rho u_j'' H''} - \overline{\tau_{ij}u_i''} + \frac{1}{2}\overline{\rho u_j'' u_i'' u_i''}\right) \\ &+ \frac{\partial}{\partial x_j}\left(\left(\overline{\tau_{ij}} - \overline{\rho u_i'' u_j''}\right)\tilde{u}_i\right),\end{aligned} \tag{2.17}$$

where in the momentum equation $\overline{\tau_{ij}}$ is given by:

$$\overline{\tau_{ij}} = -\frac{2}{3}\mu\frac{\partial \bar{u}_k}{\partial x_k}\delta_{ij} + \mu\left(\frac{\partial \bar{u}_i}{\partial x_j} + \frac{\partial \bar{u}_j}{\partial x_i}\right) \tag{2.18}$$

and H is the total enthalpy, defined as $H = h + \frac{1}{2}(u^2 + v^2 + w^2)$, with h the enthalpy. As can be seen from (2.16) and (2.17) there are three terms in these equations that are unknown, these must be modelled, i.e. the system of equations that must be solved is not closed. The first of these three terms, $\overline{\rho u_i'' u_j''}$, is called the Favre-averaged turbulent stress tensor it is modelled by the commonly used "Boussinesq hypothesis" [27]:

$$\overline{\rho u_i'' u_j''} = -\frac{2}{3}\mu_T \frac{\partial \bar{u}_k}{\partial x_k}\delta_{ij} + \mu_T\left(\frac{\partial \bar{u}_i}{\partial x_j} + \frac{\partial \bar{u}_j}{\partial x_i}\right) - \frac{2}{3}\bar{\rho} k \delta_{ij}, \tag{2.19}$$

where k is the turbulent kinetic energy (TKE), defined as: $k = \frac{1}{2}\cdot\overline{u_i'' u_i''}$. The second unknown that must be modelled is the Favre-averaged turbulent heat flux vector $\overline{\rho u_i'' H''}$. Here it is modelled as follows [27]:

$$\overline{\rho u_j'' H''} = -\frac{\mu_T c_p}{\mathrm{Pr}_T}\frac{\partial \tilde{T}}{\partial x_j} = -\frac{\mu_T}{\mathrm{Pr}_T}\frac{\partial \tilde{H}}{\partial x_j}, \tag{2.20}$$

where μ_T is the turbulent dynamic viscosity, c_p is the specific heat at constant pressure and Pr_T is the turbulent Prandtl number ($\mathrm{Pr}_T = \mu_T c_p / k_t$, where k_t is the thermal conductivity).

The last term that must be modelled is the Favre-averaged turbulent molecular diffusion and turbulent transport term $\overline{\tau_{ij} u_j''} + \frac{1}{2}\overline{\rho u_j'' u_i'' u_i''}$ [27]:

$$\overline{\tau_{ij} u_i''} + \frac{1}{2}\overline{\rho u_j'' u_i'' u_i''} = \left(\mu + \frac{\mu_T}{\sigma_k}\right)\frac{\partial k}{\partial x_j}, \tag{2.21}$$

where σ_k is a constant (its value depends on the turbulence model used).

In the following, the term "RANS equations" will refer to (2.15) till (2.17), i.e. to the Favre-Averaged Navier-Stokes equations.

BOUNDARY CONDITIONS

In order to solve the RANS equations, boundary conditions are needed. At the airfoil surface the no-slip condition is applied, i.e. the velocity vector is zero ($\vec{u} = \vec{0}$). At the boundaries of the simulation domain a farfield boundary condition is used. TAU assigns inflow/outflow conditions to the nodes at this boundary depending on the flow direction. For turbulent and transition modelling the turbulence intensity Tu and eddy viscosity ratio μ_T/μ are specified at the farfield boundary. This is discussed in more detail after the turbulence and transition models have been presented. To assure two-dimensional flow, symmetry boundary conditions are used at the symmetry planes, i.e. the velocity in y-direction is set to zero and the gradients of scalars in y-direction are set to zero.

TURBULENCE MODEL

A two-equation turbulence model consists of two additional transport equations, one for the turbulent kinetic energy k and another one for the dissipation rate ϵ or the specific dissipation rate ω, which is defined as: $\omega = \epsilon/k$. Here ϵ is the dissipation rate, i.e. the rate at which the turbulent kinetic energy dissipates into internal energy. The Menter Shear-Stress Transport (SST) is an extension to the Menter baseline model. This baseline model is actually a combination of the Wilcox k-ω model and the k-ϵ model. The k-ω is accurate in the near-wall region, whereas the k-ϵ model is independent of the free-stream in the outer layer [28]. The transport equation for the turbulent kinetic energy k is the same as for that of the Wilcox k-ω model. The transport equation for ω has been changed, such that extra cross-diffusion terms appear and the modelling constants are

variable [28]. The transport equations for k and ω of the Menter SST turbulence model are given by:

$$\frac{\partial(\bar{\rho}k)}{\partial t}+\frac{\partial}{\partial x_j}\left(\tilde{u}_j\bar{\rho}k\right)-\frac{\partial}{\partial x_j}\left(\left(\mu+\sigma_k\mu_T\right)\frac{\partial k}{\partial x_j}\right)=P_k-\beta^*\bar{\rho}k\omega, \tag{2.22}$$

$$\frac{\partial(\bar{\rho}\omega)}{\partial t}+\frac{\partial}{\partial x_j}\left(\tilde{u}_j\bar{\rho}\omega\right)-\frac{\partial}{\partial x_j}\left(\left(\mu+\sigma_\omega\mu_T\right)\frac{\partial \omega}{\partial x_j}\right)=\frac{\gamma_1\bar{\rho}}{\mu_T}P_\omega-\beta\bar{\rho}\omega^2 +2\sigma_{\omega_2}\left(1-F_1\right)\frac{\bar{\rho}}{\omega}\frac{\partial k}{\partial x_j}\frac{\partial \omega}{\partial x_j}, \tag{2.23}$$

where β^*, σ_ω, γ_1, β and σ_{ω_2} are constants. F_1 is a blending function between the k-ω and the k-ϵ model [28]. The eddy viscosity μ_T is modelled in the Menter SST model as:

$$\mu_T=\frac{\rho a_1 k}{\max\left(a_1\omega;\Omega F_2\right)}, \tag{2.24}$$

where a_1 is a constant equal to 0.31, Ω is the absolute value of the vorticity and F_2 is a function that is one in a boundary-layer flow and zero in a free shear-layer flow. Further details can be found in [28].

2

TRANSITION MODEL

When computations with free boundary layer transition are performed, the so-called $\gamma-\mathrm{Re}_\theta$ transition model developed by Langtry [29] and Menter et al. [30] is used. This model is based on two additional transport equations. The first equation is a transport equation for the intermittency γ. The intermittency indicates whether the flow is laminar (then $\gamma=0$) or turbulent ($\gamma=1$). In the transition region the intermittency factor has a value between zero and one. γ is used to switch on the production of turbulent kinetic energy in the turbulent part of the boundary layer.

The second transport equation is for the transition onset momentum-thickness Reynolds number $\overline{\mathrm{Re}}_{\theta_t}$. The idea behind this equation is that Re_{θ_t} is seen as a transported scalar quantity. The non-local effect of freestream turbulence intensity and pressure gradient at the boundary layer edge is taken into account via an empirical correlation

$$\mathrm{Re}_{\theta_t}=f\left(\mathrm{Tu},\,dp/ds\right).$$

The turbulence intensity Tu is defined as [31]:

$$\mathrm{Tu}=100\cdot\frac{\sqrt{\frac{1}{3}\left(\overline{u''^2}+\overline{v''^2}+\overline{w''^2}\right)}}{U_\infty}, \tag{2.25}$$

where u'', v'' and w'' are the velocity fluctuations of the freestream in x-, y- and z-direction, respectively. The turbulence intensity is usually defined in %. The empirical correlation for Re_{θ_t} is used in the production term in the transport equation for $\overline{\mathrm{Re}}_{\theta_t}$. The details of this empirical correlation can be found in [29].

The transport equation for the intermittency γ and the transition momentum thickness Reynolds number $\overline{\mathrm{Re}}_{\theta_t}$ are given by [29, 30]:

$$\frac{\partial(\bar{\rho}\gamma)}{\partial t} + \frac{\partial(\bar{\rho}\tilde{u}_j\gamma)}{\partial x_j} = P_{\gamma_1} - E_\gamma + \frac{\partial}{\partial x_j}\left(\left(\mu + \frac{\mu_T}{\sigma_f}\right)\frac{\partial\gamma}{\partial x_j}\right), \tag{2.26}$$

$$\frac{\partial\left(\bar{\rho}\overline{\mathrm{Re}}_{\theta_t}\right)}{\partial t} + \frac{\partial\left(\bar{\rho}\tilde{u}_j\overline{\mathrm{Re}}_{\theta_t}\right)}{\partial x_j} = P_{\theta_t} + \frac{\partial}{\partial x_j}\left(\sigma_{\theta_t}(\mu+\mu_T)\frac{\partial\overline{\mathrm{Re}}_{\theta_t}}{\partial x_j}\right), \tag{2.27}$$

where P_{γ_1} is the transition source term, E_γ is the destruction or relaminarisation source, σ_f is a constant, P_{θ_t} is the source term of the momentum thickness Reynolds number and σ_{θ_t} is a constant. P_{γ_1} is zero in the laminar part of the boundary layer and it equal to one when the transition starts, this is controlled by an onset function. Furthermore, another function, F_{length}, that is part of this production term, controls the length of the transition region. The onset function depends on the critical Reynolds number Re_{θ_c}, which is connected to Re_{θ_t} via an empirical correlation. The correlation between the transition Reynolds number and the F_{length} function is obtained from experiments. E_γ is a destruction term when the intermittency increases from zero to one and a relaminarisation term when the intermittency decreases from one towards zero. Some modifications to the model are made in case of separated flow transition [30]. More details about the $\gamma - Re_\theta$ transition model can be found in [29, 30].

Although, boundary-layer transition remains difficult to predict, the $\gamma - \mathrm{Re}_\theta$ transition model as used in this thesis, is an effective model for transition prediction. The model is effective especially in case of bypass transition i.e. when the freestream turbulence intensity is large and the linear growth phase of the Tollmien-Schlichting-waves is bypassed. The $\gamma - \mathrm{Re}_\theta$ transition model is able to predict a transition region by increasing the value of γ. In contrast, the e^N-method developed by van Ingen [32] and Smith and Gamberoni [33], can only predict the linear growth phase of Tollmien-Schlichting (TS) waves, i.e. at the transition onset location predicted by the e^N-method the flow becomes fully turbulent immediately. Although, the linear growth phase of TS-waves comprises the largest part of the boundary layer transition process, in reality transition takes place over a finite length and hence the transition onset and transition length concepts of the $\gamma - \mathrm{Re}_\theta$ model are more realistic than the e^N-method. On the other hand, the e^N-method can also predict cross-flow instabilities, which cannot be predicted by the standard $\gamma - \mathrm{Re}_\theta$ method. Hence, the standard $\gamma - \mathrm{Re}_\theta$ method is not suited for boundary-layer transition studies of three-dimensional configurations where cross-flow instabilities are expected to be dominant. However, there are several developments to solve this problem, see e.g. Grabe and Krumbein [34].

In this thesis a natural transition test case is considered and therefore a low turbulence intensity is chosen. Seyfert and Krumbein [35] have shown that in such a case the transition locations on the NLF(1)-0416 airfoil as predicted by both the e^N-method and the $\gamma - \mathrm{Re}_\theta$ method (with the correlation of Langtry [29]) agree well with experimental results. Also, Langtry and Menter [36] have shown a good agreement between experimental results and the numerical results from the $\gamma - \mathrm{Re}_\theta$ method, for the PAK-B blade cascade at low turbulence intensity levels and similar Reynolds number as considered in this thesis. Hence, from these investigations it is confirmed that the $\gamma - \mathrm{Re}_\theta$ method

is a valid transition prediction method for the purposes of this thesis. The model will be applied for the subsonic flow test case shown in Section 5.2.3.

BOUNDARY CONDITIONS FOR THE TURBULENCE AND TRANSITION MODELS

In order to use the turbulence and transition models the turbulence intensity has to be specified at the farfield boundary upstream of the airfoil. However, a certain intensity is required at the leading edge of the airfoil. Therefore, Langtry [29] describes a method to estimate the decrease in turbulence intensity from the farfield boundary to the leading edge of the airfoil. The turbulence kinetic energy decreases according to:

$$k = k_{\text{inlet}} \left(1 + \omega_{\text{inlet}} \beta t\right)^{\frac{-\beta^*}{\beta}}, \tag{2.28}$$

where β and β^* are now equal to 0.09 and 0.0828, respectively and t is a timescale given by: $t = x/U_\infty$, where x is the distance from the farfield boundary to the airfoil. The turbulence intensity at the airfoil's leading edge can be computed from the turbulence intensity at the inlet and the eddy viscosity ratio at the inlet by using equation (2.29);

$$\text{Tu} = \left(\text{Tu}_{\text{inlet}}^2 \left(1 + \frac{3\rho U_\infty x \beta \text{Tu}_{\text{inlet}}^2}{2\mu \left(\mu_T/\mu\right)_{\text{inlet}}} \right)^{\frac{-\beta^*}{\beta}} \right)^{\frac{1}{2}}. \tag{2.29}$$

The eddy viscosity ratio at the inlet influences how fast Tu decays. When $\left(\mu_T/\mu\right)_{\text{inlet}}$ is large, then the decay rate will be small. The turbulent kinetic energy at the farfield boundary k_{inlet} is determined from the turbulence intensity at the farfield boundary Tu_{inlet} and the freestream velocity. At the airfoil's surface k is zero. ω_{inlet} is determined from k_{inlet}, the eddy viscosity and the density at the farfield boundary. At the airfoil's surface ω is determined from the distance of the point closest to the surface and the viscosity. More details on the boundary conditions for k and ω can be found in TAU's technical documentation [37]. For the transition model, the boundary conditions are stated by Menter et al. [30], i.e. γ is 1 at the farfield boundary and at the airfoil's surface a zero normal flux is invoked. The boundary condition for $\overline{\text{Re}}_{\theta_t}$ at the farfield boundary can be computed from the empirical correlation for Re_{θ_t} with Tu at the farfield boundary. At the airfoil's surface a zero flux of $\overline{\text{Re}}_{\theta_t}$ is again invoked.

DISCRETISATION

In this thesis a moving airfoil is simulated. Hence, the unsteady RANS (URANS) approach is used. This means the time derivatives in (2.15)-(2.17) are retained. When the airfoil is not moving, the RANS equations are solved with pseudo time stepping.

A cell-vertex finite volume method is applied to solve the RANS equations. The temporal discretisation has been realised by Jameson's dual time stepping [38] with the 2nd order accurate Backward Differencing Formula (BDF2) integration scheme for the physical time stepping. For solving steady state problems, the concept of local time stepping is applied in combination with the multigrid method. For spatial discretisation the 2nd-order central scheme [39] has been used.

COMPUTATIONAL MESHES

The computational meshes that have been used for solving the fluid equations are unstructured when the Euler equations are solved and completely structured when the RANS equations are solved. Figure 2.3 shows zooms of the meshes used in this thesis near the airfoil. To minimise the reflections from the farfield boundary, this boundary is placed 100 chord lengths away from the airfoil. The structured O-type mesh consisting of rectangles that used for all RANS CFD simulations, has 65888 points. The non-dimensional first cell height y^+ of this mesh was estimated to be is 0.75. For the Euler simulations an unstructured mesh of triangles with 10369 points has been used, except for the validation of the amplitude-dependent p-k method in Chapter 4. For that study a coarse mesh of 1135 points has been used. A grid convergence study has been performed to ensure that the meshes shown in Figure 2.3 are fine enough for the investigations carried out in this thesis. The results of these studies are shown in Appendix B.

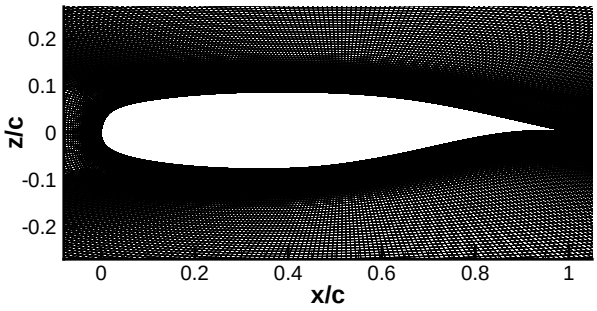

(a) RANS mesh

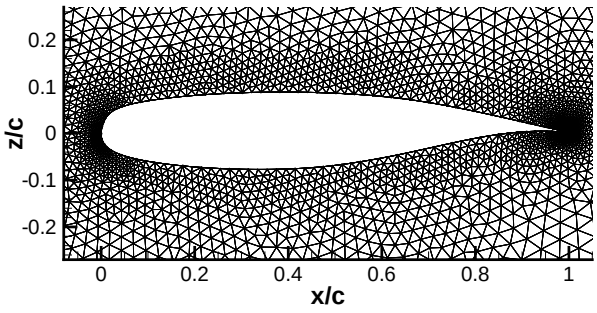

(b) Euler mesh

Figure 2.3: Meshes used for CFD simulations

2.3. FLUID-STRUCTURE COUPLING IN THE TIME DOMAIN

Time integration is the most general method to solve the equations of motion (2.7). When this is done directly, so-called fluid-structure coupling is applied. The structural motions (displacements, velocities, accelerations) are then part of the solution. When the equations of motion of an aeroelastic system are solved in the time domain, usually coupling between the structural and the aerodynamic solvers is required. This coupling can be performed in two ways: partitioned or monolithic. Monolithic coupling means that (2.7) is satisfied at the end of each time step. In a partitioned approach separate algorithms are used to solve the structural dynamics and the fluid dynamics problems. The force and displacement vectors are exchanged at the end of a time step. This introduces a partition error. Furthermore, numerical stability problems can arise. However, the advantage of a partitioned approach is that separate solvers, each with a higher efficiency and accuracy, can be used.

Partitioned coupling can be either loose or strong. When the partitioned coupling is loose, the displacement and force vectors are exchanged between the fluid and the structure at the end of each time step. This means that at the end of each time step equation (2.7) is not satisfied, since either the structural or the fluid solver has used information from the previous time step. In contrast, in a strongly coupled partitioned approach, separate solvers are used for the fluid and the structure as well, but the forces and displacements are exchanged multiple times during each time step. Hence, at the end of a time step, (2.7) is satisfied to within some tolerance. Therefore, the result of the strong partitioned fluid-structure coupling is similar to that of the monolithic coupling approach.

In this thesis a partitioned, strongly coupled, approach is used to solve the equations of motion in the time domain. This is achieved by performing the fluid-structure coupling at each pseudo time step of the CFD solver. Particularly, the equations of motion are solved as illustrated below.

Consider the equations of motion (2.7). The equivalent first order system is obtained by letting $\vec{v} = \dot{\vec{x}} = [\dot{h}, \dot{\alpha}]^T$:

$$\underbrace{\begin{bmatrix} \dot{\vec{v}} \\ \dot{\vec{x}} \end{bmatrix}}_{\dot{\vec{u}}} + \underbrace{\begin{bmatrix} \mathbf{M}^{-1}\mathbf{D} & \mathbf{M}^{-1}\mathbf{K} \\ -\mathbf{I} & \mathbf{0} \end{bmatrix}}_{\mathbf{B}} \underbrace{\begin{bmatrix} \vec{v} \\ \vec{x} \end{bmatrix}}_{\vec{u}} = \underbrace{\begin{bmatrix} \mathbf{M}^{-1}\vec{f} \\ \vec{0} \end{bmatrix}}_{\vec{w}}. \tag{2.30}$$

Hence, four equations for the time derivatives of the components of the vectors $\vec{v}$ and $\vec{x}$ must be solved. These are integrated in time using the BDF2 integration scheme. When $\vec{u} = [\dot{h}, \dot{\alpha}, h, \alpha]^T$, then temporal discretistation results in:

$$\frac{\frac{3}{2}\vec{u}^{n+1} - 2\vec{u}^{n} + \frac{1}{2}\vec{u}^{n-1}}{\Delta t} + \mathbf{B}\vec{u}^{n+1} - \vec{w}^{n+1} = 0, \tag{2.31}$$

where n indicates the current time step. The aerodynamic lift and moment are not available at the current time step. Therefore, the predictor-corrector method is applied. At each time step the forces and moments from the CFD code are requested. These are defined to be their values at the next time step $n+1$. Then the state vector $\vec{u}^{n+1}$ can be computed from (2.31). It is then transferred to the CFD solver. This is called the predictor step. The CFD code then performs one iteration in pseudo time. Then a corrector

step is applied, i.e. the forces computed at the last pseudo time step are now assigned to $\vec{w}^{n+1}$ and (2.31) is again solved for $\vec{u}^{n+1}$. This new state vector is applied to the CFD solver again. Then the CFD code performs one iteration in pseudo time again and so on. When the CFD solver has reached convergence at the current time step or when the maximum number of pseudo time steps is reached, the state vector $\vec{u}^{n+1}$ and the aerodynamic force vector $\vec{w}^{n+1}$ have reached their final values at $n+1$. The state vector $\vec{u}^{n+1}$ is then passed to the previous time level.

In TAU, the displacement of the airfoil is performed by a displacement of the complete grid. In this way the grid cells keep their form and no grid deformation is necessary. The additional fluxes that are introduced by displacing the grid are taken into account such that the geometric conservation law is satisfied.

In Section 3.2.3 it is verified that the fluid-structure coupling in the time domain has been correctly implemented.

2.4. LINEAR FLUTTER IN THE FREQUENCY DOMAIN

Alternatively to the time domain, the equations of motion can be solved in the frequency domain. This has the advantage that aerodynamics and structure can be treated separately. Hence, when the generalised aerodynamic forces at a certain Mach number and angle of attack are known, the structural model can be varied without the need to do expensive CFD simulations again. Three well-known frequency domain methods to solve linear flutter problems are: the k-method, the p-k-method and the p-method [40]. Another approach is the so-called $U-g$-method, where g is the structural damping coefficient [41]. In this thesis the p-k method has been used. This section first describes the conventional p-k method as used to solve linear flutter problems. Then it is explained how the aerodynamic forces are computed. Finally, the process of finding the flutter onset speed is addressed. Note that, in this section, the notations from classical flutter analysis are used. Hence, the symbols p, ω, x and k are used again, but with a different meaning then in Section 2.2.3.

2.4.1. CONVENTIONAL P-K METHOD

The conventional p-k method for classical flutter computations was developed by Hassig [42]. In this method a solution to the equations of motion (2.7) of the form:

$$\vec{x}(t) = \vec{\hat{x}} e^{pt}, \tag{2.32}$$

is assumed. Here $\vec{\hat{x}}$ indicates a complex-valued eigenvector and p is a complex-valued eigenvalue, defined by:

$$p = \delta + i\omega, \tag{2.33}$$

where δ is the damping and ω the angular frequency. The non-dimensional reduced frequency k is computed from the angular frequency via $k = \omega c / U_\infty$. In addition, it is assumed that the aerodynamic response of the system is also a harmonic motion. The aerodynamic force vector $\vec{f}$ is given by:

$$\vec{f}(t) = \vec{\hat{f}} e^{pt}, \tag{2.34}$$

where $\vec{\hat{f}}$ is the complex amplitude vector of the aerodynamic force. The aerodynamic force vector $\vec{\hat{f}}$ can be written as a Taylor series. Since in linear flutter one is only concerned about flutter onset, the motion is of small amplitude. Hence, the aerodynamic response is expected to be of small amplitude as well. Therefore, the Taylor series is truncated after the first term. Assumming linearity, $\vec{\hat{f}}$ can be written as the product of a Generalised Aerodynamic Force (GAF) matrix $\mathbf{A}(k)$ and the eigenvector $\vec{\hat{x}}$:

$$\vec{\hat{f}} = \mathbf{A}(k)\vec{\hat{x}}. \tag{2.35}$$

The GAF matrix consists of the complex-valued derivatives of the aerodynamic forces and moments with respect to the degrees of freedom (or the chosen generalised coordinates). In the p-k method the GAF matrix is a function of k only [43], i.e. for the two DoF system considered here:

$$\vec{\hat{f}} = \underbrace{\begin{bmatrix} -\frac{\partial \hat{L}}{\partial h}(k) & -\frac{\partial \hat{L}}{\partial \alpha}(k) \\ \frac{\partial \hat{M}}{\partial h}(k) & \frac{\partial \hat{M}}{\partial \alpha}(k) \end{bmatrix}}_{\mathbf{A}(k)} \vec{\hat{x}}. \tag{2.36}$$

It is assumed that inclusion of the damping in the computation of the aerodynamic forces does not influence the resulting aerodynamic derivatives significantly. In the p-method the GAF matrix is a function of p and hence of the damping as well [40, 42]. Hassig [42] compared the results of the p- and the p-k method. He showed that when the damping is low, computing the aerodynamic forces from constant amplitude harmonic motions is a valid approach, since the frequency and damping curves obtained from both methods as well as the predicted flutter point were in perfect agreement. Substituting the assumed solution (2.32)-(2.35) into the equations of motion (2.7) yields:

$$p^2\mathbf{M}\vec{\hat{x}} + p\mathbf{D}\vec{\hat{x}} + \mathbf{K}\vec{\hat{x}} = \mathbf{A}(k)\,\vec{\hat{x}}. \tag{2.37}$$

The left-hand side of this equation is a function of p and the right-hand side of k only, hence the name p-k method. In the k-method both left- and right-hand side only consider the frequency, see [42] for more details. The eigenvalue problem (2.37) must be solved iteratively, since the GAF matrix is a function of the reduced frequency, which is in turn part of the sought solution p. The GAF matrix is computed by forcing the system to perform a harmonic motion around its structural mode shape (i.e. the mode shape in the absence of aerodynamic forces) at various frequencies in a fluid flow. Alternatively, a pulse simulation can be used to obtain the complete frequency response function (FRF) at once. In case of a two DoF system, the airfoil is forced to pitch or plunge.

The iterative procedure for computation of the eigenvalues of (2.37) is:

1. Fix the freestream velocity U_∞.
2. Initialise the reduced frequency k.
3. Compute the GAF matrix $\mathbf{A}(k)$ at k by interpolation.
4. Solve the eigenvalue problem (2.37) for p and $\vec{\hat{x}}$.

5. Take new $\omega = \Im(p)$ (and hence $k = \omega c/U_\infty$).

6. Iterate steps 3-5 until converged.

This procedure is repeated for several freestream velocities. Once a converged solution has been obtained at a certain freestream velocity, the velocity is increased and the value for k obtained at the previous velocity is used as an initial guess for k in step 2. At the lowest freestream velocity, k is initialised using the uncoupled natural plunge frequency $\omega_h = \sqrt{K_h/m}$ or the uncoupled natural pitch frequency $\omega_\alpha = \sqrt{K_\alpha/I_\alpha}$, which are the structural angular frequencies that would exist in the absence of aerodynamic forces (i.e. at $U_\infty = 0$). The freestream velocity at which the real part of p, $\Re(p)$, becomes zero, is the flutter onset velocity. When this velocity is exceeded, flutter occurs. That is, the amplitude of the motion will grow exponentially. More details on the conventional p-k method can be found in Hassig [42].

2.4.2. FREQUENCY RESPONSE FUNCTIONS

In order to be able to solve (2.37) the frequency response functions must be determined. In case of a two DoF system this means that the complex-valued derivatives of the aerodynamic lift and moment with respect to either pitch or plunge have to be obtained. Therefore, the airfoil is forced to undergo either a pitching or a plunging motion of small amplitude. Equations (2.38) and (2.39) describe the pitching and plunging motion, respectively;

$$\alpha(t) = \Delta\alpha \cdot \sin(\omega t) \quad \text{or} \tag{2.38}$$

$$h(t) = \Delta h \cdot \sin(\omega t), \tag{2.39}$$

where $\Delta\alpha$ is the pitch amplitude, Δh is the plunge amplitude and ω is the angular frequency. The response of the lift and the moment is represented by a Fourier series. Since the lift and moment are linear, usually the higher harmonic components in the response are negligible compared to the first harmonic component. Concretely, the aerodynamic lift and moment are given by:

$$L(t) = |L| \cdot \sin\left(\omega t + \phi_{Lh}\right), \tag{2.40}$$

$$M(t) = |M| \cdot \sin\left(\omega t + \phi_{M\alpha}\right), \tag{2.41}$$

where $|L|$ and $|M|$ represent the amplitude (or magnitude) of the lift and moment, respectively and ϕ_{Lh} and $\phi_{M\alpha}$ the phase difference of the lift and moment with respect to the plunge or pitch motion, respectively. The derivatives in the GAF matrix are now computed by dividing the Fourier transform of $L(t)$ and $M(t)$ by the Fourier transform of $h(t)$ and $\alpha(t)$. That is, $\partial\hat{L}/\partial h = |L|/\Delta h \cdot e^{i\phi_{Lh}}$, etc. Alternatively, a pulse signal is given to the angle of attack or the plunge displacement and the lift and moment responses are Fourier transformed. Dividing by the Fourier transform of the corresponding pulse input signal gives the derivatives needed for the GAF matrix.

The p-k method with the GAF matrix is based on the principle of superposition. Hence, the pitching and plunging motions are performed in separate simulations and the responses resulting from these simulations are then superposed. This can only be

done correctly if the amplitude is small enough, i.e. it is no longer allowed when the amplitude of oscillation becomes larger. The amplitude at which the response is no longer linear can be found if forced pitch oscillation simulations are performed at various oscillation amplitudes. Figure 2.4 shows the magnitude of the lift coefficient for such a simulation at a Mach number of 0.75 and a mean angle of attack of 0°. At these conditions a double shock system exists on the upper surface, whereas on the lower surface a single shock just upstream of the mid-chord position exists. There is no boundary layer separation on either surface. The reduced frequency k is 0.3.

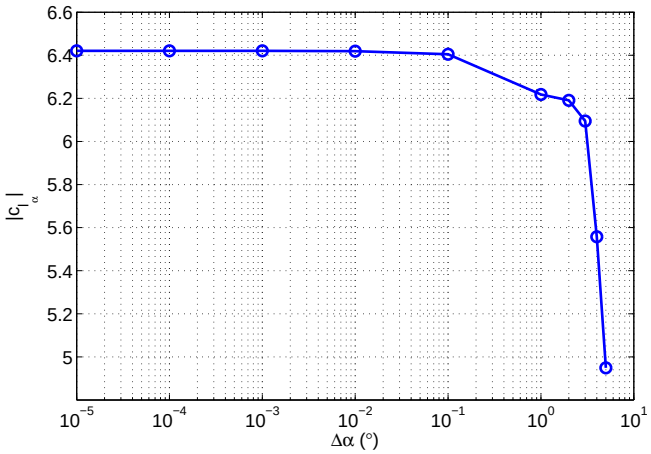

Figure 2.4: Scaled magnitude of the lift coefficient versus the pitch amplitude in viscous flow at $M = 0.75$, $\bar{\alpha} = 0°$ and $k = 0.3$

From Figure 2.4 it is observed that for amplitudes lower than 0.01° the response is linear, that is, the magnitude of the lift coefficient normalised by the pitch amplitude $|c_{l_\alpha}|$ does not vary with the pitch amplitude. For oscillation amplitudes larger than 0.01°, $|c_{l_\alpha}|$ does change when the amplitude increases. Similar behaviour is observed for the phase angle of the lift coefficient and for the response of the moment coefficient. Hence, for $k = 0.3$ the response is linear and superposition of the pitch and plunge responses is allowed for amplitudes ≤ 0.01°. For other reduced frequencies the range of amplitudes at which the response of the lift and moment is linear is similar. Thormann et al. [44] performed a similar study using the NACA0010 airfoil at $M = 0.69$, $\bar{\alpha} = 5.5°$ and a reduced frequency of 0.35. At this Mach number and angle of attack there is severe flow separation behind the shock wave. They also observed that up to an amplitude of 0.01° the magnitude of the lift coefficient is independent of the pitch amplitude. In general, the amplitude at which the aerodynamic derivatives deviate from their linear values depends on the flow conditions. At other Mach numbers or mean angles of attack, the amplitude at which the magnitude and phase angle of lift and moment start deviating might be higher or lower. In case of free boundary layer transition, for example, the amplitude at which the aerodynamic derivatives deviate from their linear values was found to be much lower. This means that

a smaller amplitude is necessary to assure a linear response such that superposition of the FRFs is valid. A similar study can be performed for a pulse simulation.

2.4.3. LINEAR FLUTTER

To determine the flutter onset speed, (2.37) must be solved for several freestream velocities and the velocity at which the damping is zero is the flutter speed. However, the FRF is only computed for one freestream speed, the reference speed. For other freestream velocities, the GAF matrix is computed proportional to the reference speed, i.e.

$$\mathbf{A} = \frac{\frac{1}{2}\rho_\infty U_\infty^2}{\frac{1}{2}\rho_{\text{ref}} U_{\text{ref}}^2} \cdot \mathbf{A}_{\text{ref}}, \tag{2.42}$$

where the subscript ref indicates the reference condition at which the FRFs were computed. When the flutter onset dynamic pressure is found, the reference dynamic pressure is compared to the dynamic pressure at flutter. When these two dynamic pressures are not identical one speaks of a non-matched flutter point. In order to match these dynamic pressures, additional iterations are necessary, i.e. the GAF matrix must be computed again at the predicted flutter dynamic pressure until the reference dynamic pressure matches the flutter onset dynamic pressure. In this thesis the computed flutter conditions are non-matched.

Since we are dealing with a two DoF system, (2.37) will have four solutions for p and four corresponding mode shapes $\vec{\hat{x}}$. However, these eigenvalues are complex conjugates. Hence, only those with a positive imaginary part are taken into account in the flutter analysis; the others are non-physical. The corresponding eigenvectors are used to determine the flutter mode shape. Figure 2.5 shows an example of the damping δ and the angular frequency ω versus the freestream speed for two modes computed at $M = 0.74$ and $\bar{\alpha} = 0°$ in inviscid flow (using the structural model of Table 2.1 without structural damping). Note that positive damping indicates a motion growing in amplitude, i.e. an amplification. In order to compute the eigenvalues, the Mach number and freestream density (= 1.2925 kg/m^3) have been kept constant and the freestream pressure is varied. The aerodynamic forces are computed at standard sea level conditions. From Figure 2.5(a) it can be observed that the damping becomes positive for mode two at a freestream velocity of about 131 m/s. So at velocities higher than about 131 m/s the amplitude of the motion of the airfoil will grow unbounded, i.e. flutter occurs. Since the natural pitch frequency ω_α is 290 rad/s and the natural plunge frequency ω_h is 202.6 rad/s, the plunge mode is the one that becomes unstable. From the mode shape at flutter it is concluded that the flutter mechanism is a complex pitch-plunge motion (the magnitude of the complex amplitude ratio between pitch and plunge is about 0.9 and the phase is about 5°). The flutter boundary is obtained when the flutter speed is computed for several Mach numbers (for each Mach number a new GAF matrix is computed).

2.5. LIMIT-CYCLE OSCILLATIONS IN THE FREQUENCY DOMAIN

The conventional p-k method cannot be used for predicting limit-cycle oscillations. At least not in its original form, since in LCOs the aerodynamic forces are not linear functions of the displacements, i.e. $\mathbf{A}(k)$ does not exist in the non-linear case. Therefore,

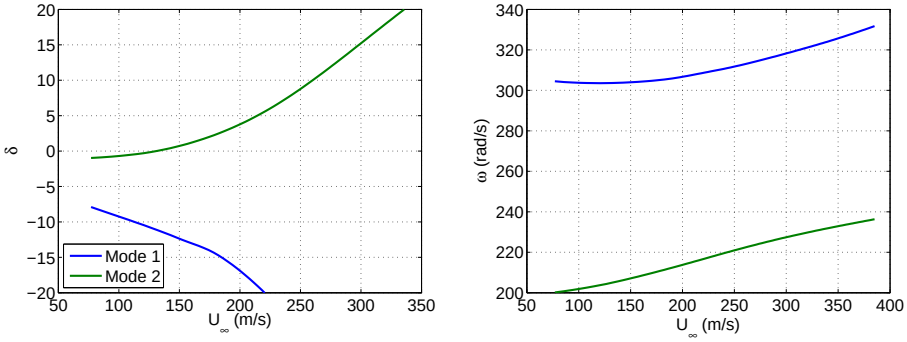

(a) Damping (b) Angular frequency

Figure 2.5: Damping and angular frequency versus freestream speed in inviscid flow at $M = 0.74$, $\bar{\alpha} = 0°$

a new adapted version of the p-k method has been developed in this thesis, which is presented in this section. Furthermore, it is shown how the aerodynamic forces are now obtained. Then, the process of finding the bifurcation behaviour of the LCO amplitude is described. The sampling and interpolation methods used to sample and interpolate the aerodynamic forces are discussed shortly in Section 2.5.4. Section 2.5.5 puts the method developed in this section in perspective. Note that the symbols p, ω, x and k in this section, have the same meaning as in Section 2.4.

2.5.1. AMPLITUDE-DEPENDENT P-K METHOD (ADEPK)

In the amplitude-dependent p-k method, or ADePK for short, again a solution to the equations of motion (2.7) of the form (2.32) is assumed similar to the conventional p-k method (with p defined by (2.33)). For the aerodynamic response of the system only the complex-valued first harmonic component is considered, since the higher harmonics are not of interest (as will be explained in Section 2.5.2), i.e. (2.34). Substituting the assumed solution (2.32)-(2.34) into the equations of motion (2.7) yields:

$$p^2\mathbf{M}\vec{\hat{x}} + p\mathbf{D}\vec{\hat{x}} + \mathbf{K}\vec{\hat{x}} = \vec{\hat{f}}\left(k, \vec{\hat{x}}\right). \tag{2.43}$$

In the conventional p-k method the right-hand side vector is written as a GAF matrix times the eigenvector (see (2.35)). In case of an LCO, this is no longer allowed. The aerodynamic force vector is now not only a non-linear function of the frequency, but also a non-linear function of the amplitudes of both input degrees of freedom and the phase angle between the degrees of freedom. Therefore, $\vec{\hat{x}}$ is now called the motion vector and (2.43) can no longer be solved as an eigenvalue problem, but must be solved iteratively, for example using Newton's method. The method uses the tangent to the function f at a certain x_n, i.e. for a one-dimensional function:

$$y = f'(x_n) \cdot (x - x_n) + f(x_n), \tag{2.44}$$

where the f' denotes the derivative of the function f. The root is found when y is zero. This process is repeated for the new x-value (i.e. $x_n = x$) until convergence is reached.

In order to uniquely determine $\vec{\hat{x}}$ one of the amplitudes (either pitch or plunge) is pre-set. The motion vector then becomes:

$$\vec{\hat{x}} = \begin{bmatrix} \theta_{h\alpha} \cdot c \\ 1 \end{bmatrix} \cdot \Delta\alpha. \tag{2.45}$$

Then (2.43) is solved for two unknowns: the complex eigenvalue p and the complex amplitude ratio $\theta_{h\alpha} = (\Delta h/c)/\Delta\alpha \cdot e^{i\phi_{h\alpha}}$. This is done for each pre-set amplitude ($\Delta\alpha$ or Δh, here $\Delta\alpha$ has been used). Since the force vector depends on the frequency and on the mode shape, the equations of motion need to be solved iteratively. Hence, the following problem must be solved:

$$\begin{cases} p^2\mathbf{M}\vec{\hat{x}} + p\mathbf{D}\vec{\hat{x}} + \mathbf{K}\vec{\hat{x}} = \vec{\hat{f}}\left(k, \vec{\hat{x}}\right), \\ \Delta\alpha = \text{constant}, \\ \vec{\hat{f}}\left(k, \vec{\hat{x}}\right) \approx \vec{\hat{f}}_i\left(k, \vec{\hat{x}}\right), \end{cases} \tag{2.46}$$

where $\vec{\hat{f}}_i$ represents the interpolated aerodynamic force vector. As for the conventional p-k method the following steps are performed to obtain p and the complex amplitude ratio at a certain freestream velocity U_∞:

1. Fix the pitch amplitude $\Delta\alpha$.
2. Initialise the reduced frequency k and the complex amplitude ratio $\theta_{h\alpha}$.
3. Compute the aerodynamic force vector $\vec{\hat{f}}_i$ at k and $\vec{\hat{x}}$ (by interpolation).
4. Solve the system of equations (2.43) for p and $\theta_{h\alpha}$.
5. Take new $\omega = \Im(p)$ (i.e. $k = \omega c/U_\infty$) and $\vec{\hat{x}} = [\theta_{h\alpha} \cdot c,\ 1]^T \cdot \Delta\alpha$.
6. Iterate steps 3-5 until converged.

Once a converged solution has been obtained, this procedure is repeated for another (larger) pitch amplitude. At this new amplitude, the reduced frequency and amplitude ratio are initialised in step 2 using the values obtained at the previous amplitude. At the first amplitude, the initial guesses for k and $\theta_{h\alpha}$ are obtained from the flutter frequency and mode shape at the chosen U_∞. The amplitude $\Delta\alpha$ at which the damping, i.e. $\delta = \Re(p)$, becomes zero, is the predicted LCO amplitude. The other LCO properties, i.e. the plunge amplitude Δh, the magnitude of the amplitude ratio $|\theta_{h\alpha}|$ and the phase difference between pitch and plunge $\phi_{h\alpha}$, are determined from $\vec{\hat{x}}$. The reduced frequency is determined from the imaginary part of p. The ADePK method as described here can be used to determine the LCO amplitude when $\vec{\hat{f}} = [\hat{L}, \hat{M}]^T$ is known in advance as a function of the frequency, pitch amplitude, plunge amplitude and the phase difference. Here, $\hat{L}$ and $\hat{M}$ describe the complex-valued responses of the aerodynamic lift and moment.

In order to determine the aerodynamic lift and moment at each combination of amplitudes, frequency and phase difference, a so-called response surface is built using harmonic forced motion CFD simulations. Interpolation on this response surface is then applied during the iterations of ADePK. The sampling and interpolation techniques used will be discussed in Section 2.5.4.

The ADePK method presented here is similar to the harmonic balance (HB) method as presented by Greco et al. [45] and Thomas et al. [46]. However, in contrast to the harmonic balance method, in the ADePK method the aerodynamic forces are obtained from interpolation on the response surface, whereas in the HB method the frequency-domain HB-CFD solver is called at each iteration during the solution procedure of the aeroelastic equations of motion. For further details on the HB method see Section 1.3.

2.5.2. HARMONIC FORCED MOTION OSCILLATIONS

In order to determine the aerodynamic lift $\hat{L}$ and moment $\hat{M}$ at each combination of amplitudes, frequency and phase difference, a so-called response surface is built using harmonic forced motion CFD simulations. Interpolation on this response surface is then applied during the iterations of ADePK. For these harmonic forced motion oscillations the time signal of the pitch angle α and the plunge displacement h are given by:

$$h(t) = \Delta h \cdot \sin\left(\omega t + \phi_{h\alpha}\right), \tag{2.47}$$

$$\alpha(t) = \Delta\alpha \cdot \sin\left(\omega t\right). \tag{2.48}$$

Note that the motion contains no higher harmonics. The phase difference $\phi_{h\alpha}$ is computed by subtracting the phase of the angle of attack ϕ_α from that of the plunge displacement ϕ_h, i.e. $\phi_{h\alpha} = \phi_h - \phi_\alpha$. That is, when $\phi_{h\alpha}$ is positive plunge leads pitch. The response of the aerodynamic forces to this harmonic motion is given by (2.40) and (2.41).

In the non-linear case, when the oscillation amplitude becomes too large, linearisation of the aerodynamic forces is no longer allowed and therefore both motions need to be applied simultaneously to account for non-linear coupling terms in the response. Furthermore, the oscillation amplitudes of both the pitching and the plunging motion as well as the phase difference between both motions must to be taken into account, as illustrated in (2.47) and (2.48). Hence, the non-linear force vector is obtained as

$$\vec{\hat{f}} = \begin{bmatrix} \hat{L} \\ \hat{M} \end{bmatrix} = \begin{bmatrix} f_L\left(\Delta\alpha, |\theta_{h\alpha}|, k, \phi_{h\alpha}\right) \\ f_M\left(\Delta\alpha, |\theta_{h\alpha}|, k, \phi_{h\alpha}\right) \end{bmatrix}.$$

FIRST HARMONIC ASSUMPTION

In ADePK, only the complex-valued first harmonic of the motion and the aerodynamic response are taken into account. That is, the aerodynamic lift and moment can again be represented by (2.40) and (2.41). Although there are significant higher harmonics in the aerodynamic response (as observed from coupled FSI simulations), the work they perform on the airfoil is negligible, since the higher harmonic components in the motion of the structure are very small compared to the first harmonic component.

The ratio of the higher order harmonic components to the first harmonic component in the structural motion has been computed for a viscous flow at $M = 0.74$, $\bar{\alpha} = -0.8°$,

Re = $2 \cdot 10^6$, see Figure 2.6. The LCO obtained at these conditions will be discussed in Chapter 3. From Figure 2.6 it is observed that for plunge the ratio is an order of magnitude smaller than for pitch. As the second order harmonic is more than one order of magnitude, or in case of plunge two orders of magnitude, smaller than the first order harmonic, the LCO can be approximated using a single harmonic sinusoidal with reasonable accuracy. Similar results were found at other conditions.

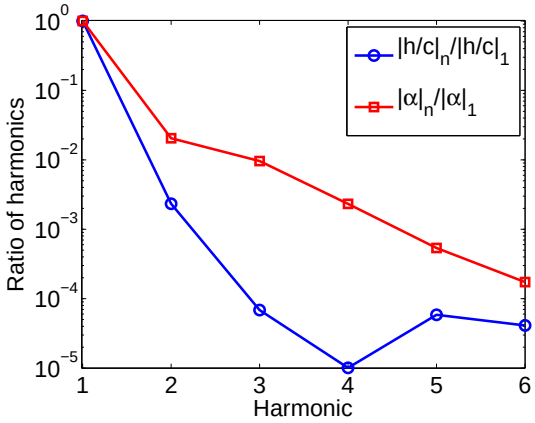

Figure 2.6: Ratio of higher harmonics to first harmonic of the LCO

Furthermore, the higher harmonics in the aerodynamic response do not perform work on the first harmonic of the structural motion. Therefore, if the LCO is (almost) first harmonic, taking into account the first harmonics of the aerodynamic forces is sufficient. If the LCO has significant higher order components it is expected that ADePK will fail to predict the correct LCO amplitude. However, no higher order harmonics were observed from CFD simulations and experiments of LCOs resulting from aerodynamic non-linearities only, see Figure 2.6, [6, 8, 9, 47] and see Chapters 3 and 4. Therefore, in this thesis it is assumed that an LCO can be represented by a first order harmonic motion and that the aerodynamic forces are first order harmonic as well. Further evidence that the first order harmonic is sufficient to model the LCOs considered in this thesis is given in Section 3.3.3.

SUPERPOSITION

As described earlier in this section, the response surface is, in the non-linear case, obtained from simulations where pitch and plunge are simultaneously applied. Another possibility to compute the aerodynamic forces, is to use so-called describing functions (DFs) [48]. A DF, which is a well-known concept in control theory, expresses the (aerodynamic) response as a function of the frequency and the oscillation amplitude of a single DoF [48]. Instead of applying forced motion oscillation simulations in a four dimensional parameter space, the parameter space can then be reduced two dimensions if superposition of the describing functions is applied, i.e. when a quasi-linearisation is

applied. In that case, the pitching and plunging motions are applied to the airfoil in separate simulations for several frequencies and amplitudes (according to (2.38) or (2.39)). The resulting responses in terms of the aerodynamic forces are then added to describe the combined pitch/plunge motion, i.e.

$$\vec{\hat{f}} = \begin{bmatrix} \hat{L} \\ \hat{M} \end{bmatrix} = \begin{bmatrix} f_L\left(\Delta\alpha = 0, |\theta_{h\alpha}| = \infty, k, \phi_{h\alpha} = 0\right) + f_L\left(\Delta\alpha, |\theta_{h\alpha}| = 0, k, \phi_{h\alpha} = 0\right) \\ f_M\left(\Delta\alpha = 0, |\theta_{h\alpha}| = \infty, k, \phi_{h\alpha} = 0\right) + f_M\left(\Delta\alpha, |\theta_{h\alpha}| = 0, k, \phi_{h\alpha} = 0\right) \end{bmatrix}.$$

In this approach, the aerodynamic forces due to the combination of a pitching and a plunging motion must not be taken into account. Hence, the samples at various phase differences are not necessary in the quasi-linearised case, reducing the computational effort.

Ueda et al. [49], He et al. [50] and Somieski [51] used superposition of describing functions to compute the aerodynamic forces by superposition of the pitching and plunging motions at the amplitudes and the frequency predicted by their extended p-k solvers. However, strictly speaking, superposition can no longer be applied to describing functions, as the higher order terms in the Taylor series are no longer small due to the larger amplitude. Nevertheless, this approach has been compared to the full non-linear approach in this thesis.

The complex-valued superposed aerodynamic lift force is obtained from:

$$\hat{L} = \theta_{Lh} \cdot \hat{h} + \theta_{L\alpha} \cdot \hat{\alpha} = |\theta_{Lh}| \cdot |\theta_{h\alpha}| \cdot \Delta\alpha \cdot c \cdot e^{i(\phi_{Lh} + \phi_{h\alpha})} + |\theta_{L\alpha}| \cdot \Delta\alpha \cdot e^{i\phi_{L\alpha}}, \tag{2.49}$$

where $\hat{L}$ is the complex-valued amplitude of the lift (i.e. $L = \hat{L}e^{i\omega t}$), $|\theta_{Lh}|$ is magnitude of the complex-valued ratio of the first harmonic components of the lift w.r.t. plunge (i.e. $|\theta_{Lh}| = |L|/\Delta h$, ϕ_{Lh}) is the phase angle of the lift w.r.t plunge, $|\theta_{L\alpha}|$ is the magnitude of the complex-valued ratio of the first harmonic components of the lift w.r.t. pitch (i.e. $|\theta_{L\alpha}| = |L|/\Delta\alpha$) and $\phi_{L\alpha}$ is the phase angle of the lift w.r.t. pitch. These magnitudes and phase angles are a function of the amplitude of the motion and the frequency. The superposed aerodynamic moment is obtained similarly. Figure 2.7 shows the magnitude and phase angle of the moment versus the phase difference for two different pitch amplitudes ($\Delta\alpha = 1°$ and $\Delta\alpha = 5°$) at a Mach number of 0.74 and a mean angle of attack of $-1.5°$ in inviscid flow (this test case is used for validation of ADePK in Chapter 4). The amplitude ratio is 1 and the reduced frequency is 0.3. At $\Delta\alpha = 1°$ the describing function obtained from superposition agrees well with the describing function computed from forced motion oscillation simulations. There are only small deviations. At $\Delta\alpha = 5°$ on the other hand, the shape of the describing functions of the moment is not correctly predicted at all. For the lift the agreement at $\Delta\alpha = 5°$ is better for this test case, but also small deviations are present. For this test case, the plunge only describing functions also have a larger relative change in the magnitude and phase angle of the aerodynamic moment than for the lift. The results shown in Figure 2.7 are exemplary for other test cases. In viscous transonic flow for example, it was found that the deviations for the lift are significant as well (at $\Delta\alpha = 5°$).

Figure 2.7 shows that if superposition of the DFs is applied, the resulting aerodynamic forces deviate from their actual non-linear aerodynamic forces, as expected. This deviation increases with increasing pitch amplitude. Hence, the error made due to the

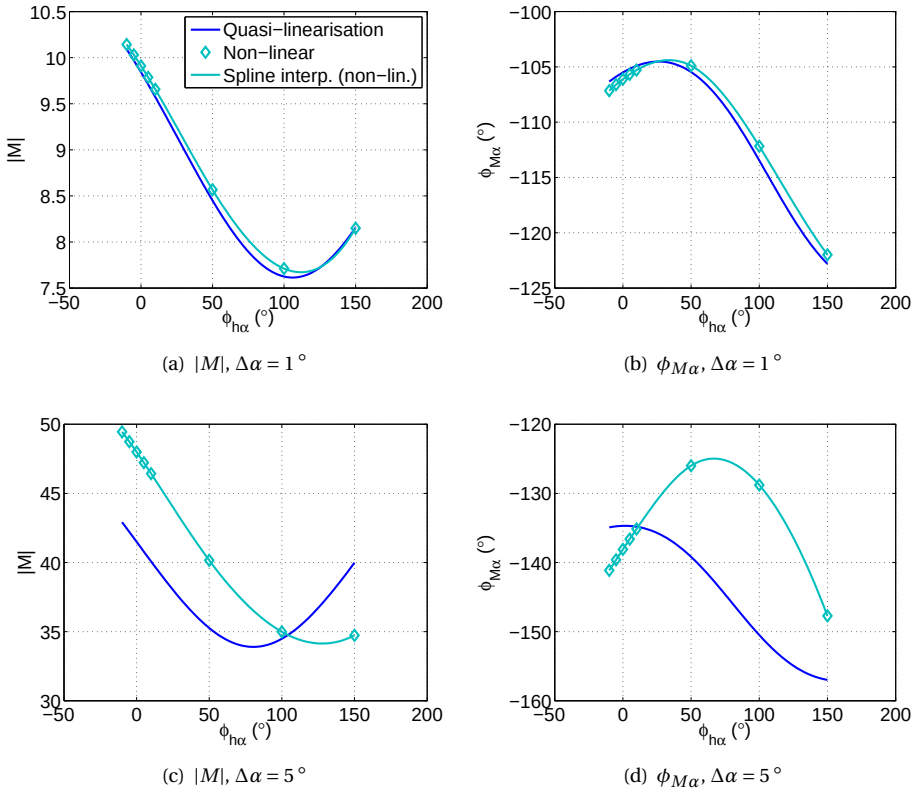

(a) $|M|$, $\Delta\alpha = 1\,°$ (b) $\phi_{M\alpha}$, $\Delta\alpha = 1\,°$

(c) $|M|$, $\Delta\alpha = 5\,°$ (d) $\phi_{M\alpha}$, $\Delta\alpha = 5\,°$

Figure 2.7: Magnitude and phase angle of the moment versus the phase difference at two pitch amplitudes in inviscid flow at $M = 0.74$, $\bar{\alpha} = -1.5°$, $|\theta_{h\alpha}| = 1$, $k = 0.3$

neglection of the coupling terms, increases with increasing amplitude. In this thesis, LCO amplitudes up to 5° are considered (see Chapters 4 and 5). Therefore, if the accuracy of the predicted LCOs must be for example 10%, the aerodynamic forces should not be computed from interpolation on a quasi-linearised response surface at an LCO amplitude of 5°. However, at 1°, a quasi-linearised response surface, as depicted in Figure 2.7, would predict an LCO amplitude within 10% of its value obtained from ADePK using a non-linear response surface. In this thesis a non-linear response surface will be used to avoids errors due to neglection of coupling terms. In Chapter 4, the quasi-linearised approach is compared with the non-linear approach to investigate the impact on the bifurcation behaviour of the LCO amplitude.

2.5.3. LIMIT-CYCLE OSCILLATIONS

In Section 2.5.1 it was explained how the limit-cycle oscillation amplitude and mode shape are predicted using ADePK. This section will describe how the stability of the predicted LCO can be determined and how the bifurcation behaviour of the LCO solution is

computed.

LIMIT-CYCLE OSCILLATION STABILITY

From ADePK the LCO amplitude is obtained. In order to determine the stability of the limit-cycle oscillation, the damping must be examined. By solving (2.46), the damping δ ($= \Re(p)$) is obtained as function of the amplitude. To determine the stability of the LCO, the sign of the derivative of the damping w.r.t. the amplitude at the intersection with the abscissa is considered. Figure 2.8 schematically presents two possible damping curves as obtained from a computation with ADePK. The pre-set amplitude $\Delta\alpha$ is depicted on the horizontal axis. A positive δ indicates an amplified motion and a negative δ indicates a damped motion. The blue curve shows a positive δ at low amplitudes, then the damping becomes negative with increasing amplitude. The LCO that occurs at zero damping is stable, i.e. it is an attractor. The red curve shows two intersections with the horizontal axis. At the first intersection, δ changes from negative to positive with increasing amplitude, i.e. an unstable LCO occurs, whereas at the second intersection with the horizontal axis, δ changes from positive to negative with increasing amplitude, i.e. a stable LCO occurs. The unstable LCO is a repeller as indicated by the arrows.

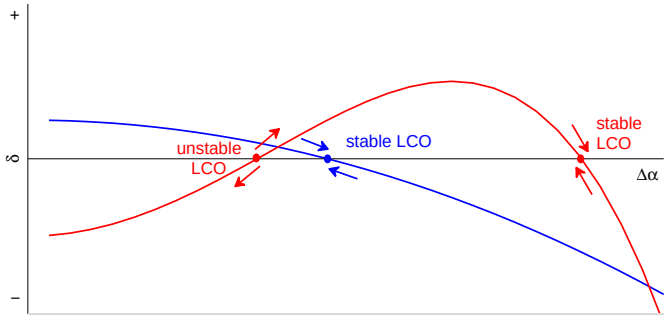

Figure 2.8: Sketch of damping versus amplitude

BIFURCATION BEHAVIOUR

As in the case of linear flutter, the aerodynamic forces are computed at a certain free-stream velocity, the reference velocity. Hence, to compute the damping as a function of amplitude at another velocity, this velocity (and density) must be pre-multiplied, as in (2.42). Except now the GAF matrix is replaced by the aerodynamic force vector $\tilde{\tilde{f}}$.

In order to study the bifurcation behaviour of a limit-cycle oscillation, a certain parameter, the so-called bifurcation parameter, is varied, keeping all other parameters fixed. Hence, the velocity or the dynamic pressure q_∞ are ideal candidates to be the bifurcation parameter, since they only have to be pre-multiplied. In this thesis the free-stream velocity has been used as bifurcation parameter. To obtain the bifurcation behaviour, (2.46) is solved at various velocities and at each velocity the amplitude(s) at which the damping becomes zero is/are determined. When these amplitudes are then

plotted versus the freestream velocity, one obtains a so-called bifurcation diagram. The types of bifurcations that generally occur for LCOs of an airfoil caused by aerodynamic non-linearities were described in Section 1.2, see Figure 1.2.

2.5.4. SAMPLING AND INTERPOLATION TECHNIQUES

SAMPLING

In to apply ADePK, as described in Section 2.5.1, a response surface must be constructed. Therefore, harmonic forced motion oscillations simulations must be performed at certain combinations of the amplitudes, frequency and the phase difference between the two degrees of freedom, as described in Section 2.5.2. Each of these parameters has a certain range in which they must be known. The simplest way to set up a response surface is to make a tensor-product grid. This method has been applied in this thesis. This might not lead to an optimal number of samples, but it ensures that the whole four dimensional space is covered with samples. Although, an optimisation of the arrangement of the samples could reduce the number of samples necessary and hence improve the accuracy of ADePK, the focus of this thesis is on the application of the method to the exploration of the LCO behaviour. Section 4.3.2 outlines how the range of the samples is obtained in detail.

INTERPOLATION

When the response surface is available, interpolation must be applied to find the aerodynamic force vector at the desired amplitudes, frequency and phase difference. Several interpolation methods are applied in this thesis; polynomial interpolation, cubic spline interpolation and linear interpolation. The results obtained with these three interpolation methods, in terms of the response surface itself and in terms of the bifurcation behaviour of the LCO solution, will be compared in Chapter 4. In Section 5.2 the bifurcation behaviour obtained from these three different methods of response surface interpolation will be compared as well. In the remaining sections of Chapter 5 cubic spline interpolation is used. Further details on the three interpolation methods used in this thesis can be found in Appendix C.

2.5.5. THE ADEPK METHOD IN PERSPECTIVE

The amplitude-dependent p-k method as presented in this section is valid for two degree-of-freedom systems that exhibit limit-cycle oscillations where the first harmonic component is dominant. ADePK can in general be extended to higher-DoF systems. However, the dimensions of the response surface would then increase significantly with each additional DoF. If n represents the number of DoFs, the dimensions of the response surface would increase as $n+1+n(n-1)/2$. Hence, ADePK would be computationally infeasible for systems with more than two or three DoFs. However, for these systems, there are usually only two degrees-of-freedom that contribute to the dominant flutter mechanism (e.g. classical bending-torsion flutter of aircraft wings). Since the bifurcation behaviour starts from the linear flutter point, close to the flutter point, these two DoFs will most likely be the main contributors to non-linear flutter as well. Hence, ADePK could be used only on those two DoFs that couple during flutter in order to predict limit-cycle oscillations of actual more-than-two-DoF systems.

ADePK only considers the first harmonic component of the motion and the aerodynamic forces. Although it should be noted that the effect of the higher harmonics components of the aerodynamic forces on the first harmonic component of the aerodynamic forces is naturally included in the first harmonic component of those forces. The assumption of a first harmonic LCO was found to be valid for the test cases used in this thesis by comparing with coupled fluid-structure interaction simulations, see Section 2.5.2 and Section 3.3.3. The results shown in Chapter 4, which shows the verification and validation of the ADePK method, further demonstrate the validatity of this assumption in terms of the bifurcation behaviour of the LCO solution. Furthermore, the higher harmonics of the aerodynamics will by definition not perform any work on the first harmonic of the structural motion and hence can be neglected. Naturally, when the higher harmonics of the structural motion become significant in comparison to the first harmonic, i.e. of the same order of magnitude, this approach will no longer be valid. The higher harmonics could be taken into account in ADePK, i.e. then additional response surfaces for higher-harmonic motions need to be constructed. However, this would lead to a massive increase in computational work. Further study is needed to address the accuracy of ADePK in case of significant higher harmonic components in the structural motion.

In the ADePK method, the aerodynamic forces and the structure are decoupled in order to be able to quickly address the effects of structural parameter variations on the LCO bifurcation behaviour. However, when considering a variation in the structural stiffness for example, the equilibrium position of the system will change. Marques et al. [52] for example, have taken into account this dependence of the equilibrium position when studying the effect of the structural parameter variations on the flutter behaviour of a wing and a fighter aircraft. A change in equilibrium position could be taken into account when ADePK is used, however, since a new mean angle of attack would require the construction of a new response surface, this would violate the idea of the quick assessment of the effect of structural parameter variations. Therefore, this effect has not been taken into account in this thesis. It is not clear how large the influence of the structural parameters on the equilibrium position is. Further study is necessary to evaluate the impact of decoupling of fluid and structure as performed in this thesis.

Construction of the response surface is an important aspect of ADePK. More details on how this response surface is constructed can be found in Sections 2.5.4 and 4.3.2. The number of samples and the distribution of the samples determine the accuracy with which the response surface is interpolated. Especially in amplitude- and reduced frequency-directions the interpolated response surface and therefore the LCO bifurcation behaviour are sensitive to the choice of sampling. Therefore, it should always checked whether adding or removing a sample in these two directions will lead to a different response surface. For validation and to determine the number of samples necessary in each direction of the response surface, slices of the interpolated response surface in each of the direction have been compared to dense-sample harmonic forced motion oscillation simulations on each slice (for the test case shown in Section 4.3.2). In most cases, the interpolation was found to give a good representation of the response surface slice. For the imaginary part of the lift and the real part of the moment, the slices in the reduced frequency-direction were found to exhibit a slight waviness for reduced

frequencies smaller than 0.2, which was not represented by the interpolation. It is not clear whether this waviness influences the LCO analysis. Further study is needed to clarify this.

In case of infinitely many samples, all interpolation methods should result in the same interpolated response surface. As will be shown in Section 4.3.2, although the number of samples used in this thesis is quite high (> 1000), in some directions there are still deviations between the three interpolated response surfaces. This was expected for linear interpolation. However, for cubic spline and polynomial interpolation, the difference was expected to be smaller. In addition, in this thesis, the response surface has been set up using a tensor-product grid. Other, sampling techniques, such as latin-hypercube sampling or sparse grid sampling, might lead to a better sample distribution for the same number of samples and thus a better interpolated response surface. Hence, in order to make the ADePK method more accurate, more samples, a better distribution of the samples, a better interpolation method or a combination of these three is necessary.

Nevertheless, considering all these aspects, the amplitude-dependent p-k method significantly reduces the computational effort compared to fluid-structure interaction simulations, while being accurate enough for the purpose of this thesis (see Chapter 4 which validates the method). Studies of the LCO bifurcation behaviour would not be possible with fluid-structure interaction simulations especially when structural parameter variations are of interest, as in this thesis. Furthermore, even though the ADePK method is only used for a two-dimensional section of a wing, the basic mechanisms that describe the LCO bifurcation behaviour are expected to be present and can probably be translated to three-dimensional cases (e.g. classical bending-torsion flutter). In addition, the conventional p-k method is widely used in the aircraft industry for linear flutter prediction. LCOs caused by aerodynamic non-linearities are usually not considered, unless they occur inside the flight envelope. Hence, no tools are available in the industry that can relatively quickly predict LCOs. Therefore, the amplitude-dependent p-k method for LCO prediction will be a useful tool for the aircraft industry, since the adaptations to the conventional p-k method are relatively small.

REFERENCES

[1] J. Zwaaneveld, *Aerodynamic characteristics of the supercritical shock-free airfoil section NLR 7301*, Tech. Rep. NLR TR 76052 C (1976).

[2] J. Zwaaneveld, *NLR 7301 airfoil,* in *EXPERIMENTAL DATA BASE FOR COMPUTER PROGRAM ASSESSMENT - Report of the Fluid Dynamics Panel Working Group 04*, AGARD AR-138 (1979) pp. A4–1–A4–22, NATO - ADVISORY GROUP FOR AEROSPACE RESEARCH AND DEVELOPMENT.

[3] R. Zwaan, *NLR 7301 supercritical airfoil oscillatory pitching and oscillating flap,* in *Compendium of unsteady aerodynamic measurements*, AGARD AR-702 (1982) NATO - ADVISORY GROUP FOR AEROSPACE RESEARCH AND DEVELOPMENT.

[4] S. Davis, *NLR 7301 supercritical airfoil oscillatory pitching,* in *Compendium of un-*

steady aerodynamic measurements, AGARD AR-702 (1982) pp. 5–1–5–27, NATO - ADVISORY GROUP FOR AEROSPACE RESEARCH AND DEVELOPMENT.

[5] G. Schewe, A. Knipfer, H. Mai, and G. Dietz, *Experimental and Numerical Investigation of Nonlinear Effects in Transonic Flutter*, Internal Report DLR IB 232 - 2002 J 01 (Deutsches Zentrum für Luft- und Raumfahrt e.V. (DLR), Institut für Aeroelastik, Göttingen, Germany, 2002).

[6] G. Schewe, H. Mai, and G. Dietz, *Nonlinear effects in transonic flutter with emphasis on manifestations of limit cycle oscillations,* Journal of Fluids and Structures **18**, 3 (2003).

[7] G. Dietz, G. Schewe, F. Kiessling, and M. Sinapius, *Limit-cylce-oscillation experiments at a transport aircraft wing model,* (Deutsches Zentrum für Luft- und Raumfahrt, Institut für Aeroelastik, Amsterdam, The Netherlands, 2003) international Forum on Structural Dynamics and Aeroelasticity (IFASD).

[8] G. Dietz, G. Schewe, and H. Mai, *Experiments on heave/pitch limit-cycle oscillations of a supercritical airfoil close to the transonic dip,* Journal of Fluids and Structures **19**, 1 (2004).

[9] G. Dietz, G. Schewe, and H. Mai, *Amplification and amplitude limitation of heave/pitch limit-cycle oscillations close to the transonic dip,* Journal of Fluids and Structures **22**, 505 (2006).

[10] S. Weber, K. Jones, J. Ekaterinaris, and M. Platzer, *Transonic flutter computations for a 2d supercritical wing,* (Naval Postgraduate School, Monterey, CA, Reno, NV, 1999) 37th AIAA/ASME/ASCE/AHS/ASC Structures, Structural Dynamics, and Materials Conference and Exhibit.

[11] B. Castro, K. Jones, J. Ekaterinaris, and M. Platzer, *Analysis of the effect of porous wall interference on transonic airfoil flutter,* (Naval Postgraduate School, Monterey, CA, Anaheim, CA, 2001) 31st AIAA Fluid Dynamics Conference & Exhibit.

[12] L. Tang, R. Bartels, P. Chen, and D. Liu, *Numerical investigation of transonic limit cycle oscillations of a two-dimensional supercritical wing,* Journal of Fluids and Structures **17**, 29 (2003).

[13] B. Wang and G.-C. Zha, *Numerical simulation of transonic limit cycle oscillations using high-order low-diffusion schemes,* Journal of Fluids and Structures **26**, 579 (2010).

[14] J. Thomas, E. Dowell, and K. Hall, *Modeling viscous transonic limit cycle oscillation behavior using a harmonic balance approach,* (Duke University, Durham, NC, Denver, CO, 2002) 43rd AIAA/ASME/ASCE/AHS/ASC Structures, Structural Dynamics, and Materials Conference and Exhibit.

[15] J. Thomas, E. Dowell, and K. Hall, *Modeling limit cycle oscillations for an NLR 7301 airfoil aeroelastic configuration including correlation with experiment,* (Duke University, Durham, NC, Norfolk, VA, 2003) 44th AIAA/ASME/ASCE/AHS/ASC Structures, Structural Dynamics, and Materials Conference and Exhibit.

[16] S. Weber, K. Jones, J. Ekaterinaris, and M. Platzer, *Transonic flutter computations for the NLR 7301 supercritical airfoil,* Aerosp. Sci. Technology **5**, 293 (2001).

[17] L. Tang, R. Bartels, P. Chen, and D. Liu, *Simulation of transonic limit cycle oscillations using a CFD time-marching method,* (Seattle, WA, 2001) 42nd AIAA/ASME/ASCE/AHS/ASC Structures, Structural Dynamics, and Materials Conference and Exhibit.

[18] O. Bendiksen, *Transonic limit cycle flutter/lco,* (Univerisity of California, Los Angelos, Palm Springs, California, 2004) 45th AIAA/ASME/ASCE/AHS/ASC Structures, Structural Dynamics, and Materials Conference.

[19] K. Saitoh and H. Kheirandish, *Numerical simulation of small amplitude lco for NLR-7301 profile,* (Stockholm, Sweden, 2007) international Forum on Structural Dynamics and Aeroelasticity (IFASD).

[20] K. Saitoh, R. Voss, and H. Kheirandish, *Numerical study of nonlinearity of unsteady aerodynamics for NLR7301 profile,* (Munich, Germany, 2005) international Forum on Structural Dynamics and Aeroelasticity (IFASD).

[21] J. Boerstoel and G. Huizing, *Transonic shock-free aerofoil design by analytic hodograph methods*, Tech. Rep. NLR MP 73023 U (1973).

[22] J. Boerstoel and J. van Egmond, *Design of shock-free, basic aerofoils for a supercritical wing*, Tech. Rep. NLR TR 75077 C (1975).

[23] T. Gerhold and M. Galle, *Calculation of complex three-dimensional configurations employing the DLR TAU-code.* AIAA Paper 97-0167 (1997).

[24] J. D. Anderson, *Fundamentals of Aerodynamics*, 4th ed. (McGraw-Hill, 2007).

[25] A. Favre, *Equations des gaz turbulents compressibles. formes générales.* Journal de Mecanique **4**, 361 (1965).

[26] A. Favre, *Equations des gaz turbulents compressibles ii. méthode des vitesses moyennes; méthode des vitesses macroscopiques pondérées par la masse volumique.* Journal de Mecanique **4**, 391 (1965).

[27] T. Chung, *Computational Fluid Dynamics*, 1st ed. (Cambridge University Press, 2002).

[28] F. Menter, *Two-equation eddy-viscosity turbulence models for engineering applications,* AIAA Journal **32**, 1598 (1994).

[29] R. B. Langtry, *A Correlation-Based Transition Model using Local Variables for Unstructured Parallelized CFD codes*, Ph.D. thesis, University of Stuttgart (2006), faculty of Mechanical Engineering, Institut fuer Thermische Stroemungsmaschinen und Maschinenlaboratorium.

[30] F. Menter, R. Langtry, and S. Voelker, *Transition modelling for general purpose CFD codes,* Flow Turbulence Combustion **77**, 277 (2006).

[31] I. Tani, *Boundary-layer transition,* Annual Review of Fluid Mechanics **1**, 169 (1969).

[32] J. van Ingen, *A suggested semi-emprical method for the calculation of the boundary layer transition region*, Tech. Rep. V.T.H.-74 (Delft University of Technology, Aerospace Engineering, 1956).

[33] A. Smith and N. Gamberoni, *Transition, Pressure Gradient and Stability Theory*, Tech. Rep. ES-26388 (Douglas Aircraft, 1956).

[34] C. Grabe and A. Krumbein, *Correlation-based transition transport modeling for three-dimensional aerodynamic configurations,* Journal of Aircraft **50** (2013).

[35] C. Seyfert and A. Krumbein, *Evaluation of a correlation-based transition model and comparison with the e^n method,* Journal of Aircraft **49** (2012).

[36] R. Langtry and F. Menter, *Correlation-based transition modeling for unstructured parallelized computational fluid dynamics codes,* AIAA Journal **47** (2009).

[37] *Technical Documentation of the DLR TAU-Code Release 2012.1.0*, Deutsches Zentrum fuer Luft- und Raumfahrt, Institute of Aerodynamics and Flow Technology, Braunschweig (2012).

[38] A. Jameson, *Time dependent calculations using multigrid, with applications to unsteady flows past airfoils and wings,* AIAA Paper 91-1596 (1991), AIAA 10th Computational Fluid Dynamics Conference.

[39] A. Jameson, W. Schmidt, and E. Turkel, *Numerical solutions of the Euler equations by finite volume methods using Runge-Kutta time-stepping schemes,* (1981).

[40] D. H. Hodges and G. A. Pierce, *Introduction to Structural Dynamics and Aeroelasticity* (Cambridge University Press, 2002).

[41] E. Dowell, *A Modern Course in Aeroelasticity* (Kluwer Academic Publishers, 2004).

[42] H. Hassig, *An approximate true damping solution of the flutter equation by determinant iteration,* Journal of Aircraft **8** (1971).

[43] R. Scanlan and R. Rosenbaum, *Outline of an Acceptable Method of Vibration and Flutter Analysis for a Conventional Airplane*, Tech. Rep. (CAA Aviation Safety Release 302, 1948).

[44] R. Thormann, J. Nitzsche, and M. Widhalm, *Time-linearized simulation of unsteady transonic flows with shock-induced separation,* in *Proceedings of the 6th European Congress on Computational Methods in Applied Sciences and Engineering (ECCOMAS 2012)* (2012).

[45] P. Greco, C. Lan, and T. Lim, *Frequency domain unsteady transonic aerodynamics for flutter and limit cycle oscillation prediction,* (Reno, NV, USA, 1997) 35th AIAA Aerospace Sciences Meeting & Exhibit.

[46] J. Thomas, E. Dowell, and K. Hall, *Nonlinear inviscid aerodynamic effects on transonic divergence, flutter and limit-cycle oscillations,* AIAA Journal **40**, 638 (2002).

[47] A. van Rooij, J. Nitzsche, H. Bijl, and L. Tichy, *Limit-cycle oscillations of a supercritical airfoil,* (Bristol, UK, 2013) international Forum on Structural Dynamics and Aeroelasticity (IFASD).

[48] A. Gelb and W. V. Velde, *Multiple-input describing functions and nonlinear system design* (McGraw-Hill, 1968).

[49] T. Ueda and E. Dowell, *Flutter analysis using nonlinear aerodynamic forces,* Journal of Aircraft **21** (1984).

[50] S. He, Z. Yang, and Y. Gu, *Transonic limit cycle oscillation analysis using aerodynamic describing functions and superposition principle,* AIAA Journal **52** (2014).

[51] G. Somieski, *An eigenvalue method for calculation of stability and limit cycles in nonlinear systems,* Nonlinear Dynamics **26**, 3 (2001).

[52] S. Marques, K. Badcock, H. Khodaparast, and J. Mottershead, *Transonic aeroelastic stability predictions under the influence of structural variability,* Journal of Aircraft **47**, 1229 (2010).

3

ENERGY BUDGET ANALYSIS OF LIMIT-CYCLE OSCILLATIONS

3.1. INTRODUCTION

To study the causes of amplitude limitation, Dietz et al. [1] conducted wind tunnel experiments in which an unstable aeroelastic two DoF system was forced to oscillate at several constant amplitudes by the use of a flutter control-system. The oscillations were prevented from growing or decaying in amplitude by applying an additional excitation force on the heave DoF. This variable-gain additional force was proportional to the heave velocity and effectively acted as a viscous damping element. At the LCO amplitude the exciter force did not do any work to the system. At constant-amplitude oscillations smaller than the LCO amplitude, energy was extracted from the system, whereas at oscillation amplitudes larger than the LCO amplitude, energy had to be fed into the system. It is important to note, that with this experimental set-up the viscous damping was modified slightly, whereas the eigenfrequencies and complex-valued mode shapes of the coupled aeroelastic system remained (largely) intact. In a post-processing step the contributions of several components (damping, aerodynamic lift, aerodynamic moment) to the total power fed into or extracted from the system were analysed for (forced) constant-amplitude oscillations at several amplitudes. At the (natural) LCO amplitude the total power, i.e. the sum of aerodynamic power and structural damping power averaged over one oscillation cycle, was zero, as expected. Both the power of the aerodynamic lift and moment were found to be weakly non-linear with amplitude, leading to a nearly glancing intersection of the total power curve with the zero axis [1]. Furthermore, Dietz et al. [1, 2] observed that the phase difference between heave and pitch that they found during the (forced) LCO experiments was small enough (in the order of $5-10^{\circ}$) such that the LCOs they observed can be seen as a single degree-of-freedom motion with its rotation point upstream of the airfoil. Bendiksen [3] also observed that for LCOs close

Parts of this chapter have been published in van Rooij et al., Energy budget analysis of limit-cycle oscillations, Journal of Fluids and Structures (2017), 69, pp. 174-186, http://dx.doi.org/10.1016/j.jfluidstructs.2016.11.016

to the linear flutter boundary, the mode shape resembles a single-DoF pitching motion.

Although Dietz et al. [1] performed a good account of work on analysing the energy budget of limit-cycle oscillations of a two DoF system, several questions remain unanswered. E.g. why does the total power behave in the way it does, i.e. why do we have a nearly glancing intersection of the total power with the zero axis? And what are the causes of this, i.e. what global and local features are responsible for this? In order to answer these questions, an energy budget analysis is applied in this thesis using numerical simulations. Following standard-procedure, fluid-structure-coupled simulations of a two DoF airfoil system above the flutter boundary were performed. Furthermore, forced motion oscillation simulations were performed at several constant oscillation amplitudes. In both cases the averaged aerodynamic power components were calculated on the basis of the aerodynamic forces and the motion data. To find the causes for the amplitude limitation, the deviations of these power components with respect to the linearised (flutter) case are analysed and the sources of aerodynamic non-linearity are traced back. Although several investigations have used local power or work distributions to study limit-cycle oscillations e.g. [2, 4–6], little work has been performed on the global energy budget of limit-cycle oscillations. This work bridges between the initial work done on the global energy budget of LCOs by Dietz et al. [1] and the local approaches of [2, 4–6]. However, the goal of this work is not to validate the numerical results against the wind tunnel experiments performed at German Aerospace Center [1, 2, 7–9]. Therefore, no attempt is made to directly compare the results obtained here with those of Dietz et al. [1, 2]. Only indirect comparisons of the energy budget will be made.

Section 2 of this Chapter describes the computational methods used in this chapter. In Section 3 the results of the forced motion oscillation simulations and the FSI simulations are presented and analysed. Finally, conclusions are drawn.

3.2. COMPUTATIONAL METHODS

This section describes the computational methods and set-up used in the current investigation. First, the CFD code will be briefly discussed. Second, the structural model is addressed. Then, the fluid-structure coupling and the LCO modelling using forced motion oscillations are presented. Finally, the results of a mesh- and time step convergence study are presented.

3.2.1. CFD CODE AND SET-UP

The CFD code used is the DLR-TAU code developed by the German Aerospace Center [10]. This code is a finite-volume, cell-vertex-based, unstructured compressible RANS solver. For spatial discretisation a 2nd order central scheme [11] is used. Temporal discretisation is realised by dual time stepping [12] with the 2nd order accurate Backward Differencing Formula (BDF2) integration scheme for the physical time. The turbulence model used for closure is the Menter SST model. More details on the CFD code can be found in Section 2.2.3.

The airfoil used in this study is the supercritical NLR7301 airfoil with a blunt trailing edge (coordinates were taken from [13]). Its design Mach number is 0.721 and its design lift coefficient is 0.595, see Section 2.2.1 for more details on the NLR7301 airfoil. The

Reynolds number with respect to the chord length was set to $2 \cdot 10^6$ for all CFD simulations. The chord length of the airfoil is 0.3 m. In order to simulate a two-dimensional airfoil a straight three dimensional wing is used, with symmetry planes at both sides. In this work a wing with a span of 1.0 m is used. The unstructured O-type mesh consisting of hexahedrons that has used for all CFD simulations, has 65888 points. The non-dimensional first cell height y^+ is smaller than 1. The mesh has one cell in span-wise direction. Figure 2.3(a) shows a zoom of the mesh near the airfoil. This mesh has been selected after a mesh convergence study, which is shown in Section B.1.2. It is thought to be a compromise between accuracy and computational work. Furthermore, the results obtained in chapter are only compared to each other and hence a very high resolution of the mesh is not required, since no (direct) validation with experimental results is intended. The time step Δt used for the forced motion simulations as well as for the FSI simulations is $1 \cdot 10^{-4}$ s. This is equivalent to a non-dimenstional time step size of 0.082 (based on the freestream velocity) or a number of time steps per oscillation periods of 303. This time step size has been selected from a time step convergence study, which is shown in Section B.2.2. The error made when using a time step of $1 \cdot 10^{-4}$ s, or 303 time steps per oscillation period, is acceptable for the investigations in this chapter.

The motion of the airfoil is achieved by a rigid-body displacement of the complete grid. In this way the grid cells keep their form and no grid deformation in the classical sense is necessary. The additional fluxes that are introduced by displacing the complete grid are taken into account such that the geometric conservation law is satisfied.

The airfoil was tested at various angles of attack and at $M = 0.74$. The static temperature has been set to 273 K. The flow is fully turbulent in all simulations.

3.2.2. STRUCTURAL MODEL

In this work the airfoil is modelled using a linear structural model with two degrees of freedom (pitch and plunge). The elastic axis is located at the quarter-chord point for the investigations in this chapter. A schematic representation of the aeroelastic system system is shown in Figure 2.1. The structural properties of the two-degree-of-freedom system have been taken from the wind-tunnel model of the NLR7301 airfoil used by Dietz et al. [1]. They are depicted in Table 2.1.

3.2.3. FLUID-STRUCTURE INTERACTION

The equations of motion of the system depicted in Figure 2.1 were given by (2.7). They are repeated here (note that x_{ea} is zero in this chapter):

$$\mathbf{M}\ddot{\vec{x}} + \mathbf{D}\dot{\vec{x}} + \mathbf{K}\vec{x} = \vec{f}, \tag{3.1}$$

where the mass matrix $\mathbf{M}$, damping matrix $\mathbf{D}$, stiffness matrix $\mathbf{K}$, force vector $\vec{f}$ the displacement vector $\vec{x}$ are defined as:

$$\mathbf{M} = \begin{bmatrix} m & S_\alpha \\ S_\alpha & I_\alpha \end{bmatrix}, \mathbf{D} = \begin{bmatrix} D_h & 0 \\ 0 & D_\alpha \end{bmatrix},$$
$$\mathbf{K} = \begin{bmatrix} K_h & 0 \\ 0 & K_\alpha \end{bmatrix}, \vec{f} = \begin{bmatrix} -L \\ M \end{bmatrix} = \begin{bmatrix} -(\tilde{L} - L_0) \\ \tilde{M} - M_0 \end{bmatrix} \text{ and } \vec{x} = \begin{bmatrix} h \\ \alpha \end{bmatrix} = \begin{bmatrix} \tilde{h} - h_0 \\ \tilde{\alpha} - \alpha_0 \end{bmatrix}. \tag{3.2}$$

Here L is the lift, M the aerodynamic moment and h and α are the plunge displacement and pitch angle, respectively. In order to trim the airfoil at a desired mean angle of attack α_0 (and possibly at a desired plunge position h_0), the steady loads at this desired mean angle of attack (L_0, M_0) are subtracted from the actual loads ($\tilde{L}$, $\tilde{M}$).

The system (3.1) is solved using fluid-structure coupling, where the pitch angle α, plunge displacement h, angular velocity $\dot{\alpha}$ and the plunge velocity $\dot{h}$ as well as the resulting forces and moments are exchanged between the CFD code and the structural solver. This is done multiple times during each time step, such that at the end of each time step an equilibrium is achieved. Hence, the FSI coupling as applied here is commonly referred to as "strong". This is in contrast to a so-called weak coupling, where both the fluid and the structure are converged separately and forces and displacements are exchanged after each time step. Strong coupling therefore avoids additional errors due to partitioning. The second order backward differencing formula (BDF2) has been used for the numerical integration of (3.1).

In order to verify the correct implementation of the FSI coupling algorithm, the energy conservation of the algorithm has to be checked. The mean of the initial energy E_0 of the two-degree-of-freedom system should remain constant in time according to the energy conservation law. The initial energy is given by:

$$E_0 = E_{\text{kin}} + E_{\text{pot}} - W_{\text{nc}}. \tag{3.3}$$

Hence, the mean of the total of the kinetic energy $E_{\text{kin}} = {}^1/_2 \cdot \vec{\dot{x}}^T \mathbf{M} \vec{\dot{x}}$, the potential energy $E_{\text{pot}} = {}^1/_2 \cdot \vec{x}^T \mathbf{K} \vec{x}$ and the negative of the non-conservative work W_{nc} should remain constant. The non-conservative work consists of the work done by the structural damping forces and by the aerodynamic loads acting on the airfoil, i.e.:

$$W_{\text{nc}} = \int_0^t \left(\vec{\dot{x}}^T \mathbf{D} \vec{\dot{x}} - \vec{\dot{x}}^T \vec{f} \right) dt. \tag{3.4}$$

Figure 3.1 demonstrates that the mean of the initial energy E_0, as given by (3.3), is constant during the initial phase of an FSI simulation (see Figure 3.6 for the complete time signal).

3.2.4. FORCED MOTION OSCILLATIONS

In the experiments of Dietz et al. [1] the oscillation amplitude is kept constant by applying a flutter-control system, which constrains the oscillations from growing or decaying. This would be similar to constraining the oscillations to grow or decay in a coupled FSI simulation. Here, single-harmonic forced motion oscillations of constant amplitude are used to model such a forced LCO (i.e. an oscillation of constant amplitude restrained by the flutter-control system). In order to do so, the frequency and the mode shape during the LCO must be known, i.e. the frequency, the phase difference between pitch and plunge and the ratio between the pitch and plunge amplitudes are required. This is in contrast to coupled FSI simulations and the wind tunnel experiments of Dietz et al. [1], where the mode shape is implicitly known. Hence, an FSI simulation must be performed to find the mode shape of the system. The mode shape during the growth (or decay) of the oscillation amplitude can then be extracted (neglecting the higher harmonics). This information can be used as an input to the forced motion oscillation simulations.

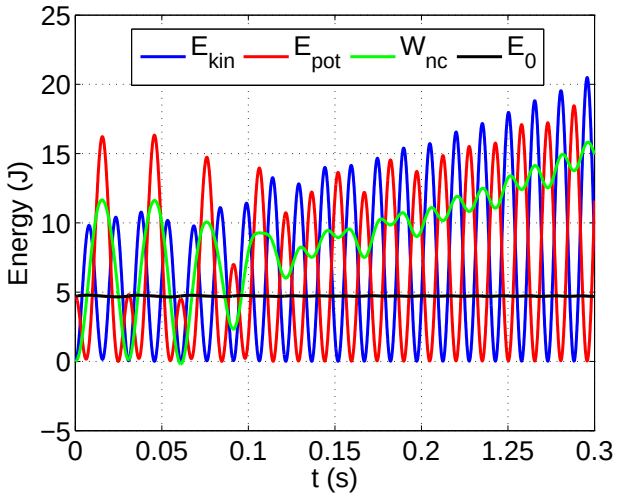

Figure 3.1: Time evolution of the energy for an FSI simulation

The motion of the airfoil during a forced motion oscillation is prescribed using (2.47) and (2.48), which are repeated here:

$$h(t) = \Delta h \cdot \sin\left(\omega t + \phi_{h\alpha}\right), \tag{3.5}$$

$$\alpha(t) = \Delta\alpha \cdot \sin\omega t, \tag{3.6}$$

where $\phi_{h\alpha}$ is the phase difference between pitch and plunge, that is, $\phi_{h\alpha} = \phi_h - \phi_\alpha$, i.e. $\phi_{h\alpha}$ is the phase of the plunging motion w.r.t. the pitching motion. Hence, when the phase difference is positive, plunge leads pitch and when $\phi_{h\alpha}$ is negative plunge lags pitch. ω is the angular frequency.
Note that in (3.5) and (3.6) only the first harmonic component is taken into account. It was observed from numerically computed LCOs as well from experimentally obtained LCOs [1, 2] that the oscillations are approximately first harmonic. Hence, it is hypothesised that the LCOs observed for the NLR7301 airfoil are purely sinusoidal in the first fundamental frequency. This issue was addressed in Section 2.5.2. Further proof of this hypothesis will be given in Section 3.3.3.

3.3. RESULTS AND DISCUSSION

This section shows the results of FSI simulations and the corresponding forced motion oscillation simulations. The results of a power analysis will be shown and discussed for both simulation methods. An analytical test case, the van der Pol-oscillator, is studied first, in both time and frequency domain. Then the two DoF airfoil system is addressed. Furthermore, the effect of oscillation amplitude is studied by comparing the non-linear aerodynamic forces and power components with their equivalent linearised counterparts. Finally, the global source of the amplitude limitation will be identified.

3.3.1. VAN DER POL-OSCILLATOR

Before looking at the energy budget of the two degree-of-freedom airfoil system, the energy budget of the limit-cycle oscillations obtained from the van der Pol-oscillator is considered. These analytical systems are used to test and verify the energy budget analysis approach. They serve as a model for the non-linear aerodynamic forces. It will be shown that the energy balance can be used to derive analytical solutions for these van der Pol-oscillators, which can be used to establish the bifurcation behaviour, as will be shown in Chapter 4.

ONE DOF VAN DER POL-OSCILLATOR

The van der Pol oscillator [14] is an example of a non-linear oscillator often used in (non-linear) dynamics. The oscillator contains a non-linear damping term that results in limit-cycle oscillations. Originally this non-linear damping term is of second order. In this thesis the non-linear damping term has been modified to a fourth order term, such that the van der Pol oscillator will exhibit subcritical bifurcations. The equation of motion of the van der Pol-oscillator then becomes:

$$\ddot{x} + x = \epsilon \left(\mu - a x^2 - d x^4\right) \dot{x}, \tag{3.7}$$

where x is the time-dependent displacement, ϵ a damping coefficient and μ a bifurcation parameter. a and d are constants.

Figure 3.2 shows the time domain solution obtained using the Dormand-Prince (DOPRI) method [15] with $\epsilon = 0.01$, $\mu = 1$, $a = 1$ and $d = 0$. Figure 3.2(a) shows the displacement versus the time and Figure 3.2(b) shows the phase portrait, i.e. $\dot{x}$ versus x.

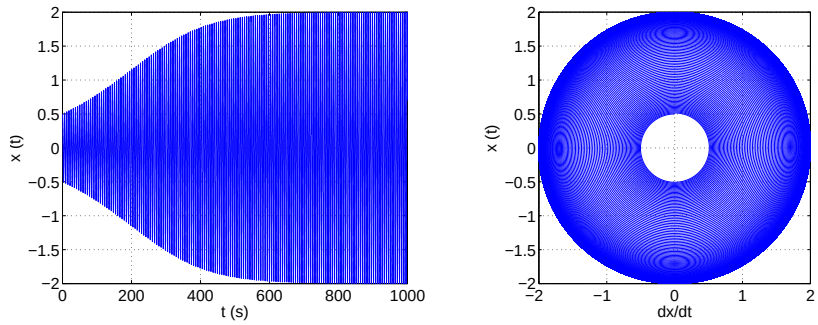

(a) Amplitude versus time

(b) Phase portrait

Figure 3.2: Time domain solution of the one degree-of-freedom van der Pol oscillator system ($\epsilon = 0.01$, $\mu = 1$, $a = 1$ and $d = 0$)

As can be seen from these figures a limit-cycle oscillation with an amplitude of approximately 2 and an angular frequency of 1.00 rad/s develops. To analyse this LCO, the principle of energy conservation is applied on this system. In order to do so, a solution of the form:

$$x(t) = \hat{x}\sin(\omega t), \tag{3.8}$$

is assumed. Here $\hat{x}$ is the amplitude. The equation of motion (3.7) is then pre-multiplied by $\dot{x}$ and integrated over one oscillation period, i.e.

$$\int_0^T \dot{x}\ddot{x}dt + \int_0^T \dot{x}x dt = \int_0^T \dot{x}\epsilon\left(\mu - ax^2 - dx^4\right)\dot{x}dt, \tag{3.9}$$

where T is the oscillation period. Performing the integration results in:

$$E_{\text{kin}} + E_{\text{pot}} = \int_0^T \dot{x}\epsilon\left(\mu - ax^2 - dx^4\right)\dot{x}dt, \tag{3.10}$$

where E_{kin} is the kinetic energy and E_{pot} is the potential energy. The left-hand side of this equation is constant, i.e. the sum of the kinetic and potential energy over one oscillation period is constant (for the constant amplitude limit-cycle oscillation). This means that the integrand on the right-hand side should be zero in order for the integral to be constant. Hence, the instantaneous power, defined by:

$$P_n = \dot{x}\epsilon\left(\mu - ax^2 - dx^4\right)\dot{x}, \tag{3.11}$$

should be zero. Inserting equation (3.8) and its derivatives yields:

$$P_n = \omega^2\hat{x}^2\epsilon\cos^2(\omega t)\left(\mu - a\hat{x}^2\sin^2(\omega t) - d\hat{x}^4\sin^4(\omega t)\right). \tag{3.12}$$

To satisfy (3.10), the mean of this equation should disappear, i.e. $\bar{P}_n = \text{mean}(P_n) = 0$. Since the mean value of $\cos^2(\omega t)$ is 1/2, the mean value of $\cos^2(\omega t)\sin^2(\omega t)$ is 1/8 and the mean value of $\cos^2(\omega t)\sin^4(\omega t)$ is 0.062375, the equation for the mean power becomes:

$$\bar{P}_n = 0.5\epsilon\omega^2\hat{x}^2\left(\mu - 0.25a\hat{x}^2 - 0.12475d\hat{x}^4\right). \tag{3.13}$$

In case of an LCO the mean power should disappear. Hence, the term between the brackets in (3.13) should be zero. The amplitude of the motion can be computed from:

$$\hat{x} = \sqrt{\frac{0.25a \pm \sqrt{0.499d\left(\mu + \frac{0.0625a^2}{0.499d}\right)}}{-0.2495d}}, \tag{3.14}$$

where the plus-sign represents the subcritical part of the bifurcation and the minus-sign the supercritical part. When the non-linear damping term is only quadratic, i.e. $d = 0$ the solution for the amplitude reduces to:

$$\hat{x} = 2\sqrt{\frac{\mu}{a}}. \tag{3.15}$$

TWO DOF VAN DER POL-OSCILLATOR

Since the system of interest in this thesis is a two degree-of-freedom system, the van der Pol-oscillator has been extended to two degrees of freedom. A fourth order non-linear damping term as for the one DoF system (see (3.7)) has been used here as well. The equations of motion of this two DoF system are given by:

$$\mathbf{M}\ddot{\vec{x}} + \mathbf{K}\vec{x} = \epsilon \begin{bmatrix} \mu - a_1 x_1^2 - b_1 x_1^4 & c_1\mu - a_2 x_1^2 \\ c_1\mu - a_3 x_2^2 & c_1\mu - a_4 x_2^2 - b_2 x_2^4 \end{bmatrix} \begin{bmatrix} \dot{x}_1 \\ \dot{x}_2 \end{bmatrix}, \tag{3.16}$$

where $\vec{x} = [x_1, x_2]^T$ is now a vector with the displacements of the two degrees of freedom and a_1, a_2, a_3, a_4, b_1, b_2 and c_1 are constants. The mass matrix $\mathbf{M}$ is chosen as the identity matrix, whereas the stiffness matrix $\mathbf{K}$ is defined as:

$$\mathbf{K} = \begin{bmatrix} 20 & -10 \\ -10 & 10 \end{bmatrix}. \tag{3.17}$$

Using the Dormand-Prince (DOPRI) method [15], a time domain solution was obtained with the parameters: $\epsilon = 0.02$, $\mu = 0.8$, $a_1 = 0.3$ and $a_2 = a_3 = a_4 = b_1 = b_2 = c_1 = 0$. The displacements of both degrees of freedom are plotted versus time in Figure 3.3 and the phase portraits are shown in Figure 3.4. For clarity reasons only the last 600 s of the time signal are plotted in the phase portraits.

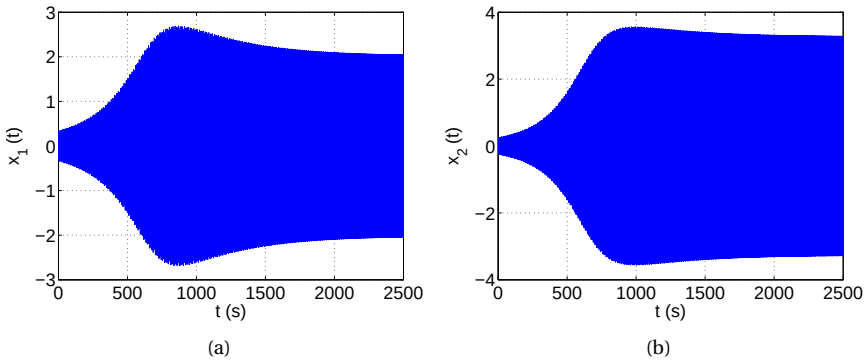

(a) (b)

Figure 3.3: Time domain solutions of mode 1 ($\omega = 5.08$ rad/s) of the two degree-of-freedom van der Pol oscillator system ($\epsilon = 0.02$, $\mu = 0.8$, $a_1 = 0.3$ and $a_2 = a_3 = a_4 = b_1 = b_2 = c_1 = 0$)

From these figures it is observed that an LCO exists with amplitudes of 1.992 and 3.259. The frequency is 5.08 rad/s. These results are obtained when the initial conditions are $\vec{x}(0) = [0.25, 0.25]^T$. Using larger initial conditions ($\vec{x}(0) = [5, 5]^T$) different amplitudes results, i.e. the second mode shape is found. Table 3.1 shows the amplitudes, the oscillation frequency and the phase difference between both degrees of freedom obtained for both mode shapes.

In order to derive an analytical solution, the principle of conservation of energy is now applied to the two DoF system as well. The instantaneous power for the two DoF system becomes:

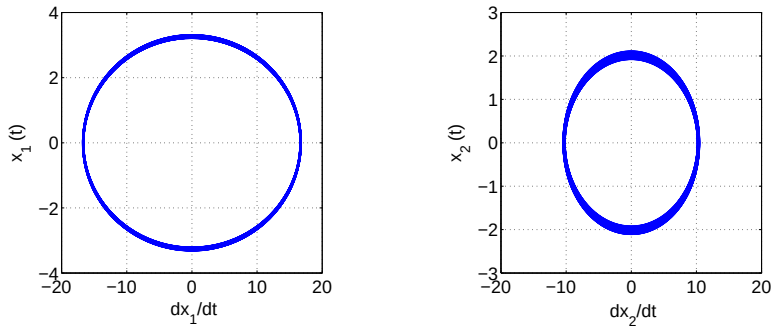

(a) (b)

Figure 3.4: Phase portraits of of mode 1 ($\omega = 5.08$ rad/s) the two degree-of-freedom van der Pol oscillator system ($\epsilon = 0.02$, $\mu = 0.8$, $a_1 = 0.3$ and $a_2 = a_3 = a_4 = b_1 = b_2 = c_1 = 0$)

	Mode 1 (5.08 rad/s)	Mode 2 (1.95 rad/s)
$\hat{x}_1$	3.259	3.263
$\hat{x}_2$	1.992	5.284
$\Delta\phi$ (rad)	π	0

Table 3.1: Time domain results for a two degree-of-freedom van der Pol oscillator ($\epsilon = 0.02$, $\mu = 0.8$, $a_1 = 0.3$ and $a_2 = a_3 = a_4 = b_1 = b_2 = c_1 = 0$)

$$P_n = \vec{\dot{x}}^T \epsilon \begin{bmatrix} \mu - a_1 x_1^2 - b_1 x_1^4 & c_1\mu - a_2 x_1^2 \\ c_1\mu - a_3 x_2^2 & c_1\mu - a_4 x_2^2 - b_2 x_2^4 \end{bmatrix} \vec{\dot{x}}. \tag{3.18}$$

This instantaneous power should be zero in case of an LCO, such that the non-conservative work is constant and energy is conserved. When a solution of the form:

$$\vec{x}(t) = \vec{\hat{x}} \sin(\omega t), \tag{3.19}$$

is assumed, then the instantaneous power becomes (after some rearranging):

$$P_n = \epsilon \left(A \cdot \cos^2(\omega t) + B \cdot \cos^2(\omega t) \sin^2(\omega t) + C \cdot \cos^2(\omega t) \sin^4(\omega t) \right), \tag{3.20}$$

where

$$A = \mu\omega^2(\hat{x}_1^2 + 2c_1\hat{x}_1\hat{x}_2 + c_1\hat{x}_2^2), \tag{3.21}$$
$$B = -\omega^2(a_1\hat{x}_1^4 + a_2\hat{x}_1^3\hat{x}_2 + a_3\hat{x}_2^3\hat{x}_1 + a_4\hat{x}_2^4), \tag{3.22}$$
$$C = -\omega^2(b_1\hat{x}_1^6 + b_2\hat{x}_2^6). \tag{3.23}$$

For an LCO to occur, the instantaneous power should disappear on the mean, i.e. $\bar{P}_n = \text{mean}(P_n) = 0$. Therefore, the mean values of the trigonometric functions in equation

(3.20) have been computed:

$$\text{mean}(\cos^2(\omega t)) = \frac{1}{2}, \tag{3.24}$$

$$\text{mean}(\cos^2(\omega t)\sin^2(\omega t)) = \frac{1}{8}, \tag{3.25}$$

$$\text{mean}(\cos^2(\omega t)\sin^4(\omega t)) = 0.062375. \tag{3.26}$$

Inserting these mean values into equation (3.20), gives:

$$\bar{P}_n = \epsilon\left(\frac{1}{2}\cdot A + \frac{1}{8}\cdot B + 0.062375\cdot C\right). \tag{3.27}$$

Combining this equation with the coefficients A, B and C yields the relation between the LCO amplitudes of the two degrees of freedom (where ω^2 has been dropped):

$$\frac{1}{2}\mu(\hat{x}_1^2 + 2c_1\hat{x}_1\hat{x}_2 + c_1\hat{x}_2^2) - \frac{1}{8}(a_1\hat{x}_1^4 + a_2\hat{x}_1^3\hat{x}_2 + a_3\hat{x}_2^3\hat{x}_1 + a_4\hat{x}_2^4) - 0.062375(b_1\hat{x}_1^6 + b_2\hat{x}_2^6) = 0. \tag{3.28}$$

From this equation the ratio of the LCO amplitudes at a certain value of the bifurcation parameter μ can be computed, i.e. if one of the LCO amplitudes is known, the LCO amplitude of the other DoF can be computed from equation (3.28). Figure 3.5 shows contours of the left-hand side of (3.28) for various amplitudes of both DoFs for $\mu = 0.8$. Note that all constants are non-zero for the results shown in this figure. The zero-contour indicates the LCO solutions. For comparison the solution as computed from the amplitude-dependent p-k method at this μ has been included as well, see Section 4.3.1. It lays exactly on the zero-contourline.

These two van der Pol-oscillators show that analysing the energy budget, or more particular the power of a non-linear oscillator system, can be a very useful tool for the study of limit-cycle oscillations. In particular, for these two non-linear oscillators relations for the LCO amplitude could be derived.

3.3.2. FLUID-STRUCTURE INTERACTION

The time evolutions of the pitch angle, plunge displacement and the sum of the kinetic and the potential energy at $M = 0.74$, $\bar{\alpha} = -0.8°$ are depicted in Figure 3.6. The results of two simulations are shown in this figure; on the left-hand side the signals obtained when simulation is started at an amplitude below the LCO amplitude (simulation 1), on the right-hand side the time history obtained when the simulation is started at an amplitude above the LCO amplitude (simulation 2). An LCO amplitude of approximately 3.11° is observed. The non-dimensional plunge amplitude $\Delta h/c$ is 0.042. The sum of the kinetic plus the potential energy averaged over one period is observed to be constant.

In order to put the obtained LCO amplitudes in perspective, a linearised flutter analysis using the p-k method [16] in the frequency domain has been performed. Figure 3.7 shows the damping δ and the angular frequency ω versus the freestream speed. A positive δ indicates a motion growing in amplitude, whereas a negative δ indicates a damped motion. The blue line represents the plunging mode and the green line the pitching mode. The plunging mode is seen to become unstable at a velocity of 204.16 m/s, i.e.

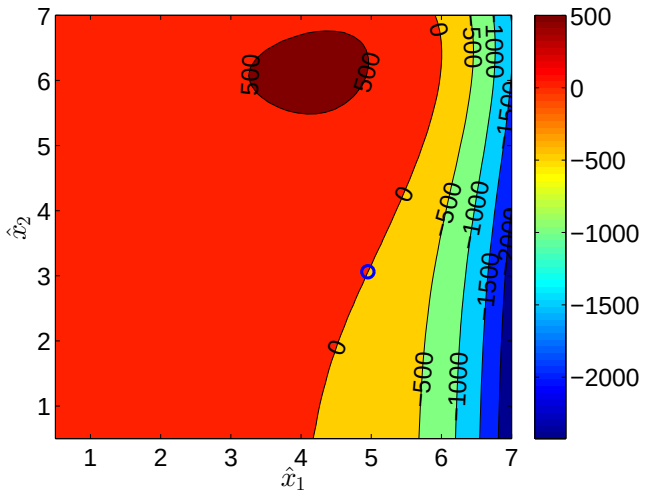

Figure 3.5: Contours of the mean power of the two degree-of-freedom van der Pol oscillator system at $\mu = 0.8$ ($\epsilon = 0.002$, $a_1 = -6$, $a_2 = -2$, $a_3 = -1$, $a_4 = -4$, $b_1 = 0.25$, $b_2 = 0.5$ and $c_1 = 1$)

this is the flutter velocity at $M = 0.74$, $\bar{\alpha} = -0.8°$. Hence, the LCO found here occurs far above the flutter boundary, since the freestream velocity is 245.15 m/s for the LCO test case. The amplitude ratio $|\theta_{h\alpha}|$ at flutter is 0.82 and the phase difference $\phi_{h\alpha}$ at flutter is 4.79°. The reduced frequency k at flutter is 0.30.

Figure 3.8 displays the amplitude ratio $|\theta_{h\alpha}|$ and the phase difference between pitch and plunge $\phi_{h\alpha}$ versus the oscillation amplitude during simulations 1 and 2. These mode shape parameters were obtained by applying a Fourier transform to the FSI time signals. In order to do so, four oscillation periods were simultaneously considered in one sliding post-processing window. For each post-processing window, a Fourier transform of the time signals was applied to obtain the magnitude and phase of the amplitude ratio. The post-processing windows were overlapping by 95%. The scatter in Figure 3.8 is caused by this overlap of the post-processing windows. Increasing the number of periods per window or decreasing the overlapping reduces the scatter, but also reduces the number of points at which the amplitude ratio and phase difference are obtained.

The amplitude ratio is seen to remain almost constant over the growth (or decay) in oscillation amplitude. However, the phase difference is observed to change slightly over the oscillation amplitude growth, from about 7.29° to about 9.46° at the LCO amplitude. The reduced frequency of the LCO is 0.254, it does not change during the development towards the LCO. Upon comparing the mode shape at the LCO with the flutter mode shape, it is observed that both $|\theta_{h\alpha}|$ and k are slightly lower at the LCO. However, $\phi_{h\alpha}$ is larger at the LCO.

In order to analyse the development of an LCO it is helpful to determine the components of the power of the system. The individual contributions of the aerodynamic lift (P_l), aerodynamic moment (P_m) and structural damping (P_d) to the total power P_{tot} can

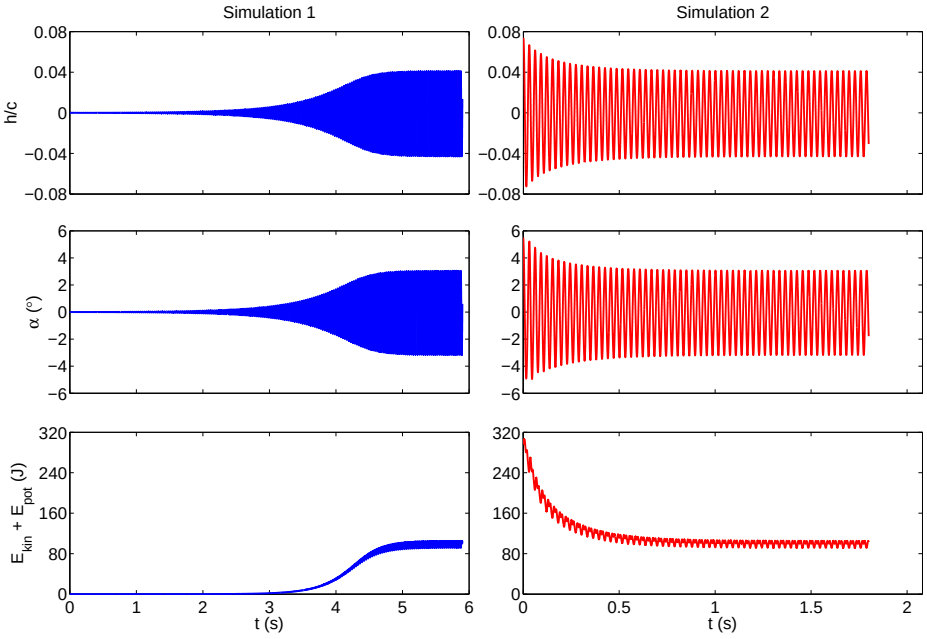

Figure 3.6: Time evolution of LCO at $M = 0.74$, $\bar{\alpha} = -0.8°$, $U_\infty = 245.15$ m/s

be determined from:

$$P_d = -D_h \dot{h}^2 - D_\alpha \dot{\alpha}^2, \tag{3.29}$$

$$P_l = -\dot{h} L, \tag{3.30}$$

$$P_m = \dot{\alpha} M, \tag{3.31}$$

$$P_{\text{tot}} = P_d + P_l + P_m. \tag{3.32}$$

The aerodynamic power is the sum of the power of the lift and of the moment: $P_{\text{aero}} = P_l + P_m$. In case of an LCO the aerodynamic power P_{aero} should compensate the structurally dissipated power P_d on average. The power components have been obtained by multiplying the time signals of the aerodynamic forces and the motion vector $\vec{x}$. To obtain the mean power components, the instantaneous power is averaged over an oscillation period, in equation form:

$$\bar{P} = \frac{1}{T} \int_t^{t+T} P dt, \tag{3.33}$$

where $\bar{P}$ is the mean power. When the instantaneous power signal is averaged a smooth curve of mean values of the power results. The oscillation amplitude at each time step has, in this case, been obtained by spline fitting through the maxima and minima of the pitch angle and the plunge displacement time signals.

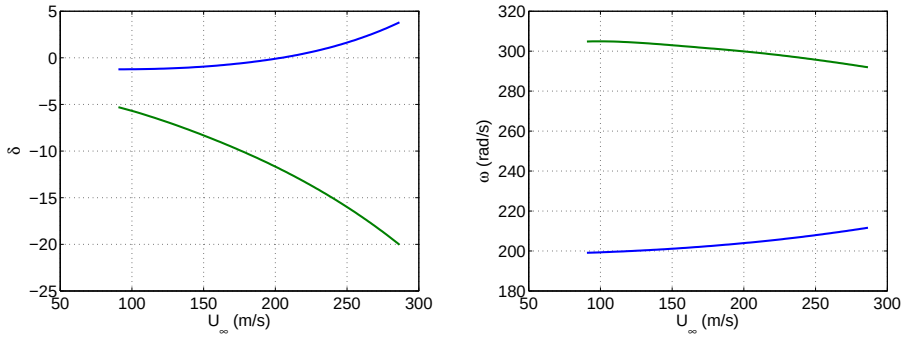

(a) Damping vs. freestream velocity

(b) Angular frequency vs. freestream velocity

Figure 3.7: Damping rate and angular frequency versus the freestream velocity at $M = 0.74$, $\bar{\alpha} = -0.8°$ (plunging mode - blue and pitching mode - green)

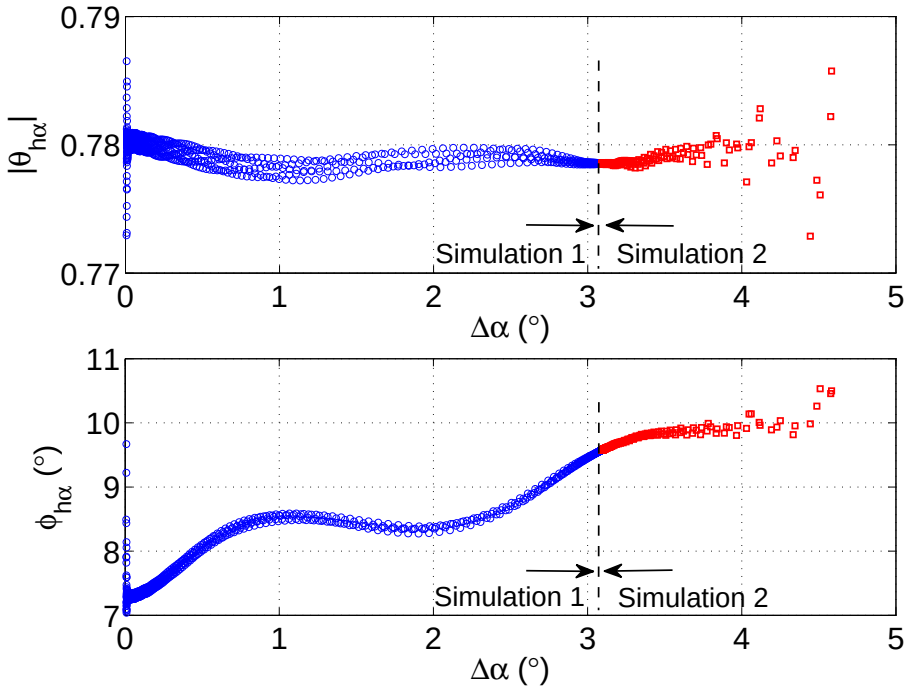

Figure 3.8: Evolution of the amplitude ratio and phase difference versus the LCO amplitude at $M = 0.74$, $\bar{\alpha} = -0.8°$

Figure 3.9 shows the mean of the power components computed in this manner versus

amplitude for simulation 1 (with an initial amplitude below the LCO amplitude) and simulation 2 (with an initial amplitude above the LCO amplitude). It is clearly seen that the total power becomes zero at an amplitude of 3.11°. This is therefore the LCO amplitude. The structural damping subtracts energy from the system. The same holds for the aerodynamic moment, whereas the lift adds energy to the system. The same behaviour was observed from the experimental results of Dietz et al. [1]. Note that they used different test cases and hence obtained different LCO amplitudes.

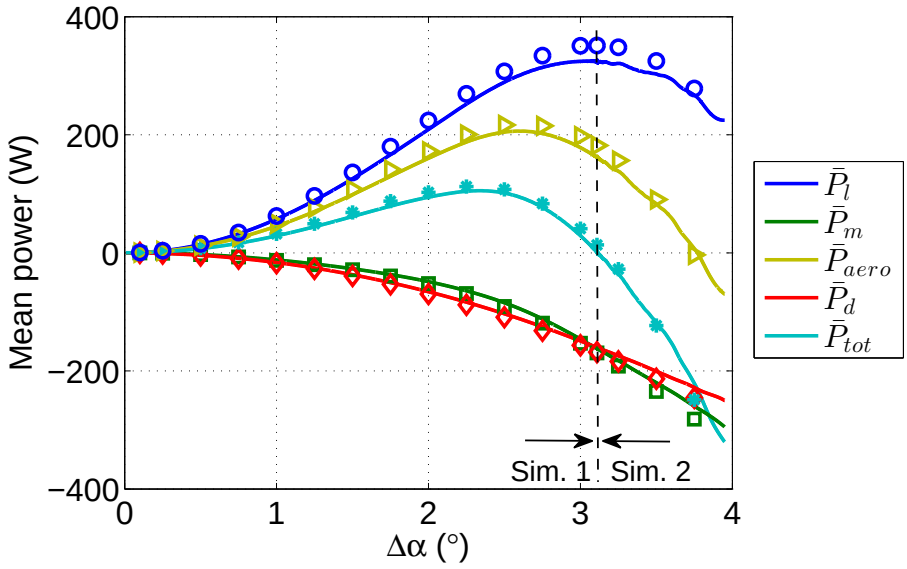

Figure 3.9: Mean power versus amplitude for LCO at $M = 0.74$, $\bar{\alpha} = -0.8°$ (FSI - lines and forced motion - symbols)

3.3.3. SINGLE HARMONIC FORCED MOTION OSCILLATIONS

Figure 3.9 shows the power components versus the amplitude as obtained from the (reference) FSI simulation (lines) and from forced motion oscillations simulations with a complex-valued amplitude ratio (symbols). The complex amplitude ratio used for each LCO amplitude (i.e. the amplitude ratio and the phase difference) has been extracted from the FSI simulations. The phase difference between pitch and plunge changes slightly over time during the coupled simulation, the same holds for the amplitude ratio (see Figure 3.8). These changes have been taken into account in the forced motion simulations As the reduced frequency is constant during the LCO development, it has been fixed at 0.254 here. Table 3.2 shows the amplitudes at which forced motion oscillation simulations were performed together with the corresponding phase differences and amplitude ratios.

As can be seen from Figure 3.9 there is a good agreement between the power compo-

$\Delta\alpha(^\circ)$	$\phi_{h\alpha}(^\circ)$	$\lvert\theta_{h\alpha}\rvert$
0.0105	7.29	0.780
0.1	7.32	0.780
0.25	7.57	0.780
0.5	8.06	0.779
0.75	8.05	0.779
1	8.50	0.778
1.25	8.51	0.778
1.5	8.41	0.779
1.75	8.36	0.778
2	8.30	0.779
2.25	8.49	0.778
2.5	8.66	0.779
2.75	9.05	0.779
3	9.46	0.779
3.11	9.57	0.779
3.25	9.73	0.779
3.5	9.85	0.779
3.75	9.90	0.779

Table 3.2: Phase difference and amplitude ratio used for forced motion oscillation simulations at $M = 0.74$, $\bar{\alpha} = -0.8^\circ$

nents obtained from the forced oscillations and those obtained from the FSI simulations. Hence, this suggests that taking into account the first order harmonic only is sufficient for modelling the LCO. The small deviations that appear in the power of the lift and in the aerodynamic power, are probably caused by the post-processing of the time signals of the FSI simulations, both in terms of the mode shape (see Figure 3.8 which shows a small band of solutions for both the amplitude ratio and the phase difference) and the power itself. A power analysis with low-pass filtered time signals, i.e. were only the first harmonics were retained, resulted in an only marginally smaller $\bar{P}_l$ and $\bar{P}_{\text{aero}}$. Hence, the higher harmonics in the coupled FSI simulations (which are not present in the forced motion simulations) are not the cause of the deviations between the mean power curves obtained from the forced oscillations and those obtained from FSI simulations.

It should be noted here that variations of the phase difference $\phi_{h\alpha}$, which are possible when using forced motion oscillation simulations, have an enormous impact on the aerodynamic power and therefore on the LCO amplitude. Corresponding forced motion oscillation simulations, with a phase difference of zero, would lead to an incorrectly predicted LCO amplitude. Figure 3.10 demonstrates this by comparing the total power as obtained from forced motion oscillation simulations in case of a zero phase difference and in case of a non-zero phase difference (i.e. in case of the actual phase difference, see Table 3.2). The symbols have been connected by interpolated splines. When the phase difference is zero an LCO with an amplitude of about 1.85° would be obtained. This LCO

amplitude is much smaller than the LCO amplitude actually obtained (3.11°). Hence, the phase difference, although small, can definitely not be ignored. This is in contrast to the observations of Dietz et al. [1] and Bendiksen [3], who suggested that the LCOs they observed during their experiments and computations, respectively, can be seen as a single-DoF motion. Note, however, that both studies conducted their investigations at different conditions and that Dietz et al. [1] observed significantly different LCO amplitudes.

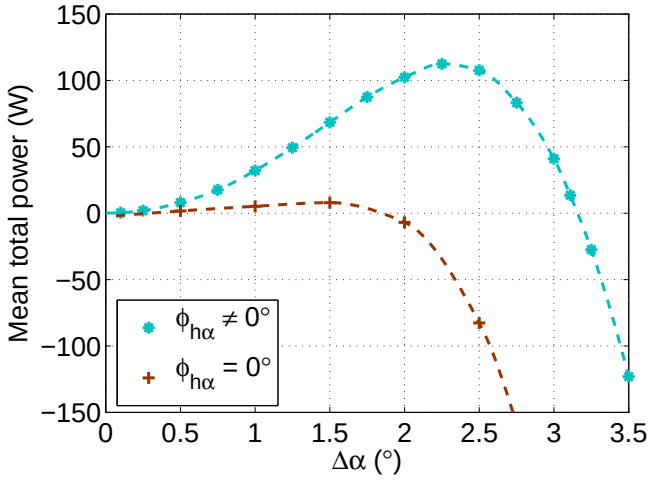

Figure 3.10: Mean total power versus amplitude for forced motion oscillations with zero and non-zero phase difference $\phi_{h\alpha}$ at $M = 0.74$, $\bar{\alpha} = -0.8°$

3.3.4. NON-LINEAR AERODYNAMIC POWER DEFECT

If the aerodynamic forces were proportional to the displacement, the power delivered by the lift would vary quadratically with amplitude. However, with increasing amplitude a non-linearity limits the (quadratic) increase of the power delivered by the lift, i.e. there exists a defect in the power of the lift (see Figure 3.9). The power of the moment is also a non-linear function of the amplitude, since it is coupled to the lift. Although, in comparison, the defect in the power of the moment is not as strong as for the power of the lift. These two effects enable the power of the structural damping to balance the aerodynamic power. However, the question is why do we have such a large defect in the power of the lift, i.e. what feature is responsible for this defect? And why is the defect so much smaller for the power of the moment?

To find the cause of this defect, one must look at the computation of the mean power of the lift, moment and damping. Assuming a harmonic input and a harmonic response,

the mean of the power of the lift, moment and damping can be computed using:

$$\bar{P}_l = -0.5\Delta h|L|\omega \sin\left(\phi_{L\alpha} - \phi_{h\alpha}\right) = -0.5\Delta h|L|\omega \sin\phi_{Lh}, \tag{3.34}$$

$$\bar{P}_m = 0.5\Delta\alpha|M|\omega \sin\phi_{M\alpha}, \tag{3.35}$$

$$\bar{P}_d = -0.5\omega^2\left(D_h(\Delta h)^2 + D_\alpha(\Delta\alpha)^2\right), \tag{3.36}$$

where $|L|$ is the magnitude of the lift, $|M|$ is the magnitude of the moment, $\phi_{L\alpha}$ is the phase of the lift with respect to the pitching motion and $\phi_{M\alpha}$ is the phase of the moment with respect to the pitching motion. Subtracting $\phi_{h\alpha}$ from $\phi_{L\alpha}$ gives the phase of the lift with respect to the plunging motion ϕ_{Lh}.

Equations (3.34) and (3.35) are used to compute the equivalent linearised power components. The equivalent linearised power is the power that would have been obtained when the small amplitude mode shape and aerodynamic forces had been retained at large amplitudes, i.e. in the case of linear flutter. The equivalent linearised complex-valued aerodynamic lift and moment needed to compute these power components, are computed by scaling up the lift and moment from the small-amplitude values of FSI simulation 1. The phase of both lift and moment is just constant in the linearised case. Figure 3.11 shows the mean of the equivalent linearised power components versus oscillation amplitude (dashed lines). The power signals from the FSI simulations have been included in Figure 3.11 as well (solid lines). The equivalent linearised power of the lift $\tilde{P}_l$ increases with amplitude and until an amplitude of about 1.85° it is approximately equal to $\bar{P}_l$. For larger amplitudes, $\bar{P}_l$ bursts and obtains a maximum. Similar behaviour is observed for the aerodynamic power and the total power. The equivalent linearised power of the moment $\tilde{P}_m$ does not decrease as fast as the non-linear power of the moment $\bar{P}_m$ with increasing amplitude. The power of the damping is the same in both cases, since it is computed from the structural properties of the system. Hence, Figure 3.11 clearly displays the non-linear aerodynamic power defect.

Now, why is there a defect in the power of lift and why is the defect in the power of the moment so much smaller? In order to answer these questions, one must look at the complex-valued ratios of the first harmonic components of the aerodynamic lift and moment during the time evolution of the LCO, i.e. θ_{Lh} and $\theta_{M\alpha}$. The magnitude and phase angles of these complex-valued ratios of the lift and moment are shown in Figure 3.12. For comparison, the equivalent linearised magnitude and phase angle of the lift and moment have been included as well. Figure 3.12 shows that the magnitude of the lift during the LCO evolution $|\theta_{Lh}|$ is almost the same in the equivalent linearised case. For the LCO amplitude a deviation of only 3% occurs. However, the phase of the lift ϕ_{Lh} changes significantly. Furthermore, ϕ_{Lh} is close to zero, hence the impact on the power of the lift will be enormous, since the sensitivity of the sine is the largest close to zero (see equation (3.34)). The magnitude of the moment $|\theta_{M\alpha}|$ deviates significantly from its equivalent linearised value at larger amplitudes. The phase of the moment $\phi_{M\alpha}$ is more negative in the equivalent linearised case than in the non-linear case. Deviations of about $5-10°$ are present. However, since the phase of the moment is about $-90°$, the impact on the power of the moment will not be as large as for power of the lift, since the slope of the sine is almost zero near $-90°$ (see equation (3.35)).

To explain the non-linear defect of the power of the lift at higher amplitudes, equation (3.34) and Figures 3.12(a) and 3.12(c) are addressed. The power of the lift is a func-

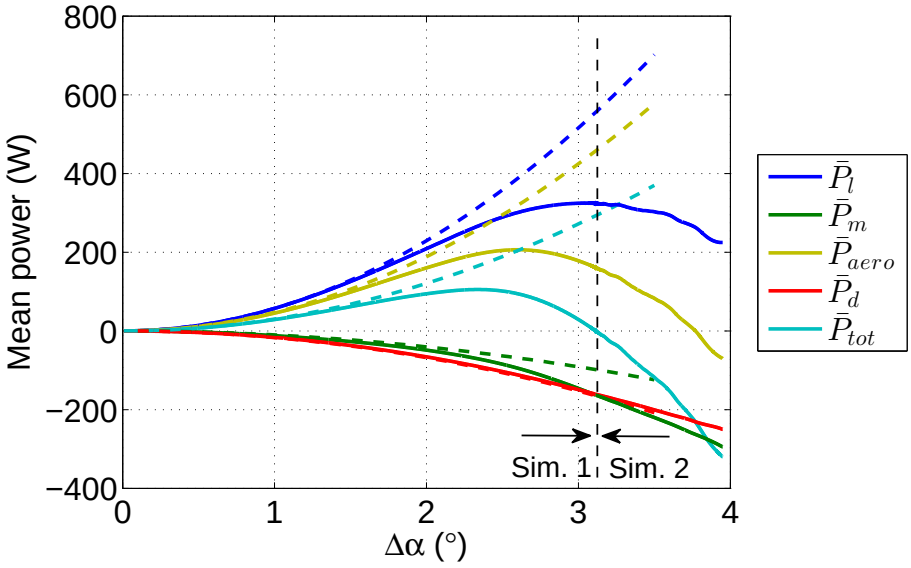

Figure 3.11: Mean power versus amplitude for LCO at $M = 0.74$, $\bar{\alpha} = -0.8°$ (FSI - full lines and equivalent linearised - dashed lines)

tion of the plunge amplitude, this amplitude changes in the same way in both the equivalent linearised and the non-linear case. The frequency is also the same in both cases. Furthermore, the magnitude of the lift $|\theta_{Lh}|$ was seen to be almost the same in both cases (see Figure 3.12(a)). That leaves the phase of the lift with respect to plunge ϕ_{Lh} as a possible source of the defect. As observed before, the sine has a large sensitivity since ϕ_{Lh} is close to zero. From Figure 3.12(c) it is seen that the difference between the phase of the lift in the linearised case and ϕ_{Lh} starts to increase rapidly at an amplitude of approximately 1.85°, i.e. at the same amplitude as the power of the lift starts to deviate. Hence, the power of the lift shows a non-linear defect due to the change in the phase of the lift with increasing oscillation amplitude. This means that for an LCO to occur the phase of the lift has to change only slightly with oscillation amplitude, provided that the value of ϕ_{Lh} is close to zero.

The defect in the power of the moment is explained in the same manner, only in this case a combination of the changes in $|\theta_{M\alpha}|$ and $\phi_{M\alpha}$ is responsible for this defect, since the phase of the moment is close to −90°. Therefore, the change in magnitude and the change in phase of the moment with increasing amplitude are responsible for the power defect of the moment. These two defects, result in a defect in the aerodynamic power, which leads to the amplitude limitation of the oscillations.

To investigate what local features are responsible for the change in the complex-valued ratios of the first harmonic components of the aerodynamic lift an moment, the un-

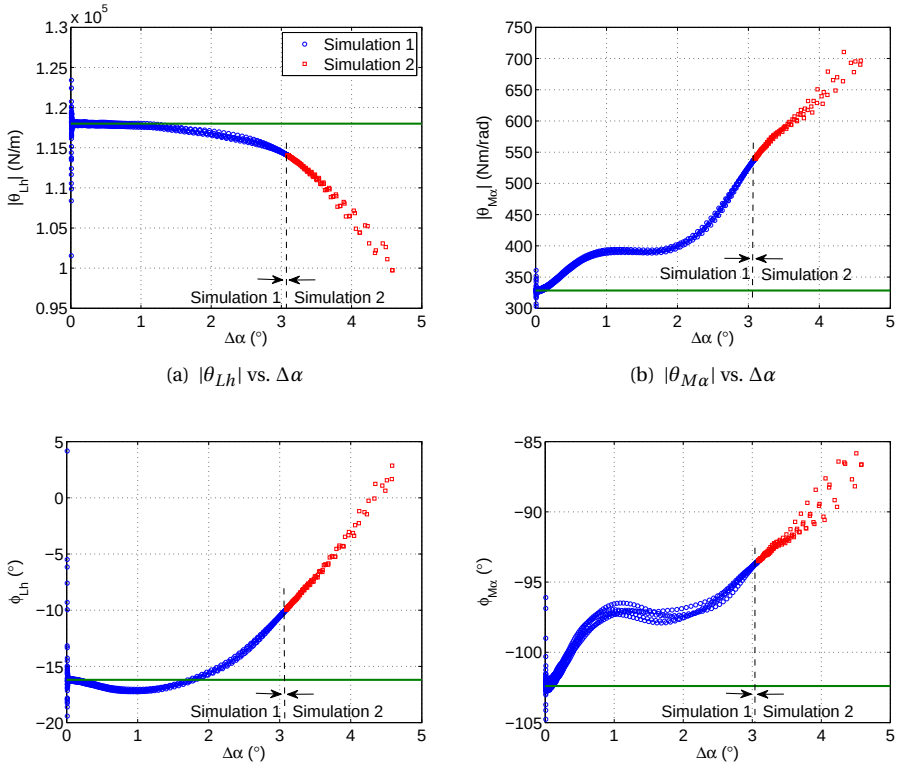

(a) $|\theta_{Lh}|$ vs. $\Delta\alpha$

(b) $|\theta_{M\alpha}|$ vs. $\Delta\alpha$

(c) ϕ_{Lh} vs. $\Delta\alpha$

(d) $\phi_{M\alpha}$ vs. $\Delta\alpha$

Figure 3.12: Magnitude and phase angle of lift and moment versus amplitude for LCO at $M = 0.74$, $\bar{\alpha} = -0.8°$

steady local force- and moment distributions at the LCO amplitude are compared to those obtained at $\Delta\alpha = 0.01048°$ (equivalent linearised condition). Figure 3.13(a) shows the steady surface pressure coefficient distribution at $M = 0.74$, $\alpha = -0.8°$. Figure 3.13(b) depicts the imaginary part of the unsteady local lift distribution with respect to the plunging motion, i.e. the imaginary part of the complex-valued ratio of the first harmonic component of the local lift force $\Im(\theta_{Lh}^{\text{local}})$. The imaginary part of the unsteady local moment distribution with respect to the pitching motion (i.e. the imaginary part of the complex-valued ratio of the first harmonic component of the local moment $\Im(\theta_{M\alpha}^{\text{local}})$) is shown in Figure 3.13(c). The solid lines represent the LCO condition and the dashed lines the equivalent linearised condition. The upper surface is shown in blue and the lower surface in green. Note that Figure 3.13(b) depicts the lift due to both pitch and plunge, it is merely referred to the plunging motion. The same holds for the local moment which is merely referred to the pitching motion in Figure 3.13(c). The surface pressure coefficient distribution shows a strong pressure increase wave near the leading edge on the upper surface. However, this re-compression is not strong enough to re-compress the air such that the velocity downstream of it becomes subsonic. Instead the re-compression on the

upper surface takes place without a shock near the mid-chord. On the lower surface a small pressure increase is also present near the leading edge. Downstream of it the flow expands and near $x/c = 0.45$ a strong shock is present.

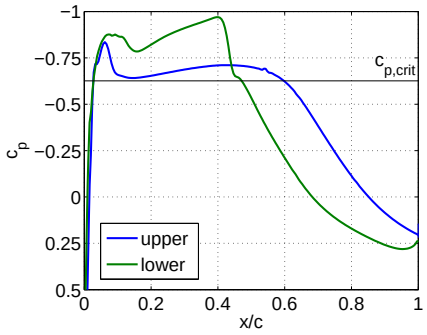

(a) Steady c_p vs. x/c

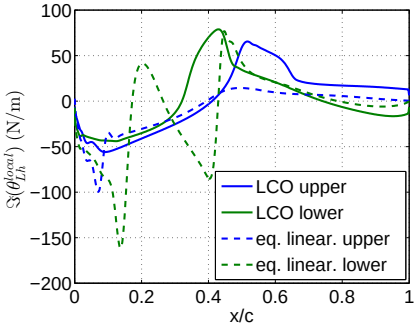

(b) $\Im(\theta^{\text{local}}_{Lh})$ vs. x/c

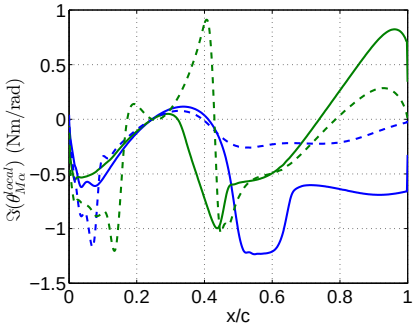

(c) $\Im(\theta^{\text{local}}_{M\alpha})$ vs. x/c

Figure 3.13: Local force- and moment distribution for LCO and equivalent linear conditions at $M = 0.74$, $\bar{\alpha} = -0.8°$

When looking at the imaginary part of the unsteady local lift $\Im(\theta^{\text{local}}_{Lh})$ it is observed that in the linearised case, several sharp peaks appear. All these peaks are related to unsteady shock motions since they are located at those locations where the steady surface pressure coefficient distribution exhibits a re-compression, re-compression shock or a small expansion. At the LCO condition these sharp peaks have disappeared and the local lift force is just smoothed out over the surface, i.e. on the lower surface the shock moves over a larger distance of the chord. On the upper surface the amplitude is large enough to establish a shock over part of the oscillation cycle, hence the wide shock peak at about mid-chord at the LCO condition. This peak and the difference in the imaginary part of the local lift force downstream of this peak cause the decrease in imaginary part of the lift from the linear condition to the LCO condition (see Figure 3.12(a) and 3.12(c)).

The dynamics and the formation of shock waves also change the power of the mo-

ment significantly. This can be explained by looking at the imaginary part of the local moment distribution with respect to the pitch amplitude, $\Im(\theta_{M\alpha}^{\text{local}})$, see Figure 3.13(c). This distribution is similar to that of the local lift, it is just weighted because of the moment arm. At $x/c = 0.25$ the local moment is zero, since this is the elastic axis location. From about mid-chord to the trailing edge the absolute value of the local moment on the upper surface is much larger in the LCO case than in the equivalent linearised case. Near the trailing edge this also holds for the lower surface. This increases the area underneath the curves such that $\Im(\theta_{M\alpha}^{\text{local}})$ is much larger in the non-linear case than in the linearised case. This corresponds to the observations from Figures 3.12(b) and 3.12(d).

From the instantaneous surface pressure coefficient distributions at several time steps it is observed that the shocks that exist on the upper surface and lower surface at the LCO condition are of Tijdeman [17] type B, since all shocks disappear during part of the oscillation cycle. Hence, from the linearised to LCO condition the type of shock motion changes from continuous (type A) to intermittent (type B). This coincides with the findings of Bendiksen [4, 5], who found that amplitude non-linearities in the aerodynamic forces are the strongest when the type of shock motion changes and these non-linearities will inevitably lead to limit-cycle oscillations. Intermittent boundary layer separation is also present on both airfoil surfaces at the LCO condition. In contrast, in the linearised case the flow remains attached. Hence, it is likely that the flow separation affects the shock wave motions in the non-linear case. However, it is not clear how large this effect is. An LCO would probably have occurred in the absence of the boundary layer as well, solely due to the amplitude non-linearities of the aerodynamic forces. Therefore it is thought that the unsteady shock wave motions are responsible for the variations in the magnitude and phase angle of the lift and the moment and hence for the non-linear defect in the aerodynamic power. However, the local trigger responsible for the amplitude limitation of the LCO studied in this work could not be identified due to the large amplitude range covered and hence the corresponding large shock movement.

3.4. CONCLUSIONS

Aerodynamic non-linearities that lead to the development of limit-cycle oscillations are a topic of current research. In this chapter the development and behaviour of LCOs were analysed using fluid-structure interaction simulations and harmonic forced motion oscillation simulations. These forced motion oscillations involved a sinusoidal oscillation at the fundamental frequency. From comparison with the FSI simulations it was observed that apparently the contribution of the higher harmonics is not significant for the LCOs considered in this work.

A power analysis of the coupled simulations showed that the slightly non-linear behaviour of the aerodynamic power enabled the occurrence of a limit-cycle oscillation. The power components in case of a limit-cycle oscillation were compared to the equivalent linearised power components that would exist in case of flutter. The defect of the power of the lift in the non-linear case was found to be caused by the changes in the phase angle of the lift w.r.t. plunge with oscillation amplitude. This phase angle was found to be close to zero and therefore very sensitive to small changes. The defect in the power of the moment was found to be much smaller than in case of the lift. In case of the moment, variations in both magnitude and phase were found to be responsible for

the defect in the power. However, since the phase of the moment is close to $-90°$, small variations of this phase, caused by oscillation amplitude variations, do not have a large influence on the power of the moment. Hence, for the LCOs studied in this work, the amplitude limitation is mainly caused by the change in the phase of the lift with oscillation amplitude. The changes in the magnitude and phase angle of the lift and moment with oscillation amplitude were found to be caused by unsteady shock wave motions.

REFERENCES

[1] G. Dietz, G. Schewe, and H. Mai, *Experiments on heave/pitch limit-cycle oscillations of a supercritical airfoil close to the transonic dip,* Journal of Fluids and Structures **19**, 1 (2004).

[2] G. Dietz, G. Schewe, and H. Mai, *Amplification and amplitude limitation of heave/pitch limit-cycle oscillations close to the transonic dip,* Journal of Fluids and Structures **22**, 505 (2006).

[3] O. Bendiksen, *Role of shock dynamics in transonic flutter,* (1992), AIAA Paper 92-2121-CP.

[4] O. Bendiksen, *Transonic limit cycle flutter/lco,* (Univerisity of California, Los Angelos, Palm Springs, California, 2004) 45th AIAA/ASME/ASCE/AHS/ASC Structures, Structural Dynamics, and Materials Conference.

[5] O. Bendiksen, *Influence of shocks on transonic flutter of flexible wings,* (University of California, Los Angeles, Palm Springs, California, 2009) 50th AIAA/ASME/ASCE/AHS/ASC Structures, Structural Dynamics, and Materials Conference.

[6] B. Stickan, J. Dillinger, and G. Schewe, *Computational aeroelastic investigation of a transonic limit-cycle-oscillation experiment at a transport aircraft wing model,* Journal of Fluids and Structures **49**, 223 (2014).

[7] G. Schewe and H. Deyhle, *Experiments on transonic flutter of a two-dimensional supercritical wing with emphasis on the non-linear effects,* (London, UK, 1996) proceedings RAeS Conference on Unsteady Aerodynamics.

[8] A. Knipfer and G. Schewe, *Investigations of an oscillating supercritical 2d wing section in a transonic flow,* (Deutsches Zentrum für Luft- und Raumfahrt, Reno, NV, 1999) 37th AIAA Aerospace Sciences Meeting and Exhibit.

[9] G. Schewe, H. Mai, and G. Dietz, *Nonlinear effects in transonic flutter with emphasis on manifestations of limit cycle oscillations,* Journal of Fluids and Structures **18**, 3 (2003).

[10] T. Gerhold and M. Galle, *Calculation of complex three-dimensional configurations employing the DLR TAU-code.* AIAA Paper 97-0167 (1997).

[11] A. Jameson, W. Schmidt, and E. Turkel, *Numerical solutions of the Euler equations by finite volume methods using Runge-Kutta time-stepping schemes,* (1981).

[12] A. Jameson, *Time dependent calculations using multigrid, with applications to unsteady flows past airfoils and wings,* AIAA Paper 91-1596 (1991), AIAA 10th Computational Fluid Dynamics Conference.

[13] J. Zwaaneveld, *NLR 7301 airfoil,* in *EXPERIMENTAL DATA BASE FOR COMPUTER PROGRAM ASSESSMENT - Report of the Fluid Dynamics Panel Working Group 04*, AGARD AR-138 (1979) pp. A4–1–A4–22, NATO - ADVISORY GROUP FOR AEROSPACE RESEARCH AND DEVELOPMENT.

[14] B. van der Pol, *Forced oscillations in a circuit with nonlinear resistance (receptance with reactive triode),* London, Edinburgh and Dublin Phil. Mag. **3**, 65 (1927).

[15] J. Dormand and P. Prince, *A family of embedded runge-kutta formulae,* Journal of Computational and Applied Mathematics **6**, 19 (1980).

[16] H. Hassig, *An approximate true damping solution of the flutter equation by determinant iteration,* Journal of Aircraft **8** (1971).

[17] H. Tijdeman, *Investigations of the transonic flow around oscillation airfoils*, Ph.D. thesis, Technische Hogeschool Delft (1977).

4

VERIFICATION AND VALIDATION OF THE AMPLITUDE-DEPENDENT P-K METHOD

4.1. INTRODUCTION

Several researchers [1–4] have studied limit-cycle oscillations that occur on the F-16 aircraft if external stores are applied. The driving mechanism of these LCOs has not yet been understood in full detail, due the complicated non-linear behaviour. Aerodynamic sources of non-linearity are thought to be related to shock wave dynamics, flow separation and/or boundary layer transition. However, analysing the aerodynamic sources of non-linearity in detail is difficult, because of the high computational costs involved in coupled fluid-structure interaction (FSI) simulations in the time domain. Moreover, time domain simulations are not suited for detailed investigations into the bifurcation behaviour of LCOs. Unstable LCOs, for example, which are repelling boundaries in the phase space, usually cannot be found directly from time domain simulations. Furthermore, often multiple nested LCOs exist. In that case an unstable LCO is accompanied by a stable LCO (of larger amplitude). However, this is not necessarily the case, i.e. there might exist unstable LCOs without stable LCOs. When unstable LCOs exist below the linear flutter speed and the LCO amplitude decreases with increasing velocity, a so-called subcritical bifurcation occurs [5]. When only stable LCOs occur above the linear flutter speed (i.e. without unstable LCOs below the flutter boundary) and the LCO amplitude increases with increasing freestream speed, a so-called supercritical bifurcation occurs [5]. A more detailed overview of stable and unstable LCOs and their bifurcation behaviour was given in Section 1.2.

To ease the investigations into the bifurcation behaviour of LCOs several alternatives to time domain methods are used, these methods were discussed in Section 1.3. A short

Parts of this chapter have been published in van Rooij et al., Prediction of aeroelastic limit-cycle oscillations based on harmonic forced motion oscillations, AIAA journal (submitted).

overview is given here. The first alternative is the aeroelastic harmonic balance (HB) method [6], which use a frequency-domain HB flow solver to solve the governing fluid dynamic equations. This solver is coupled to the structural solver to solve the aeroelastic equations of motion. This results in significant time savings compared to FSI simulations. However, an adapted flow solver, which is called during the iterations of the aeroelastic HB solver, is necessary. Recently, neural networks have also been applied to analyse limit-cycle oscillations [7–9]. These neural networks are used to establish a relation between the aerodynamic forces and the structural displacements based on a certain training signal. This relation is then used when solving the aeroelastic equations of motion in the time domain. The success of this method depends on the training signal. A third approach is to extend the frequency domain-based p-k-method, well-known in the context of linear flutter analysis. Ueda et al. [10] first applied a modified version of the p-k method, in combination with the transonic small disturbance equations, for predicting LCOs. Recently, He et al. [11] applied a extended version of the p-k method for predicting LCOs as well. They assumed superposition of the aerodynamic forces and used CFD to compute them. Furthermore, Somieski [12] applied an eigenvalue method to study LCOs of an aircraft nose landing gear. He also used superposition of the non-linear amplitude-dependent forces. He et al. [11] observed good agreement with time domain methods for weak non-linearities, whereas for strong non-linearity deviations were present. Somieski [12] obtained excellent agreement with time domain results for this eigenvalue method.

In contrast to the methods of Ueda et al. [10], He et al. [11] and Somieski [12], the amplitude-dependent p-k method ADePK as developed in this thesis, see Section 2.5, takes the amplitude dependency of the aerodynamic forces is taken into account "directly" by the use of harmonic forced-motion oscillations, but without assuming superposability of the motion-induced aerodynamic forces. The LCO is assumed to oscillate with its first fundamental frequency only (as in [10–12]), i.e. the higher order harmonic components of the LCO and the aerodynamic forces are neglected. This assumption has been justified in Chapter 3. The amplitude-dependent p-k method, presented in this thesis is similar to the HB method, as noted in Section 2.5.1. However, in contrast to the HB method, the Fourier transform of the aerodynamic forces is applied only at the output of the CFD code (i.e. at the forces themselves) in the ADePK method. Hence, for application of the ADePK method no adapted CFD solver is needed. Furthermore, the CFD solver is not called during the solution procedure of the aeroelastic equations of motion in the ADePK method. Instead, the aerodynamic forces are obtained from interpolation of the resonse surface generated from the results of harmonic forced-motion oscillations. The results of ADePK are compared to time domain simulations results. Before applying ADePK to a test case with aerodynamic non-linearities, it is verified for an analytical test case; a van der Pol-oscillator [13]. Afterwards the method is validated for a two DoF pitch/plunge airfoil system. The results of the presented amplitude-dependent p-k method will be compared to the methods of Ueda et al. [10], He et al. [11] and Somieski [12] (i.e. using superposition of the aerodynamic forces). Furthermore, a structural parameter variation is performed. That is, the structural frequency ratio is varied, similar to the investigations of Kholodar et al. [14, 15].

Section 4.2 shortly describes the test cases, the CFD code and the time and frequency

domain methods. The results of ADePK are then shown and discussed in Section 4.3 for the van der Pol-oscillator and the two DoF airfoil system. Finally, conclusions are drawn.

4.2. COMPUTATIONAL METHODS AND SET-UP

In this chapter two computational methods have been applied, a time domain method, which used a reference, and the frequency domain method ADePK developed in this thesis. In the time domain, fluid-structure coupling has been applied for validation of the frequency domain method. All methods used in this chapter have been presented in detail in Chapter 2. A short overview is given here.

4.2.1. CFD CODE AND SET-UP

To determine the aerodynamic lift and moment the DLR TAU-code [16] is used. This CFD code is a finite-volume, cell-vertex-based, unstructured, compressible solver for both the Reynolds-Averaged Navier-Stokes (RANS) and the Euler equations. In this chapter inviscid flow is considered, i.e. the Euler equations are used to represent the fluid dynamics. For spatial discretisation a 2nd-order central scheme [17] is used. Temporal discretisation is realised by dual time stepping [18], where in order to integrate in physical time, the implicit 2nd-order accurate Backward Differencing Formula (BDF2) integration scheme has been used. At each physical time step, the governing equations are integrated explicitly by adding a so-called pseudo time derivative. More details about the CFD code and its discretisation can be found in Section 2.2.3.

The airfoil used in this study is the supercritical NLR7301 airfoil with a blunt trailing edge [19]. Its design Mach number is 0.72 and its design lift coefficient is 0.60. More details about this airfoil can be found in Section 2.2.1. The chord length of the airfoil is 0.3 m. An unstructured O-type mesh with 1135 points has been used for all CFD simulations shown in this chapter. However, the mesh resolution and grid convergence are not of interest for the validation of ADePK, since the same mesh has been used for both time and frequency domain calculations. The farfield boundary has been placed 100 chord lengths away from the airfoil, in order to avoid that reflections falsify the low frequency responses. The time step size used for all unsteady simulations is $1 \cdot 10^{-4}$ s. This corresponds to 769 time steps per oscillation period for a reduced frequency of 0.1 and to 128 time steps per oscillation period for a reduced frequency of 0.6. This time step size was found to give time step size independent results, see Appendix B. The testcase considered in this chapter is at a Mach number of 0.74 and a mean angle of attack of $-1.5°$.

4.2.2. TWO DOF AIRFOIL SYSTEM

The aeroelastic system considered in this chapter is a spring-mounted airfoil with two degrees of freedom; pitch and plunge. The equations of motion of the system are given by (2.7). The structural parameters used are given in Table 2.1, see Dietz et al. [20].

4.2.3. FLUID-STRUCTURE COUPLING

For reference, limit-cycle oscillations are computed in the time domain using fluid-structure coupling. As described in Section 2.3 the coupling is partitioned, i.e. the CFD solver

and the structural solver have been coupled. To achieve so-called "strong" coupling of the CFD and the structural solver, the forces and displacements are exchanged between these solvers multiple times during each physical time step. In this thesis the coupling has been applied at each pseudo time step. In other words, at a certain time step, the forces of the previous physical or pseudo time step are used to compute the new structural displacements. These are then fed back to the CFD code to compute the new aerodynamic forces at the current pseudo time step, which then lead to new displacements. These are again fed back to the CFD code. This process is repeated for each pseudo time step until an equilibrium is established. Then the solver advances to the next time step. The numerical time integration of the fluid-structural problem (2.7) is also performed using a BDF2 integration scheme. In order to obtain the desired mean angle of attack, the airfoil is trimmed by subtracting the steady aerodynamic forces at this (mean) angle of attack, see Section 3.2.3.

In order to study the bifurcation behaviour, the freestream velocity has been varied. In the time domain simulations, this variation has been performed by varying the static temperature at constant Mach number.

4.2.4. CONVENTIONAL P-K METHOD

The conventional p-k method for classical flutter computations was developed by Hassig [21]. It assumes the first harmonic of a complex-valued exponential function as a solution to the equations of motion (see (2.32)-(2.34)). The aerodynamic forces are described using the so-called Generalised Aerodynamic Force (GAF) matrix which contains the complex-valued derivatives of the aerodynamic forces with respect to the degrees of freedom. The solution of the aerodynamic forces is truncated after the first harmonic. See Section 2.4 for more details.

4.2.5. AMPLITUDE-DEPENDENT P-K METHOD ADEPK

The amplitude-dependent p-k method ADePK is an extension of the conventional p-k method for predicting limit-cycle oscillations. It is described in detail in Section 2.5.1. Compared to the conventional p-k method, the aerodynamic forces are no longer a linear function of the displacements. Therefore, the aerodynamic forces remain as a vector in the equations of motion, see (2.43). To solve these equations, an iterative procedure is applied (as in the conventional p-k method), where the pitch amplitude must be preset. This iterative procedure finds the angular frequency ω, damping δ and the complex-valued amplitude ratio $|\theta_{h\alpha}|$. An LCO is then found from the amplitude at which δ is zero. Depending on the sign derivative of δ w.r.t. $\Delta\alpha$ at the LCO amplitude, the LCO found is either stable or unstable. Nested LCOs can also be found from ADePK, see Section 2.5.3.

In contrast to the linear case, the aerodynamic forces in the non-linear case are, next to the frequency, also a function of the pitch amplitude and the complex-valued amplitude ratio. Therefore, a so-called response surface is necessary to compute the aerodynamic forces during the iterations of ADePK. This response surface is constructed using harmonic forced motion oscillation simulations. It can either be fully non-linear or quasi-linearised (when superposition of describing function is used), see Section 2.5.2. In ADePK only the first harmonic component of the motion and the aerodynamic response is used, since from Chapter 3 and [20, 22–24], all LCOs with aerodynamic non-

linearities only, were observed to have no significant higher harmonic components. More details on ADePK can be found in Section 2.5.

4.3. RESULTS AND DISCUSSION

This section shows the results obtained from ADePK. The results are validated using time-domain FSI simulations. First, the results of the analytical test case, the one and two DoF van der Pol-oscillator are shown and discussed. Then the response surface and the results of the two-degree-of-freedom airfoil system are shown and discussed. Finally, ADePK is applied to study the bifurcation behaviour of the two DoF airfoil system when the structural frequency ratio is varied.

4.3.1. VAN DER POL-OSCILLATOR

The van der Pol-oscillator [13] is a classical example of a system with a non-linear damping force and serves here as a model for non-linear aerodynamic forces. This section will demonstrate the amplitude-dependent p-k method for a one and two degree-of-freedom van der Pol oscillator. First the time domain solution will be compared to the results of the amplitude-dependent p-k-method in terms of the bifurcation behaviour. Then the non-linear damping is increased such that the LCOs are no longer first harmonic only. The validity of the amplitude-dependent p-k method for higher harmonic motions is checked in this manner.

ONE DOF VAN DER POL-OSCILLATOR

Two test cases are used; the standard van der Pol oscillator and a modified van der Pol oscillator. For the second test case, the standard van der Pol equation was modified to investigate the possibility of a subcritical bifurcation. A fourth order polynomial was used as non-linear damping term, i.e. $F_{\text{non-lin}} = \epsilon\left(\mu - ax^2 - dx^4\right)\dot{x}$, see Section 3.3.1. The equation of motion then becomes:

$$\ddot{x} + x = \epsilon\left(\mu - ax^2 - dx^4\right)\dot{x}, \tag{4.1}$$

where x is the time-dependent displacement, ϵ a damping coefficient and μ a bifurcation parameter. a and d are constants. This equation can be solved in the time domain or in the frequency domain using the amplitude-dependent p-k-method (see Section 2.5). The analytical solution can be found using the energy balance as demonstrated in Section 3.3.1.

Now the bifurcation parameter μ is varied in order to study the bifurcation behaviour of the system. Solving for the LCO amplitude for various values of the bifurcation parameter results in the bifurcation diagram depicted in Figure 4.1. Note that no response surface must be set up, since the non-linear damping force is known analytically as a function of frequency and amplitude. From Figure 4.1 it is observed that a supercritical bifurcation of the LCO amplitude exists. This means that the amplitude increases with increasing bifurcation parameter from the flutter point (i.e. where the LCO amplitude is zero). For reference the analytical solution of equation (3.15) and the time domain solution have been included as well. The Dormand-Prince (DOPRI) method [25] has been

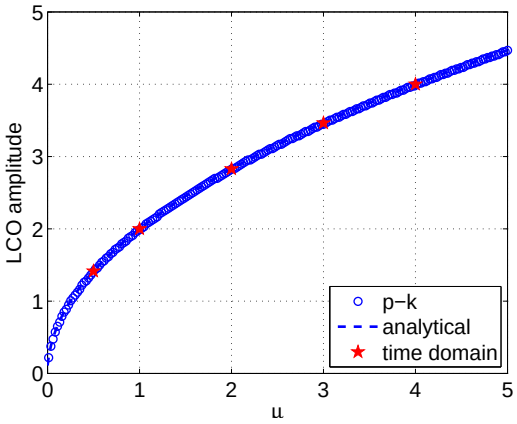

Figure 4.1: Bifurcation diagram of the one degree-of-freedom van der Pol oscillator system ($\epsilon = 0.01$, $a = 1$, $d = 0$)

used to obtain these time domain results. Excellent agreement between the results of all methods is obtained.

Now the bifurcation behaviour of the van der Pol equation with a non-zero b is investigated. With $\epsilon = 0.02$, $a = -2$, $d = 0.5$ the LCO amplitudes obtained using the various methods are obtained. Figure 4.2 shows the bifurcation diagram obtained using the amplitude-dependent p-k method. As can be seen from this figure, a stable and an unstable LCO exist. This means that the bifurcation behaviour of the LCO amplitude is subcritical.

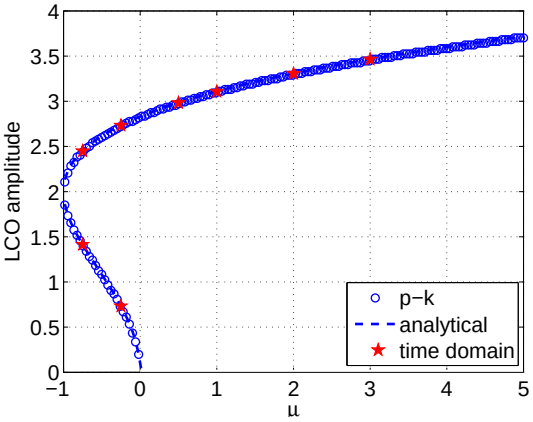

Figure 4.2: Bifurcation diagram of the one degree-of-freedom van der Pol oscillator system ($\epsilon = 0.02$, $a = -2$, $d = 0.5$)

As can be seen from Figure 4.2, the LCO amplitude first becomes larger when the bifurcation parameter is decreased and then at $\mu = -1$ the LCO amplitude increases with increasing μ. For values of μ between -1 and 0 there exist two LCOs, a so-called repeller and an attractor. A repeller is an unstable solution, whereas the attractor is a stable solution. At $\mu = -1$, a so-called saddle-node bifurcation of limit cycles occurs [26]. For such a bifurcation the stable and unstable LCOs merge. Note that a repeller cannot be found from time domain simulations (from a physical point of view). For validation purposes, it has been determined here by reversing the time, such that a repeller becomes an atrractor and an attractor becomes a repeller. The can be achieved by reversing the sign of the coefficients a and d in (4.1) in the time domain computations (at a fixed μ-value). From Figure 4.2 is observed that the solution obtained from the amplitude-dependent p-k method is in perfect agreement with the analytical solution and the time domain solution. Hence, the amplitude-dependent p-k method is able to correctly predict the bifurcation behaviour of a van der Pol oscillator with a fourth order non-linear damping force.

In the amplitude-dependent p-k solver presented in Section 2.5 the assumption has been made that the limit-cycle oscillation is a simple harmonic oscillation. Hence, it is assumed that there are no higher order harmonics in the oscillation. To check whether the amplitude-dependent p-k solver also works when higher order harmonics come into play, the non-linear damping force coefficient ϵ in (4.1) has been increased. Figure 4.3 shows the time domain solution obtained with $\epsilon = 1$, $\mu = 0.8$, $a = 0.3$, $d = 0$.

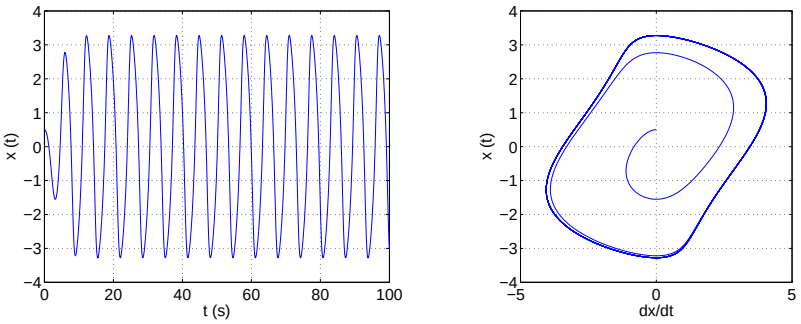

(a) Amplitude versus time

(b) Phase portrait

Figure 4.3: Time domain solution of the one degree-of-freedom van der Pol oscillator system ($\epsilon = 1$, $\mu = 0.8$, $a = 0.3$ and $d = 0$)

From Figure 4.3 it is observed that an LCO with an amplitude of 3.276 develops. The frequency is 0.962. From the amplitude-dependent p-k method an amplitude of 3.266 and a frequency of 1.135 are obtained. Hence, the agreement in amplitude is good. However, the agreement in frequency is only fair. To study the influence of the non-linear damping force coefficient ϵ in more detail, the error made (w.r.t. the time domain solution) when increasing ϵ has been computed for various values of ϵ. Figure 4.4 shows the relative error in LCO amplitude and in frequency versus the non-linear damping coefficient.

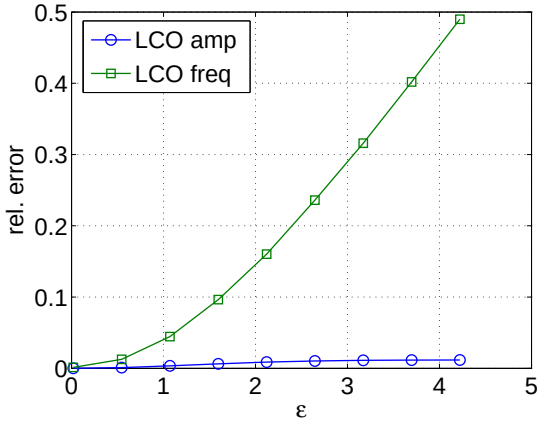

Figure 4.4: Relative error in LCO amplitude and frequency versus the damping coefficient ϵ for the one degree-of-freedom van der Pol oscillator system ($\mu = 0.8$, $a = 0.3$, $d = 0$)

The relative error is seen to increase from Figure 4.4. Especially the error made in the frequency becomes large with increasing ϵ (about 50% for a non-linear damping coefficient of about 4). The relative error made in LCO amplitude remains below 2% for ϵ-values up to 4. This suggests that only an estimation for the LCO amplitude can be obtained from the amplitude-dependent p-k method when the LCO contains higher order harmonics. Furthermore, the differences in frequency indicate that the amplitude-dependent p-k method can only be exact when the LCO is a pure first order harmonic oscillation.

4

TWO DOF VAN DER POL-OSCILLATOR

The standard van der Pol oscillator with one degree of freedom has been extended to two degrees of freedom. Furthermore, the non-linear damping force has been extended with a fourth order term. The equations of motion are given by (see (3.16) in Section 3.3.1):

$$\mathbf{M}\ddot{\vec{x}} + \mathbf{K}\vec{x} = \epsilon \begin{bmatrix} \mu - a_1 x_1^2 - b_1 x_1^4 & c_1\mu - a_2 x_1^2 \\ c_1\mu - a_3 x_2^2 & c_1\mu - a_4 x_2^2 - b_2 x_2^4 \end{bmatrix} \begin{bmatrix} \dot{x}_1 \\ \dot{x}_2 \end{bmatrix}, \tag{4.2}$$

where $\vec{x} = [x_1, x_2]^T$ is now a vector with the displacements of the two degrees of freedom and a_1, a_2, a_3, a_4, b_1, b_2 and c_1 are constants. $\mathbf{M}$ and $\mathbf{K}$ are the mass and stiffness matrices, respectively and ϵ is a damping coefficient used to scale the damping. These equations can be solved either in the time domain or in the frequency domain. When the non-linear damping force vector is reduced to a non-linear damping force in the first (or second) DoF only, an analytical solution is available. Therefore, for initial validation purposes, the coefficients a_2, a_3, a_4, b_1, b_2 and c_1 have been set to zero. The other coefficients have been taken as: $\epsilon = 0.02$, $a_1 = 0.3$. The mass matrix has been set to the identity matrix and the stiffness matrix is defined as:

$$\mathbf{K} = \begin{bmatrix} 20 & -10 \\ -10 & 10 \end{bmatrix}. \tag{4.3}$$

The analytical solution for the LCO amplitude can be computed using the principle of energy conservation, see Section 3.3.1. Since the non-linear damping force is only present in the first equation, the LCO amplitude of the other DoF is computed using the absolute value of the complex amplitude ratio. Equations (4.4) and (4.5) present the analytical solution of (4.2) (when the coefficients a_2, a_3, a_4, b_1, b_2 and c_1 are zero).

$$\Delta x_1 = 2\sqrt{\frac{\mu}{a_1}}, \tag{4.4}$$

$$\Delta x_2 = \left|\theta_{x_1 x_2}\right| \cdot 2\sqrt{\frac{\mu}{a_1}}. \tag{4.5}$$

ADePK has been used to study the bifurcation behaviour of the two DoF van der Pol oscillator by varying the parameter μ. Two LCO modes were observed from all methods, one at an angular frequency of 1.95 rad/s and one at an angular frequency of 5.14 rad/s. In Figure 4.5 the LCO amplitude is plotted as a function of μ. The blue circles and green squares show the LCO amplitude as obtained from ADePK, whereas the dashed lines show the analytical solution. Δx_1 and Δx_2 represent the amplitudes of the first and second degree of freedom, respectively. The red pentagrams and pink hexagrams show the time integration results, for the first and second DoF, respectively. Since the non-linear force vector is known analytically, it is not necessary to set up a response surface for this test case.

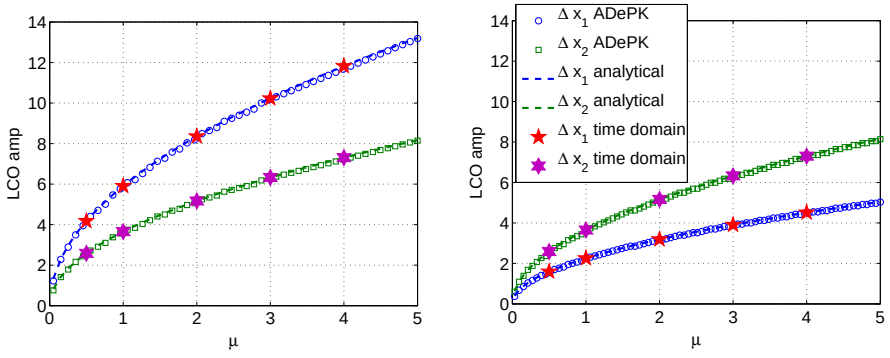

(a) Mode 1: $\omega = 1.95$ rad/s (b) Mode 2: $\omega = 5.14$ rad/s

Figure 4.5: Bifurcation diagrams of the two degree-of-freedom van der Pol oscillator system ($\epsilon = 0.02$, $a_1 = 0.3$ and $a_2 = a_3 = a_4 = b_1 = b_2 = c_1 = 0$)

The LCO amplitude increases with increasing bifurcation parameter μ, i.e. a so-called supercritical bifurcation of the LCO amplitude occurs. Excellent agreement is observed between the analytical, time-domain and the frequency-domain solutions.

Next, the influence of a fourth order non-linear damping term in the van der Pol oscillator system has been investigated. The following values for the coefficients of the non-linear damping matrix have been used: $\epsilon = 0.002$, $a_1 = -6$, $a_2 = -2$, $a_3 = -1$, $a_4 = -4$,

$b_1 = 0.25$, $b_2 = 0.5$ and $c_1 = 1$. Solving the system (4.2) a subcritical bifurcation is obtained, see Figure 4.6. Again there are two LCO modes. Mode 1 has an angular frequency of 1.96 rad/s and mode 2 has an angular frequency of 5.12 rad/s. The time domain solutions are shown as well. Note that the second mode was not found from time domain simulations.

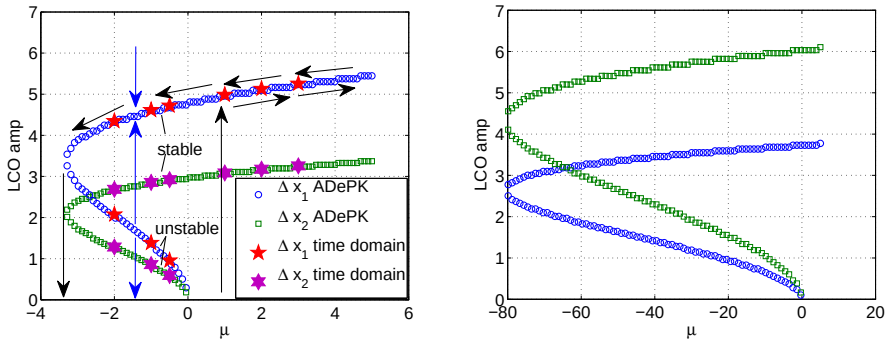

(a) Mode 1: $\omega = 1.96$ rad/s

(b) Mode 2: $\omega = 5.12$ rad/s

Figure 4.6: Bifurcation diagrams of the two degree-of-freedom van der Pol oscillator system ($\epsilon = 0.002$, $a_1 = -6$, $a_2 = -2$, $a_3 = -1$, $a_4 = -4$, $b_1 = 0.25$, $b_2 = 0.5$ and $c_1 = 1$)

From Figure 4.6 it is observed that for both modes a so-called subcritical bifurcation occurs, i.e. for values of μ smaller than zero a stable and an unstable LCO exist at one value of μ. For μ larger than zero, only one LCO exists, a stable LCO. The blue arrows indicate that the stable LCO is an attractor, whereas the unstable LCO is a repeller. In order to validate the amplitude of the unstable LCOs, this repeller has been determined from time domain simulations by reversing the time, as for the one DoF van der Pol oscillator. For the two DoF van der Pol oscillator the signs of the coefficients a_1, a_2, a_3, a_4, b_1 and b_2 are reversed in (4.2) in the time domain computations (at a fixed μ-value). Again excellent agreement is obtained between the time and frequency domain results. Furthermore, this test case suggests that for a subcritical bifurcation to occur the nonlinear damping should be of at least order four.

In this section the assumption of a simple harmonic motion will be checked in the same way as was done for the one DoF van der Pol oscillator. The two DoF van der Pol oscillator of equation (4.2) is used with $\epsilon = 1$, $a_1 = 0.3$, $\mu = 0.8$ and $a_2 = a_3 = a_4 = b_1 = b_2 = c_1 = 0$. Figures 4.7(a) and 4.7(b) show the phase portraits of the first mode, with a frequency of 1.94 rad/s, the LCO amplitudes are 3.337 and 5.407. The phase portraits of the second mode with a frequency of 5.13 rad/s are shown in Figures 4.7(c) and 4.7(d). The LCO amplitudes for this mode are 3.266 and 2.026. From the amplitude-dependent p-k solver two modes are found. The first mode has a frequency of 1.96 rad/s and LCO amplitudes of 3.265 and 5.284. The second mode has a frequency of 5.11 rad/s and LCO amplitudes of 2.018 and 3.266. Hence, there is a good agreement in both frequency and LCO amplitude for the two DoF van der Pol oscillator. Although, it should be noted that the second mode is almost first harmonic as seen from the phase portrait of the second

degree of freedom of this mode (Figure 4.7(d)).

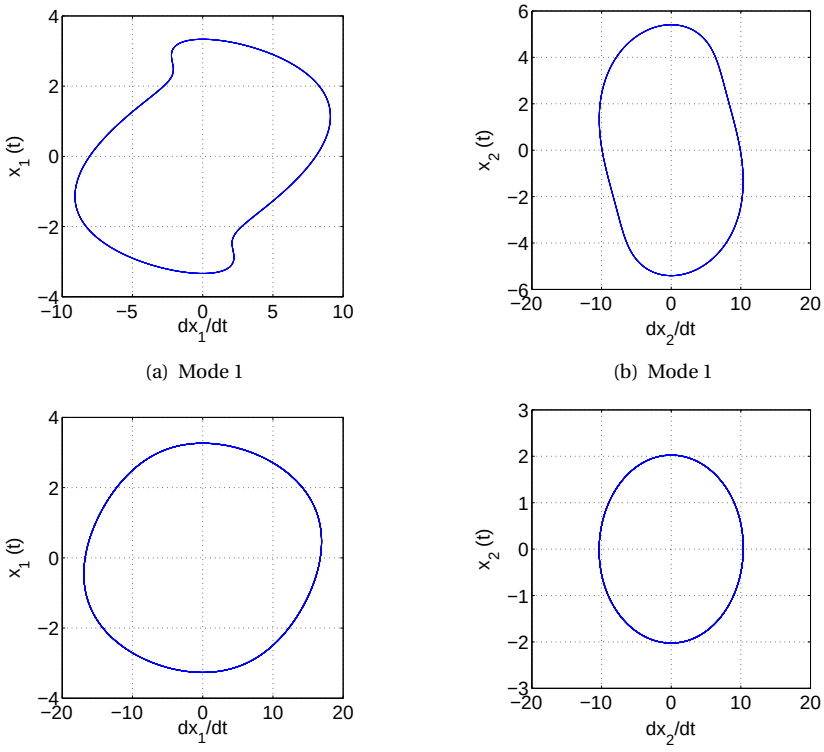

(a) Mode 1

(b) Mode 1

(c) Mode 2

(d) Mode 2

Figure 4.7: Phase portraits of the two degree-of-freedom van der Pol oscillator system ($\epsilon = 1$, $\mu = 0.8$, $a_1 = 0.3$ and $a_2 = a_3 = a_4 = b_1 = b_2 = c_1 = 0$)

To further study the validity of the first harmonic assumption the relative error made in the LCO amplitudes and in the frequency have been computed for various values of the damping coefficient ϵ. The reference solution is the time domain solution. Figure 4.8 shows the absolute value of the relative error in the LCO amplitudes and in the frequency versus ϵ for the two modes. The relative error is almost zero when ϵ is 0.02 and increases with increasing ϵ as expected. It should be noted that the relative error is still below 10% for values of the non-linear damping coefficient up to about 4. This might be an acceptable error. Overall, the amplitude-dependent p-k method is well suited to study LCOs caused by weak non-linearities (which can be represented by the first harmonic component only).

It is expected that ADePK will fail to predict the correct LCO amplitudes and frequency when the structural motion of the two DoF airfoil system contains significant higher harmonics of the same order as the first harmonic component, since the aerodynamic forces are highly dependent on the amplitudes of both DoF, the (reduced) fre-

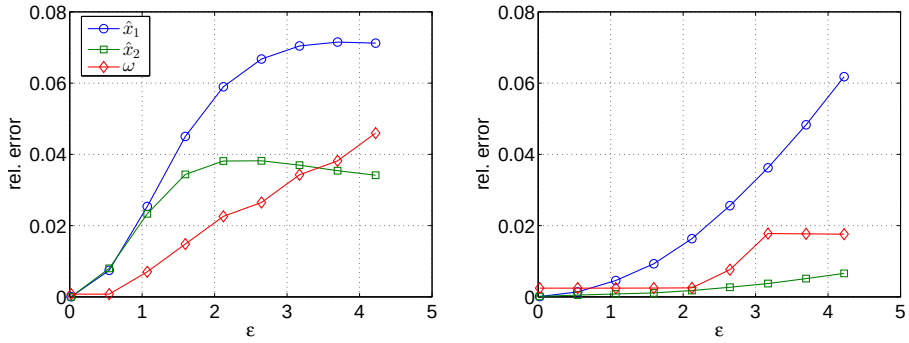

(a) Mode 1 (b) Mode 2

Figure 4.8: Relative error in LCO amplitudes and frequency versus the damping coefficient ϵ for the two degree-of-freedom van der Pol oscillator system ($\mu = 0.8$, $a_1 = 0.3$ and $a_2 = a_3 = a_4 = b_1 = b_2 = c_1 = 0$)

quency and the phase difference between both DoF. Further investigations are necessary to clarify this. However, when the LCO is first harmonic, ADePK can be used to estimate the LCO amplitude and the LCO mode shape as verified for the van der Pol oscillator in this section.

4.3.2. TWO DOF AIRFOIL SYSTEM

In order to apply ADePK to this test case, the aerodynamic forces were computed using inviscid CFD simulations. Harmonic forced-motion simulations were performed, see Section 2.5.2, that sample the parameter space spanned by reduced frequencies, amplitude ratios, phase differences between pitch and plunge and pitch amplitudes. The results are used to create a response surface, which is used for the determination of the aerodynamic forces in ADePK. For validation, the LCO amplitude has been determined from FSI simulations at several freestream velocities.

RESPONSE SURFACE CONSTRUCTION

To determine the range of the mode shape parameters and frequency required, flutter calculations were performed (using the conventional p-k method) with varying structural parameters. The flutter mode shape was extracted for each structural parameter combination. Since the LCO mode can be expected to be similar to the flutter mode shape, the range in which to select response surface samples is determined from the flutter mode shapes. For this study, the structural parameters as depicted in Table 2.1 were taken as a starting point. Table 4.1 shows the variations applied to the structural parameters. The structural damping was left unchanged. Figure 4.9 shows the resulting flutter mode shapes for all combinations of the structural parameters in Table 4.1. From Figure 4.9(a) and 4.9(b) it is seen that the phase difference at flutter $(\phi_{h\alpha})_f$ varies between 0° and 180°. However, most of the samples have a phase difference smaller than about 160°. The amplitude ratio at flutter $|\theta_{h\alpha}|_f$ varies from 0 to about 20, with the highest concentration at amplitude ratios below 5. The reduced frequency at flutter k_f

is seen to vary between 0 and about 0.6 from Figures 4.9(b) and 4.9(c).

Structural parameter	Values	Units
Mass m	10, 18, 26, 34, 42, 50	kg
Mass moment of inertia I_α	0.01, 2.008, 4.006, 6.004, 8.002, 10	kg/m^2
Torsional spring stiffness K_α	$3.323\cdot10^3$, $6.646\cdot10^3$, $9.969\cdot10^3$, $1.3292\cdot10^4$, $1.6615\cdot10^4$, $1.9938\cdot10^4$	Nm/rad
Plunge spring stiffness K_h	$5.39\cdot10^5$, $1.078\cdot10^6$, $1.617\cdot10^6$, $2.156\cdot10^6$, $2.695\cdot10^6$, $3.234\cdot10^6$	N/m
Static moment related to EA S_α	0.10, 0.68, 1.26, 1.84, 2.42, 3.0	kgm
Torsional damping constant D_α	0.0687	kgm^2/s
Plunge damping constant D_h	45.764	kg/s

Table 4.1: Values of the structural parameters used for determination of the range of response surface samples

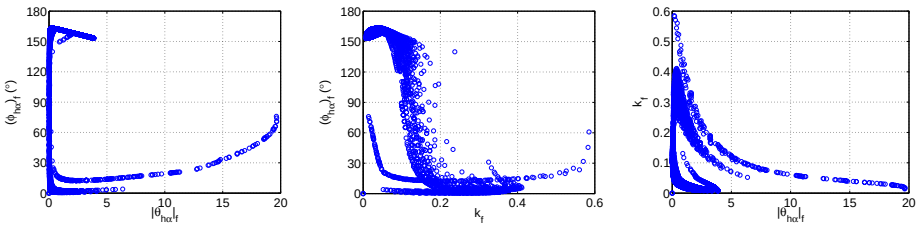

(a) Phase difference vs amplitude ratio (b) Phase difference vs reduced frequency (c) Reduced frequency vs amplitude ratio

Figure 4.9: Flutter mode shape for various structural parameters

The sampling range of the reduced frequency k was therefore taken from 0 to 0.6. For $|\theta_{h\alpha}|$, values between 0.1 and 4 were used for the response surface samples and for $\phi_{h\alpha}$ values between 5° and 150° were used. Pitch amplitudes from 0° till 5° were selected. To determine the number of samples in each direction of the response surface a comparison of an interpolated response surface slice with a dense-sampled response surface slice obtained from forced motion oscillation simulations was made. The number of samples in each direction was chosen based on sufficient agreement between the two slices. Table 4.2 displays the sample locations of the mode shape parameters for determination of the response surface and Figure 4.10 shows an exemplary cut through the response surface in terms of the complex-valued lift and the complex-valued moment versus the mode shape parameters. The interpolated response surface is shown by dashed lines. Three different interpolation methods have been applied: linear interpolation (green dashed line), cubic spline interpolation (red dashed line) and polynomial interpolation (in multiple dimensions, blue dashed line). The slices versus pitch amplitude and amplitude ratio have been normalised by $\Delta\alpha$ and $|\theta_{h\alpha}|$, respectively. In order

to normalise with respect to $|\theta_{h\alpha}|$, the aerodynamic force (or moment) at $|\theta_{h\alpha}| = 0$ is first subtracted.

Mode shape parameter	Values
Pitch amplitude $\Delta\alpha$ (°)	0, 0.1, 0.5, 1, 2, 3, 4, 5
Amplitude ratio $\|\theta_{h\alpha}\|$	0.1, 0.5, 1, 4
Reduced frequency k	0, 0.1, 0.2, 0.25, 0.3, 0.4, 0.5, 0.6
Phase difference $\phi_{h\alpha}$ (°)	5, 10, 50, 100, 150

Table 4.2: Values of the mode shape parameters used for determination of the response surface of two DoF NLR7301 airfoil system

Figure 4.10 shows that the real and imaginary parts of lift and moment varied most with reduced frequency as could be expected. The deviation with respect to the linear part of response surface is clearly seen in the direction of the pitch amplitude. The slice of the response surface for the amplitude ratio was found to be only slightly non-linear, since the variations in the normalised real and imaginary of the lift and moment are small (much smaller than in the amplitude direction). For the phase difference the response surface slice seems to have a sine-like shape.

Note that in the amplitude ratio direction samples in a smaller range than that found from the structural parameter variation in the flutter case were used (0.1 till 4 instead of 0.1 till 20). This is not expected to be a problem for the structural frequency ratio considered in this chapter (see Section 4.3.3). In total 1280 samples were used (see Table 4.2). From those 980 are the output of forced motion oscillation simulations. The remaining samples at a pitch amplitude of zero are zero and those at a reduced frequency of zero have been determined from quasi-steady values.

The response surface is, in the non-linear case, obtained from simulations where pitch and plunge are simultaneously applied, i.e.

$$\vec{\hat{f}} = [f_L\left(\Delta\alpha, |\theta_{h\alpha}|, k, \phi_{h\alpha}\right), f_M\left(\Delta\alpha, |\theta_{h\alpha}|, k, \phi_{h\alpha}\right)]^T.$$

Instead of applying forced motion oscillation simulations in a four dimensional parameter space, the parameter space can also be reduced two dimensions when superposition of the describing functions is applied, i.e. when a quasi-linearisation is applied, see Section 2.5.2. Ueda et al. [10], He et al. [11] and Somieski [12] used superposition of describing functions to compute the aerodynamic forces at the amplitudes and the frequency predicted by their extended p-k solver. To compare ADePK with the approach of [10–12], in addition to a non-linear response surface, describing functions are also used to compute the aerodynamic forces at the LCO mode shape during the iterations of ADePK in this chapter (see later in this section).

BIFURCATION BEHAVIOUR

Using the samples as specified in Table 4.2, ADePK has been applied to study the bifurcation behaviour of LCO amplitude of the NLR7301 airfoil. The amplitude at which δ becomes zero has been determined for several freestream velocities. As explained in

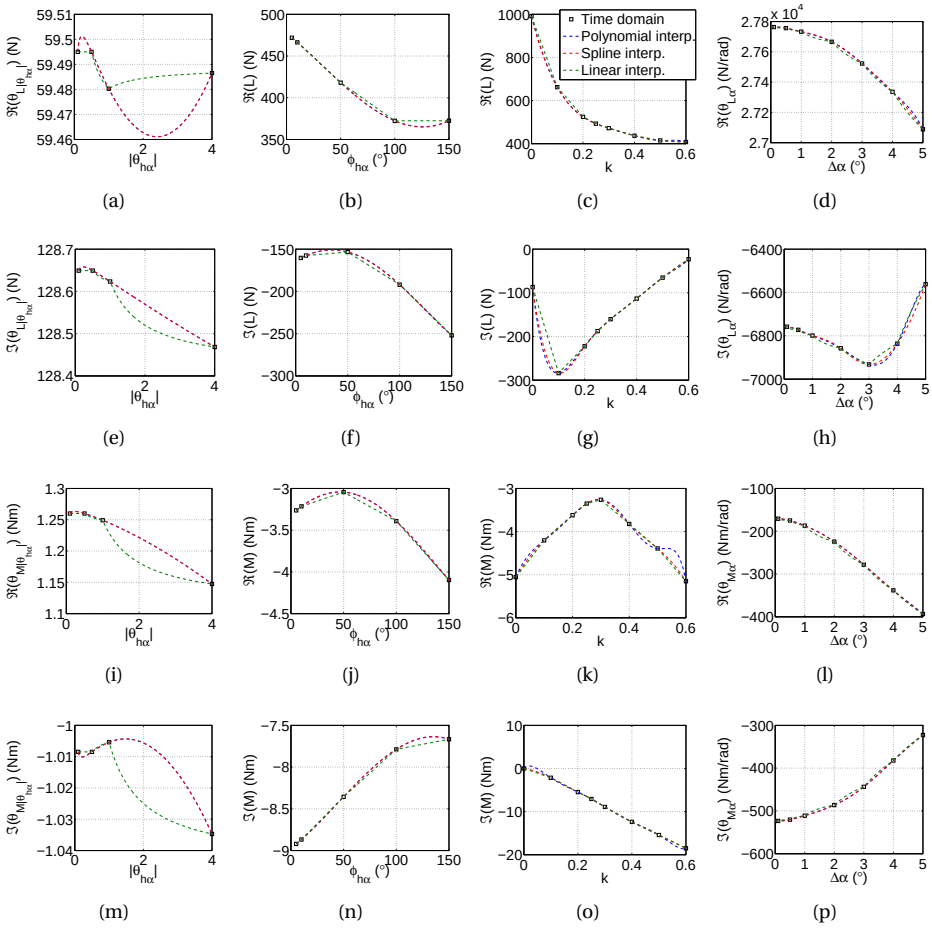

Figure 4.10: Response surface at $\Delta\alpha = 1°$, $\phi_{h\alpha} = 5°$, $|\theta_{h\alpha}| = 0.5$, $k = 0.3$ (blue - polynomial interpolation, red - cubic spline interpolation, green - linear interpolation)

Section 2.5.3, the aerodynamic forces at each freestream velocity have been determined by pre-multiplication of the dynamic pressure q_∞ and dividing by the reference dynamic pressure at which the aerodynamic forces were computed q_{ref}, i.e. $\vec{\hat{f}} = q_\infty / q_{\text{ref}} \cdot \vec{\hat{f}}_{\text{ref}}$. This means that formally the results are non-matched, as no additional iterations are performed to match the reference velocity with the computed flutter and LCO solution bifurcation velocities.

Figure 4.11 shows the results from ADePK together with the results from fluid-structure interaction simulations. Since it takes a lot of computational effort to determine the LCO amplitude in the time domain, at each freestream velocity several FSI simulations have been performed, each simulation with a different initial amplitude. From each of these simulations it has been determined whether the oscillations of the system were growing

or decaying in amplitude. In this manner, the bounds between which the LCO amplitude should lie have been determined. The blue circles and the red squares depict the lower and upper bounds between which a stable LCO occurs, respectively. Furthermore, unstable LCOs have also been found from time domain simulations at various velocities. These were found from FSI simulations that decay in amplitude for a certain initial amplitude and increase in amplitude for a higher initial amplitude. The blue diamonds and red pentagrams depict the lower and upper bounds of these unstable LCOs, respectively. The black triangles at zero amplitude show the results of FSI simulations for which the amplitude decays towards zero (at all initial amplitudes tested). The solid blue, red and green lines in Figure 4.11 show the frequency domain solution using polynomial, cubic spline and linear interpolation, respectively. The flutter velocity obtained from the p-k method (using cubic spline interpolation) is plotted in Figure 4.11(a) with a green diamond at a zero amplitude. Figures 4.11(b) till 4.11(d) show the other LCO mode shape parameters (amplitude ratio, reduced frequency and phase difference between pitch and plunge) as obtained from ADePK versus the freestream velocity. For comparison the FSI simulation results are also shown.

From the time domain simulations it is seen that the unstable LCO amplitude decreases with increasing freestream velocity for amplitudes up to approximately 1°. For larger amplitudes the LCO amplitude increases with increasing amplitude, i.e. the bifurcation is supercritical. Below a freestream velocity of approximately 196.78 m/s all FSI simulations decay towards zero amplitude, i.e. no LCOs occur. The agreement of the results of ADePK with the time domain results is good for all interpolation methods. All interpolation methods predict unstable LCOs at small amplitudes. The polynomial interpolation results agree the best with the time domain results. The linear interpolation results are shifted to lower velocities at small amplitude and underpredict the LCO amplitude at higher velocities. Cubic spline interpolation results in nested LCOs. However, the shifts of the curves on the abcissa are very small (i.e. note the scale). The variations in the bifurcation behaviour between the various interpolation methods are a result of the differences in the response surface for the different interpolation methods, see Figure 4.10. Although the differences in the response surface are relatively small they can have an enormous impact, as all mode shape parameters are linked. More samples or another distribution of the samples, might be necessary to better predict the LCO amplitude using these interpolation methods. In the case of infinitely many samples, all interpolation methods should give the same response surface and hence the same bifurcation behaviour.

To investigate the source of the deviations between the bifurcation behaviour obtained using cubic spline interpolation and the polynomial interpolation, a sensitivity study w.r.t. to the interpolation methods has been performed. Since from Figure 4.10 (and other slices of the response surface that are not shown) it is observed that cubic spline and polynomial interpolation result in almost the same response surface, the interpolation methods for the response surface have been interchanged. That is, one of the aerodynamic forces (real and imaginary parts of lift and moment) has been interpolated by cubic splines and the rest by polynomials. This is done for all the aerodynamic forces. The same bifurcation behaviour as when polynomial interpolation is used for all aerodynamic forces is observed when cubic spline interpolation is applied instead of

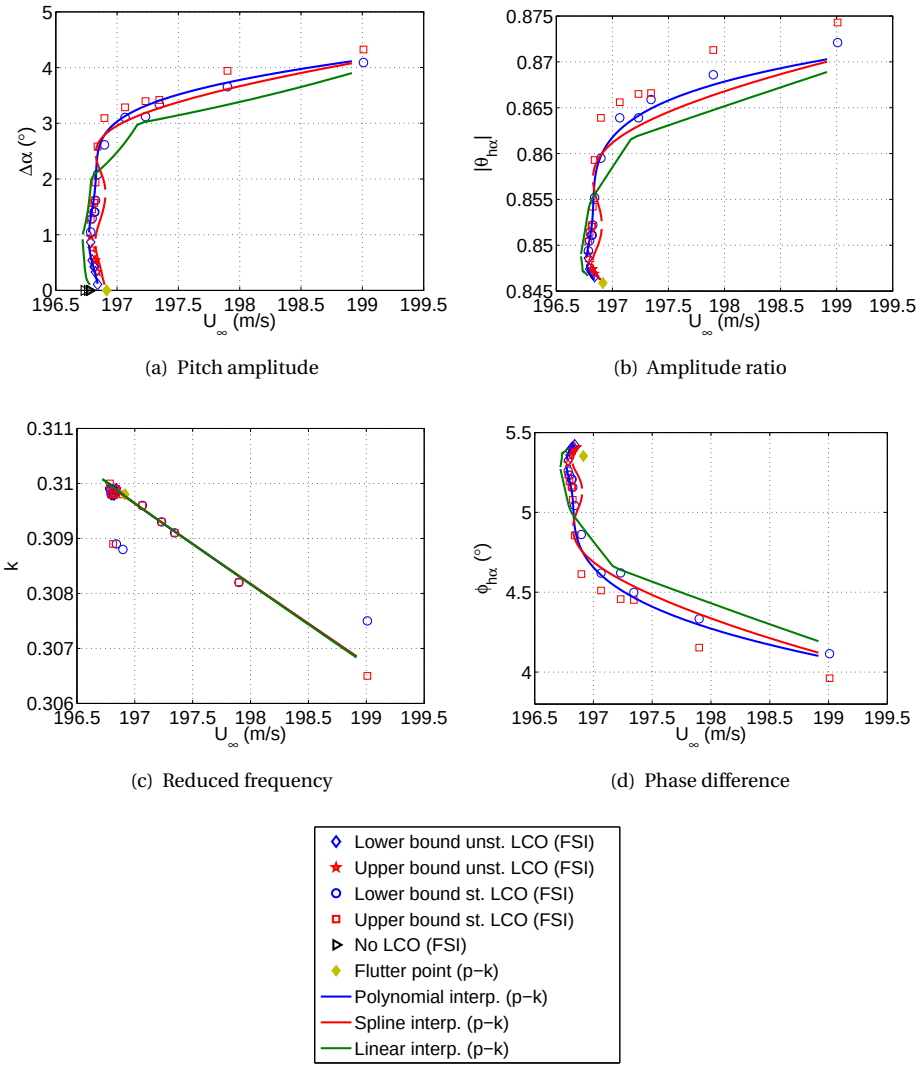

(a) Pitch amplitude

(b) Amplitude ratio

(c) Reduced frequency

(d) Phase difference

(e)

Figure 4.11: LCO mode shape versus freestream velocity

polynomial interpolation for the real part of the lift and the real and imaginary part of the moment. However, when using cubic splines for the interpolation of the imaginary part of the lift and polynomial interpolation for the remaining aerodynamic forces, the same bifurcation behaviour is obtained as when cubic spline interpolation is used for all aero-

dynamic forces. This suggests that the imaginary part of the lift is the most important response surface parameter. However, the differences between cubic spline and polynomial interpolation are hardly visible from Figure 4.10(h). When looking at the relative difference of the interpolated curves at the same condition as in Figure 4.10, which is plotted in Figure 4.12(a), it is seen that the relative difference is of the order of $1 \cdot 10^{-3}$ for the imaginary part of the lift. For the real part of the lift the relative difference is of order $1 \cdot 10^{-4}$ and for the real and imaginary part of the moment of order $1 \cdot 10^{-5}$ (not shown here). Note that at the sample points the relative difference between the two response surfaces is zero and that the difference increases with amplitude. The differences in the response surface between cubic spline and polynomial interpolation are better visible when looking the phase of the lift in the same slice of the response surface, see Figure 4.12(b). This figure shows that the response surfaces are identical up to an amplitude of about 1.0° and start to deviate for larger amplitudes. This is reflected in the bifurcation behaviour, Figure 4.11(a), which shows that the bifurcation curve is merely shifted to larger velocities for amplitudes up to 1.0° in case of cubic spline interpolation. For larger amplitudes the deviations in shape of the bifurcation curve become significant. Hence, Figure 4.12 gives the sources of the deviations in the bifurcation behaviour obtained with either cubic spline or polynomial interpolation.

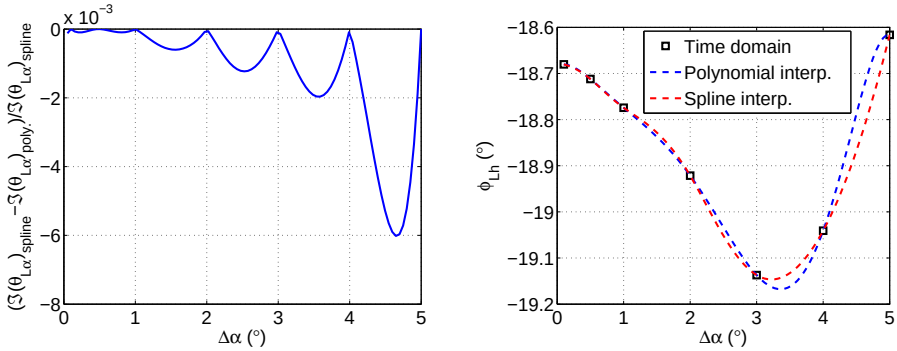

Figure 4.12: Relative difference in imaginary part of the lift and phase of the lift versus amplitude at $\phi_{h\alpha} = 5°$, $|\theta_{h\alpha}| = 0.5$, $k = 0.3$

Figure 4.11(b) shows a supercritical bifurcation of the amplitude ratio with the free-stream velocity. The phase difference decreases with increasing airspeed, see Figure 4.11(d), meaning that the pitching and plunging motions tend to get more in phase. The small positive phase difference indicates that plunge leads pitch. The reduced frequency is monotonically decreasing with freestream velocity, because k is an inverse function of the velocity (i.e. $k = \omega c / U_\infty$). Although it should be noted that the variation of reduced frequency is minimal, because the velocity variation is small.

Upon comparing the results from ADePK to the time domain results, it is concluded that the bifurcation behaviour is globally correctly predicted by ADePK. Small discrepancies can be attributed to interpolation errors.

SUPERPOSITION OF DESCRIBING FUNCTIONS

Figure 4.13 shows the bifurcation diagrams of the LCO mode shape for the fully non-linear case (combined pitch/plunge simulations, blue) and for the quasi-linearised case (superposition of describing functions, red). Cubic spline interpolation has been used for both cases. Unstable LCOs are predicted at small amplitudes for both the non-linear and the quasi-linearised case. However, in case of superposition of the DFs the LCOs become stable already at about 0.3°, whereas in the non-linear case the trend of the FSI results is followed and stable LCOs occur only just below 1°. Then, with increasing amplitude, the LCOs become stable, then unstable and then stable again. The variations in the bifurcation behaviour between the two different response surface set-ups are most likely a result of differences in the response surface. The non-linear results agree better to the time domain results than the results obtained with superposition of DFs. Especially for the amplitude ratio and the phase difference the relative deviations are large between the quasi-linearised and the non-linear results. To obtain the non-linear results 1280 samples were used (980 forced motion simulations). The superposition results were obtained using the same samples as depicted in Table 4.2 except the phase difference samples, hence 256 samples were used. This means that a significant amount of computational time is saved when the principle of superposition is applied. Therefore, applying superposition of the describing functions as suggested by [11, 12] is a alternative when computational resources are limited. However, when accuracy is important, ADePK with fully non-linear aerodynamic forces should be used.

4.3.3. STRUCTURAL PARAMETER VARIATION

To demonstrate the capabilities of the proposed amplitude-dependent p-k method, ADePK has been used to study a structural parameter variation. Due to the separation of aerodynamics and structure, the structural model parameters can be easily varied in ADePK. There is no need to set up a new response surface (that is only necessary when the aerodynamic conditions are changed). Hence, variations in the bifurcation behaviour of the LCO amplitude and in the type of bifurcation can be studied very fast once the response surface is available. Here the natural structural frequency ratio (SFR) has been varied, similar to [14, 15], who performed a SFR variation for the NACA64010A airfoil. The bifurcation of the LCO mode shape obtained when varying the natural structural frequency ratio ω_h/ω_α from 0.49 to 1.21, is shown in Figure 4.14. The response surface has been interpolated using cubic spline interpolation. The variation of the structural frequency ratio has been obtained by varying the plunge spring stiffness K_h. The response surface has been obtained from combined pitch/plunge motions.

From Figure 4.14(a) it is observed that the flutter speed first decreases and then increases with increasing structural frequency ratio. Furthermore, Figure 4.14(b) shows that the bifurcation behaviour becomes subcritical when the structural frequency ratio increases. The limit-cycle oscillations are plunge dominated, with a large $|\theta_{h\alpha}|$ ($>> 1$), when the frequency ratio is small and pitch dominated, with a very small $|\theta_{h\alpha}|$ ($<< 1$), for the larger SFRs. This was also observed by Kholodar et al. [14]. The phase difference is close to zero for small frequency ratios and becomes very large for large SFRs. The reduced frequency increases with increasing structural frequency ratio. However, for $\omega_h/\omega_\alpha > 0.90$ the reduced frequency decreases. Upon comparing the frequency at flut-

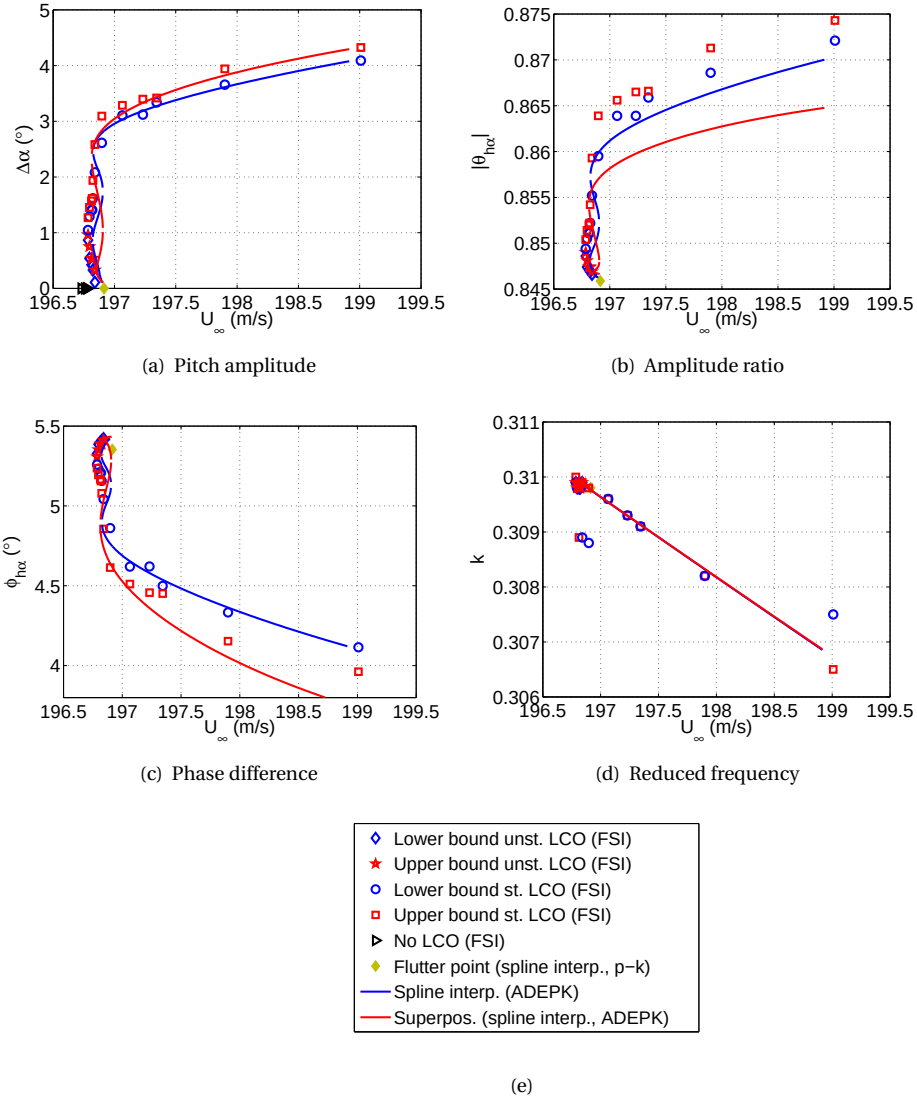

(a) Pitch amplitude

(b) Amplitude ratio

(c) Phase difference

(d) Reduced frequency

(e)

Figure 4.13: LCO mode shape versus freestream velocity at $M = 0.74$, $\tilde{\alpha} = -1.5°$ (non-linear vs. quasi-linearised)

ter to the uncoupled reduced natural plunge frequency k_h^*, it is seen that for the lowest SFRs, at which the bifurcation behaviour is supercritical, the flutter frequency is larger than k_h^*, whereas for the other SFRs, with a subcritical bifurcation behaviour, the flutter frequency is smaller than k_h^*.

This structural parameter variation has been performed using the 1280 samples, i.e.

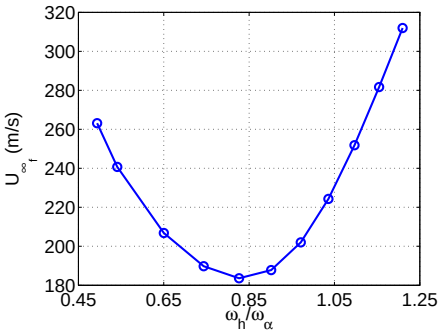

(a) Flutter speed

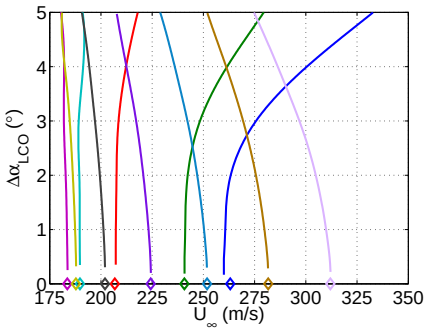

(b) Pitch amplitude

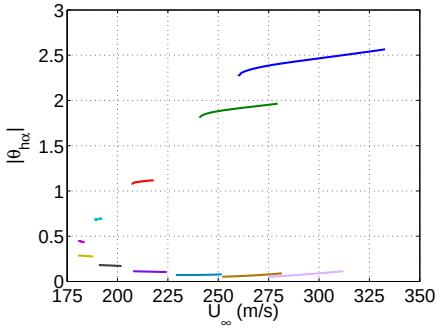

(c) Amplitude ratio

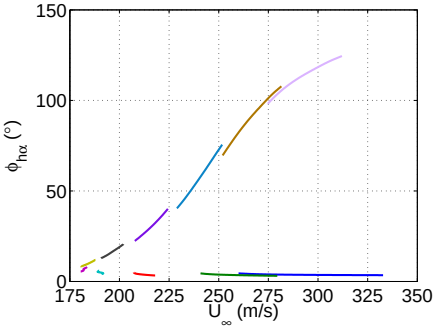

(d) Phase difference

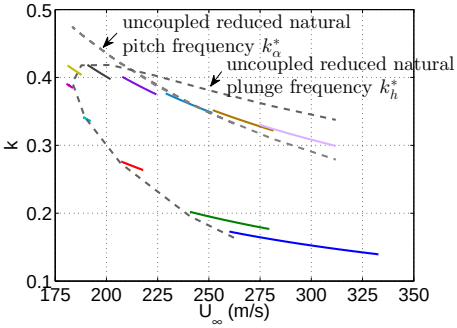

(e) Reduced frequency

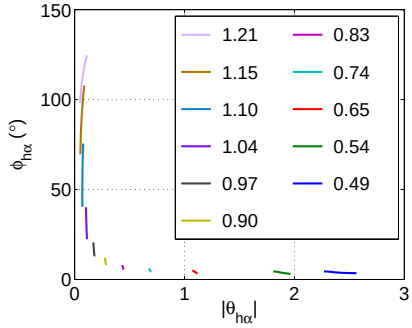

(f) Phase difference vs. amplitude ratio

Figure 4.14: LCO mode shape versus freestream velocity for various SFRs at $M = 0.74$, $\bar{\alpha} = -1.5°$ (cubic spline interpolation)

980 forced motion oscillation simulations have been performed, after which a response surface has been built. Hence, the computational effort to built a response surface suit-

able for predicting limit-cycle oscillations using ADePK is large. However, the use of time domain simulations would have resulted in a much higher computational effort, especially since new simulations are required as soon as a structural parameter is changed. Therefore, ADePK is a suitable tool to systematically investigate the bifurcation behaviour of limit-cycle oscillations, especially when structural parameter variations are of interest.

4.4. CONCLUSIONS

In this chapter the amplitude-dependent p-k method has been verified and validated for two test cases: a van der Pol-oscillator and a two-degree-of-freedom airfoil system. The one and two-DoF van der Pol oscillator test cases showed an excellent agreement between the time domain, frequency domain and the analytical solutions. Adding a fourth order damping term, resulted in a subcritical bifurcation behaviour of the LCO amplitude. This demonstrates that unstable LCOs can be found using the amplitude-dependent p-k method ADePK.

For the two degree-of-freedom airfoil system a response surface for the aerodynamic forces has been built using harmonic forced-motion simulations. This response surface has been used to determine the aerodynamic forces during the iterations of the p-k method. From both the time domain and frequency domain simulations a supercritical bifurcation is observed for large amplitudes. Close to the flutter speed unstable LCOs were predicted by both methods. Overall, the agreement between the LCO amplitude and mode shape obtained from both methods is good. Hence, ADePK can be used to predict limit-cycle oscillations. Furthermore, taking into account only the first harmonic component of the aerodynamic forces is sufficient for the LCOs observed in this chapter. Therefore, once a response surface has been built for a certain Mach number and mean angle of attack, structural parameter studies can be easily performed using ADePK, as demonstrated in this chapter. Furthermore, superposition of describing functions can save further computational time with respect to the fully non-linear amplitude-dependent p-k method - although some accuracy is lost. ADePK could be extended to more than two DoFs, although the dimension of the problem will increase with the number of DoFs n of the system according to $n+1+n(n-1)/2$. However, ADePK could be applied to systems with more than two DoFs in the following manner: first a classical flutter analysis is performed. From this analysis the two degrees of freedom that couple during flutter are identified. These two degrees of freedom are then used to predict limit-cycle oscillations with ADePK.

REFERENCES

[1] C. Denegri, *Limit cycle oscillation flight test results of a fighter with external stores,* Journal of Aircraft **37**, 761 (2000).

[2] R. Bunton and C. Denegri, *Limit cycle oscillation characteristics of fighter aircraft,* Journal of Aircraft **37**, 916 (2000).

[3] C. Dreyer and D. Shoch, *F-16 flutter testing at eglin air force base,* (Las Vegas, NV, USA, 1986) 3rd Flight Testing Conference.

[4] P. Chen, D. Sarhaddi, and D. Liu, *Limit-cycle-oscillation studies of a fighter with external stores,* (1998) AIAA Paper 98-1727.

[5] E. Dowell, J. Edwards, and T. Strganac, *Nonlinear aeroelasticity,* Journal of Aircraft **40**, 857 (2003).

[6] K. Hall, J. Thomas, and W. Clark, *Computation of unsteady nonlinear flows in cascades using a harmonic balance technique,* AIAA Journal **40** (2002).

[7] M. Balajewicz and E. Dowell, *Reduced-order modeling of flutter and limit-cycle oscillations using the sparse volterra series,* Journal of Aircraft **49** (2012).

[8] W. Zhang, B. Wang, Z. Ye, and J. Quan, *Efficient method for limit cycle flutter analysis by nonlinear aerodynamic reduced-order models,* AIAA Journal **50** (2012).

[9] A. Mannarino and P. Mantegazza, *Nonlinear aeroelastic reduced order modeling by recurrent neural networks,* Journal of Fluids and Structures **48**, 103 (2014).

[10] T. Ueda and E. Dowell, *Flutter analysis using nonlinear aerodynamic forces,* Journal of Aircraft **21** (1984).

[11] S. He, Z. Yang, and Y. Gu, *Transonic limit cycle oscillation analysis using aerodynamic describing functions and superposition principle,* AIAA Journal **52** (2014).

[12] G. Somieski, *An eigenvalue method for calculation of stability and limit cycles in nonlinear systems,* Nonlinear Dynamics **26**, 3 (2001).

[13] B. van der Pol, *Forced oscillations in a circuit with nonlinear resistance (receptance with reactive triode),* London, Edinburgh and Dublin Phil. Mag. **3**, 65 (1927).

[14] D. Kholodar, E. Dowell, J. Thomas, and K. Hall, *Limit-cycle oscillations of a typical airfoil in transonic flow,* Journal of Aircraft **41** (2004).

[15] D. Kholodar, J. Thomas, and E. Dowell, *A parameter study of transonic airfoil flutter and limit cycle oscillation behaviour,* (Denver, CO, 2002) 43rd AIAA/ASME/ASCE/AHS/ASC Structures, Structural Dynamics, and Materials Conference and Exhibit.

[16] D. Schwamborn, T. Gerhold, and R. Heinrich, *The DLR TAU-code: Recent applications in research and industry,* (The Netherlands, 2006) ECCOMAS CFD conference.

[17] A. Jameson, W. Schmidt, and E. Turkel, *Numerical solutions of the Euler equations by finite volume methods using Runge-Kutta time-stepping schemes,* (1981).

[18] A. Jameson, *Time dependent calculations using multigrid, with applications to unsteady flows past airfoils and wings,* AIAA Paper 91-1596 (1991), AIAA 10th Computational Fluid Dynamics Conference.

[19] J. Zwaaneveld, *NLR 7301 airfoil,* in *EXPERIMENTAL DATA BASE FOR COMPUTER PROGRAM ASSESSMENT - Report of the Fluid Dynamics Panel Working Group 04,* AGARD AR-138 (1979) pp. A4–1–A4–22, NATO - ADVISORY GROUP FOR AEROSPACE RESEARCH AND DEVELOPMENT.

[20] G. Dietz, G. Schewe, and H. Mai, *Experiments on heave/pitch limit-cycle oscillations of a supercritical airfoil close to the transonic dip,* Journal of Fluids and Structures **19**, 1 (2004).

[21] H. Hassig, *An approximate true damping solution of the flutter equation by determinant iteration,* Journal of Aircraft **8** (1971).

[22] G. Schewe, H. Mai, and G. Dietz, *Nonlinear effects in transonic flutter with emphasis on manifestations of limit cycle oscillations,* Journal of Fluids and Structures **18**, 3 (2003).

[23] G. Dietz, G. Schewe, and H. Mai, *Amplification and amplitude limitation of heave/pitch limit-cycle oscillations close to the transonic dip,* Journal of Fluids and Structures **22**, 505 (2006).

[24] A. van Rooij, J. Nitzsche, H. Bijl, and L. Tichy, *Limit-cycle oscillations of a supercritical airfoil,* (Bristol, UK, 2013) international Forum on Structural Dynamics and Aeroelasticity (IFASD).

[25] J. Dormand and P. Prince, *A family of embedded runge-kutta formulae,* Journal of Computational and Applied Mathematics **6**, 19 (1980).

[26] C. Gros, *Bifurcations and Choas in Dynamical Systems*, Tech. Rep. (Goethe Universität Frankfurt am Main, 2014) lecture notes course Self-Organization: Theory and Simulation.

5

BIFURCATION BEHAVIOUR OF LIMIT-CYCLE OSCILLATION SOLUTIONS

5.1. INTRODUCTION

Limit-cycle oscillations due to aerodynamic non-linearities can be caused by several sources of non-linearity in the flow. Shock waves and separation as well as boundary layer transition are thought to be reasons for the amplitude limitation. Several investigations have been performed into the aerodynamic sources of non-linearity responsible for LCOs. However none have systematically investigated LCO behaviour and linked it to the local aerodynamic features. Bendiksen [1] came close in his study of the Goland wing, where he identified the change in type of shock wave motion as the source for the amplitude limitation. However, no systematic investigations were performed. Kholodar et al. [2, 3] did a systematic study into the changes of the LCO bifurcation behaviour of the NACA 64A010A airfoil in inviscid flow. They varied the Mach number and the natural structural frequency ratio as well as the mass ratio. They observed that there is a high sensitivity of the bifurcation behaviour of the LCO solution with respect to Mach number, especially in the transonic regime. Both supercritical and subcritical bifurcations were observed. However, they did not analyse the LCO bifurcation behaviour and its corresponding source (the aerodynamic forces) in detail. Poirel and Mendes [4] investigated a variation in the plunge stiffness for the NACA0012 airfoil in incompressible flow at transitional Reynolds numbers. However, they did not study the bifurcation behaviour of the LCO amplitude in detail either. Why does a certain bifurcation behaviour establish itself? And can this behaviour be correlated with the behaviour of the flow and/or

Parts of this chapter have been published in van Rooij et al., Bifurcations of limit-cycle oscillations of a two degree-of-freedom airfoil caused by aerodynamic non-linearities, Proceedings of the 58th AIAA/ASCE/AHS/ASC Structures, Structural Dynamics, and Materials Conference, AIAA Science and Technology Forum and Exposition (SciTech), 2017.

the structure? This chapter analyses the bifurcation behaviour of LCOs of the NLR7301 airfoil for various Mach numbers and angles of attack as well as for various structural parameters and identifies possible sources of amplitude limitation.

The results of four separate studies are shown in this chapter. Each of the following sections represents one of these independent studies, i.e. it is not necessary to read certain sections of this chapter in order to understand the others. Readers interested in the LCO bifurcation behaviour due various sources of aerodynamic non-linearity, are invited to read Section 5.2. In Section 5.3 the effect of a Mach number variation in inviscid flow is studied, i.e. those who are interested in the link between the linear and the non-linear flutter behaviour are encouraged to read this section. Several structural parameter variations are applied to the test cases presented in Section 5.2 and the effect of these variations on the bifurcation behaviour is investigated in Section 5.4. Finally, readers who want to learn about the relation between the bifurcation behaviour and the form of the response surface of the aerodynamic forces should go to Section 5.5.

5.2. SOURCES OF AERODYNAMIC NON-LINEARITY

There are various sources of aerodynamic non-linearity that might lead to a limit-cycle oscillation, such as shock waves, boundary layer separation or boundary layer transition. These were considered by a few research groups, as noted in Section 1.3. Subcritical bifurcations were only observed in inviscid transonic flow [2, 3]. However, for viscous flows no subcritical bifurcations of the LCO amplitude were observed. Furthermore, these separate studies have shown that LCOs can occur in certain flow regimes for various airfoils. However, no systematic investigations of the LCO bifurcation behaviour exist in which a single airfoil is considered in all of these flow regimes. That is, certain airfoils might exhibit LCOs at one flow condition, but do they also appear at a completely different condition for the same airfoil? And for what aerodynamic non-linearities can subcritical bifurcations be observed? Hence, this section considers four different aerodynamic sources of non-linearity in order to identify and compare the bifurcation behaviour caused by these various non-linearities in the flow around a single airfoil, the NLR7301 airfoil. Furthermore, in this way the strength of the non-linearities can be compared.

This section will show the steady flow fields for each test case and the bifurcation behaviour as a function of the freestream speed with the structural parameters as depicted in Table 2.1 with zero structural damping. Three different interpolation methods (linear, cubic spline and polynomial) are again considered for interpolation of the response surface, in order to compare the bifurcation behaviour obtained with these interpolation methods for test cases with other, possibly stronger, sources of non-linearity than that tested in Section 4.3.2. First, inviscid transonic flow is considered in Section 5.2.1. Nested LCOs are observed for this test case. The second test case is in viscous transonic flow with trailing-edge separation. Supercritical bifurcation behaviour with a strong non-linearity is observed, see Section 5.2.2. In subsonic flow at high angle of attack (with trailing-edge separation) a small subcritical bifurcation is observed, with stable and unstable LCOs just below the linear flutter boundary, see Section 5.2.3. Finally, Section 5.2.4 concerns transitional flow in the laminar drag bucket. LCOs are again observed below the flutter boundary.

5.2.1. TRANSONIC INVISCID FLOW

To study the effects of shock dynamics only, a test case at $M = 0.74$ and $\alpha = 0°$ has been selected. The NLR7301 airfoil is simulated at $T_\infty = 273.15$ K and $p_\infty = 101325$ Pa. The steady pressure distribution at these conditions is shown in Figure 5.1. The solid line displays the upper surface and the dashed line the lower surface. A black horizontal line has been drawn at the critical pressure. A strong shock wave is present on the upper surface near 65% of the chord length.

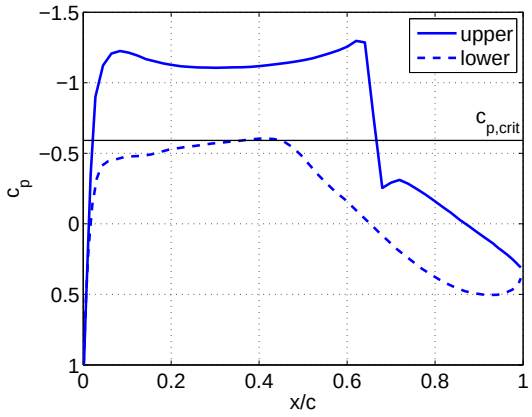

Figure 5.1: Steady pressure distribution at $M = 0.74$, $\tilde{\alpha} = 0°$

Table 5.1 shows the locations of the response surface samples used for the LCO bifurcation analysis with ADePK. A tensor-product grid is built from these locations and CFD simulations are performed at each of the grid points, resulting in 6*4*7*5 = 840 forced motion oscillation simulations. At zero pitch amplitude the response is identically zero and at a reduced frequency of zero, a quasi-steady response is used (difference of two steady simulations at each amplitude). This results in a total of 1120 sample points. The structural properties used for this Mach number variation are those of Dietz et al. [5], see Table 2.1, with zero damping. ADePK, as described in Section 2.5, is applied using linear, cubic spline and polynomial interpolation. Figure 5.2 shows the bifurcation behaviour versus the freestream speed. The flutter mode shape is depicted with a black diamond. From Figure 5.2(a), at small amplitudes, stable LCOs are observed. Then subcritical bifurcation behaviour is observed. Hence, so-called nested LCOs are observed, i.e. a stable and an unstable LCO exist simultaneously. For LCO amplitudes larger than 5°, two stable LCOs and one unstable LCO might exist simultaneously. Since the amplitude ratio is close to 1 and the phase difference has a small positive value, the LCO mode shape is a complex pitch-plunge motion where plunge slightly leads pitch. All interpolation methods show similar results. Note that the velocity range covered by the bifurcation is very small, only about 2 m/s are covered by LCOs of amplitudes up to 5°.

Parameter	Values
Pitch amplitude $\Delta\alpha(^\circ)$	0, 0.1, 0.5, 1, 2, 3, 5
Amplitude ratio $\lvert\theta_{h\alpha}\rvert$	0.01, 0.75, 2, 4
Reduced frequency k	0, 0.1, 0.2, 0.3, 0.4, 0.5, 0.6, 0.7
Phase difference $\phi_{h\alpha}(^\circ)$	5, 10, 50, 100, 150

Table 5.1: Sample points for CFD samples at $M = 0.74$, $\bar{\alpha} = 0^\circ$

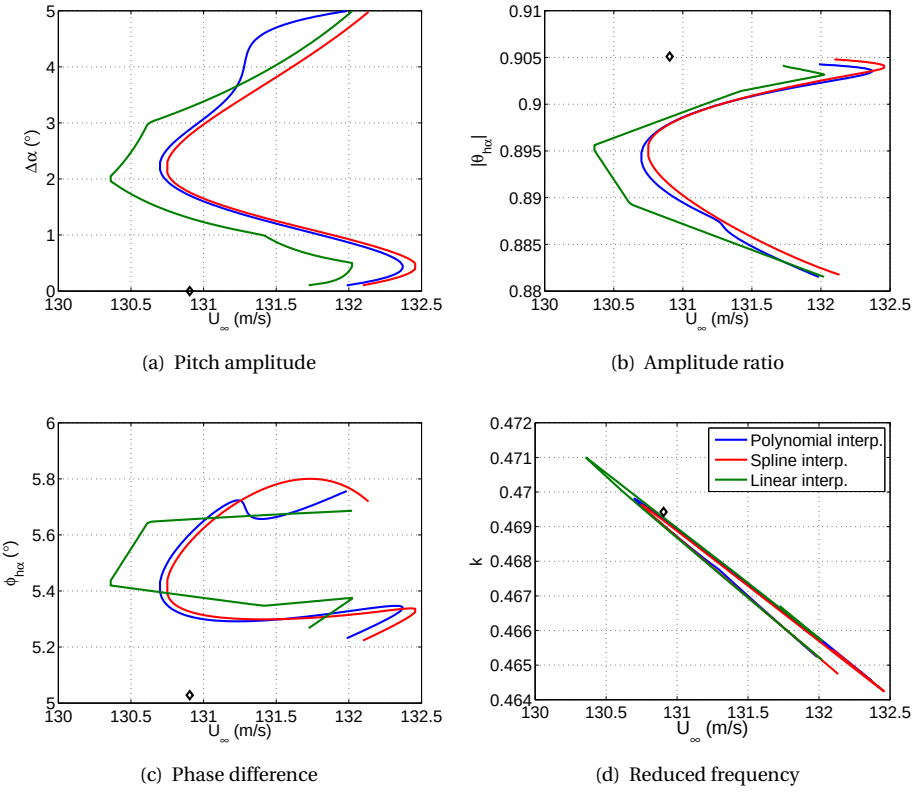

(a) Pitch amplitude

(b) Amplitude ratio

(c) Phase difference

(d) Reduced frequency

Figure 5.2: LCO mode shape vs freestream velocity at $M = 0.74$, $\bar{\alpha} = 0^\circ$

5.2.2. TRANSONIC FLOW WITH TRAILING-EDGE SEPARATION

To investigate the effect of separation on the LCO bifurcation behaviour the NLR7301 airfoil is considered at $M = 0.75$, $\alpha = 0.7^\circ$ and $\mathrm{Re} = 2 \cdot 10^6$. Trailing-edge separation on the upper surface is observed (at $T_\infty = 273.15$ K). Figure 5.3 shows the steady pressure and skin friction distributions at these conditions. A shock wave is present on the upper surface, near the mid-chord position. From the skin friction distribution, Figure 5.3(b), trailing-edge separation is observed on the upper surface.

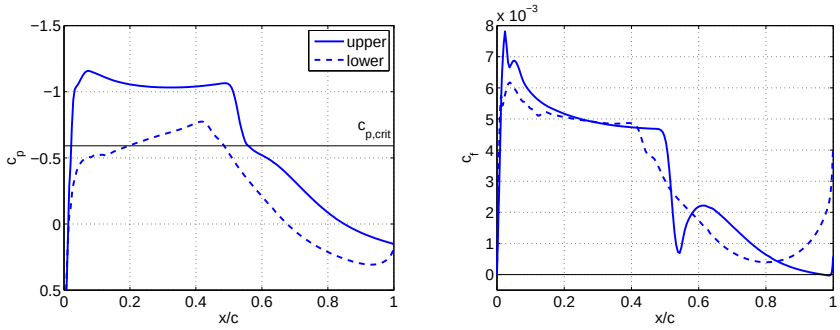

(a) (b)

Figure 5.3: Steady pressure and skin friction distributions at $M = 0.75$, $\alpha = 0.7°$

To study the bifurcation behaviour of the NLR7301 airfoil system at $M = 0.75$ and $\alpha = 0.7°$, the response surface samples as depicted in Table 5.2 are used. Figure 5.4 shows the bifurcation behaviour for this test case using the structural parameters from the wind-tunnel experiments of Dietz et al. [5] (see Table 2.1), except that the structural damping has been set to zero. The results using three different interpolation methods are again shown: linear, cubic spline and polynomial interpolation. All methods result in a supercritical bifurcation. For amplitudes larger than about 4.7° unstable LCOs are observed in case of polynomial interpolation. This is caused by the differences in the interpolated response surface, as also noted in Section 4.3.2. From Figure 5.4 it is seen that the range of the freestream speed covered by the supercritical bifurcation is about 200 m/s. Hence, in comparison to the validation test case (see Figure 4.11(a)) and the inviscid transonic test case (Figure 5.2(a)), the non-linearity is very strong. This behaviour was expected, since the boundary layer will interact with the shock waves. The separation of the boundary layer (both trailing-edge separation and shock-induced separation, which appears at larger angles of attack) will probably cause a reversed shock motion, as described by e.g. Bendiksen [1, 6]. Also, when comparing the aerodynamic forces of forced pitch oscillations with respect to the pitch amplitude at a certain frequency, it was observed that for the viscous case the deviation from the linear value at a certain amplitude is much larger than in the inviscid case at the same amplitude (see also Section 2.4.2). Hence, this explains the stronger non-linearity observed for this viscous test case.

The amplitude ratio of the LCOs also decreases by almost 30% with increasing freestream velocity, see Figure 5.4(b). Furthermore, because of the large velocity range, the phase difference also increases much more than in the previous inviscid cases. The reduced frequency decreases strongly from 0.35 at linear flutter to 0.17 at an LCO amplitude of 5°. Note that the differences in the bifurcation behaviour obtained with the various interpolation methods are small for this test case. However, when considering the same velocity range as for the other test cases, the differences become more noticeable.

Parameter	Values
Pitch amplitude $\Delta\alpha(^\circ)$	0, 0.1, 0.5, 1, 2, 3, 4, 5
Amplitude ratio $\lvert\theta_{h\alpha}\rvert$	0.01, 0.75, 2, 4
Reduced frequency k	0, 0.1, 0.2, 0.3, 0.4, 0.5, 0.6, 0.7
Phase difference $\phi_{h\alpha}(^\circ)$	5, 10, 50, 100, 150

Table 5.2: Sample points for CFD samples at $M = 0.75$, $\bar{\alpha} = 0.7^\circ$

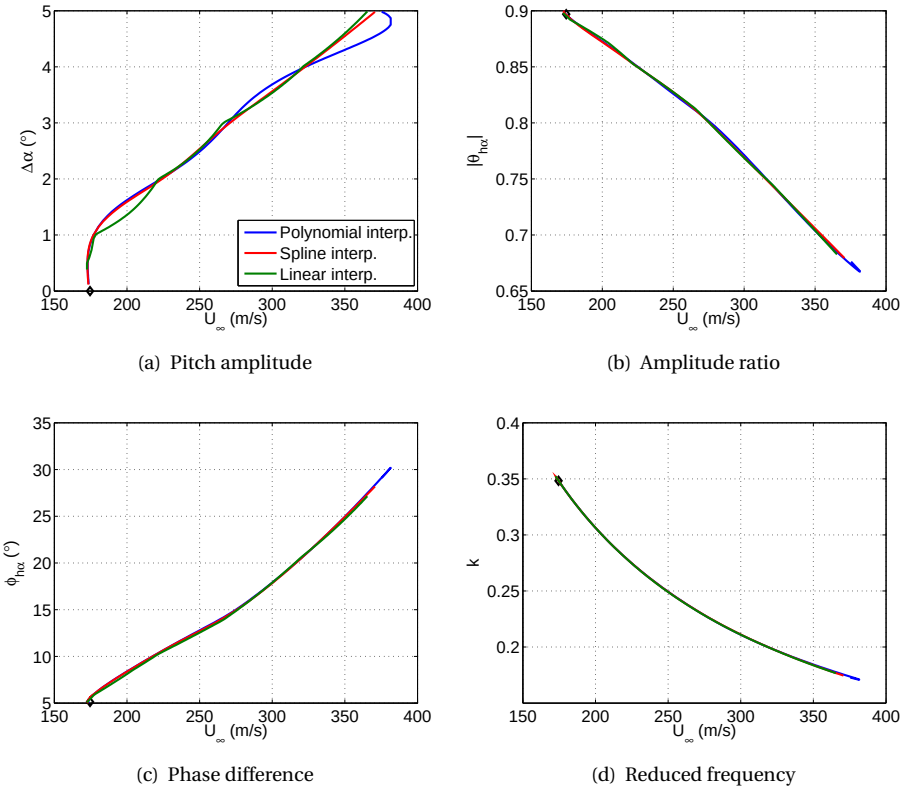

(a) Pitch amplitude

(b) Amplitude ratio

(c) Phase difference

(d) Reduced frequency

Figure 5.4: LCO mode shape vs freestream velocity at $M = 0.75$, $\bar{\alpha} = 0.7^\circ$

5.2.3. SUBSONIC FLOW WITH TRAILING-EDGE SEPARATION

To study non-linearities from trailing-edge separation without shock waves, the NLR7301 airfoil is studied at $M = 0.3$, $\mathrm{Re} = 2 \cdot 10^6$, $\alpha = 9.0^\circ$ and $T_\infty = 273.15$ K. At these conditions, the NLR7301 airfoil is near the maximum lift coefficient, which occurs at 14.4° for this Mach number. This can be seen from Figure 5.5, which shows the lift polar. The flow around the airfoil is completely subsonic at this condition. Figure 5.6 shows the steady pressure and skin friction distributions at these conditions. The pressure distribution

shows a large suction peak near the leading edge on the upper surface. Furthermore, trailing-edge separation is present on the upper surface.

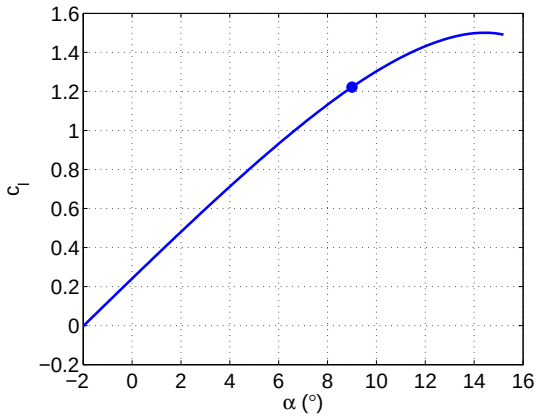

Figure 5.5: Lift polar at $M = 0.3$ and $Re = 2 \cdot 10^6$

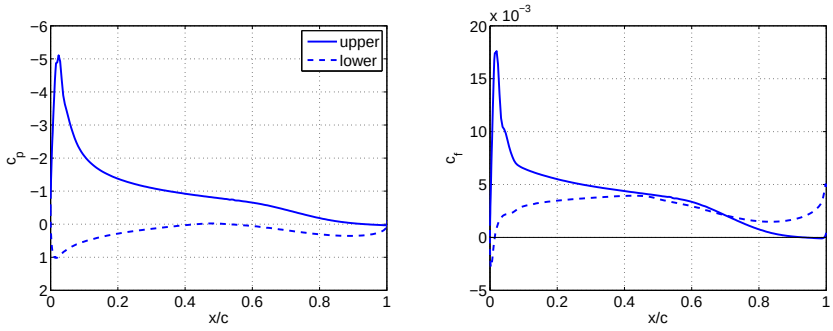

(a) (b)

Figure 5.6: Steady pressure and skin friction distributions at $M = 0.3$, $\bar{\alpha} = 9.0°$

To study the bifurcation behaviour for this test case a response surface has been set up. The sample locations are shown in Table 5.3. The samples have been distributed more evenly in all dimensions for this test case. However, the number of samples in amplitude-direction has been reduced to 6, since using 8 samples resulted in high-order wiggles upon interpolation on the response surface. Figure 5.7 shows the bifurcation diagrams for this test case as function of the freestream speed. The structural model of Dietz et al. [5] (see Table 2.1) has again been used with zero structural damping. Using polynomial or spline interpolation results in almost the same bifurcation behaviour, i.e. a slightly subcritical bifurcation with unstable LCOs with amplitudes just below 1°. Note

Parameter	Values
Pitch amplitude $\Delta\alpha(^\circ)$	0, 0.714, 1.429, 2.857, 3.571, 5
Amplitude ratio $\lvert\theta_{h\alpha}\rvert$	0.01, 1.673, 3.337, 5
Reduced frequency k	0, 0.1, 0.2, 0.3, 0.4, 0.5, 0.6, 0.7
Phase difference $\phi_{h\alpha}(^\circ)$	0, 37.5, 75, 112.5, 150

Table 5.3: Sample points for CFD samples at $M = 0.3$, $\bar{\alpha} = 9.0^\circ$

the freestream velocity range covered is again small, about 10 m/s for polynomial and spline interpolation. The amplitude ratio decreases with increasing freestream speed. The phase difference increases about 2°. The reduced frequency slightly reduces during the bifurcation to an LCO amplitude of 5°.

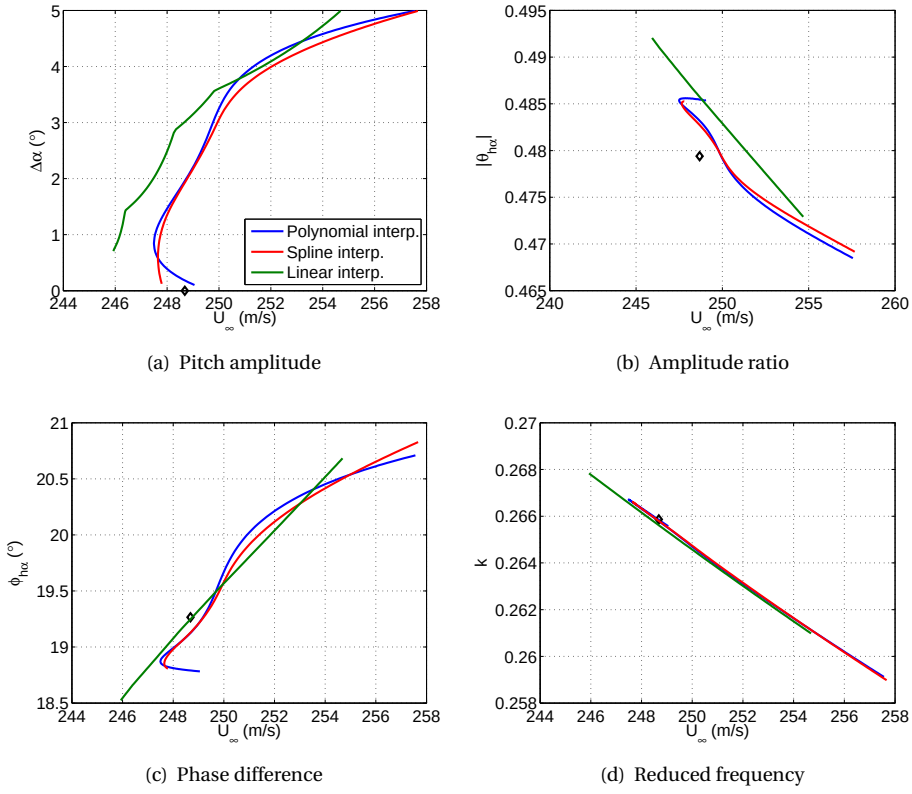

(a) Pitch amplitude

(b) Amplitude ratio

(c) Phase difference

(d) Reduced frequency

Figure 5.7: LCO mode shape vs freestream velocity at $M = 0.3$, $\bar{\alpha} = 9.0^\circ$

5.2.4. SUBSONIC FLOW WITH FREE BOUNDARY-LAYER TRANSITION

To study non-linearities due to boundary-layer transition and separation, the NLR7301 airfoil is studied at $M = 0.3$, $\alpha = -1.3°$, $\mathrm{Re} = 5 \cdot 10^5$ and $T_\infty = 273.15\,\mathrm{K}$. At these conditions, this airfoil is inside the laminar drag bucket when boundary layer transition is free. Figure 5.8 shows the lift-drag polar at $M = 0.3$ for angles of attack from $-10°$ to $10°$. The turbulence intensity has been set to 0.05% near the airfoil's nose. Inside the laminar drag bucket the drag coefficient is much lower in case of transitional flow than for a fully turbulent flow (with forced transition near the leading edge), at the same lift coefficient. The drag bucket is caused by jumps in the transition location. Figure 5.9 shows the separation and transition locations versus the angle of attack for both upper and lower surface. The start of the drag bucket at negative lift coefficients (i.e. at negative angles of attack) is caused by a disappearing separation bubble on the lower surface near the leading edge and a separation bubble that develops on this surface just behind the mid-chord position. This causes the transition location to jump from near the leading edge (downstream of the separation bubble) to behind the mid-chord position on the lower surface. The drag buckets ends due to an appearing separation bubble near the leading edge on the upper surface, which causes a more upstream transition location and hence a jump compared to the transition location inside the drag bucket, which is much more downstream on the upper surface. The transition location was determined here as the local maximum in the skin friction coefficient-distribution that occurs downstream of the separation bubble. This approach was verified by comparing several skin friction distributions in case of free transition with those that occur in fully turbulent flow (see also Figure 5.10(b)). In case of two separation bubbles (at large negative angles of attack), transition was found to occur behind the first separation bubble, since the largest increase in skin friction coefficient occurs there.

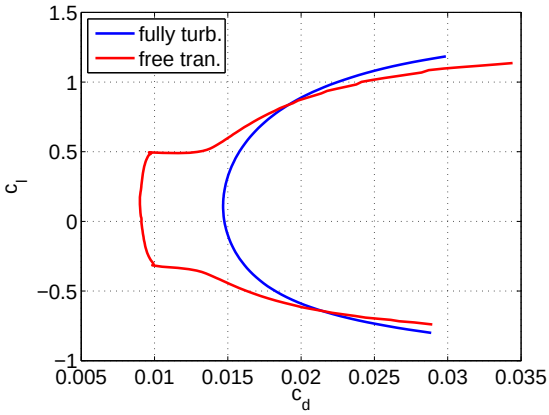

Figure 5.8: Lift-drag polar at $M = 0.3$, $\mathrm{Re} = 5 \cdot 10^5$ and Tu = 0.05% in fully turbulent and transitional flow

Figure 5.10 shows the steady pressure and skin friction distributions in both fully turbulent and transitional flow at an angle of attack of $-1.3°$. The blue lines depict the fully

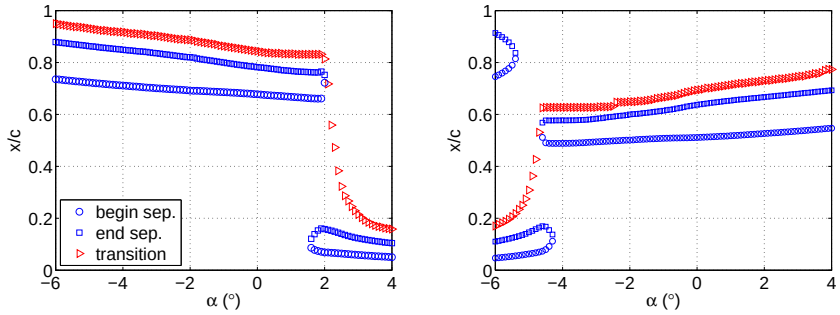

(a) Upper surface (b) Lower surface

Figure 5.9: Separation and transition locations versus angle of attack at $M = 0.3$, $\mathrm{Re} = 5 \cdot 10^5$ and Tu = 0.05% in transitional flow

turbulent case and the red lines the free transition case. This angle of attack is in the middle of the laminar drug bucket. The pressure distributions for both cases are nearly identical with a small shift. The skin friction distributions in Figure 5.10(b) show no separation in the fully turbulent case. In case of free boundary layer transition a separation bubble occurs on both upper and lower surface. On the upper surface it starts at about $x/c = 0.68$ and ends at $x/c = 0.8$. On the lower surface it starts at $x/c = 0.5$ and ends at $x/c = 0.6$. Transition occurs at reattachment on both surfaces. An angle of attack of $-1.3°$ was selected for further investigations into the LCO behaviour, because jumps in the transition locations are likely to be a type of aerodynamic non-linearity that will lead to limit-cycle oscillations.

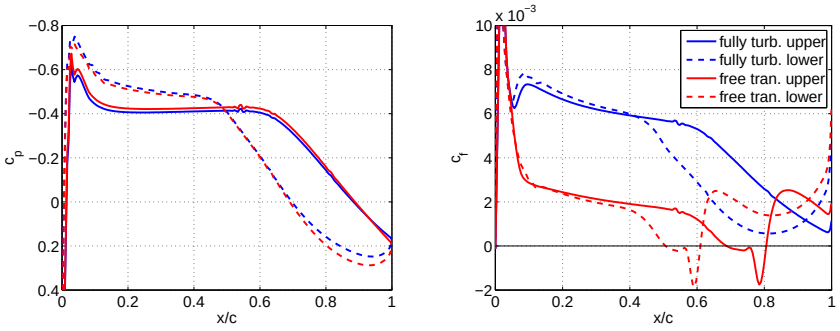

(a) (b)

Figure 5.10: Steady pressure and skin friction distributions at $M = 0.3$, $\bar{\alpha} = -1.3°$, $\mathrm{Re} = 5 \cdot 10^5$ and Tu = 0.05% in fully turbulent and transitional flow

For this test case the response surface used to study the bifurcation behaviour is set up with less samples than for the other test cases, because of the high computational effort

necessary (the number of pseudo time steps is very large compared to the fully turbulent case, i.e. 2.5 times larger). Table 5.4 shows the samples used to set up the response surface. No amplitudes larger than 3° have been selected, because of even larger number of pseudo time steps necessary for convergence at large amplitudes in case of free boundary layer transition (six times more than in the fully turbulent case).

Parameter	Values
Pitch amplitude $\Delta\alpha(^\circ)$	0, 0.1, 0.5, 1, 2, 3
Amplitude ratio $\lvert\theta_{h\alpha}\rvert$	0.01, 0.75, 4
Reduced frequency k	0, 0.1, 0.2, 0.3, 0.4
Phase difference $\phi_{h\alpha}(^\circ)$	5, 50, 150

Table 5.4: Sample points for CFD samples at $M = 0.3$, $\bar{\alpha} = -1.3^\circ$

Figure 5.11 shows the bifurcation diagrams for this test case. As is seen from Figure 5.11(a) unstable LCOs with an amplitude of up to 0.4° exist, i.e. the bifurcation is slightly subcritical. All interpolation methods show similar results. The velocity range covered about 3 m/s. Hence, the non-linearity is rather weak compared to the transonic viscous test case (see Figure 5.2(a)). The LCO amplitude ratio slightly decreases with increasing freestream speed, whereas the phase difference slightly increases. The reduced frequency is almost constant.

Figure 5.12 shows a comparison of the bifurcation behaviour in transitional and fully turbulent flow (using cubic spline interpolation). The freestream velocity has been normalised by the flutter velocity in order to be able to directly compare the bifurcation behaviour. The response surface has been built using the same sample points in fully turbulent case as in the transitional case. The LCO amplitude shows very similar behaviour in the fully turbulent case. Hence, for the flow conditions and amplitude range considered here, boundary-layer transition and/or separation does not seem to be the cause of the LCO bifurcation behaviour. However, it is expected that for larger amplitudes deviations in the bifurcation behaviour will occur, as for larger amplitudes angles of attack outside of the drag bucket angles will be reached. The LCO mode shape also shows similar behaviour for the fully turbulent case. Note from the scale in Figure 5.12 that the differences in the mode shape values are minimal.

5.2.5. CONCLUSIONS

This section has addressed the bifurcation behaviour of LCOs caused by various sources of aerodynamic non-linearity. These sources of non-linearity have been investigated previously by other researchers, see Section 1.3. However, none of these investigations have found subcritical bifurcations except in inviscid transonic flow. Furthermore, these different aerodynamic non-linearities have not been studied for a single airfoil as in this thesis work. By considering these various sources of aerodynamic non-linearity in parallel, the strength of the non-linearities could be compared directly. Based on the results shown in this section, the non-linearity was found to be the strongest in the case of viscous transonic flow, which is reflected in the supercritical bifurcation behaviour with a small slope. Upon comparing this with the transonic inviscid flow test case, it is seen that

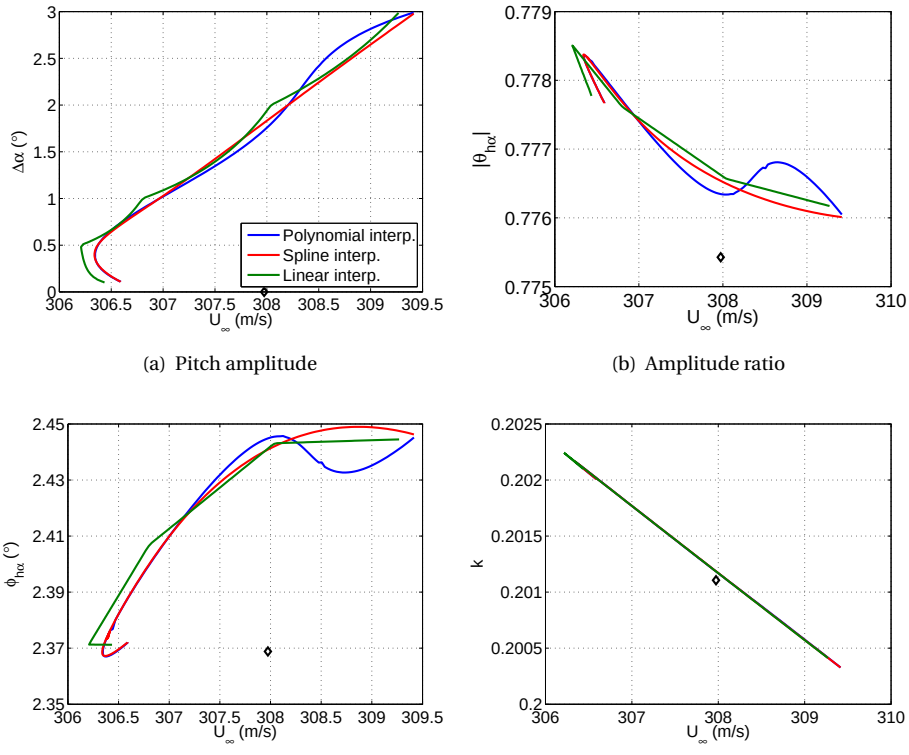

(a) Pitch amplitude

(b) Amplitude ratio

(c) Phase difference

(d) Reduced frequency

Figure 5.11: LCO mode shape vs freestream velocity at $M = 0.3$, $\bar{\alpha} = -1.3°$, Re $= 5 \cdot 10^5$ and Tu $= 0.05\%$ in transitional flow

5

the non-linearity observed in that case is almost negligible, although it should be noted that a slightly different Mach number and angle of attack were considered, so a direction comparison cannot be made. However, the results of Section 5.3 which considers several Mach numbers in inviscid flow also suggest a weaker non-linearity. A weak non-linearity is much more dangerous than a strong non-linearity as the LCO amplitude grows much faster with freestream velocity (in case of linear flutter infinitely fast). This behaviour is expected, since in the viscous case the the shock interacts with the boundary layer, resulting in for example a reversed shock motion, see e.g. Bendiksen [1, 6] who outlines the differences between viscous and inviscid unsteady transonic flow. Furthermore, similar observations with regard to the bifurcation behaviour were made by Thomas et al. [7], who directly compared the bifurcation behaviour of the NLR7301 airfoil in inviscid and viscous transonic flow as well. They observed a stronger shock in the inviscid case. In contrast to the results of Thomas et al. [7], nested LCOs were found for the inviscid test case investigated here (see Section 5.2.1), i.e. a sudden disturbance of large enough amplitude causes a jump to another stable LCO. Kholodar et al. [3] also observed subcritical

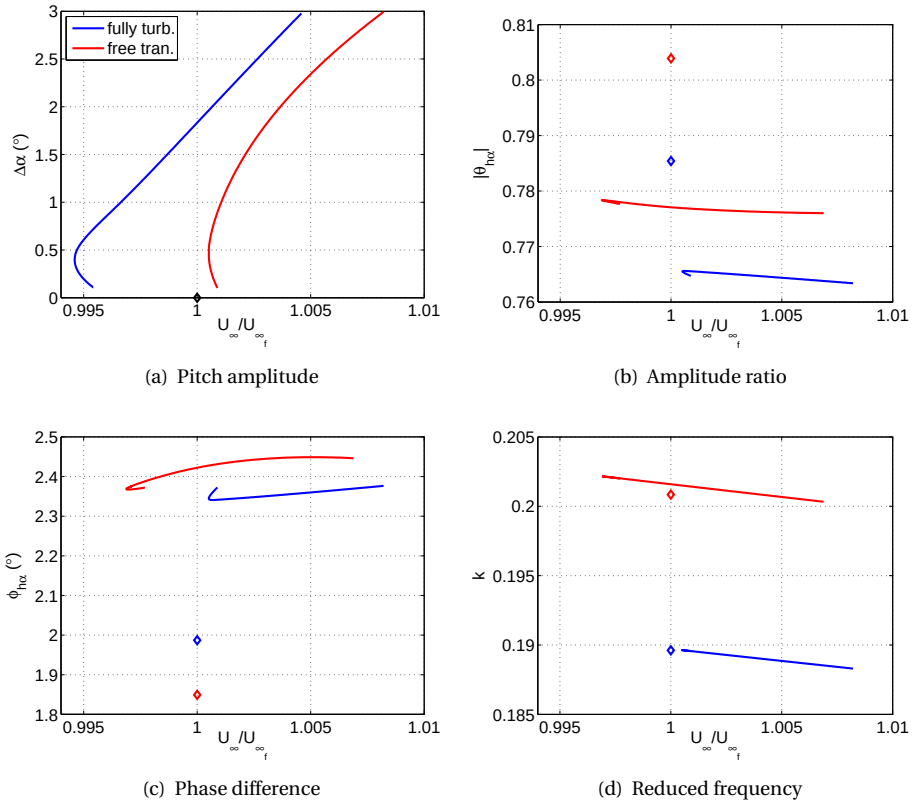

(a) Pitch amplitude

(b) Amplitude ratio

(c) Phase difference

(d) Reduced frequency

Figure 5.12: LCO mode shape vs normalised freestream velocity at $M = 0.3$, $\bar{\alpha} = -1.3°$, Re $= 5 \cdot 10^5$ and Tu $=$ 0.05% in fully turbulent and transitional flow

bifurcations for the NACA 64A010A airfoil in inviscid flow (at different freestream conditions and with a different structural model as used in this thesis though).

The subsonic flow test cases shown in this section exhibit a slightly subcritical bifurcation with unstable LCO amplitudes below the linear flutter boundary of up to about 0.5° in case of cubic spline interpolation. This agrees with the findings of Poirel and Mendes [4], since they did not observe (stable) LCO amplitudes smaller than 2° for the NACA0012 in transitional flow either. However, Poirel and Mendes considered different conditions. In Section 5.2.4 similar bifurcation behaviour of the LCO amplitude up to 3° was found in both transitional and fully turbulent flow. This suggests that the laminar separation bubbles and the transition of the boundary layer are not the cause of the limit-cycle oscillation for the transitional test case considered in this thesis. This is in contrast to the findings of Poirel et al. [4, 8–10] and Yuan et al. [11], who did not observe limit-cycle oscillations when a transition strip was applied. However, further investigations into the behaviour of the aerodynamic forces in both transitional and fully turbulent flow are necessary to investigate this in more detail.

The bifurcation behaviour obtained in subsonic flow with trailing-edge separation did not agree with the findings of recent measurements by Razak et al. [12] who studied the NACA0018 airfoil at high angles of attack. They observed supercritical bifurcation behaviour of the LCO amplitude caused by classical bending-torsion coupling at an angle of attack of 11° in contrast to the slightly subcritical bifurcation observed in Section 5.2.3. However, these measurements were at much lower airspeeds. At larger mean angles of attack Razak et al. [12] observed non-linear stall flutter, which happens due to the highly non-linear behaviour of the aerodynamic forces caused by dynamic stall, instead of due almost linear aerodynamic forces and bending-torsion coupling [12, 13] and hence those results are not relevant here.

The observations made in this section already (partly) answered the main research question of this thesis, i.e. whether subcritical bifurcations can exist, especially in a viscous flow. This issue will be further addressed in Sections 5.3 and 5.4.

5.3. MACH NUMBER VARIATION IN INVISCID FLOW

Small-amplitude limit-cycle oscillations have been observed during wind-tunnel experiments ([5, 14–16]) at transonic Mach numbers (at low mean angles of attack) for the NLR7301 airfoil. No LCOs with amplitudes smaller than 2° (which was defined as small by [15]) were observed for the NACA0012 airfoil [14, 15] in transonic flow. Schewe et al. [15] suggested two mechanisms that cause these differences; oscillating shock waves or trailing-edge separation. Section 5.2 showed that LCOs with amplitudes smaller than 2° can also occur even in subsonic flow. Therefore, in order to investigate whether these small-amplitude LCOs are the rule or the exception for the NLR7301 airfoil, the linear and non-linear flutter behaviour for several Mach numbers is computed with the conventional p-k method and with ADePK in inviscid flow. Kholodar et al. [2, 3] performed a similar study for the NACA64A010A airfoil. The results obtained here will be compared to those of Kholodar et al. [2, 3].

The flow is represented by the Euler equations in the standard atmosphere at sea level (T_∞ = 273.15 K and p_∞ = 101325 Pa). The mean angle of attack is 0°. The structural properties of Dietz et al. [5] are used as depicted in Table 2.1 (with zero structural damping however). At each Mach number a response surface is set up to determine the bifurcation behaviour, the samples used are depicted in Table 5.1. ADePK with cubic spline interpolation has been used to determine the bifurcation behaviour of the LCO solution.

5.3.1. FLUTTER BEHAVIOUR

Figure 5.13 shows the flutter speed U_{∞_f} versus the Mach number at a mean angle of attack of 0°. The flutter speed decreases with increasing Mach number, at transonic Mach numbers a minimum is reached, the so-called “transonic dip”. The flutter boundary shown in Figure 5.13 shows two transonic dips, at M = 0.72 and at M = 0.78. The heave mode was the first mode to become unstable for all Mach numbers. At Mach numbers of 0.76 and larger the second mode, the pitch mode, becomes unstable as well. However, this occurs at much higher freestream velocity then the heave mode. Such a flutter boundary is typical for Euler-based flow calculations [17]. A similar-shaped flut-

ter boundary was found by Yang et al. [17] and Hall et al. [18] for the NACA 64A010 airfoil. The secondary unstable mode disappears in viscous flow. Therefore, in this section only the first unstable mode will be considered in the study of the LCO behaviour of the NLR7301 airfoil.

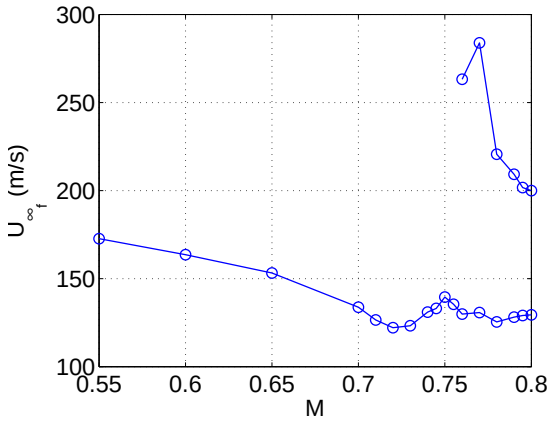

Figure 5.13: Flutter speed as a function of Mach number at $\bar{\alpha} = 0°$ in inviscid flow

Usually the location of the transonic dip can already be seen from the quasi-steady lift-curve slope versus Mach number (see [19]). Therefore, Figure 5.14 shows this lift-curve slope versus the Mach number at an angle of attack of 0°. The slope has been computed using two steady flow simulations at $\pm 10^{-3}°$. The theoretical value of the lift-curve slope (2π per radian) has been corrected by the Prandtl-Glauert correction and is depicted in Figure 5.14(c) by the red dashed line. The moment-curve slope has also been determined and is plotted in Figure 5.14(d). It is seen that the lift-curve slope is much larger than its theoretical value, as expected. The deviation increases with increasing Mach number. At $M = 0.72$ the lift-curve slope obtains a maximum. This coincides with the first minimum in the flutter boundary. For Mach numbers larger than 0.75, the lift-curve slope shows a maximum at $M = 0.78$, the location of the second transonic dip. The moment-curve slope also obtains a maximum at $M = 0.72$. It is even positive, hence statically unstable, for this Mach number. However, at $M = 0.78$ no extreme is observed in the moment-slope curve.

Figure 5.15 shows the reduced frequency, amplitude ratio and phase difference at flutter versus the Mach number at a mean angle of attack of 0°. The reduced frequency at flutter k_f increases with increasing Mach number and shows the opposite behaviour of the freestream speed, since a maximum is obtained at $M = 0.72$ and $M = 0.78$. This is expected since the reduced frequency is the product of the angular velocity, chord length and the reciprocal of the freestream velocity ($k = \omega c / U_\infty$). The amplitude ratio at flutter $|\theta_{h\alpha}|_f$ increases from 0.72 at $M = 0.55$ to about 0.9 at transonic Mach numbers. Similar behaviour was observed by Kholodar et al. [2, 3] for the amplitude ratio at flutter at an ω_h/ω_α of 0.8 for the NACA64A010A airfoil. (Here $\omega_h/\omega_\alpha = 0.70$.) The phase difference

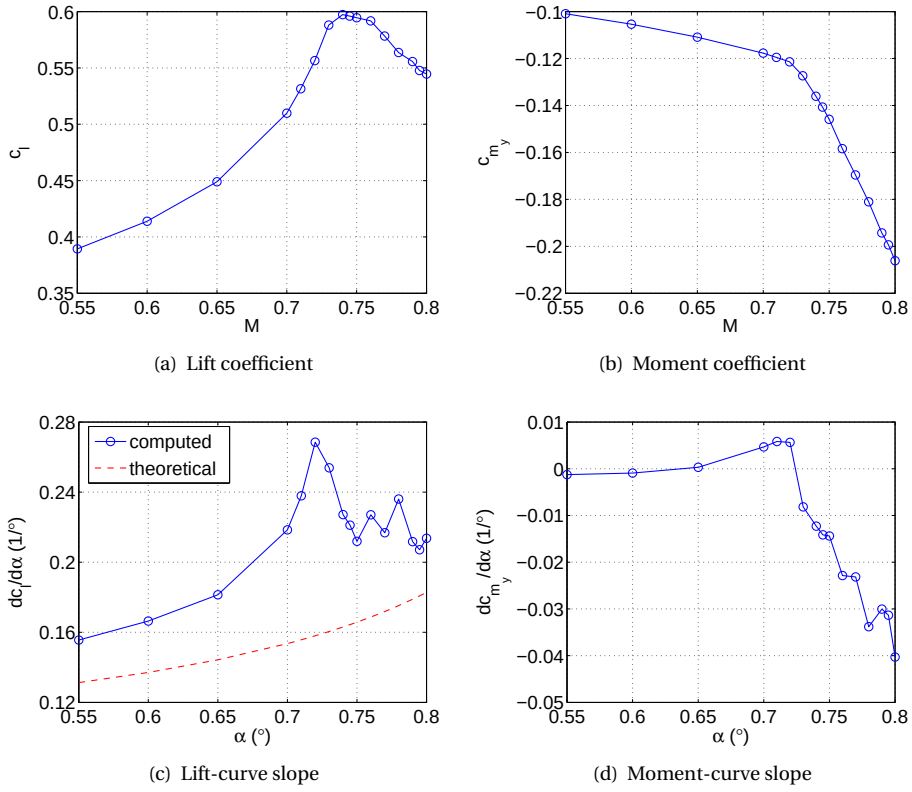

(a) Lift coefficient

(b) Moment coefficient

(c) Lift-curve slope

(d) Moment-curve slope

Figure 5.14: Lift and moment coefficient and lift-curve and moment-curve slope as a function of Mach number at $\bar{\alpha} = 0°$ in inviscid flow

between pitch and plunge at flutter $(\phi_{h\alpha})_f$, increases from about 9° at $M = 0.55$ to about 15° at $M = 0.71$ and then decreases until to almost 0° at $M = 0.8$. Hence, the lag of the pitching motion w.r.t. the plunging motion first increases, and then decreases again.

5.3.2. LCO BIFURCATION BEHAVIOUR

ADePK has been used to compute the bifurcation behaviour at several Mach numbers ($M = 0.55$, 0.6, 0.65, 0.7, 0.72, 0.74, 0.75 and 0.8). Figure 5.16 shows contours levels of the LCO amplitude at several Mach numbers versus the freestream velocity. The flutter boundary has also been included (zero amplitude). Stable LCOs are shown with circles and unstable LCOs with squares. The dashed lines connect the unstable LCOs and the full lines the stable LCOs. It is observed that at subsonic Mach numbers the contour lines are much closer than near the transonic dip. This means that the bifurcation diagrams are much steeper at subsonic Mach numbers than near the transonic dip. Furthermore, when LCOs of a certain amplitude are allowed, for example with an amplitude of 3°, the transonic dip would be less deep than in case of flutter (zero amplitude). Hence, the non-

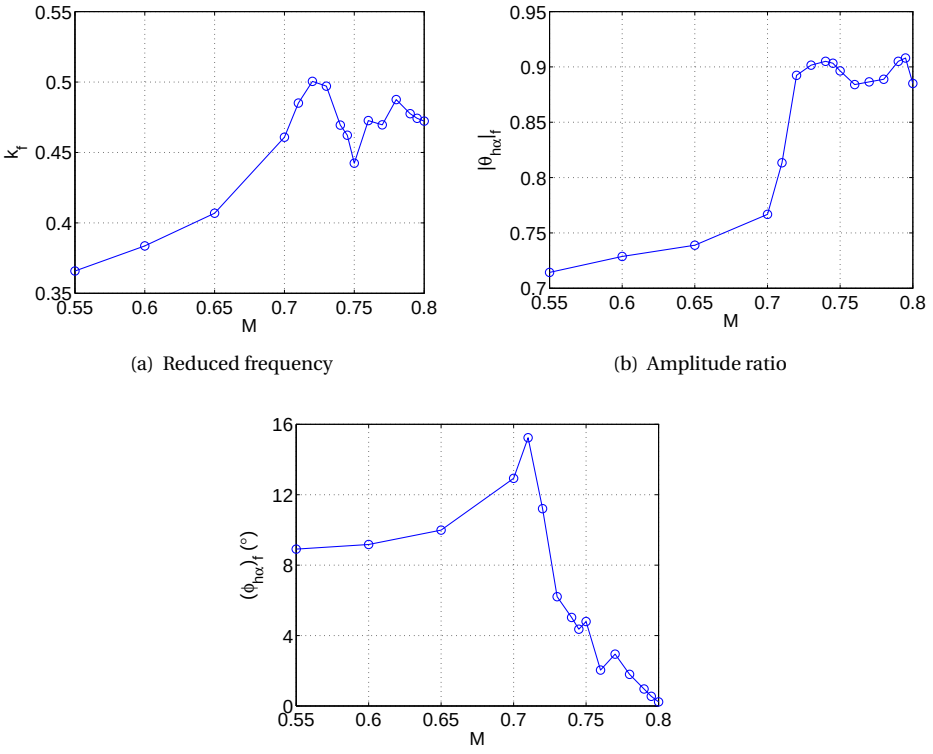

(a) Reduced frequency

(b) Amplitude ratio

(c) Phase difference

Figure 5.15: Reduced frequency, amplitude ratio and phase difference as a function of Mach number at $\bar{\alpha} = 0°$ in inviscid flow

5

linearity is much stronger at $M = 0.72$ and $M = 0.75$ than at $M = 0.55$, 0.6 and 0.65. This can be seen more clearly from the bifurcation diagrams shown in Figure 5.17. This figure shows the LCO mode shape versus the freestream velocity. The bifurcation of the LCO amplitude is supercritical for the smallest two Mach numbers ($M = 0.55$ and 0.6). Then it becomes subcritical with increasing Mach number, i.e. for $M = 0.65$ and $M_\infty = 0.7$. The bifurcation becomes supercritical again when further increasing Mach number. At $M = 0.74$ multiple stable and unstable LCOs exists. At $M = 0.75$ the bifurcation is subcritical as well, with stable LCOs of noticeable amplitude (up to 5°) that occur below the flutter boundary. This is also seen in Figure 5.16. At $M = 0.8$ the bifurcation is supercritical. Figure 5.17(b) shows that amplitude ratio decreases during the bifurcation for most Mach numbers, except for $M = 0.7$. Hence, the LCO mode shape becomes slightly more pitch-dominated during the bifurcation of the LCO solution. Only at $M_\infty = 0.7$ the motion tends to become a more complex pitch-plunge motion. This is also depicted in Figure 5.18, which shows the phase difference versus the amplitude ratio. From Figure 5.17(c), the phase difference increases with freestream speed for Mach numbers up to

0.6. At $M = 0.65$ it increases with decreasing freestream velocity, whereas for $M = 0.72$ it decreases with increasing U_∞. For $M = 0.7$ and the largest three Mach numbers the phase difference shows a more complex bifurcation behaviour. The same holds for the amplitude ratio at these Mach numbers. The bifurcation behaviour of the reduced frequency, shown in Figure 5.17(d), is dictated by its inverse relationship with the freestream velocity.

Upon comparing the results obtained here with the Mach number variations performed by Kholodar et al. [2, 3], it is noted that they observed, at an ω_h/ω_α of 0.8, unstable LCOs (up to 7°) for Mach numbers far below the transonic dip (which is at about $M = 0.8$ in their case), whereas for the NLR7301 airfoil at $M = 0.55$ and $M = 0.6$ stable LCOs are observed. Closer to the transonic dip and in the transonic dip region itself, i.e. in the Mach number range from 0.78 to 0.85, Kholodar et al. [2, 3] observed supercritical bifurcations for the NACA64A010A airfoil as also observed here (i.e. at $M = 0.72$). Directly after the dip the LCOs became unstable again and then stable again for the NACA64A010A airfoil, as for the NLR7301 airfoil. Hence, except for the supercritical bifurcation behaviour for subsonic Mach numbers, the NLR7301 and the NACA64A010A airfoil seem to exhibit similar bifurcation behaviour close to the flutter boundary.

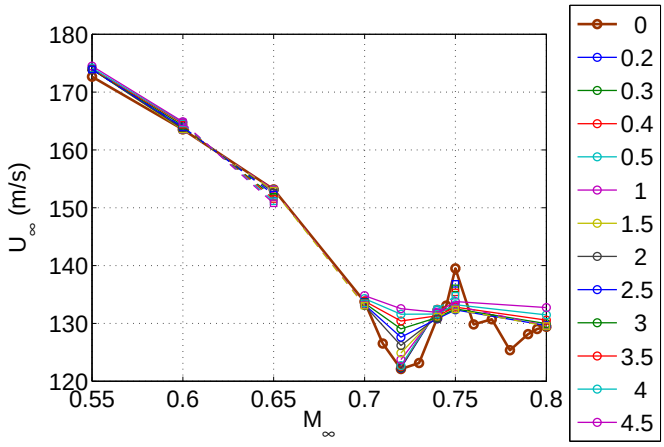

Figure 5.16: Flutter speed and LCO amplitude contours as a function of Mach number at $\bar{\alpha} = 0°$ in inviscid flow

Figures 5.16 and 5.17 show that the linear flutter boundary is significantly changed when aerodynamic non-linearities are taken into account. When LCO amplitudes of up to 4.5° are considered, the transonic dip is significantly less deep. It is expected that LCOs of higher amplitude will make the dip disappear altogether. Furthermore, small-scale LCOs are observed for all Mach numbers. However, they occur much close to the flutter boundary for subsonic Mach numbers. Hence, the bifurcation is much steeper for these Mach numbers and the non-linearity smaller than for transonic Mach numbers.

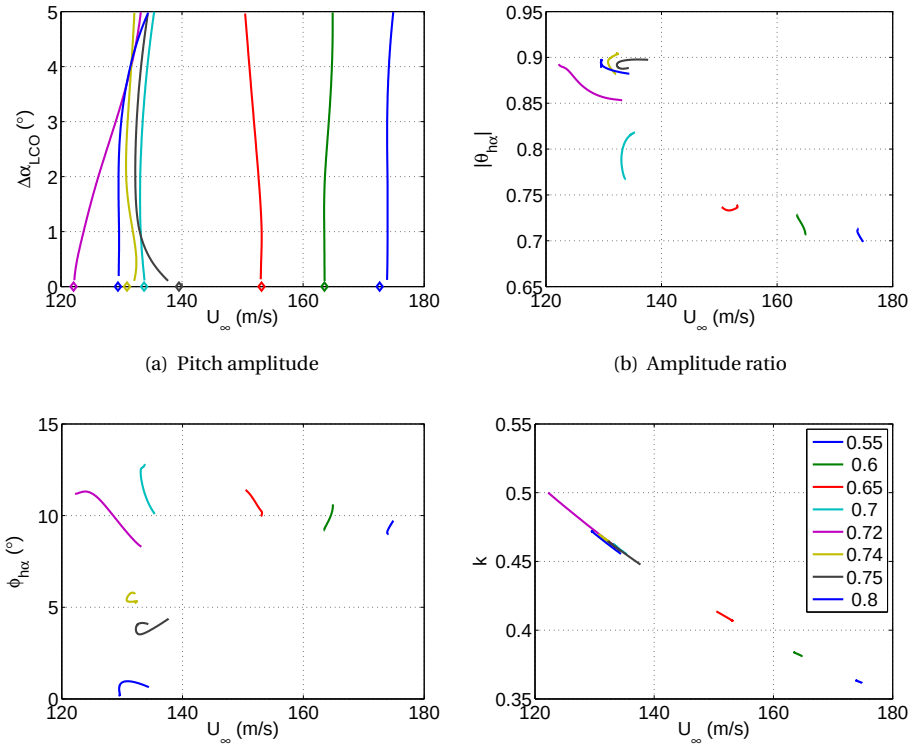

(a) Pitch amplitude

(b) Amplitude ratio

(c) Phase difference

(d) Reduced frequency

Figure 5.17: LCO mode shape vs freestream velocity for various Mach numbers for Euler simulation at $\bar{\alpha} = 0°$

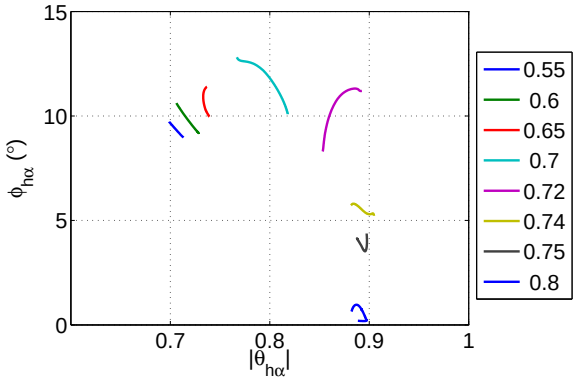

Figure 5.18: LCO phase difference versus the amplitude ratio for various Mach numbers at $\bar{\alpha} = 0°$ in inviscid flow

5.3.3. CONCLUSIONS

This section has investigated the effect of the Mach number on the bifurcation behaviour of the LCO solution. It was observed that LCOs of small amplitude as defined by Schewe et al. [15] can occur at both subsonic and transonic Mach numbers in inviscid flow. Furthermore, when following the contour lines of constant LCO amplitude, the flutter boundary is located at significantly higher velocities at the location of the transonic dip in the non-linear case. For subsonic Mach numbers, the non-linearity is much smaller than for Mach numbers near the transonic dip, as already observed in Section 5.2. For Mach numbers just below the transonic dip (at $M = 0.65$ and $M = 0.7$) as well just above the transonic dip (at $M = 0.74$ and $M = 0.7$) subcritical bifurcation behaviour of the LCO amplitude is observed, whereas supercritical bifurcation behaviour exists at the location of the transonic dip (at $M = 0.72$) and in subsonic flow (at $M = 0.5$ and $M = 0.6$). This is in contrast to the observations of Kholodar et al. [2, 3] who observed only unstable LCOs for subsonic Mach numbers for the NACA64A010A airfoil in inviscid flow. However, near the transonic dip the bifurcation behaviour of the LCO amplitude seems to be similar to that of the NACA64A010A airfoil.

5.4. STRUCTURAL PARAMETER VARIATION

During the initial design phase of an aircraft the structural parameters are not known in detail. Furthermore, the structural model can be epistemically uncertain even after final design. In addition, subcritical bifurcations of the LCO solution might occur for certain structural parameter values. Therefore, it is important to study the effect of a variation in the structural model. In this section the effect of structural parameter variations on the bifurcation behaviour of the limit-cycle oscillations of the NLR7301 airfoil experiencing various aerodynamic non-linearities is studied. Section 4.3.3 already demonstrated the capabilities of ADePK for the study of structural model variations. Only a few researchers have studied the effect of structural parameter variations as noted in Section 5.1 and Section 1.3.2. In this section all aerodynamic sources of non-linearity of Section 5.2 are used as an input to ADePK. Due to the decoupling of fluid and structure, the structural model can be varied without performing new CFD simulations. However, in this thesis it has been assumed that the equilibrium position of the system is independent of the structural parameters, see Section 2.5.5. All results shown in this section have been computed using cubic spline interpolation of the response surface.

The results of a variation in the structural uncoupled natural frequency ratio ω_h/ω_α are shown first in Section 5.4.1. It is observed that the bifurcation behaviour of the LCO amplitude can change from supercritical to subcritical or the other way around when the structural frequency ratio is increased. Furthermore, the pitch- or plunge domination of the mode shape is found to be independent of the stability of the LCOs or the type of bifurcation that occurs. Second, the effect of variations in the mass ratio is studied in Section 5.4.2. In transonic viscous flow the non-linearity becomes weaker with decreasing mass ratio and hence the slope of the bifurcation diagram decreases, however the type of bifurcation of the LCO amplitude does not change when the mass ratio is varied. Only when the non-linearity is already very weak, i.e. when the bifurcation behaviour is close to the linear flutter behaviour, a change of bifurcation type might occur under a variation of the mass ratio. See Sections 5.4.2 and D.1.1 for more details. Third, the

effects of structural damping on the LCO bifurcation behaviour are addressed in Section 5.4.3 (and in Section D.1.2). As for the mass ratio variation, adding structural damping changes the strength of the non-linearity and hence the slope of the bifurcation diagram. However, only in case of weakly non-linear bifurcation behaviour of the LCO amplitude, the bifurcation type changes from supercritical to subcritical for example. Fourth, the bifurcation behaviour due to a variation in the location of the elastic axis is investigated in Section 5.4.4. In comparison to the effects of a mass ratio variation and the addition of various structural damping values, the influence of the elastic axis location on the bifurcation behaviour of the LCO amplitude and mode shape is more significant. A change of the bifurcation type from supercritical to subcritical (in viscous flow) or the other way around (in inviscid flow) is achieved sooner than in case of a mass ratio or structural damping variation, when the non-linearity is weak. Finally, conclusions about the effects of the structural parameter variations on the bifurcation behaviour of the LCO solution are drawn.

5.4.1. STRUCTURAL FREQUENCY RATIO

The structural uncoupled natural frequency ratio, or structural frequency ratio (SFR) for short, has been varied from 0.49 to 1.21 for all aerodynamic sources of non-linearity. In order to achieve this, the plunge stiffness K_h has been changed. The remaining structural parameters are constant. Their values are given in Table 2.1. The structural damping has been set to zero.

TRANSONIC INVISCID FLOW

Figure 5.20 shows the bifurcation diagrams of the LCO mode shape parameters and the LCO reduced frequency versus the freestream speed U_∞ for the NLR7301 airfoil in inviscid flow at $M = 0.74$ and $\bar{\alpha} = 0°$. Figure 5.20(e) shows the phase difference versus the amplitude ratio. Figure 5.19 shows the LCO amplitudes versus the freestream speed normalised by the flutter speed. From this diagram it is immediately clear that for small values of ω_h/ω_α the bifurcation is subcritical. For larger SFRs, the bifurcation is supercritical. For these large SFRs, the slope of the bifurcation diagram decreases with increasing SFR. This indicates that the non-linearity becomes larger when the SFR is increased from 0.74 to 1.21. For the small SFRs the strength of the non-linearity decreases with increasing SFR. From Figure 5.20(b), the amplitude ratio $|\theta_{h\alpha}|$ decreases with increasing SFR. During the bifurcation, the amplitude ratio decreases with freestream speed for SFRs from 0.83 till 1.04. For larger SFRs, $|\theta_{h\alpha}|$ increases with increasing U_∞, whereas for smaller SFRs, the amplitude ratio shows a more complicated bifurcation behaviour. The phase difference $\phi_{h\alpha}$ first decreases somewhat with SFR, but then it increases up to about 110° at $\omega_h/\omega_\alpha = 1.21$. For $\omega_h/\omega_\alpha \geq 0.74$, $\phi_{h\alpha}$ increases during the bifurcation. For smaller SFRs, the bifurcation behaviour of $\phi_{h\alpha}$ is more complicated. The reduced frequency at flutter increases up to an SFR of 0.90, then it decreases with increasing SFR. This is caused by the inverse relation of the reduced frequency with the freestream velocity. This relation also dictates the bifurcation behaviour of the reduced frequency (as a function of the freestream velocity).

As expected because of the structural frequency ratio values, Figure 5.20(e) shows a plunge dominated mode shape for small SFRs with a large amplitude ratio and a pitch

dominated mode shape for large SFR (with an amplitude ratio $\ll 1$). For the test case considered here, i.e. shown in Figure 5.20, at small SFRs a subcritical bifurcation occurs that has a plunge dominated mode shape, whereas the pitch dominated cases are supercritical. This is in contrast to the validation test case where the plunge dominated cases showed stable LCOs only, i.e. a supercritical bifurcation behaviour (see Figure 4.14). Furthermore, the pitch dominated cases are supercritical in inviscid flow at $M = 0.74$, $\bar{\alpha} = 0°$ (Figure 5.20), whereas for the validation test case (Figure 4.14) they show subcritical bifurcation behaviour. Kholodar et al. [3] observed similar behaviour as for the validation test case, i.e. supercritical bifurcations which are plunge dominated at $\omega_h/\omega_\alpha = 0.5$ and subcritical bifurcations which are pitch dominated at $\omega_h/\omega_\alpha = 1.8$ for the NACA64010A airfoil in inviscid flow. To further investigate these differences in bifurcation behaviour, the structural frequency ratio of the NLR7301 airfoil was varied for two other Mach numbers in inviscid flow. From a SFR-variation of the NLR7301 airfoil at $M = 0.75$, $\bar{\alpha} = 0°$ in inviscid flow, unstable LCOs with a plunge- as well as a pitch dominated mode shape were found as well. For $M = 0.72$, $\bar{\alpha} = 0°$ on the other hand, plunge dominated LCO solutions that undergo supercritical bifurcations were observed at small SFRs. These observations suggest that there is no correlation between the type of bifurcation (i.e. supercritical or subcritical) that occurs and the mode shape (i.e. pitch- or plunge-dominated) in inviscid flow.

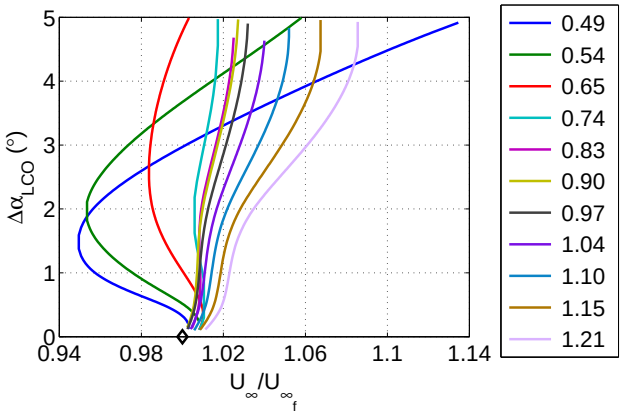

Figure 5.19: LCO pitch amplitude vs freestream velocity normalised by the linear flutter speed at $M = 0.74$, $\bar{\alpha} = 0°$ in inviscid flow

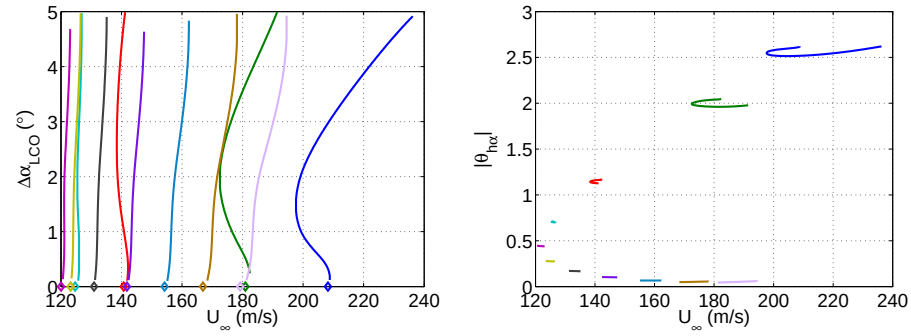

(a) Pitch amplitude

(b) Amplitude ratio

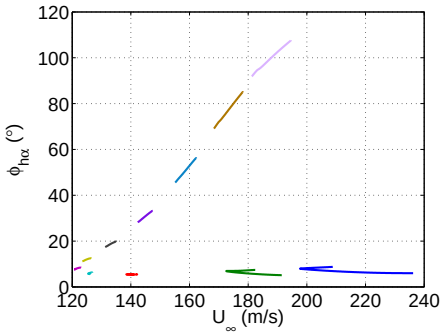

(c) Phase difference

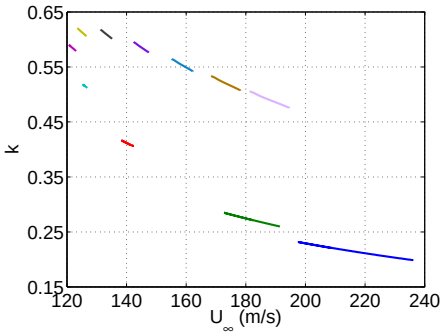

(d) Reduced frequency

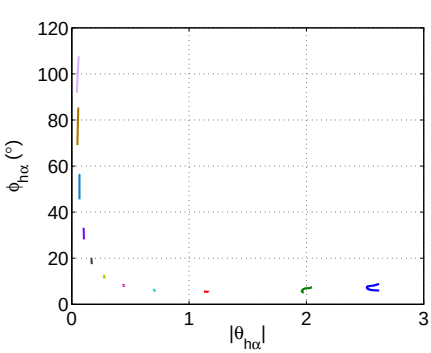

(e) Phase difference vs. amplitude ratio

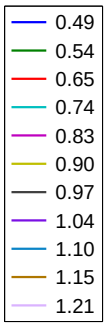

(f)

Figure 5.20: LCO mode shape vs freestream velocity at $M = 0.74$, $\bar{\alpha} = 0°$ in inviscid flow

TRANSONIC FLOW WITH TRAILING-EDGE SEPARATION

The results of an SFR-variation in case of transonic flow with trailing-edge separation ($M = 0.75$, $\bar{\alpha} = 0.7°$, $\mathrm{Re} = 2 \cdot 10^6$) are shown in Figure 5.22, which shows the LCO mode

shape and frequency versus the freestream velocity. Figure 5.21 shows the LCO amplitude versus the freestream velocity normalised by the flutter speed. For this test case it is observed that the bifurcation behaviour is supercritical for SFRs up to and including 1.21, in contrast to the validation test case (see Section 4.3.3). Therefore, the bifurcation behaviour has been investigated at $\omega_h/\omega_\alpha = 1.56$ as well. At this SFR the bifurcation behaviour becomes subcritical. For SFRs smaller than 1.56, from Figure 5.21 the velocity range covered by the LCOs up to $\Delta\alpha_{LCO} = 5°$ initially increases with increasing SFR (i.e. the slope of the bifurcation diagram for amplitudes larger than about 1° decreases). Then at $\omega_h/\omega_\alpha = 0.83$ the velocity range is maximal (and the slope minimal), whereas for $\omega_h/\omega_\alpha > 0.83$, the velocity range decreases. Hence, for the supercritical bifurcations, the non-linearity becomes stronger with increasing SFR up to a value of 0.83, and for larger ω_h/ω_α the non-linearity diminishes again. For $\omega_h/\omega_\alpha = 1.56$ the non-linearity is again stronger. Now, what are the implications of these changes? A larger range of frequency ratios for which supercritical bifurcations occur (i.e. for $\omega_h/\omega_\alpha = 0.49$ till 1.21), means that LCOs up to 5° will not occur below the flutter speed, but only above the linear flutter boundary. Hence, in that case a linearised flutter prediction would suffice. However, for larger SFRs this would not suffice, since the bifurcation then becomes subcritical (i.e. at $\omega_h/\omega_\alpha = 1.56$).

For all SFRs, except for the largest four, the phase difference starts at a small value and increases with freestream speed. For $\omega_h/\omega_\alpha = 1.15$, 1.21 and 1.56 the phase difference starts at 100° or above. At $\omega_h/\omega_\alpha = 1.56$ the phase difference increases with decreasing freestream speed. Note that at this SFR the phase difference has been extrapolated, since the largest sample point is at $\phi_{h\alpha} = 150°$. Figure 5.22(e) clearly shows the large range of phase difference covered by SFRs near 1. Furthermore, at small SFR the LCOs are stable, the mode shape is plunge dominated and $|\theta_{h\alpha}|$ decreases with increasing U_∞. At large SFR the LCOs are stable at small to moderate amplitudes and unstable at large amplitudes, the mode shape is pitch dominated and $|\theta_{h\alpha}|$ first increases with increasing U_∞ and then increases further with decreasing U_∞. This behaviour is similar to that of

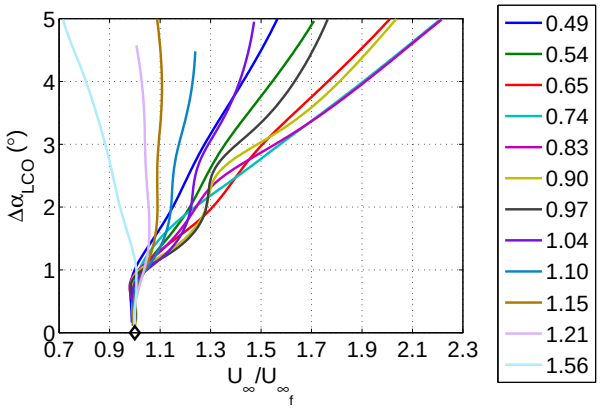

Figure 5.21: LCO pitch amplitude vs freestream velocity normalised by the linear flutter speed at $M = 0.75$, $\bar{\alpha} = 0.7°$ in viscous flow

the validation test case (see Section 4.3.3) and that observed by Kholodar et al. [3]. However, it is in contrast to that of the inviscid flow test case of Figures 5.19 and 5.20. The reduced frequency at flutter shows similar behaviour as the inviscid flow test case of the

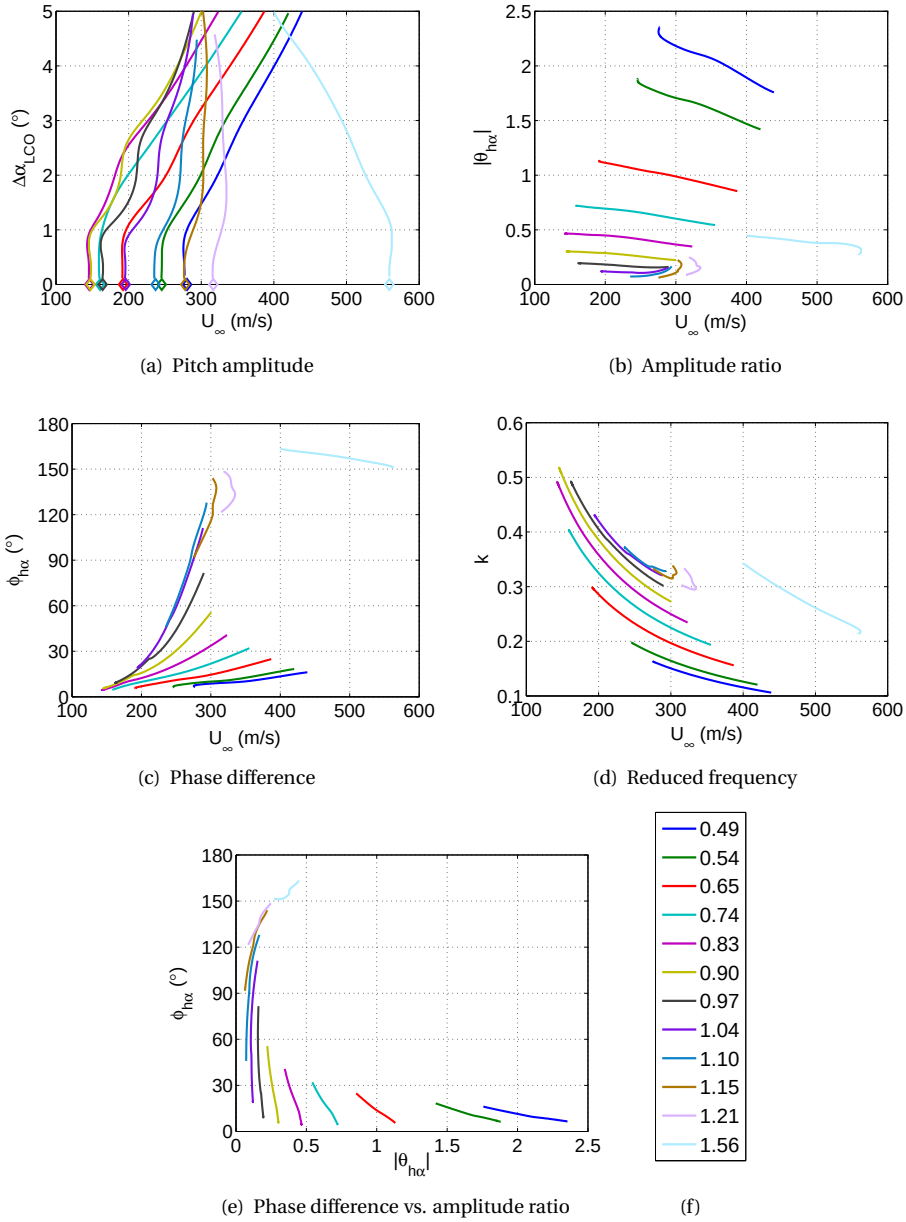

(a) Pitch amplitude

(b) Amplitude ratio

(c) Phase difference

(d) Reduced frequency

(e) Phase difference vs. amplitude ratio

(f)

Figure 5.22: LCO mode shape vs freestream velocity at $M = 0.75$, $\bar{\alpha} = 0.7°$ in viscous flow

previous section and that of Section 4.3.3, i.e. it increases with increasing SFR up until 0.90, for larger SFRs it decreases. Furthermore, as expected due to the inverse relation with U_∞, for the supercritical bifurcations the reduced frequency decreases with free-stream speed, whereas for the subcritical bifurcation at $\omega_h/\omega_\alpha = 1.56$ it increases with decreasing U_∞.

SUBSONIC FLOW WITH TRAILING-EDGE SEPARATION

Figure 5.23 shows the bifurcation diagrams of the pitch amplitude, amplitude ratio, phase difference and reduced frequency versus the freestream speed for the NLR7301 airfoil in subsonic flow with trailing-edge separation at $M = 0.3$, $\alpha = 9.0°$ and $\mathrm{Re} = 2 \cdot 10^6$. For this test case it should be noted that for an SFR of 1.04 and larger the bifurcation becomes subcritical. The slope of the stable LCO-part of the bifurcation diagram decreases with increasing ω_h/ω_α. Upon comparing with the validation test case (see Section 4.3.3, Figure 4.14), it is noted that in that case, the subcritical bifurcations at large ω_h/ω_α consist of unstable LCOs to an amplitude of 5° only. No stable LCOs (of up to 5°) are observed below the linear flutter boundary. The same holds for the transonic test case with trailing-edge separation. This is more dangerous than in the case of stable LCOs with amplitudes smaller than 5° below the flutter boundary, as it might give the impression that the linear flutter solution is correct and hence no flutter occurs below the flutter boundary. However, in reality LCOs of very large amplitude (much larger than 5°) might exist below the linear flutter point. When stable LCOs already exist below the linear flutter boundary, such as for small SFRs at $M = 0.74$, $\bar{\alpha} = 0°$ and for large SFRs at $M = 0.3$, $\bar{\alpha} = 9.0°$, there is a false sense of safety as well, but at least the effect might not be as detrimental as when only unstable LCOs of up to 5° occur below the linear flutter boundary. Note that for the largest three SFRs the phase difference is larger than 150°, i.e. extrapolation of the aerodynamic forces is applied here. Therefore, the results for these three SFRs should be treated with care. Studying the response surface has shown that the range of the stable LCOs of large amplitude at $\omega_h/\omega_\alpha > 1.04$ is probably not as large as computed here. Instead the largest stable LCO (of 5°-amplitude) is expected to occur below the flutter speed (as for $\omega_h/\omega_\alpha = 1.04$).

When looking at the LCO mode shape it is observed that the amplitude ratios achieved are much lower than for the other test cases. At the smallest SFR the amplitude ratio is about 1.18 at its maximum, whereas for the other test case amplitude ratios above 2 are observed for the smallest SFR. The amplitude ratio is seen to decrease with increasing freestream velocity for small SFRs. For large SFRs, $|\theta_{h\alpha}|$ first decreases slightly with decreasing freestream speed and then it increases with increasing freestream velocity. The mode shape is again plunge dominated for small ω_h/ω_α and pitch dominated for large ω_h/ω_α. Again the stable LCOs show a plunge dominated mode shape and the unstable LCOs a pitch dominated mode shape. Although, from Figure 5.23(e) both the amplitude ratio and phase difference increase for SFRs larger than one. This is probably caused by the large range covered by stable LCOs at large SFRs (as described above). Hence, there is a tendency of the stable LCOs at large SFRs to become more plunge dominated, i.e. the amount of plunge in the LCO mode shape increases.

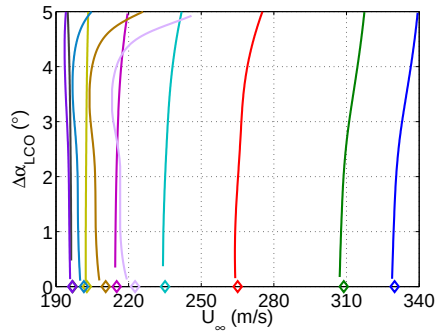

(a) Pitch amplitude

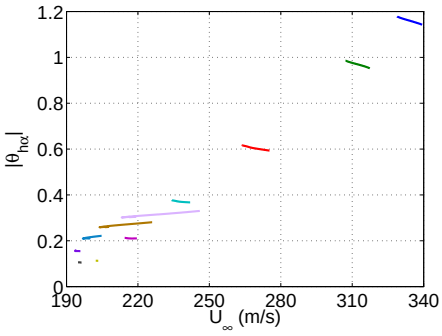

(b) Amplitude ratio

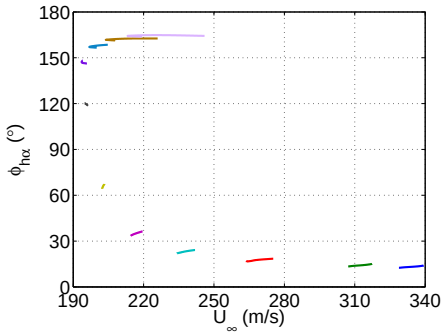

(c) Phase difference

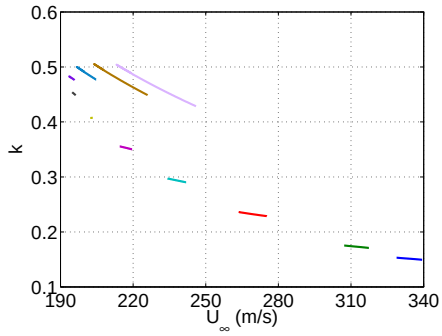

(d) Reduced frequency

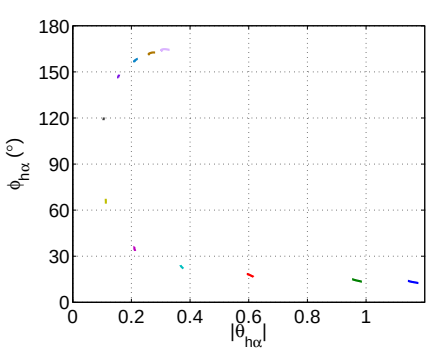

(e) Phase difference vs. amplitude ratio

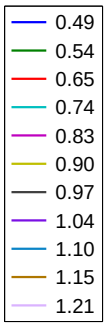

(f)

Figure 5.23: LCO mode shape vs freestream velocity at $M = 0.3$, $\bar{\alpha} = 9.0°$ in viscous flow

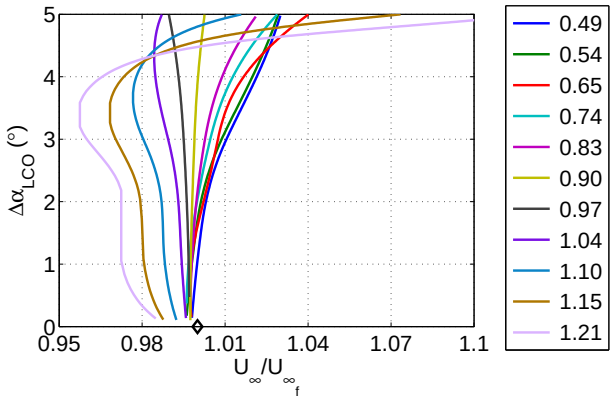

Figure 5.24: LCO pitch amplitude vs freestream velocity normalised by the linear flutter speed at $M = 0.3$, $\bar{\alpha} = 9.0°$ in viscous flow

SUBSONIC FLOW WITH FREE BOUNDARY-LAYER TRANSITION

The effects of an SFR variation on the bifurcation behaviour of the NLR7301 airfoil at $M = 0.3$, $\bar{\alpha} = -1.3°$, $\mathrm{Re} = 5 \cdot 10^5$ and $\mathrm{Tu} = 0.05\%$ in transitional flow are shown in Figures 5.25 and 5.26. Note that pitch amplitudes up to 3° are shown, as explained in Section 5.2.4. It is observed that at small amplitudes the LCOs are unstable. They become stable as the LCO amplitude increases for SFRs up to 0.83. For larger SFRs the LCOs become unstable again at large amplitude. In general, the velocity range covered by the bifurcation diagrams is very small and hence the non-linearity is relatively weak. In contrast, Poirel and Mendes [4] obtained a shift of the stable LCOs towards larger amplitudes when the structural frequency ratio was increased from 0.74 to 1.2 and to lower LCO amplitudes when the SFR was increased from 1.2 to 1.63 for the NACA0012 airfoil in transitional flow. Note however that the test cases cannot be directly compared, since the flow conditions are different (the Reynolds number is much lower in the work of Poirel and Mendes) and the (linear) structural model as well as the airfoil shape are different as well. Furthermore, the LCOs observed by Poirel and Mendes are at much larger amplitude (2°-7.5°). From Figure 5.25(b) it is observed that the LCO mode shape changes from plunge dominated with amplitude ratios larger than 1 at the smallest two SFRs to pitch dominated at large SFR. At SFRs smaller than 1.10, the amplitude ratio decreases with increasing freestream velocity. For the largest three SFRs the amplitude ratio increases again, i.e. the amount of plunge in the LCO mode shape becomes larger. The phase difference increases with increasing SFR and it increases with freestream velocity for all SFRs. The reduced frequency at flutter shows a similar trend as for the transonic inviscid flow test case, it first increases with increasing ω_h/ω_α. However, for $\omega_h/\omega_\alpha > 0.90$ it decreases with increasing SFR.

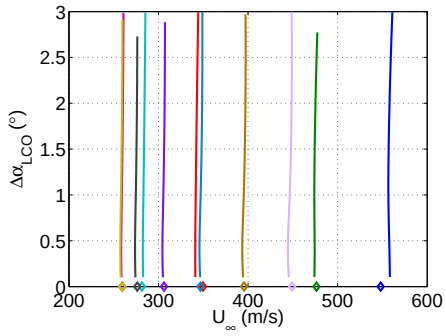

(a) Pitch amplitude

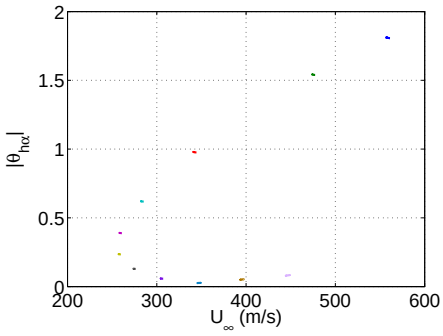

(b) Amplitude ratio

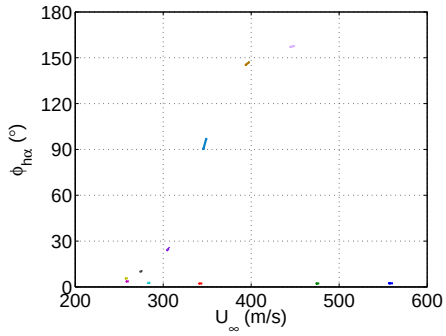

(c) Phase difference

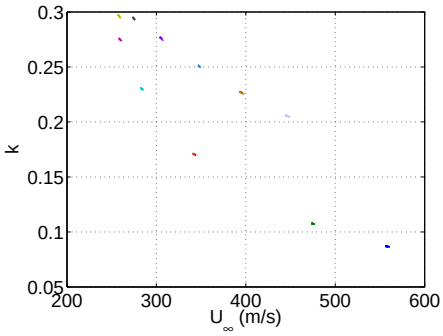

(d) Reduced frequency

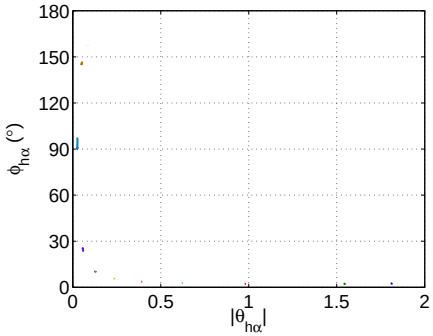

(e) Phase difference vs. amplitude ratio

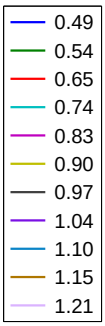

(f)

Figure 5.25: LCO mode shape vs freestream velocity at $M = 0.3$, $\tilde{\alpha} = -1.3°$, Re $= 5 \cdot 10^5$ and Tu $= 0.05\%$ in transitional flow

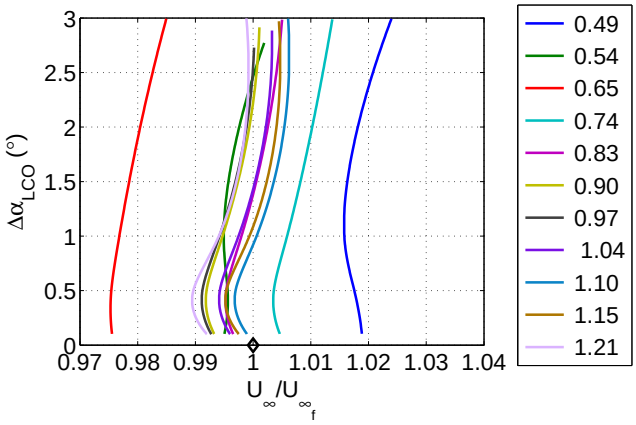

Figure 5.26: LCO pitch amplitude vs freestream velocity normalised by the linear flutter speed at $M = 0.3$, $\bar{\alpha} = -1.3°$, $\mathrm{Re} = 5 \cdot 10^5$ and $\mathrm{Tu} = 0.05\%$ in transitional flow

5.4.2. MASS RATIO

The mass ratio μ non-dimensionalises the mass m, i.e.

$$\mu = \frac{m}{\frac{1}{4}\pi\rho_\infty c^2}. \tag{5.1}$$

Since (5.1) contains the freestream density ρ_∞, the mass ratio has different values for each of the aerodynamic non-linearities considered. Table 5.5 summarises the densities and corresponding mass ratios for each test case of Section 5.2 considering the mass as given in Table 2.1 (i.e. $m = 26.264$ kg). Note that due to low density for the transonic viscous test case at $M = 0.75$ and for the free transition test case at $M = 0.3$, the mass ratio using the standard mass is much higher than for the other cases.

M	$\bar{\alpha}$ (°)	Euler/RANS	ρ_∞ (kg/m^3)	μ
0.74	0.0	Euler	1.2925	287.52
0.75	0.7	RANS	0.4606	806.77
0.3	9.0	RANS	1.1516	322.71
0.3	-1.3	RANS	0.2879	1290.83

Table 5.5: Freestream density and corresponding mass ratio for all test cases

The mass ratio is varied at constant radius of gyration about the elastic axis $r_\alpha \left(= \sqrt{I_\alpha / (mc^2)}\right)$ and at constant static unbalance x_α $(= S_\alpha / (mc))$. These parameters have values of 0.1828 and 0.0420, respectively for the structural parameters considered in Table 2.1. The plunge and torsional spring stiffnesses are also kept fixed at their values of Table 2.1. Since the trends in the bifurcation behaviour of the NLR7301 airfoil due to a change in mass ratio are similar for all aerodynamic non-linearities, this section only

shows the most non-linear test case, the transonic flow with trailing-edge separation test case. The results of a mass ratio variation for the other three test cases are shown in Section D.1.1.

The influence of changes in the mass ratio on the bifurcation behaviour of the limit-cycle oscillations of the airfoil in transonic viscous flow ($M = 0.75$, $\bar{\alpha} = 0.7°$) is shown in Figure 5.27. The shape of the bifurcation does not change significantly for the mass ratios considered. It stays supercritical. However, the slope of the bifurcation diagram increases with decreasing mass ratio, see Figure 5.27(f). Hence, the non-linearity becomes weaker with decreasing mass ratio. This was also observed by Kholodar et al. [3] for the NACA64010A airfoil in inviscid transonic flow at $\omega_h/\omega_\alpha = 0.5$ and $M = 0.8$. The amplitude ratio is seen to decrease with increasing freestream speed for most mass ratios. However, for $\mu = 100$ the amplitude ratio increases with freestream speed. Hence, the stable LCOs will show a more complex pitch-plunge motion with increasing LCO amplitude for $\mu = 100$. In contrast for the other mass ratios the motion tends to become more pitch dominated with increasing LCO amplitude. The phase difference increases with freestream speed for all mass ratios. The reduced frequency decreases with increasing mass ratio and with increasing freestream speed. For this test case a variation in SFR has been applied at various mass ratios as well. Figure 5.28 shows the LCO amplitude versus the freestream speed normalised by the flutter speed for two different frequency ratios. For $\omega_h/\omega_\alpha = 0.97$ similar trends as for an SFR of 0.70 (Figure 5.27(f)) are observed, except that around an LCO amplitude of 2° the curves become very steep and then decrease in slope again. This is most pronounced for $\mu = 600$. This also occurs at $\omega_h/\omega_\alpha = 1.21$ only around 3°. Generally, for this SFR the bifurcation behaviour does not vary much with mass ratio, except for $\mu = 100$. Only a larger range of velocities is covered by the unstable LCOs below the flutter speed when the mass ratio increases. Note that, since extrapolation on the response surface in the reduced frequency-direction is required for $\mu = 100$ at $\omega_h/\omega_\alpha = 0.97$, the bifurcation diagram for this mass ratio is not included Figure 5.28(a). Instead the bifurcation diagram at a mass ratio of 200 has been included.

From the observations in this section it is concluded that the mass ratio does not significantly influence the type of bifurcation. When the non-linearity is very weak, a change in bifurcation type may result when the mass ratio is varied. Otherwise the bifurcation type remains the same, only the slope of the bifurcation diagram might change.

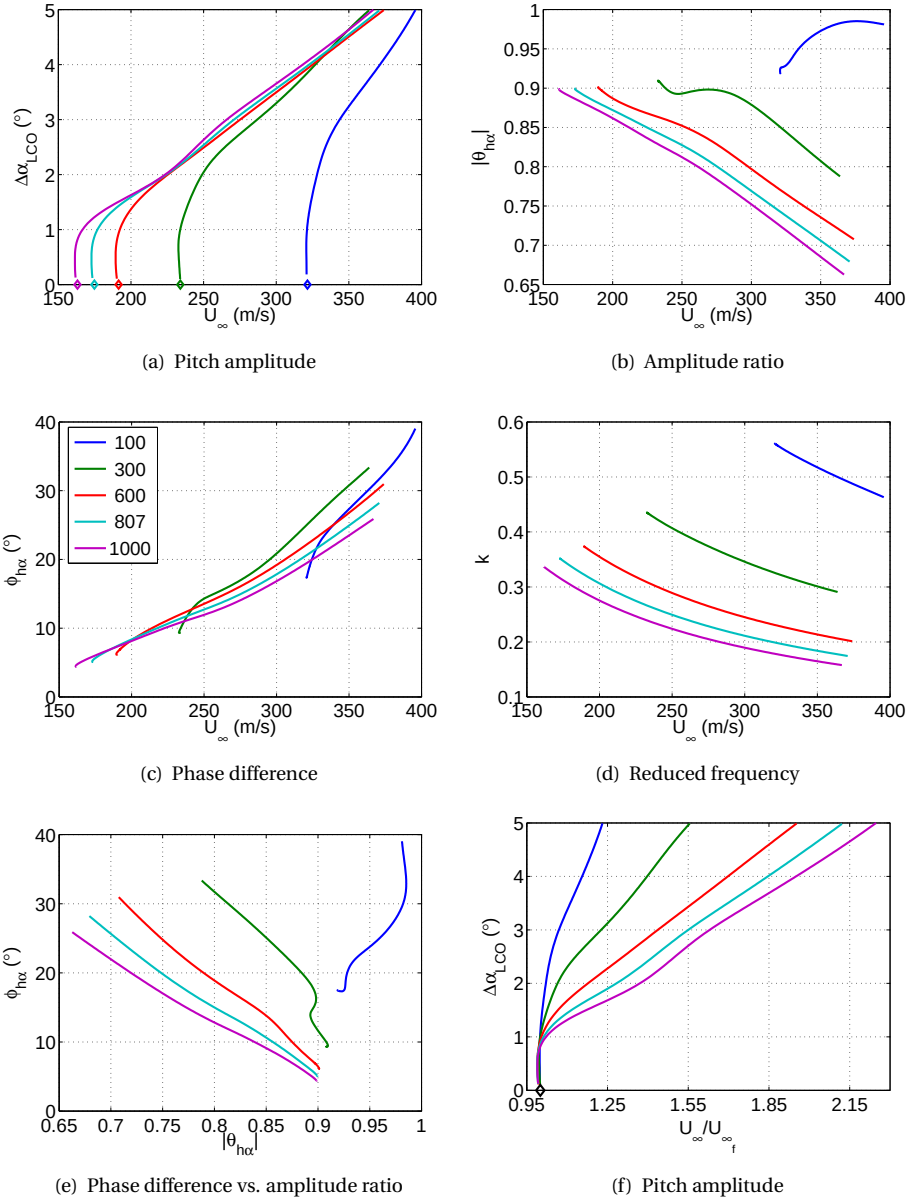

(a) Pitch amplitude

(b) Amplitude ratio

(c) Phase difference

(d) Reduced frequency

(e) Phase difference vs. amplitude ratio

(f) Pitch amplitude

Figure 5.27: LCO mode shape vs freestream velocity for a mass ratio variation at $M = 0.75$, $\bar{\alpha} = 0.7°$

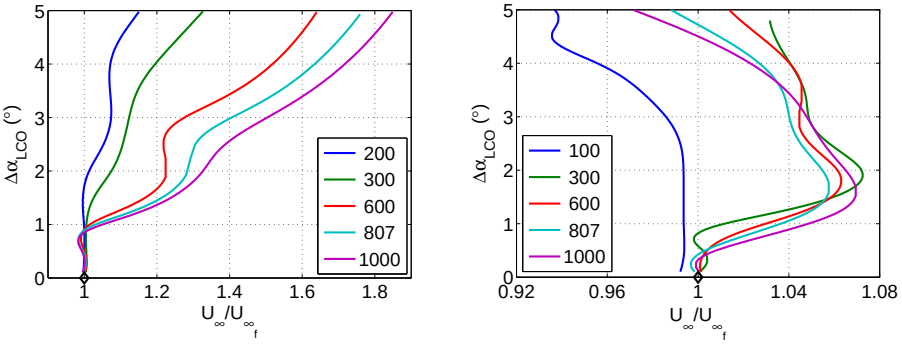

(a) $\omega_h/\omega_\alpha = 0.97$ (b) $\omega_h/\omega_\alpha = 1.21$

Figure 5.28: LCO mode shape vs freestream velocity normalised by the linear flutter speed for a mass ratio variation at $M = 0.75$, $\bar{\alpha} = 0.7°$ and two different SFR

5.4.3. STRUCTURAL DAMPING

The structural damping was set to zero for all test cases in this thesis (except for the validation test case of chapter 4) in order to investigate the effect of aerodynamic damping only. Now, structural damping is added to the airfoil system and its effect on the bifurcation behaviour is studied. The addition of damping causes, as expected, an increase in the flutter speed. Hence, all bifurcation diagrams are shifted to larger freestream velocities. Figure 5.29 depicts the bifurcation behaviour of the LCO mode shape for the viscous transonic flow test case at $M = 0.75$, $\bar{\alpha} = 0.7°$. The structural damping of both degrees of freedom has been increases simultaneously by the same amount, i.e. the damping matrix has be pre-multiplied. To indicate the variation of the structural damping matrix, in Figure 5.29, variations of the value of D_h are depicted. The results of the other test cases are shown in Figures D.7, D.8 and D.9 in Section D.1.2. There is almost no variation in the type of bifurcation at an SFR of 0.70. The aerodynamic non-linearity is apparently too strong to cause significant changes when up to ten times the structural damping of Table 2.1 is added to the system. However, the range of freestream velocities covered by LCO up to an amplitude of 5° decreases with increasing structural damping, i.e. the strength of the (aerodynamic) non-linearity decreases. This holds for all viscous test cases. For the inviscid test case $M = 0.74$, $\bar{\alpha} = 0°$, see Figure D.7, the freestream velocity range covered by the LCO amplitude increases with increasing structural damping values. For the viscous test case shown in Figure 5.29, the phase difference is seen to increase with increasing structural damping and with increasing freestream speed. The reduced frequency decreases with increasing structural damping, which is expected as it is inversely proportional to the freestream velocity (which increases with increasing damping, as the flutter speed increases). For the inviscid test case, the amplitude ratio variation increases with increasing damping, see Figure D.7. For the viscous test cases, increasing the structural damping leads to a decrease in the amplitude ratio. For those test cases, the amplitude ratio also decreases with freestream velocity for all structural damping values.

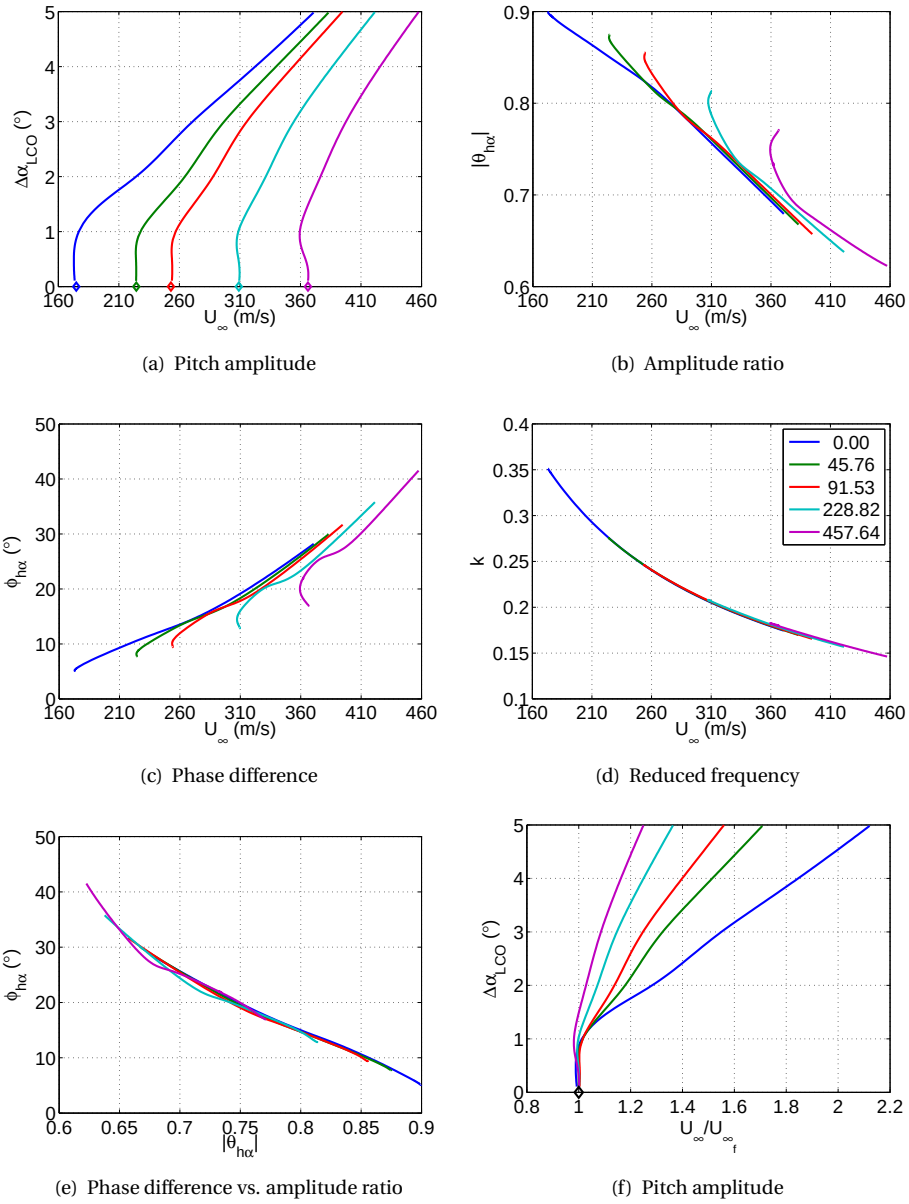

(a) Pitch amplitude

(b) Amplitude ratio

(c) Phase difference

(d) Reduced frequency

(e) Phase difference vs. amplitude ratio

(f) Pitch amplitude

Figure 5.29: LCO mode shape vs freestream velocity for a damping variation at $M = 0.75$, $\bar{\alpha} = 0.7°$ (value of D_h is shown in the legend)

If the structural frequency ratio is increased to 0.97, applying ten times the structural damping of Table 2.1 causes a change in bifurcation type from subcritical to supercritical for the test case at $M = 0.3$, $\bar{\alpha} = 9.0°$, see Figure 5.30. The same conclusions can be drawn

as for the mass ratio; only when the non-linearity is very weak changes in the structural damping can change the bifurcation type.

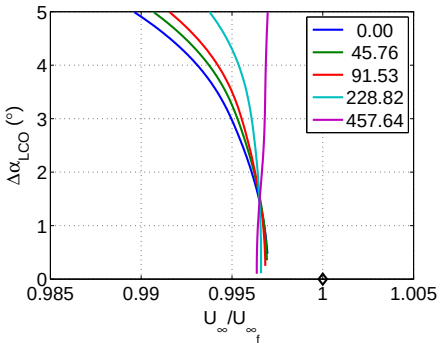

Figure 5.30: LCO mode shape vs freestream velocity normalised by the linear flutter speed for a damping variation at $M = 0.3$, $\bar{\alpha} = 9.0°$, $\omega_h/\omega_\alpha = 0.97$ (value of D_h is shown in the legend))

5.4.4. ELASTIC AXIS LOCATION

In order to investigate the generality of the results obtained in this thesis, the elastic axis location has been varied, keeping the remaining structural parameters constant. Figure 5.31 show the result in terms of the bifurcation behaviour for the transonic viscous test case at $M = 0.75$, $\bar{\alpha} = 0.7°$. Note that the non-dimensional elastic axis location from the quarter-chord point is shown in this figure, where a positive distance indicates that the elastic axis is located aft of the quarter-chord point, see Figure 2.1. The results for the other sources of non-linearity are shown in Section D.1.3. From Figure 5.31 it is observed that the slope of the supercritical bifurcation increases when the elastic axis is located further aft of the quarter-chord point, i.e. the non-linearity becomes weaker. However, the bifurcation type remains the same. For this test case, the amplitude ratio decreases with increasing freestream velocity, except when the elastic axis is located upstream of the quarter-chord point, then it first increases and then decreases, see Figure 5.31(b). The phase difference increases with increasing freestream velocity for all elastic axis locations. When the elastic axis is located at 75% of the chord length, i.e. 0.5c behind the quarter-chord point, the phase difference increases dramatically. This happens at very small amplitude ratios, as can been from Figure 5.31(e). This means that for $x_{ea} = 0.5c$, the LCO mode shape becomes almost a pure pitch motion where plunge leads pitch. The reduced frequency increases with increasing distance between the quarter-chord point and the elastic axis, although it decreases with increasing freestream velocity for a particular elastic axis position, as expected due to the inverse relation with the freestream velocity.

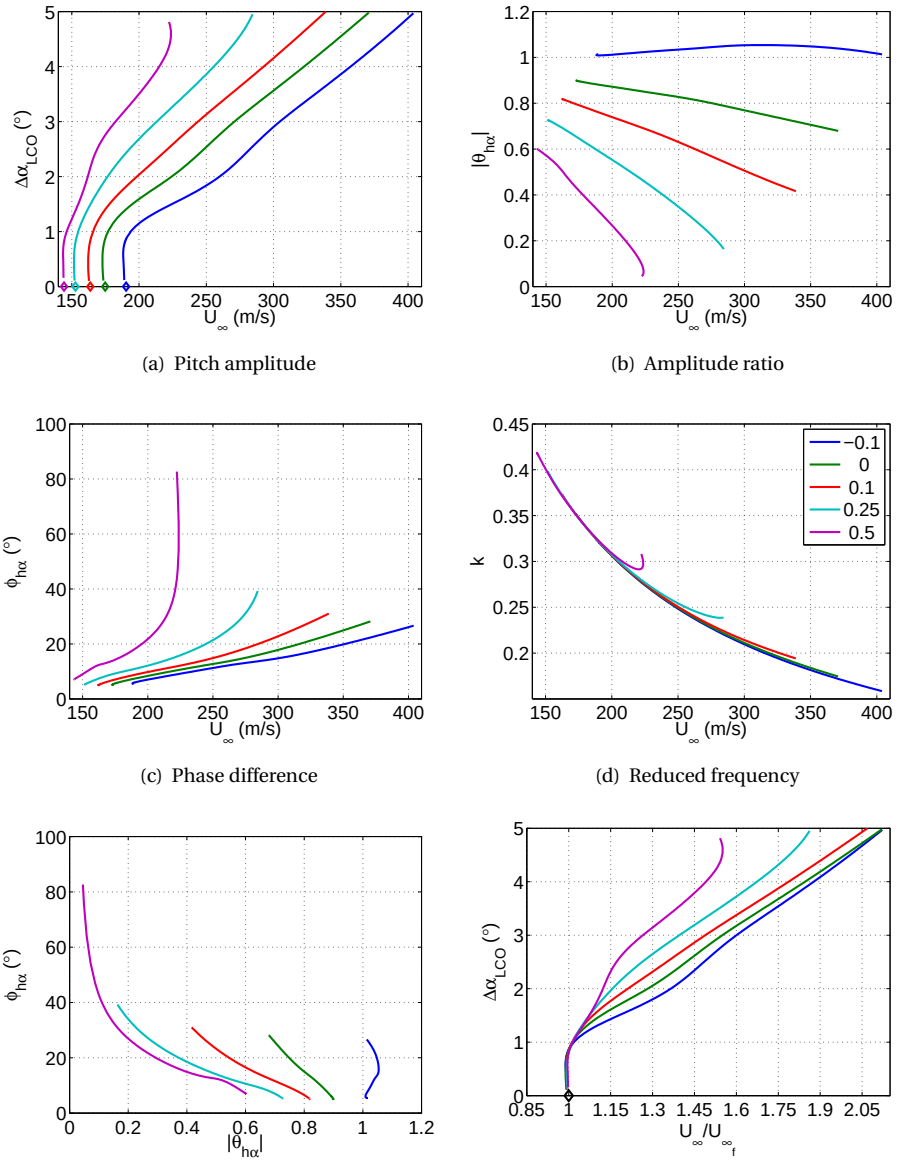

(a) Pitch amplitude

(b) Amplitude ratio

(c) Phase difference

(d) Reduced frequency

(e) Phase difference vs. amplitude ratio

(f) Pitch amplitude

Figure 5.31: LCO mode shape vs freestream velocity for a variation of the non-dimensional elastic axis location at $M = 0.75$, $\bar{\alpha} = 0.7°$ (value of x_{ea}/c is shown in the legend)

Increasing the structural frequency ratio to 1.21 results in a change of bifurcation type as illustrated in Figure 5.32. Note that the most aft elastic axis location is no further than 35% of the chord length aft of the quarter-chord point, because no flutter was observed

for more aft locations of the elastic axis. A change from supercritical to subcritical bifurcation with the aft movement of the elastic axis is also observed for the subsonic flow test case with trailing-edge separation at $\omega_h/\omega_\alpha = 0.70$, see Section D.1.3. Although, it should be noted that the non-linearity causing the supercritical bifurcation at the nominal elastic axis location is already relatively weak. For the transonic inviscid test case, a transition from subcritical to supercritical bifurcation behaviour at the nominal structural frequency ratio (0.70) is observed when the elastic axis is moved aft, see Section D.1.3 as well. Hence, these results show that, when the elastic axis location is shifted, the strength of the non-linearity changes and a change in bifurcation behaviour might occur.

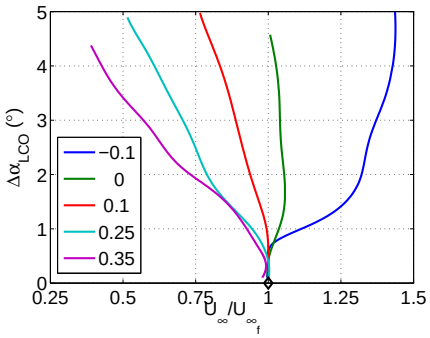

Figure 5.32: LCO mode shape vs freestream velocity normalised by the linear flutter speed for a variation of the non-dimensional elastic axis location at $M = 0.75$, $\bar{\alpha} = 0.7°$, $\omega_h/\omega_\alpha = 1.21$ (value of x_{ea}/c is shown in the legend)

5.4.5. CONCLUSIONS

This section has shown the effect of a variation of several structural parameters, i.e. the structural frequency ratio, the mass ratio, the structural damping and the elastic axis location, on the LCO bifurcation behaviour. From the structural frequency ratio variation, as shown in Section 5.4.1, it was found that in most cases the bifurcation behaviour of the LCO amplitude is supercritical at small structural frequency ratios ($\omega_h << \omega_\alpha$) and becomes subcritical when the structural frequency is increased to values larger than one (i.e. when $\omega_h >> \omega_\alpha$). Similar behaviour was observed for the inviscid validation test case in Section 4.3.3 and by Kholodar et al. [3] for the NACA64010A airfoil in inviscid flow. However, for the transonic inviscid test case at $M = 0.74$ and $\bar{\alpha} = 0°$ opposite behaviour is observed, see Figure 5.19. Furthermore, at small ω_h/ω_α the mode shape is found to be plunge dominated and at large ω_h/ω_α the mode shape is pitch dominated, as expected due to the structural frequency ratio. Combined with the observations on the bifurcation behaviour, this implies that an LCO solution that is plunge dominated can undergo either a supercritical or a subcritical bifurcation. Hence, the bifurcation type is not necessarily related to a certain LCO mode shape. In addition to subcritical bifurcations that start with unstable LCOs at small amplitude and stable LCOs of larger amplitudes, also bifurcations were observed where the small-amplitude LCOs are sta-

ble and at larger amplitudes the LCOs become unstable, in transonic viscous flow. Also, subcritical bifurcations with only unstable LCOs up to 5° were found for the transonic viscous test case at $\omega_h/\omega_\alpha = 1.56$ and for the subsonic test case with trailing-edge separation at $\omega_h/\omega_\alpha = 0.97$, see Figures 5.21 and 5.24. Kholodar et al. [3] observed such subcritical bifurcations with unstable LCOs only (up to 7°) for the NACA64010A airfoil as well (in inviscid flow however). These subcritical bifurcations with unstable LCOs only (up to 5°) are dangerous as a stable LCO of an amplitude much larger than 5° might occur. In general, the subcritical bifurcations observed for the test case in subsonic flow with trailing-edge separation, clearly show what happens in the non-linear case and how incorrect a linearised analysis could be (although the large amplitude results at the highest three SFRs should be treated with care). In subsonic flow with free boundary layer transition the bifurcation behaviour was observed to be almost independent of the structural frequency ratio. Poirel and Mendes [4] found a more significant variation of the bifurcation behaviour when the structural frequency ratio was varied than the variation obtained here. Although it should be noted that they considered the NACA0012 airfoil at different flow conditions and with a different (linear) structural model.

The effect of a variation of the mass ratio was shown in Section 5.4.2 for the transonic viscous flow test case. The results for the other test cases are shown in Section D.1.1. For all test cases, it was found that the mass ratio does not significantly influence the bifurcation type, only when the non-linearity is weak a change in bifurcation type might occur. However, the non-linearity is observed to increase in strength when the mass ratio is increased, as observed from e.g. Figure 5.27(f). Similar observations were made by Kholodar et al. [3] for the NACA64010A airfoil in inviscid transonic flow.

Section 5.4.3 discussed the effect of added structural damping on the bifurcation behaviour. Similar to the mass ratio variation, no significant changes in the bifurcation behaviour were observed unless the non-linearity was weak (at $\omega_h/\omega_\alpha = 0.97$ in subsonic flow with trailing-edge separation, see Figure 5.30). However, the strength of the aerodynamic non-linearity was seen to decrease with increasing value of the structural damping for the viscous test cases. In inviscid transonic flow, opposite behaviour regarding the strength of the non-linearity is observed, see Figure D.7.

A variation in the elastic axis location has been performed in order to assure that the results produced in this thesis are also valid for other elastic axis locations than the quarter-chord point (at which x_{ea} is zero). The effect of such a variation on the bifurcation behaviour of the LCO solution is shown in Section 5.4.4. It was found that the elastic axis location significantly influences the bifurcation behaviour. When the non-linearity is not very strong (i.e. when no strong supercritical bifurcation is observed), the bifurcation behaviour can change from supercritical to subcritical when the distance between the quarter-chord point and the elastic axis is increased in case of viscous flow. For inviscid transonic flow the opposite behaviour was observed. In comparison to the effects of variations of the mass ratio and the structural damping, it can be concluded that variation of the elastic axis location has a larger impact on the bifurcation behaviour than a variation of the former two.

5.5. RESPONSE SURFACE ANALYSIS

The input of ADePK is a response surface of the aerodynamic lift and moment. This response surface might contain some significant information about the possible bifurcations types. This issue is addressed in this section. For analytical systems of one DoF this is common practise, see for example Gros [20]. Hence, the response function of the one DoF van-der-Pol oscillator is first addressed in Section 5.5.1. For this test case it was observed that the real part of the Fourier-transformed right-hand side of the equation of motion exhibits a root at the LCO amplitude. The gradient w.r.t. amplitude at this root indicates whether the LCO is stable or unstable, as also observed by e.g. Gros [20]. However, since this thesis deals with a two DoF airfoil system, which nor has one DoF neither has an analytical (aerodynamic) response function, the one DoF van-der-Pol oscillator has been extended with a second degree of freedom in Section 5.5.2 (see also Section 3.3.1). This system has an analytical response function, such that the relation between the response surface and the LCO behaviour can be investigated, before continuing with the two DoF airfoil system. In case of a relatively "simple" non-linear damping matrix, the gradient w.r.t. amplitude at the location of the root of the response surface can still be used to determine the stability of the LCO. However, once the non-linear damping term becomes more complicated, the response surface no longer exhibits a root at the LCO amplitude. It was found that, the curvature of the response surface in phase difference direction gives an indication about the stability of the LCO, see Table 5.6.

Then the response surface of the several two-DoF-airfoil-system test cases are linked to their bifurcation behaviour in Section 5.5.3. First, the part of the aerodynamic force vector responsible for the type of bifurcation that occurs was identified, see Figures 5.39 and 5.40. Then the response surface at several mode shapes was considered in order to identify possible similarities between the response surface and the bifurcation behaviour. It was found that the sine of the phase of the lift has a shape similar to that of the freestream speed versus LCO amplitude-diagram (i.e. the rotated bifurcation diagram), see for example Figure 5.46. Finally, the aerodynamic features responsible for the form of the response surface and therefore the bifurcation behaviour are considered. A relation between the shock motion on the lower surface of the airfoil and the phase of the lift was found. For more details Section 5.5.3 should be addressed.

5.5.1. ONE DOF VAN DER POL-OSCILLATOR

For the one DoF van der Pol-oscillator, it is possible to determine the type of bifurcation that occurs or even the LCO amplitude when just looking at the response function (see e.g. Gros [20]). The response function in this case is the Fourier transform of the right-hand side of the equation of motion, i.e. the right-hand side of

$$\ddot{x} + x = \epsilon \left(\mu - a x^2 - d x^4\right) \dot{x}, \tag{5.2}$$

which has been reproduced here from (3.7). When plotting the real and imaginary parts of the response function versus the (input) amplitude for various values of μ one can gain insight into the bifurcation behaviour of the system. Figure 5.33 shows the real part of the response function versus the amplitude at $\omega = 1$, $\epsilon = 0.02$, $a = -2$ and $d = 0.5$.
From Figure 5.33 it can be seen that when μ is -2, the response function has no roots

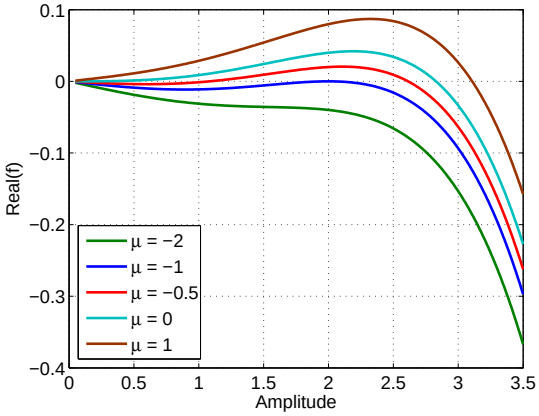

Figure 5.33: Real part of the response function versus the amplitude for the one DoF van der Pol-oscillator for various μ at $\omega = 1$ ($\epsilon = 0.02$, $a = -2$ and $d = 0.5$)

except for the origin. For $\mu = -1$ the response function has a root and a maximum at the same time. For $\mu = -0.5$ there are two non-zero roots and for $\mu = 0$ and $\mu = 1$ there is only one non-zero root. When comparing the number of non-zero roots with the bifurcation diagram of Figure 4.2 it is observed that the number of roots corresponds to the number of LCOs that exist at a certain value of μ. In addition when the maximum of the response function is a root as well, a saddle-node bifurcation of limit cycles occurs. Upon comparing the location of the roots for a certain μ with the LCO amplitudes at this μ it is seen that the root location is equal to the LCO amplitude. This means that for the van der Pol oscillator the non-zero root(s) of the real part of the response function give the LCO amplitude(s). Hence, this would mean that it is not necessary to use the p-k method to determine the amplitude at which the damping is zero. Computing the response function for various amplitudes and frequencies and finding the roots of the response function for various μ suffices for the determination of the LCO amplitude. This is known from theory [20]. Furthermore, from the sign of the gradient of the response function at the root, $\frac{\partial \Re(f)}{\partial \hat{x}}\Big|_{\Re(f)=0}$, it can be determined whether the LCO is stable or unstable. When the gradient $\frac{\partial \Re(f)}{\partial \hat{x}}\Big|_{\Re(f)=0}$ is positive the LCO is unstable, when the gradient is negative the LCO is stable. The curvature of the response function, i.e. the sign of its second derivative, can also be used to determine the stability of an LCO. From Figure 5.33 it is seen that the curvature of the response function is convex in the surroundings of the unstable LCO and concave near the stable LCO.

Figure 5.33 showed the real part of the response function for various μ values at $\omega = 1$. This is the LCO frequency. However, even when the frequency is not equal to that of the actual LCO, the number of roots of the response function is equal to the number of LCOs. This is demonstrated in Figure 5.34, which shows the real part of the response function versus the amplitude for various ω at $\mu = -0.5$.

From Figure 5.34 it is observed that the location of the root is independent of the

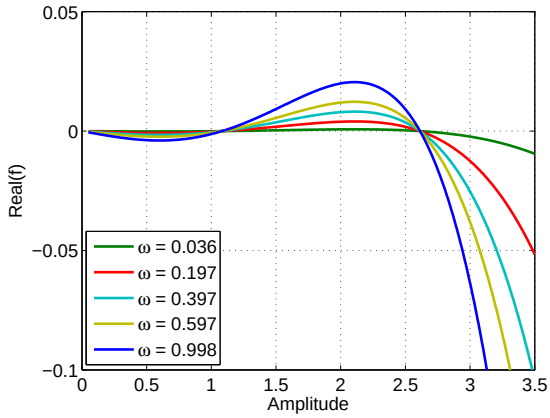

Figure 5.34: Real part of the response function versus the amplitude for the one DoF van der Pol-oscillator for various ω at $\mu = -0.5$ ($\epsilon = 0.02$, $a = -2$ and $d = 0.5$)

frequency. This means that the LCO frequency does not need to be known in advance in order to be able to determine the LCO amplitude for a certain value of μ.

The fact that the number of LCOs and the LCO amplitude can be determined solely by looking at the roots of the response function, as known from theory [20] and observed here, has important consequences for the determination of the bifurcation behaviour for a pitch/plunge airfoil system. Namely, this would mean that if the response surface has been determined, the roots of this response surface can be computed and the LCO properties can be determined without the using ADePK.

5.5.2. TWO DOF VAN DER POL-OSCILLATOR

For the one degree-of-freedom van der Pol oscillator it is possible to determine the type of bifurcation that occurs from the response function. For the two degree-of-freedom van der der Pol oscillator the right-hand side of the equations of motion is the response function vector, i.e. the right-hand side of

$$\mathbf{M}\ddot{\vec{x}} + \mathbf{K}\vec{x} = \epsilon \begin{bmatrix} \mu - a_1 x_1^2 - b_1 x_1^4 & c_1\mu - a_2 x_1^2 \\ c_1\mu - a_3 x_2^2 & c_1\mu - a_4 x_2^2 - b_2 x_2^4 \end{bmatrix} \begin{bmatrix} \dot{x}_1 \\ \dot{x}_2 \end{bmatrix}, \tag{5.3}$$

which has been reproduced from (3.16) here. This vector is dependent on the frequency, the complex amplitude ratio between the two degrees of freedom and the amplitude of the second degree of freedom. Hence, when the complex amplitude ratio is split into a magnitude and a phase, this is a four dimensional response function. Since this is not easy to visualise, two parameters are kept fixed and the other two are varied in the plots shown in this section. First the response surface is addressed when only the first degree of freedom has a non-linear damping (i.e. when $a_2 = a_3 = a_4 = b_1 = b_2 = c_1 = 0$ in (5.3)). In that case the zeros of the response function can be used to gain information about the LCO that occurs. In the full non-linear case, i.e. when both degrees of freedom have

a non-linear damping and the coefficients a_2 till c_1 are non-zero, the curvature of the response surface in phase difference direction can be used to determine the type of LCO that occurs.

ZEROS OF RESPONSE SURFACE (a_2 TILL c_1 ARE ZERO)

To look for the zeros of the response surface, the coefficients ϵ, a_1 and b_1 have been set to 0.002, -2 and 0.5 respectively. The bifurcation parameter μ is varied. Figure 5.35 shows the contours of the real part of the response plotted for various amplitudes and phase differences and at several values of μ. The amplitude ratio is 0.618 and the reduced frequency is 1.9545 rad/s. These values correspond to the stable LCO at $\mu = -0.5556$.

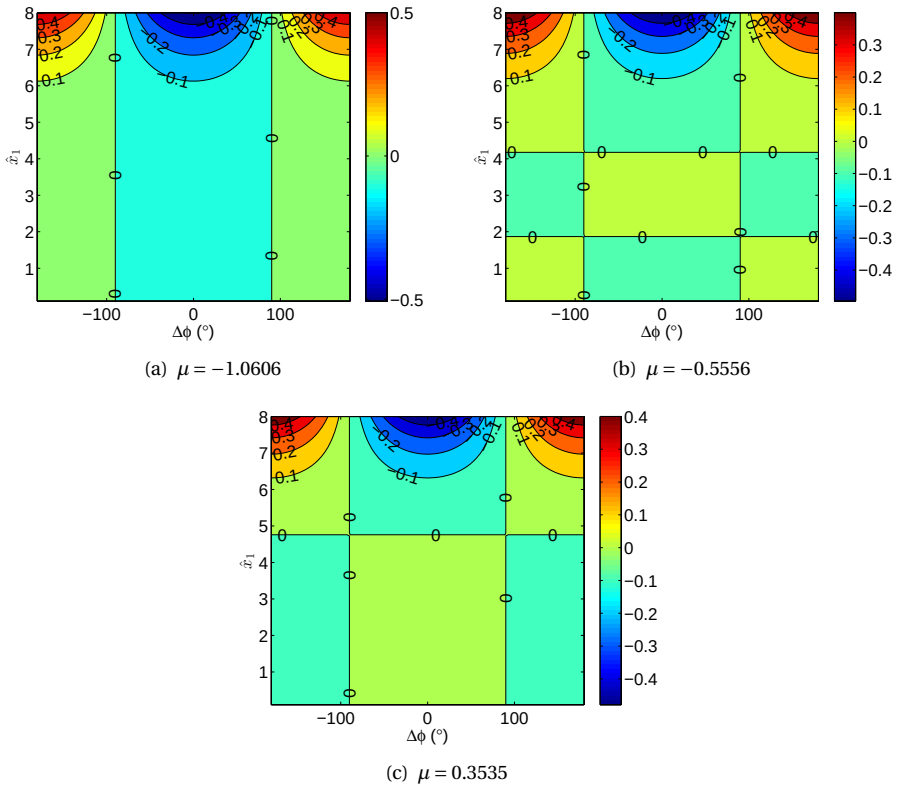

(a) $\mu = -1.0606$ (b) $\mu = -0.5556$

(c) $\mu = 0.3535$

Figure 5.35: Real part of the response surfaces of the two degree-of-freedom van der Pol oscillator system for various μ ($\hat{x}_1/\hat{x}_2 = 0.618$ and $\omega = 1.9545$ rad/s)

From Figure 5.35(a) it is observed that for μ is -1.0606, the response function only has roots at $\Delta\phi = \pm\pi/2$, independent of the amplitude of the first DoF $\hat{x}_1$. For $\mu = -0.5556$ the same roots appear at $\Delta\phi = \pm\pi/2$. In addition, there are two amplitudes at which the response function is zero for all $\Delta\phi$: $\hat{x}_1 = 1.87$ and 4.18. For $\mu = 0.3535$ there is only one amplitude at which the response function has a root, i.e. at $\hat{x}_1 = 4.76$. These am-

plitudes do not exactly match the LCO amplitudes, however the number of roots found from these figures corresponds to the number of LCOs that occur at the μ-values.

In addition to the number of LCOs that occurs, the gradient in the $\hat{x}_1$-direction of the response surface at the root location can be used to determine whether the LCO is stable or unstable. In Figure 5.35(b) for example the LCO at $\hat{x}_1 = 1.87$ is unstable, since the gradient of the response surface at this root is positive for $-\pi/2 < \Delta\phi < \pi/2$. The LCO at $\hat{x}_1 = 4.18$ on the hand, is stable, because at this root the gradient is negative for $-\pi/2 < \Delta\phi < \pi/2$.

Although Figure 5.35 only shows the response surface for an amplitude ratio of 0.618 and a frequency of 1.9545 rad/s, similar results are obtained at other amplitude ratios and frequencies. In other words, varying the amplitude ratio and frequency one-at-a-time did not significantly influence the results, i.e. the number of roots remained the same.

The results shown here show that it is possible to determine the number of LCOs that will occur based on the number of roots of the response surface. Furthermore, the stability of the LCOs can also be determined using the gradient of the response surface in the direction of the amplitude of the first degree-of-freedom.

RESPONSE SURFACE CURVATURE

When all terms in the non-linear damping matrix (i.e. the matrix on the right-hand side of (5.3)) are non-zero, the response surface no longer exhibits zeros near the LCO amplitude. Therefore, the local curvature of the response surface is inspected, as it might reveal the type of bifurcation that occurs or the stability of the LCOs. That is, the two DoF van der Pol oscillator system has been used to test which type of curvature (convex or concave) is required for a certain bifurcation type. Again, two mode shape parameters have been fixed, the amplitude ratio and the frequency, these were seen not to change significantly for the various cases tested (with different values of the constants in the non-linear force term (right-hand side of (5.3))). When $\epsilon = 0.002$, $a_1 = -6$, $a_2 = -2$, $a_3 = -1$, $a_4 = -4$, $b_1 = 0.25$, $b_2 = 0.5$ and $c_1 = 1$ and $\mu = -0.5$, then the amplitude ratio and the angular frequency of the first mode are 0.618 and 1.954 rad/s, respectively. The same values are obtained when b_1 and b_2 are set to zero (no fourth order terms). Furthermore, when the signs of a_1 till b_2 and that of μ are reversed the same amplitude ratio and frequency are obtained, also when b_1 and b_2 are set to zero in addition. Starting with the first test case ($\epsilon = 0.002$, $a_1 = -6$, $a_2 = -2$, $a_3 = -1$, $a_4 = -4$, $b_1 = 0.25$, $b_2 = 0.5$ and $c_1 = 1$ and $\mu = -0.5$), two LCOs are observed, a stable LCO with an amplitude of 0.954 ($\Delta\phi = -0.0140°$) and an unstable LCO with an amplitude of 4.721 ($\Delta\phi = 0.4454°$). The response surface for this test case is depicted in Figure 5.36. This figure shows the real and imaginary parts of the non-linear damping force of both DoFs. In addition, the two LCOs that occur at these conditions are depicted. The unstable LCO is depicted with a violet circle (for visibility reasons the phase difference has been multiplied by a factor 1000) and the stable LCO is depicted with a yellow square (with a factor 20 for the phase difference).

From Figure 5.36 it is observed that there are several extrema in the real and imaginary parts of the non-linear damping forces. To further identify the local curvature, slices of this response surface have been made at the LCO amplitudes. Figure 5.37 shows these

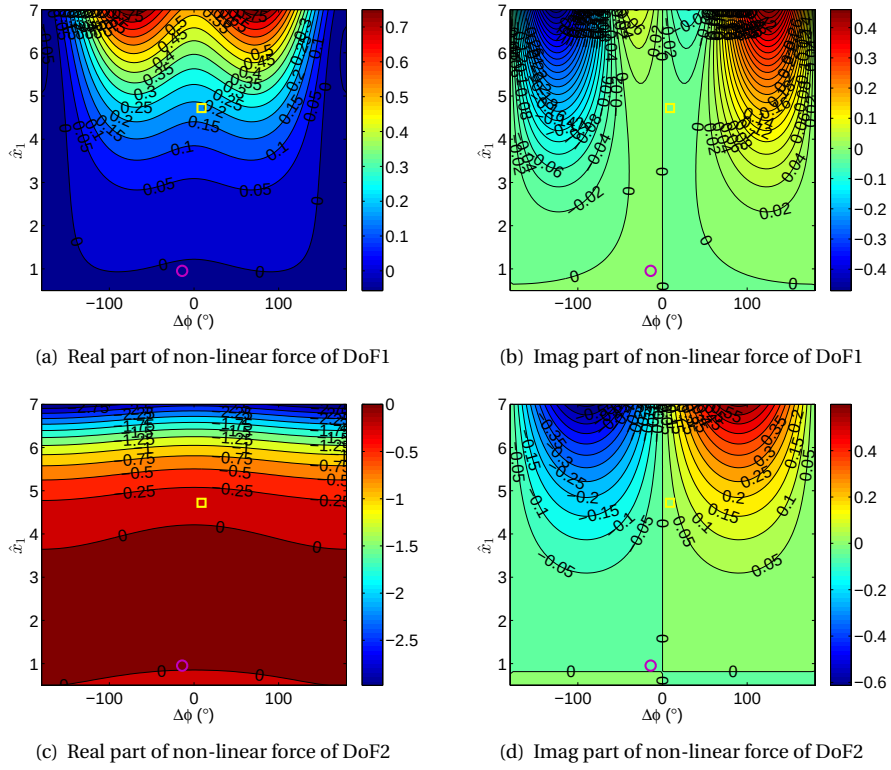

(a) Real part of non-linear force of DoF1

(b) Imag part of non-linear force of DoF1

(c) Real part of non-linear force of DoF2

(d) Imag part of non-linear force of DoF2

Figure 5.36: Contours of real and imaginary parts of the non-linear damping force for the two degree-of-freedom van der Pol oscillator at $\hat{x}_1/\hat{x}_2 = 0.618$ and $\omega_1 = 1.954$ rad/s ($\epsilon = 0.002$, $\mu = -0.5$, $a_1 = -6$, $a_2 = -2$, $a_3 = -1$, $a_4 = -4$, $b_1 = 0.25$, $b_2 = 0.5$ and $c_1 = 1$)

slices. The blue curves depict the unstable LCO mode shape and the green curves the stable LCO mode shape. For the real part of the non-linear damping force of the first DoF, Figure 5.36(a), the curvature of the response surface is convex for both amplitudes. In contrast, the imaginary part, see Figure 5.36(b), is concave for the small-amplitude case and convex for the large-amplitude case. The real part of the non-linear damping force of the second DoF, see Figure 5.36(c), is convex for the unstable LCO and concave for the stable LCO. The same holds for the imaginary part of this force. However, it should be noted that for the non-linear force of the first DoF there exist multiple minima or maxima. For the small-amplitude LCO these have approximately the same magnitude. For the large-amplitude LCO the minima or maxima close to the ordinate are much smaller in magnitude than those further away from the ordinate. Hence, when these local extrema are ignored, the curvature of the large-amplitude case becomes concave for both the real and imaginary part of the non-linear damping force of DoF one (since the phase difference is larger than zero for the large-amplitude LCO). That means, for the real part of the non-linear damping force of DoF1, that when the (local) curvature is concave the

LCO is unstable, whereas when the (local) curvature is convex the LCO is stable. For the imaginary part the curvature for both types of LCOs would then be concave (since for the small-amplitude LCO the phase difference is smaller than zero). Hence, from the curvature of the imaginary part of the non-linear damping force of the first degree of freedom no conclusions can be drawn regarding the stability of the LCO.

The small extrema near the ordinate disappear for large values of μ, see Figure 5.38, which shows the real and imaginary parts of the non-linear damping force of the first DoF versus the phase difference for $\mu = 60$. For this value of μ only one stable LCO occurs at 7.903. The LCO mode shape has changed slightly to an amplitude ratio of 0.621 and an angular frequency of 1.966. The phase difference for the stable LCO is 5.423°.

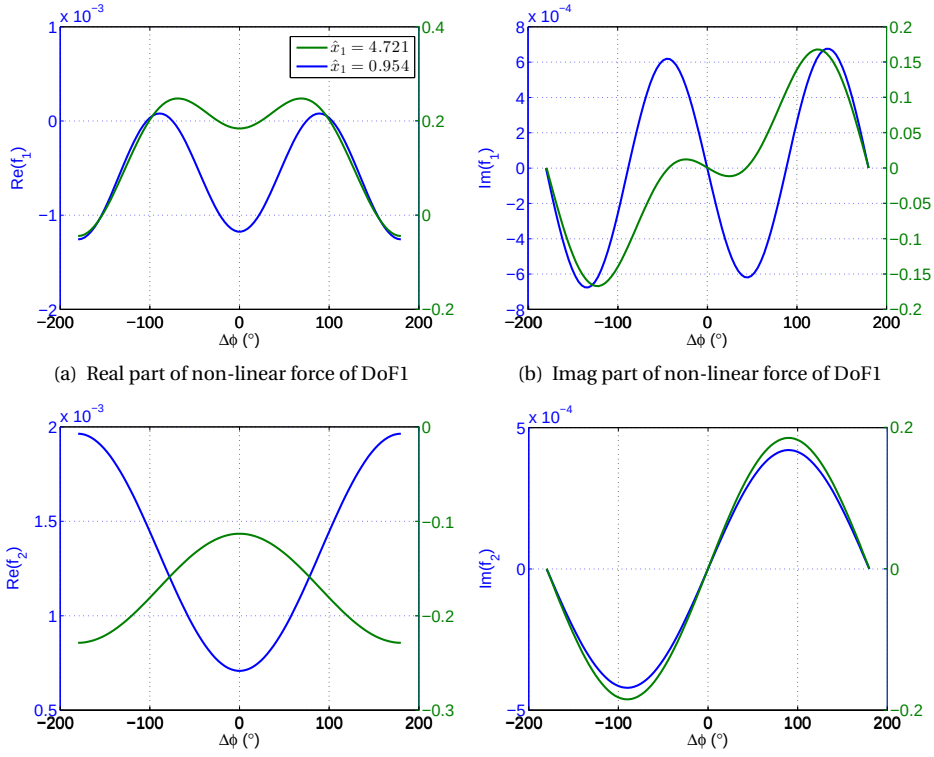

(a) Real part of non-linear force of DoF1

(b) Imag part of non-linear force of DoF1

(c) Real part of non-linear force of DoF2

(d) Imag part of non-linear force of DoF2

Figure 5.37: Real and imaginary parts of the non-linear damping force versus the phase difference for the two degree-of-freedom van der Pol oscillator at $\hat{x}_1/\hat{x}_2 = 0.618$ and $\omega_1 = 1.954$ rad/s ($\epsilon = 0.002$, $\mu = -0.5$, $a_1 = -6$, $a_2 = -2$, $a_3 = -1$, $a_4 = -4$, $b_1 = 0.25$, $b_2 = 0.5$ and $c_1 = 1$)

To draw conclusions with respect to the curvature and the type of LCO (or bifurcation) that occurs, a case with opposite signs has been investigated (i.e. a_1 till a_4, b_1, b_2 and μ with opposite signs) as well as a case were only one LCO occurs (i.e. $b_1 = b_2 = 0$). Table 5.6 summarises the results. ϵ has been set to 0.002 and c_1 has been set to 1 for all

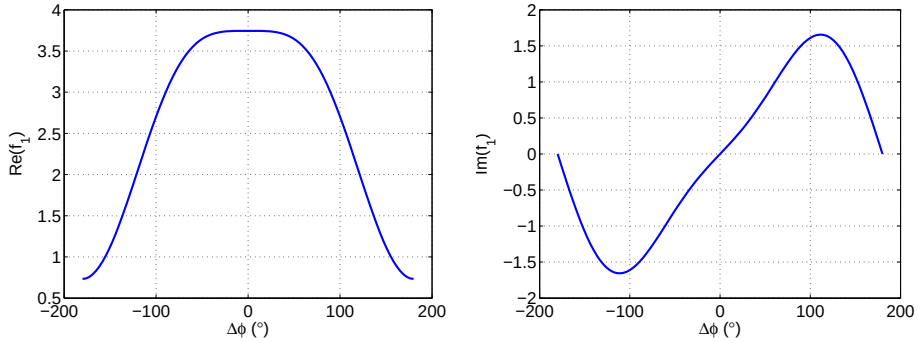

(a) Real part of non-linear force

(b) Imag part of non-linear force

Figure 5.38: Real and imaginary parts of the non-linear damping force for DoF1 versus the phase difference for the two degree-of-freedom van der Pol oscillator at $\hat{x}_1/\hat{x}_2 = 0.6214$ and $\omega_1 = 1.9656$ rad/s ($\epsilon = 0.002$, $\mu = 60$, $a_1 = -6$, $a_2 = -2$, $a_3 = -1$, $a_4 = -4$, $b_1 = 0.25$, $b_2 = 0.5$ and $c_1 = 1$)

cases. The results at large μ, or when the small extrema near the ordinate are ignored for large amplitudes, have also been included in Table 5.6. The only parameter that shows consistent curvature is the real part of the non-linear damping force of the second DoF. When the curvature of the response surface near the LCO mode shape is concave for this parameter a stable LCO occurs, when the curvature is convex an unstable LCO occurs. For the other parameters conclusions can be drawn when the global curvature is considered, i.e. when the small extrema near the ordinate are ignored (or when μ is large enough). In that case, for stable LCOs the curvature of the real part of the non-linear damping force of DoF1 is concave, whereas for unstable LCOs it is convex. The curvature of the imaginary part of the non-linear damping force of DoF1 is always concave, irrespective of the type of LCO that occurs. From the curvature of the imaginary part of the non-linear damping force of DoF2 no conclusion about the type of bifurcation can be drawn, see Table 5.6.

From the considerations concerning the two DoF van der Pol-oscillator it becomes clear that the curvature of the response surface can be used to determine the stability of the LCO.

5.5.3. TWO DOF AIRFOIL SYSTEM

In order to investigate what non-linearity is responsible for the bifurcation behaviour, each of the aerodynamic forces ($|\theta_{Lh}|$, ϕ_{Lh}, $|\theta_{M\alpha}|$ and $\phi_{M\alpha}$) has been held constant separately (one-at-a-time analysis). The forces have each been set, one at a time, to their first (non-zero) amplitude-sample-value. Then ADePK has been used to compute the bifurcation behaviour (with cubic spline interpolation). This is performed for all Mach numbers of the inviscid Mach number test case shown in Section 5.3. Figure 5.39 shows the resulting bifurcation behaviour for four Mach numbers: $M = 0.6$, $M = 0.72$, $M = 0.75$ and $M = 0.8$.

From Figure 5.39 it is clearly seen that the setting the phase of the lift constant results

							stable LCO				unstable LCO			
μ	a_1	a_2	a_3	a_4	b_1	b_2	$\Re(f_1)$	$\Im(f_1)$	$\Re(f_2)$	$\Im(f_2)$	$\Re(f_1)$	$\Im(f_1)$	$\Re(f_2)$	$\Im(f_2)$
-0.5	-6	-2	-1	-4	0.25	0.5	convex	convex	concave	concave	convex	concave	convex	convex
60	-6	-2	-1	-4	0.25	0.5	concave	concave	concave	concave	-	-	-	-
-0.5	-6	-2	-1	-4	0	0	-	-	-	-	convex	concave	convex	convex
0.5	6	2	1	4	-0.25	-0.5	concave	concave	concave	convex	concave	convex	convex	concave
-60	6	2	1	4	-0.25	-0.5	-	-	-	-	convex	concave	convex	concave
0.5	6	2	1	4	0	0	concave	concave	concave	convex	-	-	-	-

Table 5.6: Curvature of the non-linear damping forces for the two degree-of-freedom van der Pol oscillator at the corresponding LCO mode shape ($\epsilon = 0.002$ and $c_1 = 1$)

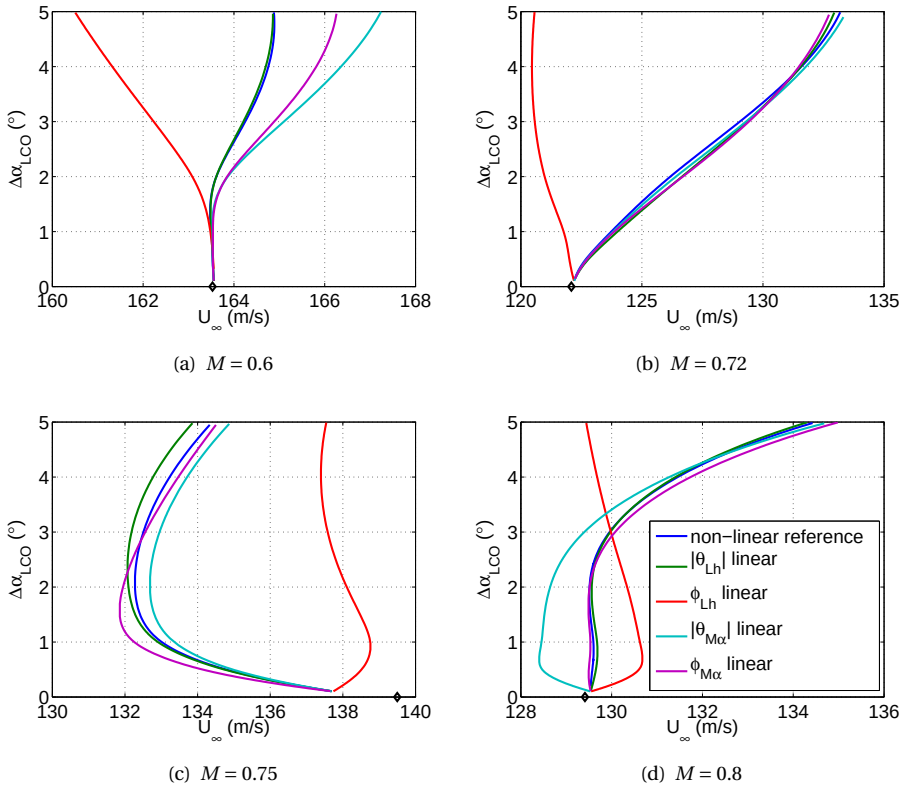

(a) $M = 0.6$ (b) $M = 0.72$

(c) $M = 0.75$ (d) $M = 0.8$

Figure 5.39: LCO amplitude vs freestream velocity for various Mach numbers in inviscid flow at $\bar{\alpha} = 0°$ applying one-at-a-time constant aerodynamic forces

in completely different bifurcation behaviour for all four Mach numbers. The importance of the non-linearity in the phase of the lift (with increasing amplitude) was already noted in Section 3.3.4 which discussed the energy budget of limit-cycle oscillations. The dependence of the bifurcation behaviour on the phase of the lift was noted before in Section 4.3.2. At $M = 0.6$ and $M = 0.72$ the bifurcation becomes subcritical, instead of the actual supercritical behaviour, when ϕ_{Lh} is held constant with amplitude. At $M = 0.75$ the LCO amplitude increases rapidly in case of a constant phase of the lift. Holding the remaining parameters constant does have a small influence on the bifurcation behaviour, but this influence is not as significant as in case of ϕ_{Lh}. However, when keeping the magnitude of the moment $|\theta_{M\alpha}|$ constant at $M = 0.8$, the bifurcation behaviour is also somewhat different from the non-linear case for amplitudes up to 4°. Although the trend towards a supercritical bifurcation is the same as in the non-linear case. This cannot be concluded in case of a constant ϕ_{Lh}. For other Mach numbers in inviscid flow similar trends regarding the bifurcation behaviour when ϕ_{Lh} is held constant are observed. The same holds for the other test cases of Section 5.2. The results of the one-at-a-time con-

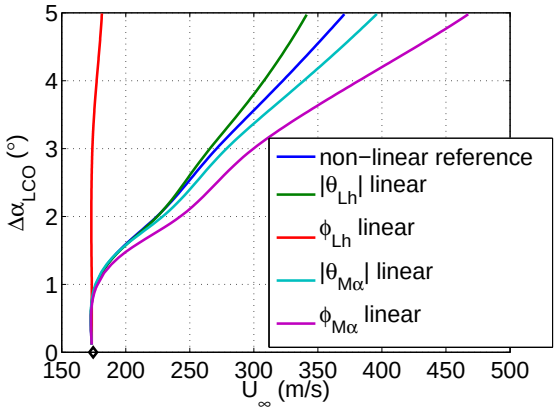

Figure 5.40: LCO amplitude vs freestream velocity in viscous flow at $M = 0.75$, $\bar{\alpha} = 0.7°$ applying one-at-a-time constant aerodynamic forces

stant aerodynamic force or moment analysis for the test case at $M = 0.75$ and $\bar{\alpha} = 0.7°$ are shown in Figure 5.40. The results for the other two aerodynamic non-linearities are shown in Section D.2 of Appendix D. From Figure 5.40 and the results shown in Section D.2, it is observed that keeping ϕ_{Lh} constant also results in the most significant deviation from the actual (non-linear) bifurcation behaviour. Hence, from this study it can be concluded that the non-linearities in the phase of the lift are responsible for the type of bifurcation that occurs. In addition, for some test cases (e.g. $M = 0.8$, $\bar{\alpha} = 0°$ in inviscid flow) non-linearities in the magnitude of the moment might influence the bifurcation type.

Now the question is can the observations and conclusions from Figures 5.39 and 5.40 be used to link a certain bifurcation behaviour to the response surface? In other words given a certain response surface, which types of bifurcations can occur provided the right structural properties are available? To answer these questions the aerodynamic response surface has been analysed through various slices. The observations from the two DoF van-der-Pol-oscillator cases as shown in Section 5.5.2 have been used. During this analysis it was noted that at those amplitudes at which the stability of the LCO changes, i.e. at a saddle-node bifurcation of limit cycles, the aerodynamic response surface also shows curvature changes. That is, the phase of the lift w.r.t. plunge shows curvature changes. Figure 5.41 depicts a slice of the response surface versus the pitch amplitude at $M = 0.75$ and $\bar{\alpha} = 0°$ in inviscid flow. The time domain reference samples at $|\theta_{h\alpha}| = 0.75$, $\phi_{h\alpha} = 5°$ and $k = 0.5$ and the interpolated response surface at this mode shape and frequency are shown in this figure by the squares and the blue dashed lines, respectively. This mode shape is close to the flutter mode shape, but at the sample locations of the response surface, such that one only sees the effect of the interpolation. Furthermore, slices of the response surface are shown versus pitch amplitude at the flutter mode shape (i.e. $|\theta_{h\alpha}| = 0.8964$, $\phi_{h\alpha} = 4.7966°$ and $k = 0.4424$, red lines) as well as at the mode shape at an LCO amplitude of 5° ($|\theta_{h\alpha}| = 0.8886$, $\phi_{h\alpha} = 4.0775°$ and $k = 0.4576$, green lines).

Figure 5.41 shows that ϕ_{Lh} exhibits a minimum at about 1.5°. From Figure 5.39(c), at this amplitude, the stability of the LCO changes from unstable to stable (i.e. a saddle-node bifurcation of LCOs occurs). $|\theta_{Lh}|$, $|\theta_{M\alpha}|$ and $\phi_{M\alpha}$ do not show this behaviour at 1.5°, although the phase of the moment changes curvature at an amplitude of 1°. The flutter and $\Delta\alpha_{LCO} = 5°$-mode shapes are very similar, they are only shifted on the ordinate. A direct comparison of the shape of ϕ_{Lh} interpolated at the flutter mode shape and that of the bifurcation diagram is obtained when the freestream velocity is plotted versus the LCO amplitude, see Figure 5.42(a). Comparing this figure with Figure 5.41(c) clearly shows that the phase of the lift and the bifurcation diagram exhibit the same shape. In general, it was found that comparing the shape of the sine of ϕ_{Lh} at the flutter- and $\Delta\alpha_{LCO} = 5°$-mode shape is a better measure for the shape of the bifurcation diagram, see Figures 5.42(a) and 5.42(b). For this test case ϕ_{Lh} is close to zero and therefore the phase of the lift exhibits the same shape as the sine of this phase. However, when the phase of the lift is not close to zero, the sine of ϕ_{Lh} naturally has a different shape.

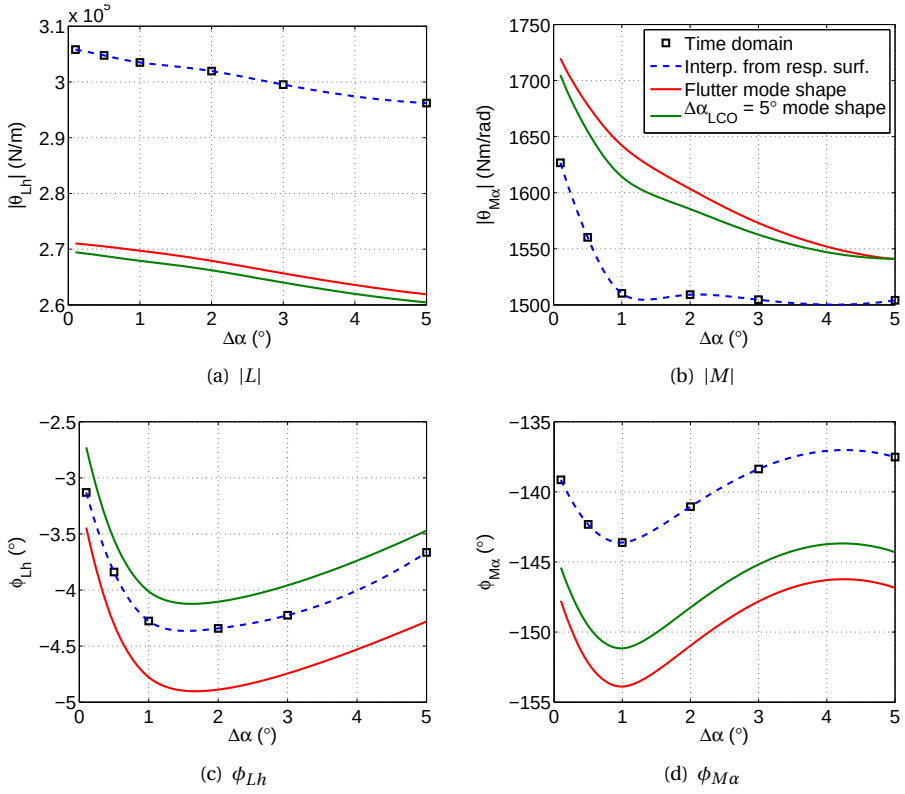

(a) $|L|$ (b) $|M|$

(c) ϕ_{Lh} (d) $\phi_{M\alpha}$

Figure 5.41: Response surface versus pitch amplitude for Euler simulations at $M = 0.75$, $\bar{\alpha} = 0°$ at $|\theta_{h\alpha}| = 0.75$, $\phi_{h\alpha} = 5°$ and $k = 0.5$, flutter mode shape and $\Delta\alpha_{LCO} = 5°$-mode shape

Figures 5.43, 5.44 and 5.45 show the freestream velocity versus the LCO amplitude and

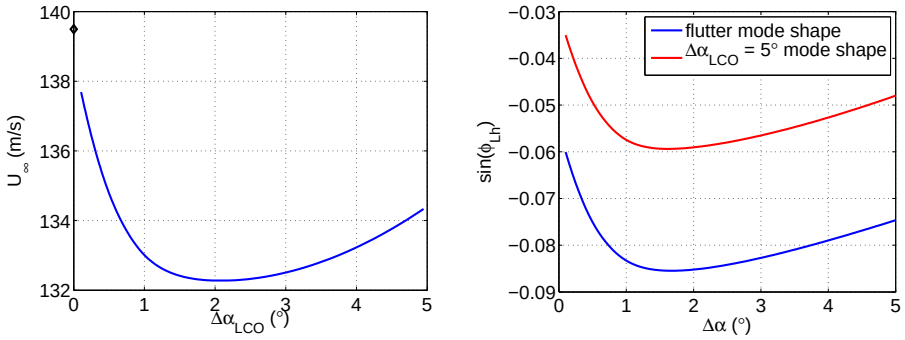

(a) U_∞ vs. $\Delta\alpha_{LCO}$ (b) $\sin(\phi_{Lh})$ vs. $\Delta\alpha$

Figure 5.42: Freestream velocity versus LCO amplitude and ϕ_{Lh} versus pitch amplitude for Euler simulations at $M = 0.75$, $\bar{\alpha} = 0°$ at flutter mode shape

the sine of the phase of the lift, interpolated at the flutter and the $\Delta\alpha_{LCO} = 5°$-mode shapes, versus pitch amplitude for $M = 0.6$, $M = 0.72$ and $M = 0.8$ (at $\bar{\alpha} = 0°$ in inviscid flow). Is is seen that at $M = 0.72$, the shape of the response surface is identical to the rotated bifurcation curve. However, at $M = 0.6$ and $M = 0.8$ the general trend at larger amplitudes is the same, but at small amplitudes there is no agreement. Upon comparing with Figure 5.39 it is noted that at these two Mach numbers the bifurcation behaviour is significantly different when the magnitude of the moment $|\theta_{M\alpha}|$ is constant, whereas for the other Mach numbers only a constant phase of the lift resulted in a completely different bifurcation behaviour. This might be the cause of the slight deviations at small oscillation amplitudes.

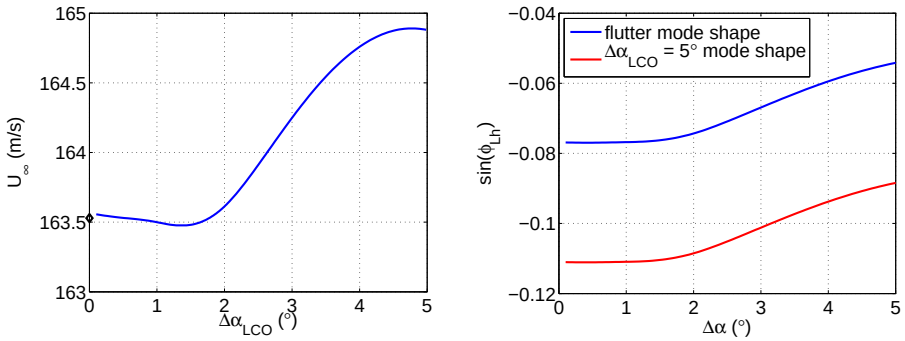

(a) U_∞ vs. $\Delta\alpha_{LCO}$ (b) $\sin(\phi_{Lh})$ vs. $\Delta\alpha$

Figure 5.43: Freestream velocity versus LCO amplitude and ϕ_{Lh} versus pitch amplitude for Euler simulations at $M = 0.6$, $\bar{\alpha} = 0°$ at flutter mode shape

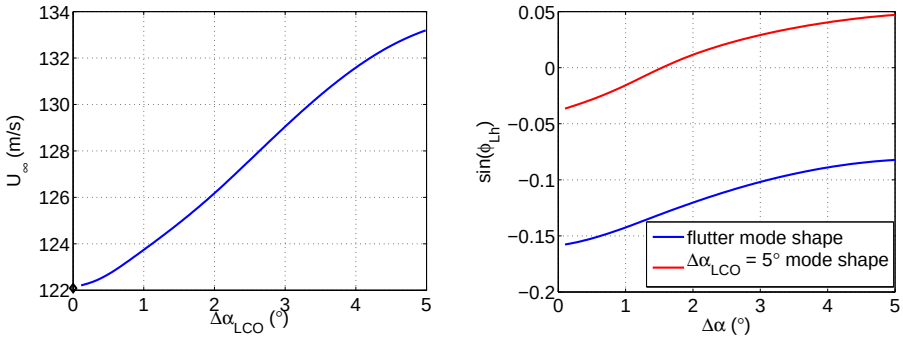

(a) U_∞ vs. $\Delta\alpha_{LCO}$ (b) $\sin(\phi_{Lh})$ vs. $\Delta\alpha$

Figure 5.44: Freestream velocity versus LCO amplitude and ϕ_{Lh} versus pitch amplitude for Euler simulations at $M = 0.72$, $\bar{\alpha} = 0°$ at flutter mode shape

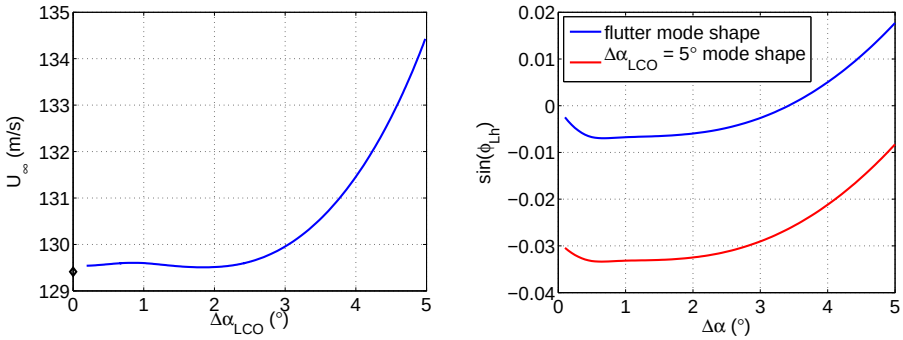

(a) U_∞ vs. $\Delta\alpha_{LCO}$ (b) $\sin(\phi_{Lh})$ vs. $\Delta\alpha$

Figure 5.45: Freestream velocity versus LCO amplitude and ϕ_{Lh} versus pitch amplitude for Euler simulations at $M = 0.8$, $\bar{\alpha} = 0°$ at flutter mode shape

The same analysis has been performed for the viscous flow test cases. The results in terms of freestream velocity versus LCO amplitude, sine of the phase of the lift interpolated at the flutter mode shape and at the $\Delta\alpha_{LCO} = 5°$-mode shape, are shown in Figure 5.46 for the test case at $M = 0.75$ and $\bar{\alpha} = 0.7°$. The results for the other two test cases are depicted in Section D.2 of the Appendix D. From all three figures it is observed that the sine of the phase of the lift and the freestream velocity exhibit the same shape. Hence, this suggests that when the non-linearity in the phase of the lift is responsible for the bifurcation behaviour (i.e. when a constant ϕ_{Lh} results in a completely different bifurcation behaviour), the shape of the response surface of the sine of the phase of the lift is the same as that of the bifurcation diagram. In case a constant magnitude of the moment $|\theta_{M\alpha}|$ results in a significantly different bifurcation behaviour, the shape of the response

surface does not exactly match that of the bifurcation diagram, but the overall trend is the same.

The observations made above are valid for test cases at the nominal structural parameters (see Table 2.1) and at zero structural damping. However, when the structural frequency ratio is changed, the shape of the bifurcation diagram is not always the same as that of the sine of ϕ_{Lh} at the flutter mode shape. In most cases there is an agreement in shape, but this is not generally true. At $M = 0.75$, $\bar{\alpha} = 0.7°$ and $\omega_h/\omega_\alpha = 1.20971$ in viscous flow for example, the shape of the rotated bifurcation diagram does not agree with either the phase of the lift nor the sine of the phase of the lift. Although the phase of the lift is the only parameter that results in a completely different bifurcation behaviour when ϕ_{Lh} is constant. Furthermore, the phase of the lift at the flutter mode shape is correctly interpolated as observed from comparison with forced motion results. Also, the non-linearity is less strong than for the nominal structural frequency ratio for this test case and non of the other aerodynamic forces show the exhibit the same shape as the bifurcation diagram. Hence, further investigations are necessary to identify why the bifurcation diagram shape and the shape of the sine of ϕ_{Lh} do not agree at $M = 0.75$, $\bar{\alpha} = 0.7°$ and $\omega_h/\omega_\alpha = 1.20971$ or to identify the shape of which parameter generally agrees better with the bifurcation diagram. For the remainder of this section the nominal structural parameters are considered and hence the the observations about the bifurcation behaviour and the shape of the response surface at the nominal structural parameters will be used.

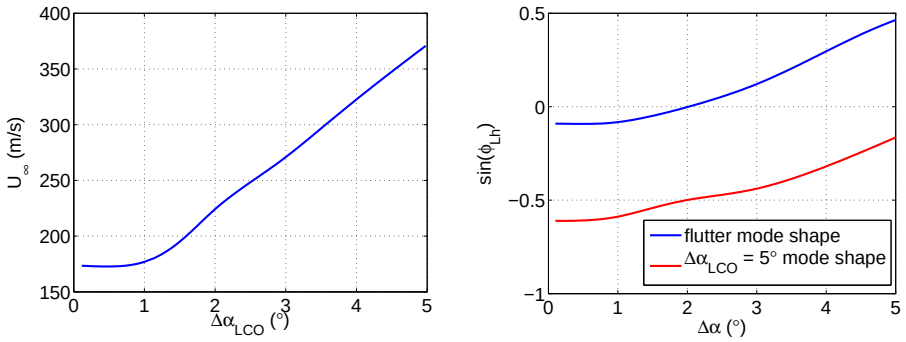

(a) U_∞ vs. $\Delta\alpha_{LCO}$ (b) $\sin(\phi_{Lh})$ vs. $\Delta\alpha$

Figure 5.46: Freestream velocity versus LCO amplitude and ϕ_{Lh} versus pitch amplitude for RANS simulations at $M = 0.75$, $\bar{\alpha} = 0.7°$ at flutter mode shape and $\Delta\alpha_{LCO} = 5°$-mode shape

Now a link has been established between the bifurcation diagram and the response surface, the response surface can be searched for changes in curvature that might result in other types of bifurcations. If these other types of bifurcations will occur depends on the structural properties. Furthermore, another open question might be answered using the link between the response surface and the bifurcation behaviour; which aerodynamic features are responsible for the form of the response surface? In order to do so, the unsteady local force distributions are considered.

For the inviscid flow case at $M = 0.75$, $\bar{\alpha} = 0°$ forced motion computations have been performed at the flutter mode shape and frequency, but with various pitch amplitudes ($\Delta\alpha = 0.1°, 0.5°, 1.0°, 2.0°, 3.0°, 4.0°$ and $5.0°$). The same phase of the lift versus amplitude was obtained as when using interpolation on the response surface, see Figure 5.47. The local force distribution was assessed to find out why the phase of the lift has this shape. The local magnitude (scaled with the pitch amplitude) and phase angle of the lift distributions are depicted in Figure 5.48. The phase of the lift is seen to decrease with increasing pitch amplitude, up to an amplitude of 2°, for larger amplitudes the phase increases again. This decrease can be explained as the typical effect that occurs with increasing pitch amplitude, i.e. the shock peaks decrease in height and spread out when the amplitude increases. This causes a decrease in the area under the local lift distribution. However, for $\Delta\alpha > 2°$ the phase of the lift increases. This increase can be explained from the local phase of the lift distribution as well. For amplitudes of 2° and larger there is a shock wave on the lower surface during part of the oscillation cycle, whereas at small amplitudes there is no shock wave on this surface. This Tijdeman [21] type B (i.e. intermittent) shock motion on the lower surface causes the phase of the lift to increase again. Hence, the shock motion on the lower surface causes the subcritical bifurcation with stable LCOs below the flutter boundary. This is in accordance with the observations of Bendiksen [1, 19], who also found that the change of the shock motion type is responsible for limit-cycle oscillations in inviscid flow.

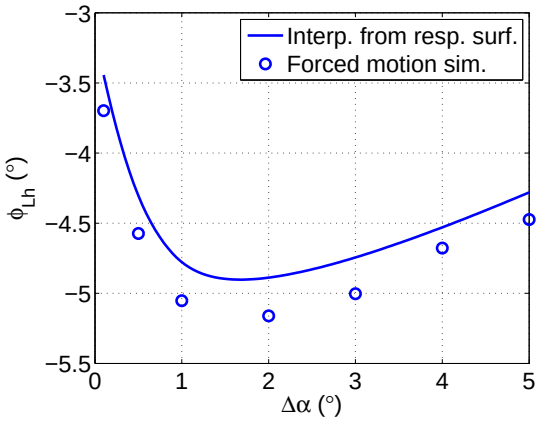

Figure 5.47: ϕ_{Lh} versus pitch amplitude for Euler simulations at $M = 0.75$, $\bar{\alpha} = 0°$ at flutter mode shape (interpolated on response surface vs. forced motion)

For the viscous test case at $M = 0.75$ and $\bar{\alpha} = 0.7°$ it is also observed that the (intermittent) shock motion of the lower surface causes the increase of the phase of the lift, see Figures 5.49 and 5.50. The Tijdeman [21] type B shock wave motion on the lower surface becomes larger and larger with increasing amplitude, this causes the phase of the lift on the lower surface to become positive over almost the complete surface. Therefore, in this case, the shock motion on the lower surface causes the supercritical bifurcation.

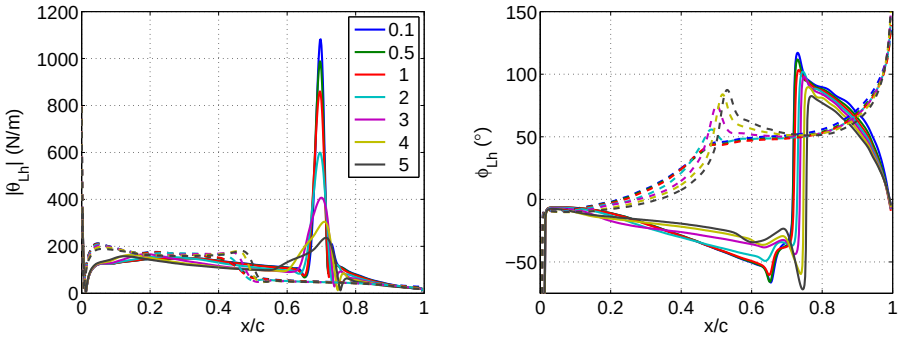

(a) $|\theta_{Lh}|$ vs. x/c (b) ϕ_{Lh} vs. x/c

Figure 5.48: Local force- and moment distribution for Euler simulations at $M = 0.75$, $\bar{\alpha} = 0°$ at flutter mode shape

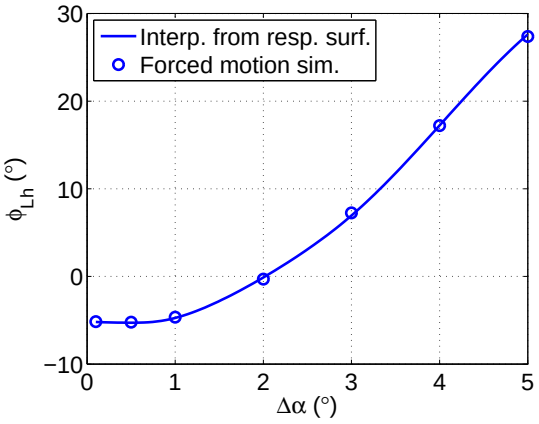

Figure 5.49: ϕ_{Lh} versus pitch amplitude for RANS simulations at $M = 0.75$, $\bar{\alpha} = 0°$ at flutter mode shape (interpolated on response surface vs. forced motion)

5.5.4. CONCLUSIONS

In order to determine whether the response surface can give hints about the LCO bifurcation behaviour, the relation between the response function or the response surface and the bifurcation behaviour has been addressed in this section. Section 5.5.1 has considered the one degree-of-freedom van der Pol oscillator system. For this system it was found that the real part of the response function (i.e. the real part of the Fourier transformed right-hand side of the non-linear damping term), shows a root at the LCO amplitude, which is known from bifurcation theory, see e.g. Gros [20]. From the gradient w.r.t. amplitude at the location of the root it can be determined whether the LCO is stable or unstable. Unstable LCOs exhibit a negative gradient w.r.t. amplitude and stable LCOs

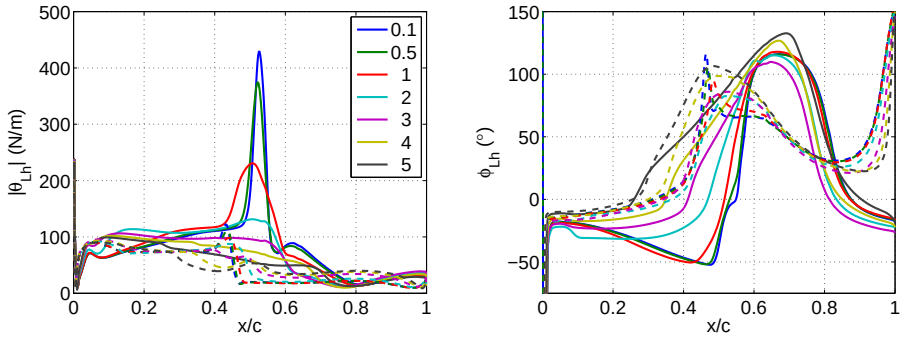

(a) $|\theta_{Lh}|$ vs. x/c (b) ϕ_{Lh} vs. x/c

Figure 5.50: Local force- and moment distribution for RANS simulations at $M = 0.75$, $\bar{\alpha} = 0^\circ$ at flutter mode shape

a positive gradient. Hence, the observations made here agree with commonly known bifurcation theory [20]. To investigate whether these observations also hold for a two-degree-of-freedom system, the van der Pol system has been extended with an additional degree of freedom. For the two degree-of-freedom van der Pol system with a "simple" non-linear damping of only one term, the gradient of the real part of the response surface w.r.t. amplitude can also be used to determine the stability of the LCO in the same way. However, once the non-linear damping force becomes more complicated, the response surface does not have a root at the LCO amplitude. In that case the curvature of the real part of the non-linear damping force of the second DoF w.r.t. the phase difference indicates the stability of the LCO. When the real part of this force shows a concave curvature in phase difference direction, the LCO is stable. When the curvature in phase difference direction is convex the LCO is unstable.

For the two DoF airfoil system, it was observed that the phase of the lift is most likely the part of the aerodynamic force vector that determines the type of bifurcation that occurs, since a linearisation of the other aerodynamic forces did mostly not result in a significantly different bifurcation behaviour. Furthermore, the shape of the sine of the phase of the lift versus pitch amplitude at the flutter mode shape was found to be very similar to the shape of the "rotated" bifurcation diagram (freestream velocity vs. LCO amplitude). For the transonic test cases, both in viscous and inviscid flow, this was found to be caused by the shock motion on the lower surface of the airfoil.

5.6. CONCLUSIONS

In this chapter the application of ADePK to various test cases was shown. The bifurcation behaviour of the limit-cycle oscillations has been studied for four different aerodynamic non-linearities; transonic inviscid flow, transonic flow with trailing-edge separation, subsonic flow with trailing-edge separation and subsonic flow with free boundary-layer transition. In case of transonic inviscid flow nested LCOs (i.e. both stable and un-

stable LCOs at one freestream velocity) are observed. In case of subsonic viscous flow, either with trailing-edge separation or with boundary layer transition, a slight subcritical bifurcation was found. The non-linearity was observed to be the largest in case of transonic viscous flow, where a supercritical bifurcation of the LCO amplitude was obtained. It was concluded that LCOs do probably occur for any Mach number and angle of attack for the NLR7301 airfoil.

The effects of variations in the Mach number in inviscid flow on the flutter boundary and the LCO bifurcation behaviour have also been studied. LCOs were observed even for subsonic Mach numbers, although the non-linearity is much smaller for these Mach numbers than for Mach number near the transonic dip. If LCOs of a certain amplitude, for example 4°, are considered, the transonic dip can be significantly reduced. It may disappear altogether if LCOs of even larger amplitude are considered. Subcritical bifurcation behaviour was observed for Mach numbers just below and just above the transonic dip location. At the transonic dip, the bifurcation was supercritical.

A variation of the (linear) structural model parameters has been applied. The structural frequency ratio, the mass ratio, the structural damping and the elastic axis location of the two DoF airfoil system have been varied. Varying the structural frequency ratio showed that even though the bifurcation at the nominal structural frequency ratio is supercritical, a change in structural frequency ratio can make the bifurcation subcritical (or the other way around). Hence, a change in structural stiffness can cause LCOs below the (linear) flutter boundary. Furthermore, it was found that a subcritical bifurcation does not always have to be pitch dominated and the supercritical bifurcation is not always plunge dominated. The type of bifurcation was found to be relatively insensitive to a variation of the mass ratio or the structural damping. Only at a structural frequency ratio at which the non-linearity is already weak, a change in mass ratio or structural damping can cause a change in the bifurcation behaviour. However, the slope of the bifurcation diagram is influenced by a change in the mass ratio or the structural damping. When the elastic axis was shifted to a location behind the quarter-chord point similar bifurcation behaviour as when the elastic axis is located at the quarter-chord point was observed. However, the slope of the bifurcation curve changed significantly. When the non-linearity is weak, shifting the elastic axis will quickly result in a change of bifurcation type. Overall, it can be concluded that variations in the structural parameters must be considered when predicting of limit-cycle oscillations, as they significantly affect the bifurcation behaviour (in both strength and type).

The response surface curvature was found to reveal the type of bifurcation behaviour that occurs. For the one DoF van der Pol-oscillator the roots of the response function indicate the LCO amplitude and the type of LCO that occurs (i.e. the gradient in amplitude-direction), whereas the curvature of the response surface in phase difference-direction indicates the stability of the LCO for the two DoF van der Pol-oscillator. The phase of the lift was found to be responsible for the type of bifurcation that occurs for the two DoF airfoil system at its nominal structural parameters. The shape of the rotated bifurcation diagram, i.e. the freestream velocity versus the LCO amplitude, is very similar to that of the sine of the phase of the lift versus oscillation amplitude at the flutter mode shape (and at the $\Delta\alpha = 5°$-mode shape). Hence, in that case, only a flutter calculation and a few forced motion oscillation simulations at the flutter mode shape would be sufficient

to determine the bifurcation behaviour. However, the sine of the phase of the lift does not always have the same shape as the LCO amplitude bifurcation diagram when the structural frequency ratio is varied. Nevertheless, for the inviscid and viscous transonic flow test cases (at the nominal structural parameters) it was investigated what causes the shape of the phase of the lift versus oscillation amplitude. For both cases, the shock motion on the lower surface was found to be responsible for the curvature of the phase of the lift and hence for the bifurcation behaviour.

REFERENCES

[1] O. Bendiksen, *Influence of shocks on transonic flutter of flexible wings,* (University of California, Los Angeles, Palm Springs, California, 2009) 50th AIAA/ASME/ASCE/AHS/ASC Structures, Structural Dynamics, and Materials Conference.

[2] D. Kholodar, J. Thomas, and E. Dowell, *A parameter study of transonic airfoil flutter and limit cycle oscillation behaviour,* (Denver, CO, 2002) 43rd AIAA/ASME/ASCE/AHS/ASC Structures, Structural Dynamics, and Materials Conference and Exhibit.

[3] D. Kholodar, E. Dowell, J. Thomas, and K. Hall, *Limit-cycle oscillations of a typical airfoil in transonic flow,* Journal of Aircraft **41** (2004).

[4] D. Poirel and F. Mendes, *Experimental small-amplitude self-sustained pitch-heave oscillations at transitional reynolds numbers,* AIAA Journal **52**, 1581 (2014).

[5] G. Dietz, G. Schewe, and H. Mai, *Experiments on heave/pitch limit-cycle oscillations of a supercritical airfoil close to the transonic dip,* Journal of Fluids and Structures **19**, 1 (2004).

[6] O. Bendiksen, *Review of unsteady transonic aerodynamics: Theory and applications,* Prog Aerospace Sci **47**, 135 (2011).

[7] J. Thomas, E. Dowell, and K. Hall, *Modeling viscous transonic limit cycle oscillation behavior using a harmonic balance approach,* (Duke University, Durham, NC, Denver, CO, 2002) 43rd AIAA/ASME/ASCE/AHS/ASC Structures, Structural Dynamics, and Materials Conference and Exhibit.

[8] D. Poirel, Y. Harris, and A. Benaissa, *Self-sustained aeroelastic oscillations of a naca0012 airfoil at low-to-moderate reynolds numbers,* Journal of Fluids and Structures **24**, 700 (2008).

[9] D. Poirel and W. Yuan, *Aerodynamics of laminar separation flutter at a transitional reynolds number,* Journal of Fluids and Structures **26**, 1174 (2010).

[10] D. Poirel, V. Métivier, and G. Dumas, *Computational aeroelastic simulations of self-sustained pitch oscillations of a naca0012 at transitional reynolds numbers,* Journal of Fluids and Structures **27**, 1262 (2011).

[11] W. Yuan, D. Poirel, and B. Wang, *Simulations of pitch-heave limit-cycle oscillations at a transitional reynolds number,* AIAA Journal **51**, 1716 (2013).

[12] N. Razak, T. Andrianne, and G. Dimitriadis, *Flutter and stall flutter of a rectangular wing in a wind tunnel,* AIAA Journal **49** (2011).

[13] E. Dowell, *A Modern Course in Aeroelasticity* (Kluwer Academic Publishers, 2004).

[14] G. Schewe, A. Knipfer, H. Mai, and G. Dietz, *Experimental and Numerical Investigation of Nonlinear Effects in Transonic Flutter*, Internal Report DLR IB 232 - 2002 J 01 (Deutsches Zentrum für Luft- und Raumfahrt e.V. (DLR), Institut für Aeroelastik, Göttingen, Germany, 2002).

[15] G. Schewe, H. Mai, and G. Dietz, *Nonlinear effects in transonic flutter with emphasis on manifestations of limit cycle oscillations,* Journal of Fluids and Structures **18**, 3 (2003).

[16] G. Dietz, G. Schewe, and H. Mai, *Amplification and amplitude limitation of heave/pitch limit-cycle oscillations close to the transonic dip,* Journal of Fluids and Structures **22**, 505 (2006).

[17] S. Yang, Z. Zhang, F. Liu, S. Luo, H.-M. Tasi, and D. Schuster, *Time-domain aeroelastic simulation by a coupled euler and integral boundary-layer method,* (Providence, RI, USA, 2004) 22nd Applied Aerodynamics Conference and Exhibit.

[18] K. Hall, J. Thomas, and E. Dowell, *Proper orthogonal decomposition technique for transonic unsteady aerodynamic flows,* AIAA Journal **38**, 1853 (2000).

[19] O. Bendiksen, *Transonic limit cycle flutter/lco,* (Univerisity of California, Los Angelos, Palm Springs, California, 2004) 45th AIAA/ASME/ASCE/AHS/ASC Structures, Structural Dynamics, and Materials Conference.

[20] C. Gros, *Bifurcations and Choas in Dynamical Systems*, Tech. Rep. (Goethe Universität Frankfurt am Main, 2014) lecture notes course Self-Organization: Theory and Simulation.

[21] H. Tijdeman, *Investigations of the transonic flow around oscillation airfoils*, Ph.D. thesis, Technische Hogeschool Delft (1977).

6

CONCLUSIONS AND OUTLOOK

In this thesis limit-cycle oscillations of a two degree-of-freedom airfoil system with aerodynamic non-linearities have been studied using the supercritical NLR7301 airfoil. In order to do so, both time and frequency domain methods have been applied. The energy budget of LCOs has been studied using simulations in the time domain, both fluid-structure coupled and forced motion. However, systematic investigations into the LCO behaviour as function of e.g. the freestream speed or the structural model are computationally expensive, or even impossible using fluid-structure coupling. Therefore, a new frequency domain method has been developed for this purpose. This method is an extension of the p-k method used in classical flutter analysis. The method was first verified and validated for a classical non-linear dynamical system, the van der Pol-oscillator. Then it was applied to a two degree-of-freedom airfoil system. Validation against coupled time domain simulations showed a very good agreement. The so-called amplitude-dependent p-k method, or ADePK for short, was then used to study the bifurcation behaviour of four test cases; each with a different aerodynamic non-linearity: inviscid transonic flow, viscous transonic flow, subsonic flow with trailing-edge separation and subsonic flow with free boundary layer transition. Furthermore, the effect of a Mach number variation in inviscid flow and the effect of structural parameter variations were studied. Finally, the response surface necessary to use ADePK was analysed, linked to the LCO bifurcation behaviour and to local features in the flow. This chapter shows the conclusions per chapter of this thesis. An outlook to further work is given at the end of this chapter.

6.1. ENERGY BUDGET ANALYSIS

Chapter 3 studied the energy budget of the limit-cycle oscillations. From the aerodynamic forces and the pitch/plunge velocities, the mean aerodynamic power components were computed as well as the mean power of the structural damping. The sum of these mean power components (mean power of the lift, moment and structural damping) is zero at the LCO amplitude, since the work done on the structure by the aerodynamic forces is compensated by the work done on the structure by the damping. The

mean power components in the LCO case have been compared to those that would have occurred in the linearised flutter case, which were obtained from harmonic forced motion oscillations at the flutter mode shape. A defect in the power of the lift and in the power of the moment is observed. However, the defect in the power of the lift is much larger than that in the power of the moment. This was found to be caused by the amplitude dependence of the phase of the lift and the phase of the moment. The phase of the lift is close to zero in the linearised case and increases for larger amplitudes. This leads to large changes in the power of the lift with amplitude, since the imaginary part of the lift will then also change a lot with amplitude. In contrast, the phase of the moment is close to $-90°$ and hence changes in the phase will not have a large influence on the imaginary part of the moment and on the power of the moment. Local force distributions revealed a complex flow behaviour with shock waves and separation. Therefore, no local source of the amplitude limitation could be identified.

In addition to FSI simulations, corresponding simulations were performed in which the airfoil undergoes a forced motion at constant amplitude at its fundamental harmonic. A comparison of the power components showed that the agreement with the time domain simulations is good. Hence, an LCO can be described with sufficient accuracy using a forced motion oscillation taking into account the first harmonic only.

6.2. VERIFICATION AND VALIDATION OF THE AMPLITUDE-DEPENDENT P-K METHOD

In Chapter 4 the amplitude-dependent p-k method ADePK that has been developed in this thesis (see Chapter 2) has been verified and validated. ADePK allows the study of limit-cycle oscillations in the frequency domain. In contrast to the conventional p-k method, the aerodynamic forces are no longer a function of frequency only, but the amplitudes of both pitch and plunge, as well as the phase difference between both motions, must be taken into account. Hence, a four dimensional response surface is needed on which the aerodynamic forces are interpolated. Response surface samples have been generated using CFD simulations. Chapter 4 showed that the range in which the samples need to be placed can be estimated based on a structural parameter variation of the linear flutter case.

The LCO bifurcation behaviour of the NLR7301 airfoil at $M = 0.74$, $\alpha = -1.5°$ in inviscid flow determined using ADePK showed good agreement to the bifurcation behaviour obtained from fluid-structure coupled simulations. Both methods predict a supercritical bifurcation. Polynomial and cubic spline interpolation shows the best agreement with the time domain results. Near the linear flutter point, small deviations are present. These are clearly a result of the response surface and hence are explained as such. The test cases in Chapter 5 also confirm that the results of polynomial and cubic spline interpolation are identical on large velocity ranges. A variation in the natural uncoupled structural frequency ratio for the validation test case showed the power of ADePK. Once a response surface at a certain Mach number and angle of attack has been set up, the structural parameters can be easily varied, which leads to significant computational time savings in comparison to coupled fluid-structure interaction simulations.

6.3. BIFURCATION BEHAVIOUR OF LIMIT-CYCLE OSCILLATION SOLUTIONS

The limit-cycle oscillation bifurcation behaviour of the NLR7301 airfoil has been studied using ADePK in Chapter 5. The two degree-of-freedom airfoil system has been subjected to four different aerodynamic non-linearities; transonic inviscid flow, transonic flow with trailing-edge separation, subsonic flow with trailing-edge separation and subsonic flow with free boundary-layer transition. LCOs were observed for each of these non-linearities. In the viscous transonic flow case the non-linearity was the strongest. In the inviscid transonic flow case both stable and unstable limit-cycle oscillations were presented at the same freestream velocity, i.e. nested LCOs occurred, with stable LCOs below the linear flutter point. From a Mach number variation in inviscid flow the non-linearity was observed to be the strongest at the transonic dip. Contours of the LCO amplitude showed a significantly less deep transonic dip when LCOs of amplitudes up to 5° were considered. Subcritical bifurcations were observed in inviscid flow at Mach numbers just below and just above the transonic dip location. Furthermore, in subsonic transitional flow slightly subcritical bifurcations were found. However, the same bifurcation behaviour was observed in fully turbulent flow at the same conditions. Therefore, the bifurcation behaviour could not be related to the boundary-layer transition or -separation behaviour. Further investigations are necessary to study this relation.

A structural parameter variation was performed for each aerodynamic non-linearity. The structural frequency ratio was varied by varying the plunge stiffness. This has shown that for all test cases a subcritical bifurcation behaviour is possible with a certain plunge stiffness, i.e. the bifurcation behaviour can change from benign to detrimental under a structural frequency ratio variation. Subcritical bifurcations consisting of unstable LCOs only (up to 5°) were found to occur at certain structural frequency ratios in viscous transonic flow, in subsonic flow at large angle of attack and in inviscid transonic flow (for the validation test case of Chapter 4). Changes of the non-dimensional mass ratio do not significantly change the bifurcation type, unless the non-linearity is very weak. The same holds for the addition of structural damping. However, the strength of the non-linearity is influenced. When the elastic axis location is moved, the changes in the bifurcation behaviour become more significant than for the mass ratio and structural damping. In case of an already weak non-linearity when the elastic axis is located at its nominal position (i.e. the quarter-chord point), a shift of the elastic axis results in a change of bifurcation type from supercritical to subcritical (or the other way around in inviscid transonic flow). For transitional flow supercritical bifurcations and slightly subcritical bifurcation of the LCO amplitude were found when the structural parameters were varied. No stable LCOs of large amplitude were found below the flutter boundary.

A study of the connection between the bifurcation behaviour and the response surface was carried out using one-at-a-time linearised analysis of the magnitude and phase of the aerodynamic lift or moment. From this study it was found that the phase of the lift is responsible for the bifurcation behaviour, similar to energy budget analysis of Chapter 3. The shape of the bifurcation diagram is the same as that of the sine of the phase of the lift in the pitch amplitude slice of the response surface. The flutter mode shape has been used to determine the variation of the phase of the lift with oscillation amplitude.

Hence, when the flutter mode shape has been computed, forced motion oscillation simulations at various amplitudes can be used to determine the variation of the sine of the phase of the lift with amplitude and hence the bifurcation behaviour. This would save further computational work. However, the observations w.r.t. the sine of the phase of the lift and the bifurcation behaviour shapes were found to be not always valid when the structural frequency ratio is varied. Therefore, this method should be treated with care.

Forced motion oscillation simulations were performed to find the local source of the shape of the phase of the lift. The shock motion of the lower surface was found to be responsible for the shape of the phase of the lift-versus-amplitude-diagram and hence for the type of bifurcation behaviour in both viscous and inviscid transonic flow.

6.4. OUTLOOK

The fundamental bifurcation behaviour of LCOs has been studied in this thesis for a two degree-of-freedom airfoil system with aerodynamic non-linearities. This thesis work serves as a basis for further studies of LCOs of airfoils and wings.

As a next step the ADePK method could be extended to a three degree-of-freedom airfoil system and then a three dimensional wing should be considered. However, extension of ADePK to three dimensional problems with more degrees of freedom is problematic, since a significant increase of the dimensions of the problems will occur. The order of the response surface will increase rapidly. One way to circumvent the problem of the higher order response surface is to first perform a flutter analysis for a higher-than-two degree-of-freedom system and to identify the two degrees of freedom that couple during flutter from this analysis. Then ADePK can be applied on those two degrees of freedom only in order to predict limit-cycle oscillations. Another way would be to use superposition of describing functions which takes into account the amplitude of both degrees of freedom, but not the phase difference between the degrees of freedom. This concept needs further exploration. It has been applied by a few researchers and was tested only briefly in this thesis. Although some accuracy is lost the same trends are observed for the case tested in this thesis. Superposition of the aerodynamic forces might be useful for the analysis of LCOs of three-dimensional wings or complete aircraft, since no combined forced motion oscillation simulations need to be performed.

Further investigations into the relation between the bifurcation behaviour and the curvature of the response surface are necessary. It might be possible to find a “rule of thumb” for the LCO bifurcation behaviour when the (linear) flutter behaviour is known. Furthermore, the concept of matched/non-matched aerodynamic forces must be addressed in order to check the influence of (small) variations of the aerodynamic forces with freestream velocity on the bifurcation behaviour. Similarly, the effect of changes in the equilibrium position of the airfoil system due changes in structural parameters should be addressed. Moreover, the free boundary-layer transition case needs further study to identify whether LCOs solely based on the non-linearities resulting from boundary layer transition (or the accompanying separation bubbles) can exist. Finally, the physical behaviour of shock waves and boundary layers and their interaction during an LCO cycle needs further study to identify the causes of amplitude limitation.

A

EXPERIMENTAL VALIDATION

In order to check whether the results of the DLR-TAU code are reliable, a comparison with the results of the wind tunnel experiments of Dietz et al. [1] has been made. Therefore, the steady pressure distributions of the test cases TL1 and TL2 of Dietz et al.'s paper are compared with the results obtained from the TAU code. In the experiments of Dietz et al. [1] a transition trip has been applied at 7% of the chord length on the upper surface and at 14% of the chord length on the lower surface. In the CFD code both completely turbulent flow (from the leading edge) as well transitional flow with the experimental transition trip locations has been simulated. The TL1 testcase is at a Mach number of 0.745, a Reynolds number of $2.26 \cdot 10^6$, a static freestream temperature of 275.26 K and an angle of attack of 0.02°. For the TL2 test case the Mach number is 0.683, the Reynolds number is $2.16 \cdot 10^6$, the static freestream temperature is 278.95 K and the angle of attack is 1.31°. Figures A.1 and A.2 show the pressure and skin friction distributions obtained from the wind tunnel experiments of Dietz et al. [1] and those obtained from TAU for TL1 and for TL2, respectively. For TL2 a very good agreement is observed on both upper and lower surface for both CFD simulations, whereas at $M = 0.745$ there are some deviations. On the upper surface the shock positions are predicted reasonably well, but the pressure maximum between the shocks obtained from the CFD results is too low. On the lower surface the pressure as predicted from TAU is somewhat too low near the quarter-chord point and somewhat too high at the shock position. Downstream of the shocks the pressure shows good agreement on both surfaces, see Figure A.1(a). The differences between a fully turbulent boundary and a tripped boundary layer are small for both test cases. Although, the CFD results for the boundary layer trip at the experimental locations seem to agree slightly better to the experimental results. Figures A.1(b) and A.2(b) verify that transition takes places at the experimental trip locations. Overall, it can be concluded that TAU predicts the steady pressure reasonable well.

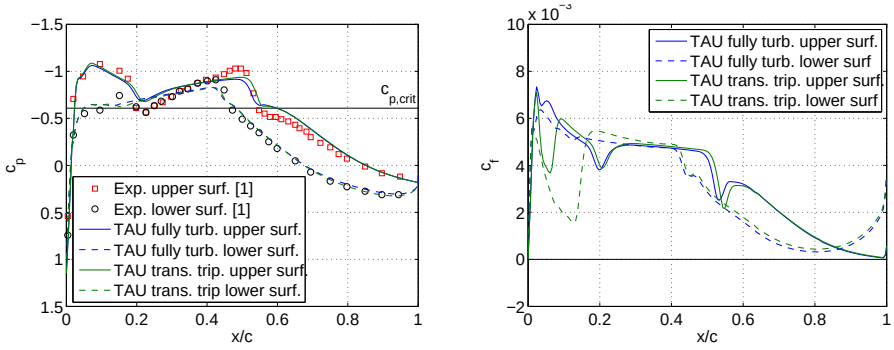

(a) (b)

A

Figure A.1: Steady pressure and skin friction distributions at $M = 0.745$, $\alpha = 0.02°$, $\mathrm{Re} = 2.26 \cdot 10^6$, $T_\infty = 275.26$ K

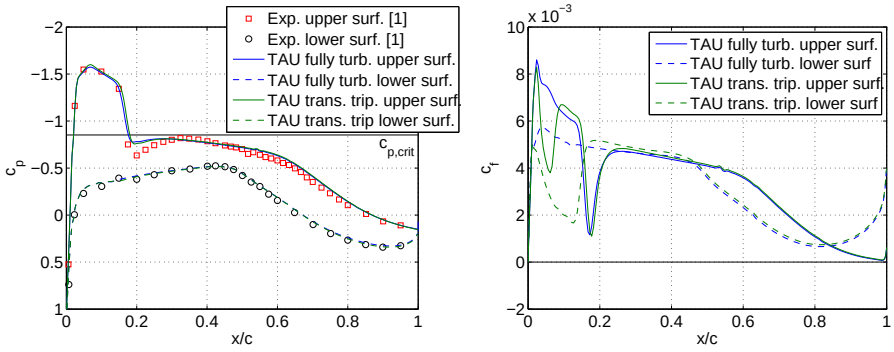

(a) (b)

Figure A.2: Steady pressure and skin friction distributions at $M = 0.683$, $\alpha = 1.31°$, $\mathrm{Re} = 2.16 \cdot 10^6$, $T_\infty = 278.95$ K

REFERENCES

[1] G. Dietz, G. Schewe, and H. Mai, *Experiments on heave/pitch limit-cycle oscillations of a supercritical airfoil close to the transonic dip,* Journal of Fluids and Structures **19**, 1 (2004).

B

MESH- AND TIME STEP CONVERGENCE

B.1. MESH

A mesh study was performed to find a suitable mesh, such that the results are accurate, but the computation is not too costly. This section shows the result of this study for two viscous and one inviscid test case. Both steady and unsteady simulation results will be compared. For both inviscid and viscous flow three different meshes were generated, unstructured mesh for the Euler simulations and structured meshes for the RANS simulations. Figure 2.3 showed the medium meshes for both flow conditions.

B.1.1. EULER SIMULATIONS

For the Euler simulations three unstructured meshes with 1135, 10369 and 69038 points, respectively, were generated. To compare the meshes the steady lift and moment coefficient, the LCO amplitude and mode shape and the magnitude and phase difference of the lift and moment due to forced motion oscillation were used. Table B.1 shows the steady aerodynamic force coefficients and the upper and lower bounds of the LCO amplitude and LCO mode shape for all meshes. Between brackets the relative deviations from the fine mesh values are shown. As can be seen from this table, the values of the medium mesh are within 1% of the fine mesh. Except for the drag coefficient c_d. However, this coefficient is not of interest for the investigations in this thesis. The LCO amplitude, amplitude ratio and phase difference were accurately predicted by the medium mesh, see Table B.1.

To study the mesh convergence for unsteady flows, the aerodynamic response due to a forced harmonic motion was computed for the three meshes. Figure B.1 shows a slice of response surface versus the reduced frequency at $M = 0.74$, $\alpha = 0°$, $\Delta\alpha = 1°$, $|\theta_{h\alpha}| = 0.75$ and $\phi_{h\alpha} = 5°$ and Figure B.2 shows the aerodynamic forces versus the pitch amplitude at $M = 0.74$, $\bar{\alpha} = 0°$, $|\theta_{h\alpha}| = 0.75$, $\phi_{h\alpha} = 5°$, $k = 0.4$. Both figures show a convergence of the first harmonic components of the lift and moment as the mesh becomes

Parameter		Coarse (1135 points)	Medium (10369 points)	Fine (69038 points)
c_l		0.5488 (+8.52%)	0.5973 (+0.44%)	0.5999
c_{m_y}		-0.1329 (+1.92%)	-0.1361 (-0.42%)	-0.1355
c_d		0.0131 (-150.21%)	0.0061 (-16.94%)	0.0052
$\Delta\alpha_{\text{LCO}}$ (◦)	lower bound	3.33 (-38.22%)	5.42 (+0.56%)	5.39
	upper bound	3.50 (-36.02%)	5.51 (+0.73%)	5.47
$\lvert\theta_{h\alpha}\rvert$	lower bound	0.8780 (+1.80%)	0.8659 (+0.39%)	0.8625
	upper bound	0.8771 (+1.68%)	0.8660 (+0.39%)	0.8626
$\phi_{h\alpha}$ (◦)	lower bound	-7.90 (+11.42%)	-7.03 (-0.85%)	-7.09
	upper bound	-7.95 (+13.09%)	-6.95 (-1.14%)	-7.03

Table B.1: Aerodynamic force coefficients and LCO mode shape parameters for various meshes for Euler simulations at $M = 0.74$, $\alpha = 0°$

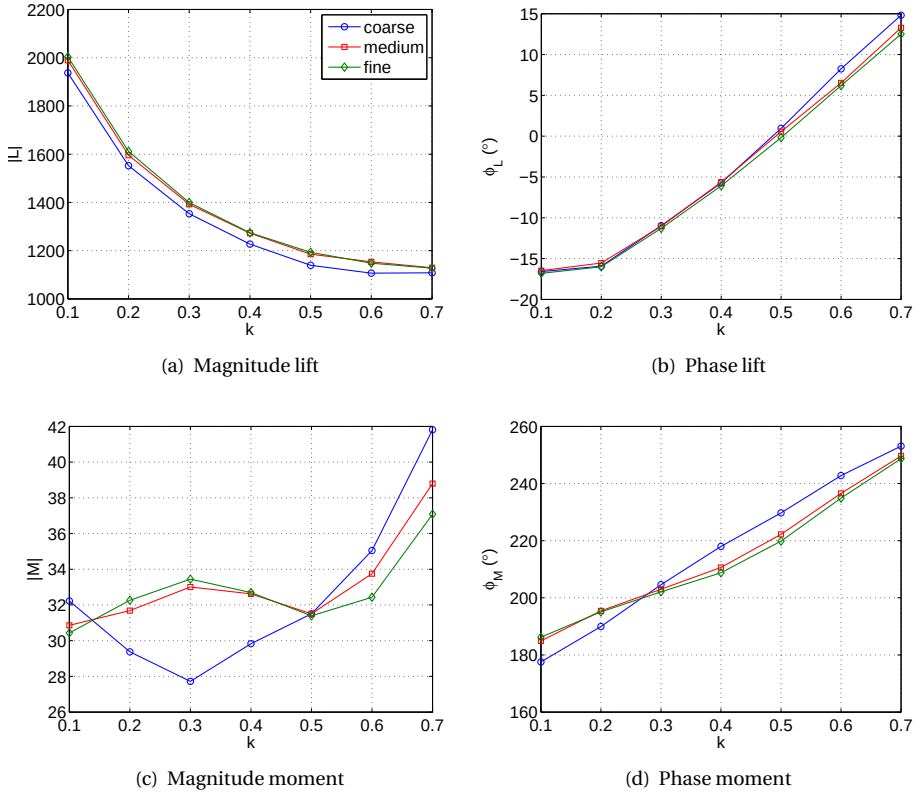

(a) Magnitude lift

(b) Phase lift

(c) Magnitude moment

(d) Phase moment

Figure B.1: Slice of the resonse surface for three different meshes for Euler simulation at $M = 0.74$, $\bar{\alpha} = 0°$, $\Delta\alpha = 1°$, $|\theta_{h\alpha}| = 0.75$, $\phi_{h\alpha} = 5°$

finer. Only for the phase of the lift and the moment versus the oscillation amplitude (Figures B.2(b) and B.2(d)) some noticeable differences are observed at small amplitude. However, the results of the medium mesh show a trend towards those of the finer mesh. Hence, the medium mesh was found to be a good compromise between accuracy and computational effort and has been used for all Euler simulations in this thesis, except for the validation test case of Chapter 4. For this test case the coarse mesh was used, see Chapter 4.

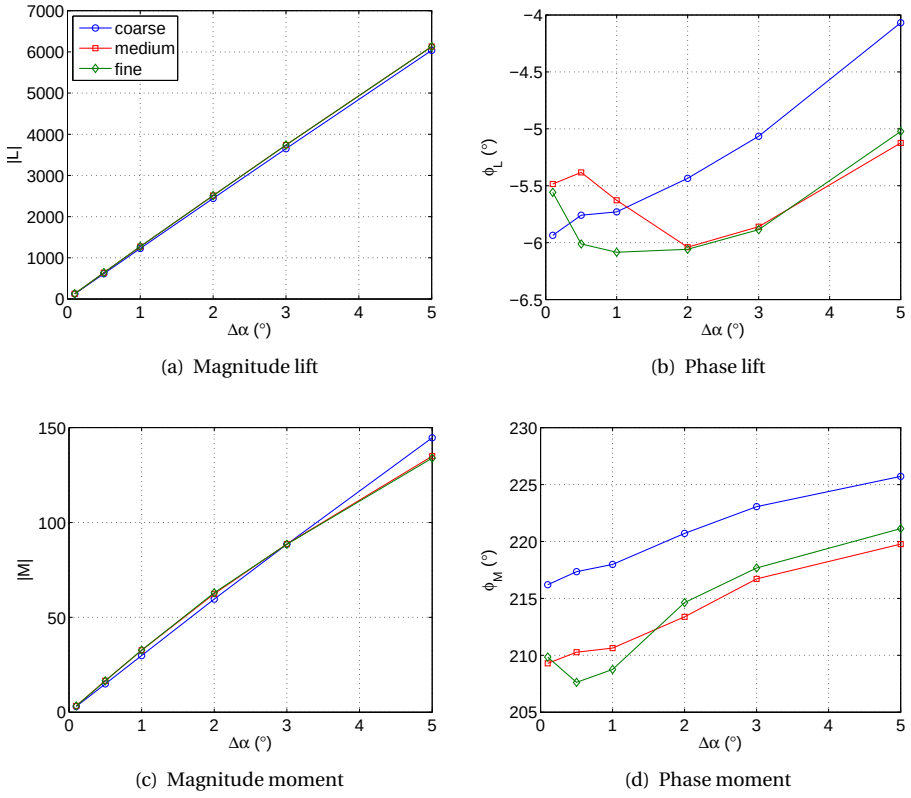

(a) Magnitude lift

(b) Phase lift

(c) Magnitude moment

(d) Phase moment

Figure B.2: Slice of the resonse surface for three different meshes for Euler simulation at $M = 0.74$, $\bar{\alpha} = 0°$, $|\theta_{h\alpha}| = 0.75$, $\phi_{h\alpha} = 5°$, $k = 0.4$

B.1.2. RANS SIMULATIONS

The mesh convergence of the results has been checked for two RANS test cases as well, at $M = 0.75$, $\bar{\alpha} = 0.7°$, $\mathrm{Re} = 2 \cdot 10^6$ and at $M = 0.74$, $\bar{\alpha} = -0.8°$ and $\mathrm{Re} = 2 \cdot 10^6$. Three meshes were again generated; a coarse mesh with 29760 points, a medium mesh with 65888 points and a fine mesh with 148248 points.

$M = 0.75$, $\bar{\alpha} = 0.7°$

Table B.2 compares the steady aerodynamic force coefficient as well as the LCO amplitude and mode shape for three meshes. The relative deviations with respect to the fine mesh are shown between brackets. It is observed that the deviations from the fine mesh are now much larger than in the inviscid case. The largest deviation is about 7% for the lift coefficient of the medium mesh. However, for the LCO amplitude and mode shape the deviations of the medium mesh become much smaller than in the steady case.

Parameter		Coarse (29760 points)	Medium (65888 points)	Fine (148248 points)
c_l		0.3467 (-5.97%)	0.3624 (-7.13%)	0.3687
c_{m_y}		-0.0645 (-3.87%)	-0.0661 (-1.49%)	-0.0671
c_d		0.0183 (+3.98%)	0.0177 (+0.57%)	0.0176
$\Delta\alpha_{\text{LCO}}$ (∘)	lower bound	1.632 (+4.21%)	1.573 (+0.45%)	1.566
	upper bound	1.654 (+5.08%)	1.587 (+0.83%)	1.574
$\lvert\theta_{h\alpha}\rvert$	lower bound	0.8339 (-0.62%)	0.8309 (-0.98%)	0.8391
	upper bound	0.8338 (-0.63%)	0.8309 (-0.98%)	0.8391
$\phi_{h\alpha}$ (∘)	lower bound	11.81 (-9.98%)	12.51 (-4.65%)	13.12
	upper bound	11.86 (-9.60%)	12.61 (-3.89%)	13.12

Table B.2: Aerodynamic force coefficients and LCO mode shape parameters for various meshes for RANS simulations at $M = 0.75$, $\bar{\alpha} = 0.7°$

To further judge on the mesh convergence two slices of the response surface are studied. Figure B.3 shows the aerodynamic forces versus the reduced frequency at $M = 0.75$, $\bar{\alpha} = 0.7°$, $\Delta\alpha = 1°$, $|\theta_{h\alpha}| = 0.75$ and $\phi_{h\alpha} = 10°$. From this figure a trend towards the results obtained on the finer mesh is observed. The aerodynamic forces are shown versus the pitch amplitude in Figure B.4 at a mode shape of $|\theta_{h\alpha}| = 0.75$, $\phi_{h\alpha} = 10°$ and $k = 0.3$. Good agreement between the three meshes is observed from this figure. From the results shown in this section, the medium mesh was found to be a good compromise between accuracy and computational effort. Therefore, it has been used in this thesis as a default grid for all viscous simulations.

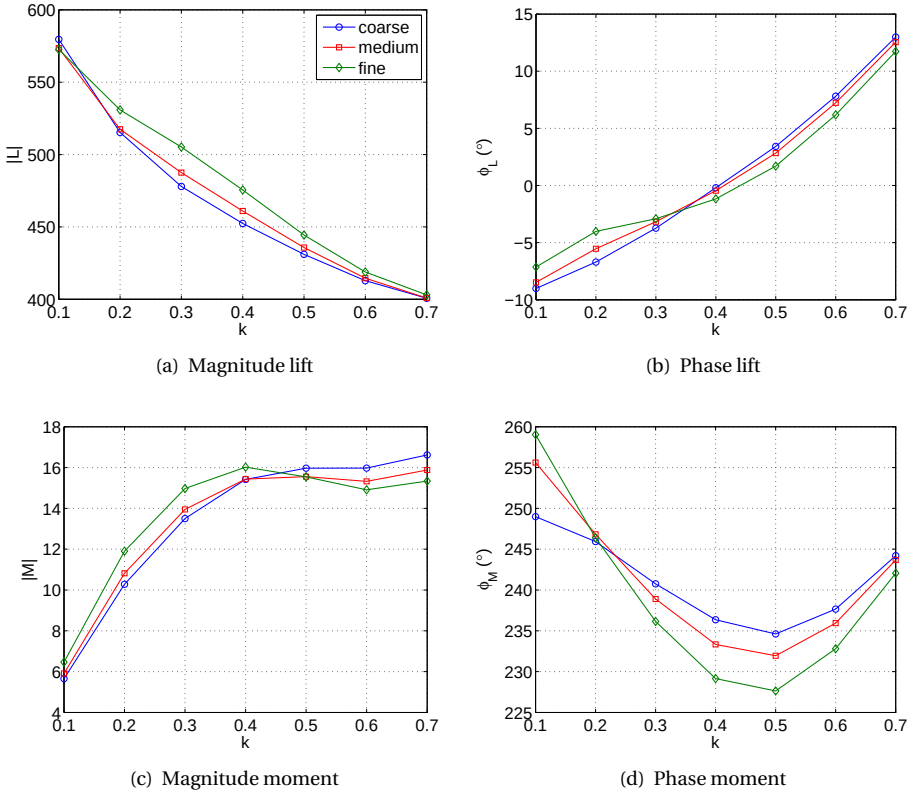

(a) Magnitude lift

(b) Phase lift

(c) Magnitude moment

(d) Phase moment

Figure B.3: Slice of the resonse surface for three different meshes for RANS simulation at $M = 0.75$, $\bar{\alpha} = 0.7°$, $\Delta\alpha = 1°$, $|\theta_{h\alpha}| = 0.75$, $\phi_{h\alpha} = 10°$

$M = 0.74$, $\bar{\alpha} = -0.8°$

A mesh convergence study has been performed for the steady CFD simulations and the FSI simulations of Chapter 3, i.e. at $M = 0.74$, $\bar{\alpha} = -0.8°$, Re $= 2 \cdot 10^6$. The results are given in Figure B.5. Figure B.5 shows the results in terms of the steady lift and moment coefficient, c_l and c_{m_y}, respectively and LCO amplitude for three different meshes at $M = 0.74$, $\bar{\alpha} = -0.8°$. Note that the moment coefficient has been multiplied by -1 for plotting purposes. The number of points on the airfoil has been increased by a factor of 1.5 between each of the meshes. In addition, the y^+-value of the first cell is kept at 0.75.

From Figure B.5 it is observed that all global values are within 15% of the medium mesh. Furthermore, the deviations of the medium mesh ($\Delta x/c = 0.0050$) with respect to the fine mesh ($\Delta x/c = 0.0033$) are smaller than those to the coarse mesh ($\Delta x/c = 0.0075$), i.e. 7.3% versus 13.6% for the lift coefficient, 1.6% versus 3.1% for the moment coefficient and 3.9% versus 9.3% for the LCO amplitude. Therefore, the medium mesh (with 65888 points) was thought to be sufficiently fine for all simulations (both FSI and forced motion) performed in Chapter 3, since there will only be a comparison of CFD simulations

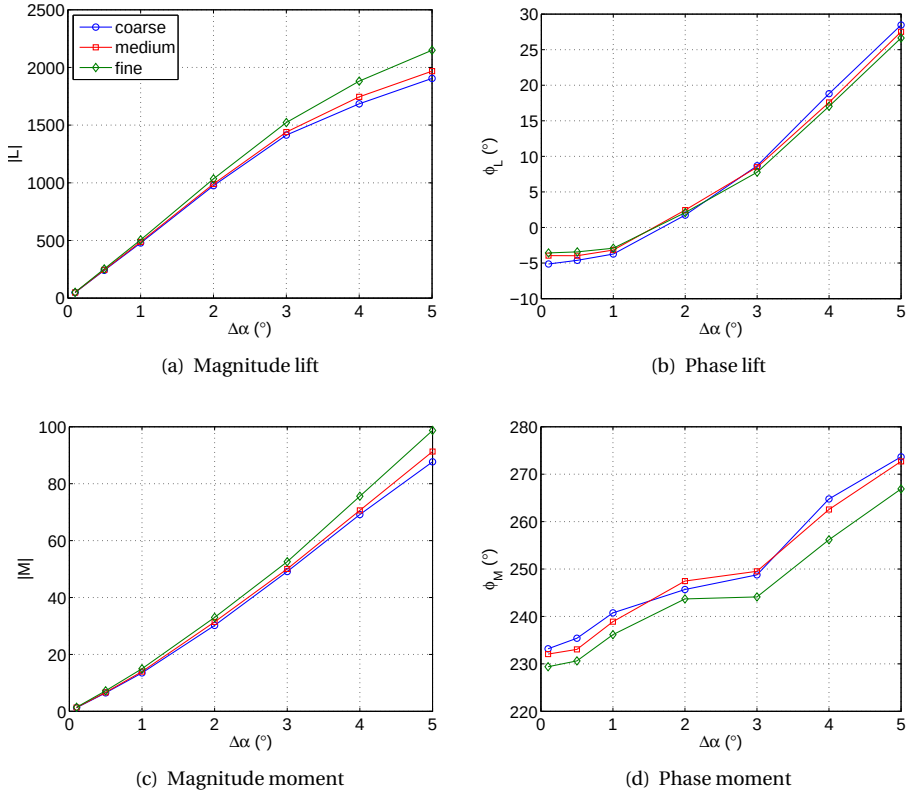

(a) Magnitude lift

(b) Phase lift

(c) Magnitude moment

(d) Phase moment

Figure B.4: Slice of the resonse surface for three different meshes for RANS simulation at $M = 0.75$, $\bar{\alpha} = 0.7°$, $|\theta_{h\alpha}| = 0.75$, $\phi_{h\alpha} = 10°$, $k = 0.3$

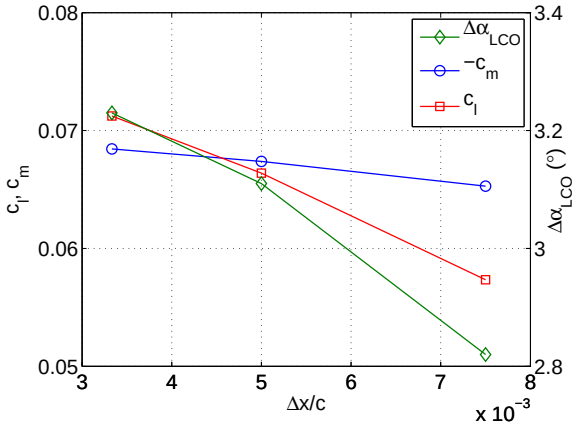

Figure B.5: Mesh convergence for steady c_l and c_{m_y} and LCO amplitudes for RANS simulation at $M = 0.74$, $\bar{\alpha} = -0.8°$

to each other, i.e. no comparisons with experiment results will be made.

B.2. TIME STEP

The temporal convergence of the solutions obtained on the medium mesh in both viscous (65888 points) and inviscid flow (10369 points) are addressed in this section. Both forced motion oscillations and FSI simulations are considered.

B.2.1. EULER SIMULATIONS

The upper and lower bounds of the LCO amplitude, amplitude ratio and phase difference obtained with three different time steps ($\Delta t = 10^{-3}$ s, 10^{-4} s and 10^{-5} s) are shown in Table B.3 for the Euler test case at $M = 0.74$ and $\bar{\alpha} = 0°$. The deviations of the LCO amplitude are very large between the largest and the smallest time step. For $\Delta t = 10^{-4}$ s and $\Delta t = 10^{-5}$ s good agreement is observed. Also, for the other mode shape parameters. Therefore, a time step of 10^{-4} s is sufficient for the fluid-structure interaction simulations.

Parameter		10^{-3} s	10^{-4} s	10^{-5} s
$\Delta\alpha_{LCO}$ (∘)	lower bound	9.03 (+67.53%)	5.42 (+0.56%)	5.39
	upper bound	9.12 (+61.99%)	5.51 (-2.13%)	5.63
$\lvert\theta_{h\alpha}\rvert$	lower bound	0.8853 (+2.33%)	0.8659 (+0.09%)	0.8651
	upper bound	0.8896 (+2.74%)	0.8660 (+0.01%)	0.8659
$\phi_{h\alpha}$ (∘)	lower bound	6.22 (-11.65%)	7.03 (-0.14%)	7.04
	upper bound	6.24 (-9.17%)	6.95 (+1.16%)	6.87

Table B.3: Time step independency check results $M = 0.74$, $\bar{\alpha} = 0°$

Figures B.6 and B.7 shows slices of the response surface in case of inviscid flow at $M = 0.74$, $\bar{\alpha} = 0°$ at three different time steps. Both figures show an excellent temporal convergence, as the results of the time step sizes $\Delta t = 10^{-4}$ s (or 192 time steps per period at $k = 0.4$) and $\Delta t = 10^{-5}$ s (or 1923 time steps per period at $k = 0.4$) are in perfect agreement (the red and the green lines are on top of each other). Furthermore, the results at the smallest time step ($\Delta t = 10^{-3}$ s or 20 time steps per period at $k = 0.4$) are not far off (except for the phase of the lift versus the pitch amplitude). Hence, taking $\Delta t = 10^{-4}$ s for the forced motion oscillation simulations should give results that are accurate enough for the studies performed in this thesis.

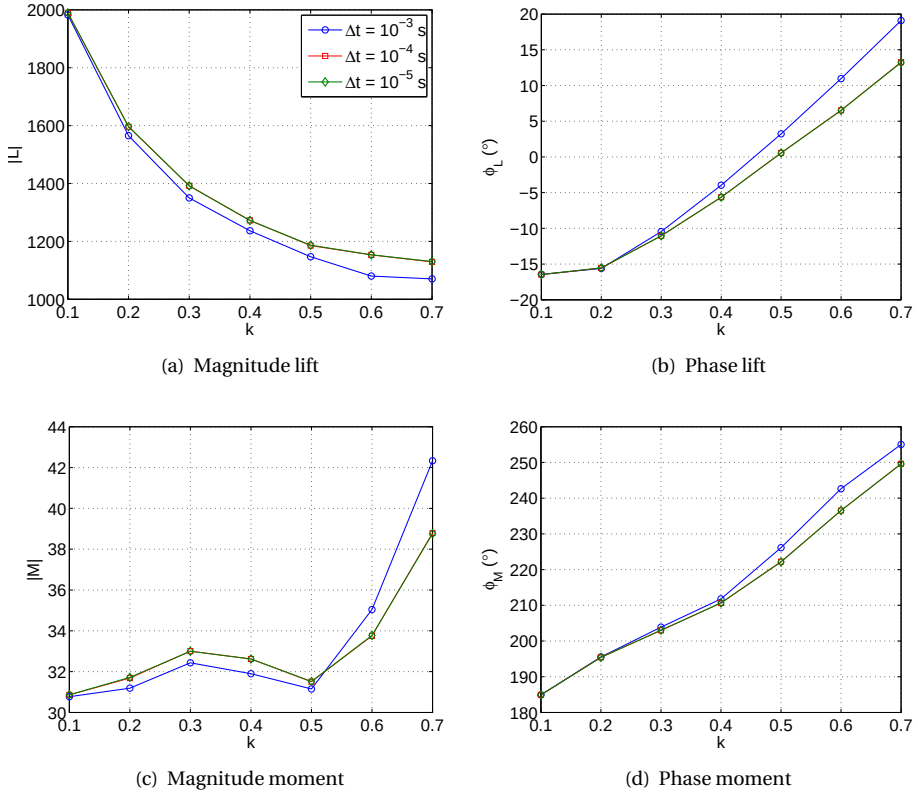

(a) Magnitude lift

(b) Phase lift

(c) Magnitude moment

(d) Phase moment

Figure B.6: Slice of the resonse surface for three different time step sizes for Euler simulation at $M = 0.74$, $\bar{\alpha} = 0°$, $\Delta\alpha = 1°$, $|\theta_{h\alpha}| = 0.75$, $\phi_{h\alpha} = 5°$

B.2.2. RANS SIMULATIONS

The temporal convergence behaviour of two RANS test cases at $M = 0.75$, $\bar{\alpha} = 0.7°$, $\mathrm{Re} = 2 \cdot 10^6$ and at $M = 0.74$, $\bar{\alpha} = -0.8°$ and $\mathrm{Re} = 2 \cdot 10^6$ is studied in this section. The computations were carried out on the medium mesh (65888 points).

$M = 0.75$, $\bar{\alpha} = 0.7°$

The LCO amplitude and mode shape were also found to be independent of time step for the test case at $M = 0.75$ and $\bar{\alpha} = 0.7°$, see Table B.4. Figure B.8 shows the describing functions versus the reduced frequency for a slice of the response surface at $M = 0.75$, $\bar{\alpha} = 0.7°$, $\Delta\alpha = 1°$, $|\theta_{h\alpha}| = 0.75$, $\phi_{h\alpha} = 10°$ at three different time step sizes. Figure B.9 shows the describing functions versus the pitch amplitude for a slice of the response surface at $M = 0.75$, $\bar{\alpha} = 0.7°$, $|\theta_{h\alpha}| = 0.75$, $\phi_{h\alpha} = 10°$, $k = 0.3$ at three different time step sizes. It is observed from these figures that the describing functions at time steps of 10^{-4} s (or 253 time steps per oscillation period at $k = 0.3$) and 10^{-5} s (or 2529 time steps per oscillation period at $k = 0.3$) are in perfect agreement. A time step size of 10^{-3} s (25

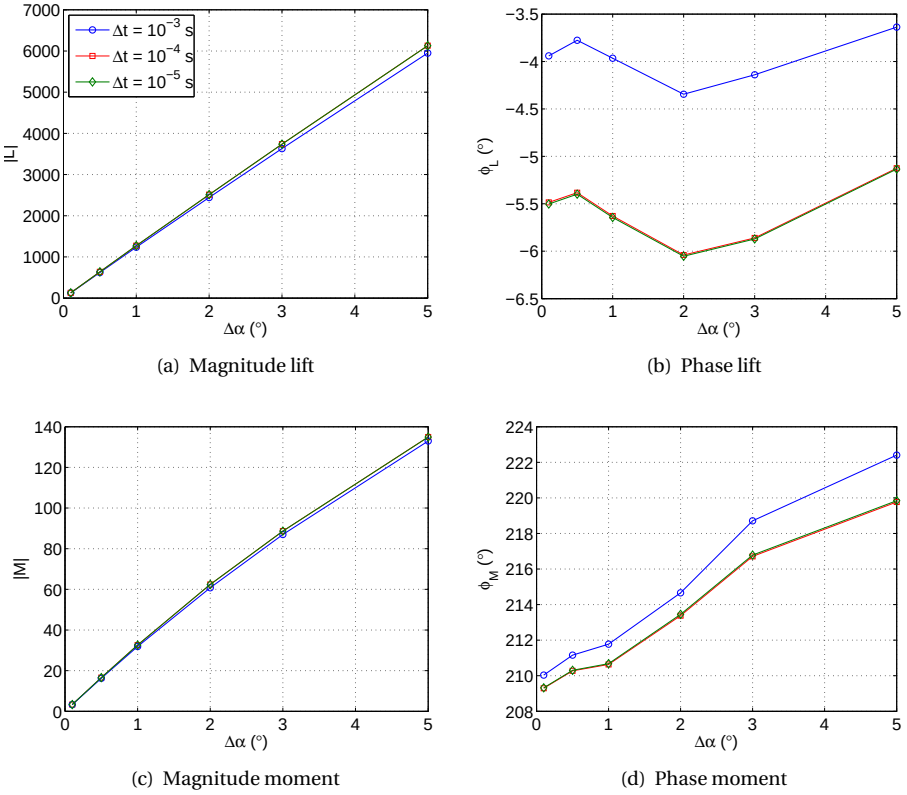

(a) Magnitude lift

(b) Phase lift

(c) Magnitude moment

(d) Phase moment

Figure B.7: Slice of the resonse surface for three different time step sizes for Euler simulation at $M = 0.74$, $\bar{\alpha} = 0°$, $|\theta_{h\alpha}| = 0.75$, $\phi_{h\alpha} = 5°$, $k = 0.4$

Parameter		10^{-3} s	10^{-4} s	10^{-5} s
$\Delta\alpha_{LCO}$ (∘)	lower bound	1.584 (-3.03%)	1.573 (+1.88%)	1.544
	upper bound	1.598 (+0.57%)	1.587 (-0.13%)	1.589
$\lvert\theta_{h\alpha}\rvert$	lower bound	0.8721 (+5.35%)	0.8309 (+0.39%)	0.8277
	upper bound	0.8692 (+4.84%)	0.8309 (+0.22%)	0.8291
$\phi_{h\alpha}$ (∘)	lower bound	13.49 (+8.00%)	12.51 (+0.16%)	12.49
	upper bound	13.59 (+8.37%)	12.61 (+0.56%)	12.54

Table B.4: Time step independency check results $M = 0.75$, $\bar{\alpha} = 0.7°$

time steps per oscillation period at $k = 0.3$) is clearly not sufficient. Hence, a time step size of 10^{-4} s has been used for the forced oscillation simulations needed to generate a response surface.

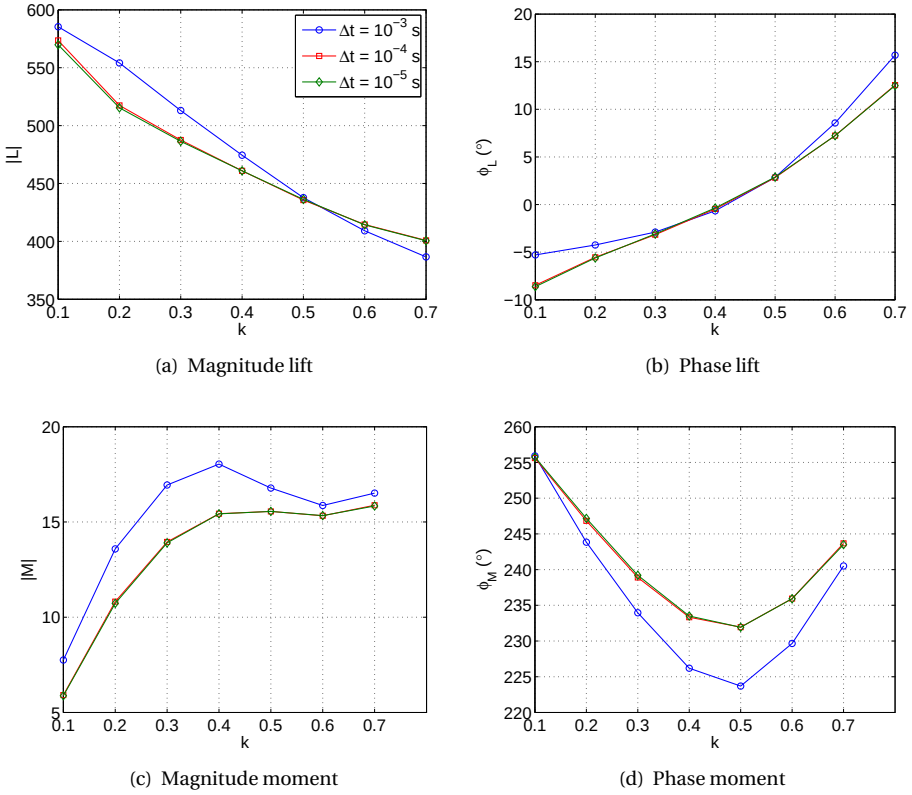

(a) Magnitude lift

(b) Phase lift

(c) Magnitude moment

(d) Phase moment

Figure B.8: Slice of the resonse surface for three different time step sizes for RANS simulation at $M = 0.75$, $\bar{\alpha} = 0.7°$, $\Delta\alpha = 1°$, $|\theta_{h\alpha}| = 0.75$, $\phi_{h\alpha} = 10°$

B

$M = 0.74$, $\bar{\alpha} = -0.8°$

A time step convergence study has been performed for the FSI simulations of Chapter 3, i.e. at $M = 0.74$, $\bar{\alpha} = -0.8°$, $\mathrm{Re} = 2 \cdot 10^6$. Three time step size have been tested, $\Delta t = 1 \cdot 10^{-3}$ s, $1 \cdot 10^{-4}$ s and $1 \cdot 10^{-5}$ s. These time step sizes correspond to a number of time steps per oscillation period of 29, 303 and 3029, respectively. The results of a time step convergence study are shown in Figure B.10, which compares the LCO amplitude obtained with different time steps at $M = 0.74$, $\bar{\alpha} = -0.8°$ (on the medium mesh). As can be seen from this figure the LCO amplitude has a deviation of 10% or less between the chosen time step sizes, with decreasing difference as the time step is refined further. Therefore, the time step used for the forced motion simulations as well as for the FSI simulations is $1 \cdot 10^{-4}$ s.

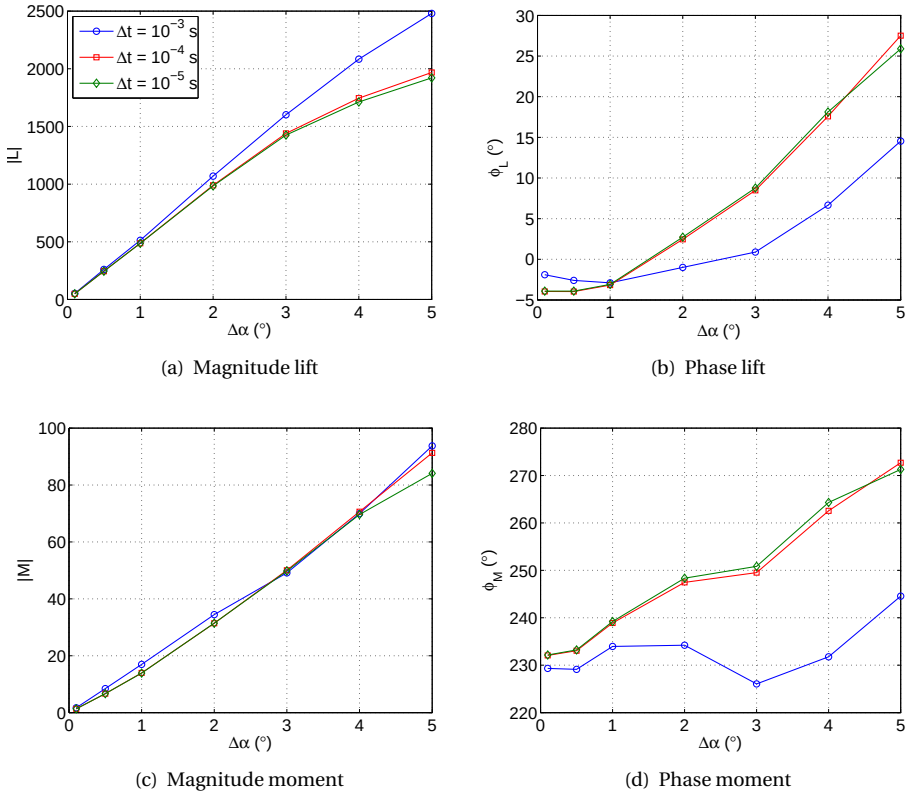

(a) Magnitude lift

(b) Phase lift

(c) Magnitude moment

(d) Phase moment

Figure B.9: Slice of the resonse surface for three different time step sizes for RANS simulation at $M = 0.75$, $\bar{\alpha} = 0.7°$, $|\theta_{h\alpha}| = 0.75$, $\phi_{h\alpha} = 10°$, $k = 0.3$

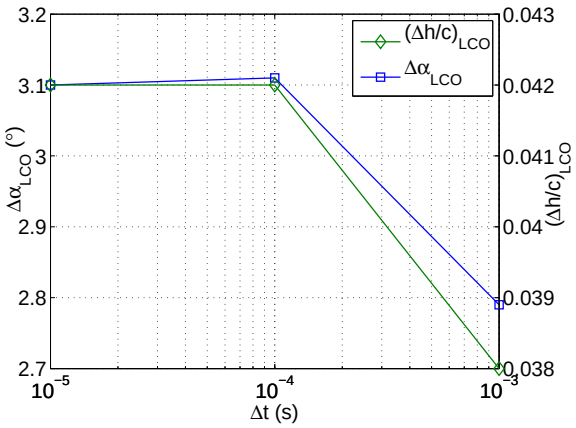

Figure B.10: Time step convergence for steady c_l and c_{m_y} and LCO amplitudes for RANS simulation at $M = 0.74$, $\bar{\alpha} = -0.8°$

C

INTERPOLATION METHODS

In order to apply the ADePK method developed in this thesis, a response surface is needed. This response surface is constructed using forced motion oscillation simulations. In ADePK, the aerodynamic forces are computed from interpolation on this response surface. In this thesis three different interpolation methods are applied; polynomial interpolation, cubic spline interpolation and linear interpolation. These will be outlined in this chapter.

C.1. POLYNOMIAL INTERPOLATION

In this thesis polynomial interpolation in multiple dimensions is applied. This section shows an example of polynomial interpolation for a second order polynomial in two dimensions. This means that six samples are necessary to obtain a polynomial of second order. Six equations can be set up as follows:

$$\underbrace{\begin{bmatrix} x^2 & y^2 & xy & x & y & 1 \\ x^2 & y^2 & xy & x & y & 1 \\ x^2 & y^2 & xy & x & y & 1 \\ x^2 & y^2 & xy & x & y & 1 \\ x^2 & y^2 & xy & x & y & 1 \\ x^2 & y^2 & xy & x & y & 1 \end{bmatrix}}_{\mathbf{C}} \underbrace{\begin{bmatrix} a_1 \\ a_2 \\ a_3 \\ b_1 \\ b_2 \\ b_3 \end{bmatrix}}_{\vec{\beta}} = \underbrace{\begin{bmatrix} z_1 \\ z_2 \\ z_3 \\ z_4 \\ z_5 \\ z_6 \end{bmatrix}}_{\vec{y}}. \tag{C.1}$$

The matrix **C** of (C.1) can be constructed using the following two matrices, **S** containing the sample locations and **P** containing the polynomial orders:

$$\mathbf{S} = \begin{bmatrix} x_1 & y_1 \\ x_2 & y_2 \\ x_3 & y_3 \\ x_4 & y_4 \\ x_5 & y_5 \\ x_6 & y_6 \end{bmatrix}, \mathbf{P} = \begin{bmatrix} 2 & 0 \\ 0 & 2 \\ 1 & 1 \\ 1 & 0 \\ 0 & 1 \\ 0 & 0 \end{bmatrix}. \tag{C.2}$$

Now each column of **C** is computed from:

$$\mathbf{C}(:,i) = \left[(\mathbf{S}(:,1))^{\mathbf{P}(i,1)} \cdot (\mathbf{S}(:,2))^{\mathbf{P}(i,2)} \right], \tag{C.3}$$

where i is a number from 1 to 6. The coefficients in vector $\vec{\beta}$ are then obtained from:

$$\vec{\beta} = \mathbf{C}^{-1} \cdot \vec{y}. \tag{C.4}$$

Hence, (C.4) gives the coefficients of the polynomial through the sample points. Interpolation at a given mode shape and frequency is then applied using:

$$y_{\text{interp.}} = \vec{c}^{\,T} \cdot \vec{\beta}, \tag{C.5}$$

where $\vec{c}^{\,T}$ is a row vector containing the polynomial terms at the given mode shape and frequency (i.e. one row of matrix **C**). A similar procedure can be applied for our four dimensional problem, where the matrices **S** and **P** then both have four columns.

C

C.2. CUBIC SPLINE INTERPOLATION

A second interpolation method that has been applied in this thesis for interpolation on the four-dimensional response surface is cubic spline interpolation. An example of cubic spline interpolation in two dimensions is shown here. Cubic spline interpolation results in a spline that is continuous up to the second derivative [1]. Consider a set of points y_0, $y_1 \ldots y_n$ in two dimensions. Figure C.1 shows these points and their interpolated cubic spline segments $Y_i(k)$.
Between two adjacent points a third-order polynomial is fitted [1], i.e.:

$$Y_i(k) = a_i + b_i k + c_i k^2 + d_i k^3, \tag{C.6}$$

where k represents the normalised interval between two adjacent points (at $k = 0$ the left-hand side of the segment is considered and at $k = 1$ the right-hand side). i represents the segment number. There are $n-1$ segments. It is known that

$$Y_i(0) = y_m = a_i \quad \text{and} \tag{C.7}$$

$$Y_i(1) = y_{m+1} = a_i + b_i + c_i + d_i, \tag{C.8}$$

where m represent the sample number, i.e. y_m is the function value of the sample on the left-hand side of the segment and hence y_{m+1} is the function value of the sample on the right-hand side of the segment. In order to determine the coefficients a_i till d_i two

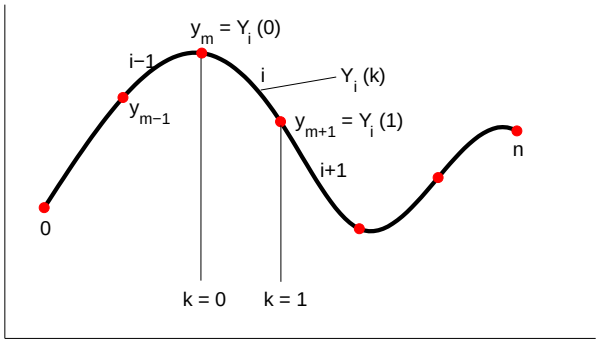

Figure C.1: Set of points and their cubic spline interpolated curve (after [1])

additional equations are necessary. These can be obtained from the derivative of (C.6) at the border points of a segment, i.e.

$$Y_i'(0) = D_m = b_i, \tag{C.9}$$
$$Y_i'(1) = D_{m+1} = b_i + 2c_i + 3d_i, \tag{C.10}$$

where e.g. D_m represents the first derivative at the left-hand side of the segment i (and at the right-hand side of segment $i-1$). Solving (C.7)-(C.10) for the coefficients results in

$$a_i = y_m, \tag{C.11}$$
$$b_i = D_m, \tag{C.12}$$
$$c_i = 3(y_{m+1} - y_m) - 2D_m - D_{m+1}, \tag{C.13}$$
$$d_i = 2(y_m - y_{m+1}) + D_m + D_{m+1}. \tag{C.14}$$

However, the first derivatives at the sample points are not known. Hence, additional equations are necessary to solve for the coefficients of the cubic polynomial. In order to obtain these equations, the fact that the first and second derivatives are continuous at a sample point for cubic spline is used [1]. In other words, the first derivative at the right-hand side of element $i-1$, $Y_{i-1}'(1)$, is equal to the first derivative at the left-hand side of element i, $Y_i'(0)$, by definition. Similarly, the second derivative is continuous at a sample point. Then, the following conditions must be satisfied at the interior sample points of a curve [1]:

$$Y_{i-1}(1) = y_m, \tag{C.15}$$
$$Y_{i-1}'(1) = Y_i'(0), \tag{C.16}$$
$$Y_i(0) = y_m, \tag{C.17}$$
$$Y_{i-1}''(1) = Y_i''(0). \tag{C.18}$$

C

In addition at the end points [1]:

$$Y_0(0) = y_0, \tag{C.19}$$
$$Y_{n-1}(1) = y_n. \tag{C.20}$$

This results in $4(n-1)+2 = 4n-2$ equations. However, there are $4n$ unknowns (the first and second derivatives at each sample point). There are several ways to add to additional equations, if the first derivatives are known at the end points, these can be used. This is called clamped cubic spline interpolation [2]. In this thesis these derivatives are not known, therefore an assumption has to be made regarding the end points. So-called not-a-knot conditions have been used [1, 2]. In that case, continuity of the third derivative at the second sample point and at the sample point $n-1$ is assumed, i.e.

$$Y_0'''(1) = Y_1'''(0), \tag{C.21}$$
$$Y_{n-2}'''(1) = Y_{n-1}'''(0). \tag{C.22}$$

This means that the same cubic function is used to represent the first and the second element and the cubic functions used to represent the last and the one-before-last element are also the same [1, 2]. With (C.15) until (C.22) there are then $4n-2$ equations and $4n-2$ unknowns.

The not-a-knot conditions were found to give accurate results compared to dense-sampled slices of the reponse surface in various directions. Although at the left end of the computational domain (i.e. the linear end), a natural boundary condition, where the second derivative at the endpoint is set to zero [1, 2], might have been better, since in that case the first segment is approximated with a linear curve, which is most likely a good approximation. Therefore, further work is necessary to investigate the effect of the end conditions on the interpolation of the response surface.

C.3. LINEAR INTERPOLATION

The third interpolation method that is applied in this thesis is linear interpolation. Again an example for two dimensions is given here. During linear interpolation two adjacent sample points (x_A, y_A) and (x_B, y_B) in two dimensions, are connected by a straight line. The function value at a location between these two adjacent points y can then be computed from the equal slopes of the two parts of the straight line, i.e.

$$y = y_A + (y_B - y_A) \cdot \frac{x - x_A}{x_B - x_A}. \tag{C.23}$$

Similar equations can be derived in multiple dimensions.

REFERENCES

[1] R. Bartels, J. Beatty, and B. Barsky, *An Introduction to Splines for Use in Computer Graphics and Geometric Modelling* (Morgan Kaufmann, 1998).

[2] S. Klugman, H. Panjer, and G. Willmot, *LOSS MODELS - From Data to Decisions* (John Wiley & Sons, Inc., 2008).

D

ADDITIONAL RESULTS OF THE AMPLITUDE-DEPENDENT P-K METHOD

This chapter shows a few additional results to those results presented in Chapter 5. The LCO bifurcation behaviour of the NLR7301 airfoil under various structural parameter variations is shown in Section D.1 for the aerodynamic source of non-linearity not considered in Chapter 5. Furthermore, the results of a response surface analysis for the subsonic flow test cases of Section 5.2 are shown in Section D.2 of this Chapter.

D.1. STRUCTURAL PARAMETER VARIATION

This section shows the effect of a mass ratio variation, the effect of the addition of structural damping and the effect of an elastic axis location variation. Transonic inviscid flow, subsonic flow with trailing-edge separation and subsonic flow with free boundary-layer transition are the aerodynamic non-linearities considered in this section.

D.1.1. MASS RATIO

TRANSONIC INVISID FLOW

Figure D.1 shows a variation in the mass ratio from 100 to 500 for the NLR7301 airfoil in inviscid flow at $M = 0.74$ and $\bar{\alpha} = 0°$. The structural frequency ratio is 0.70. It is observed that the number of stable LCOs for LCO amplitudes above 2° increases when the mass ratio is increased. Furthermore, the slope of the upper part of the bifurcation diagram (i.e. the stable LCOs with amplitudes larger than 2°) decreases, hence the non-linearity becomes stronger at larger mass ratio, see Figure D.1(f). The amplitude ratio slightly increases and the phase difference decreases with increasing mass ratio. The reduced frequency also decreases. The mode shape is a complex pitch-plunge motion since the amplitude ratio is close to one, see Figure D.1(e). However, it tends to become more pitch dominated as the amplitude ratio decreases during the bifurcation. Increasing the SFR

and applying the same mass ratio variation results in the bifurcation diagrams shown in Figure D.2, which shows the LCO pitch amplitude versus the normalised freestream speed for ω_h/ω_α = 0.97 and 1.21. From this figure it is seen that increasing the mass ratio also leads to a decreasing slope of the bifurcation diagram and hence a stronger non-linearity. For both SFRs unstable LCOs of large amplitude occur for the highest two mass ratios.

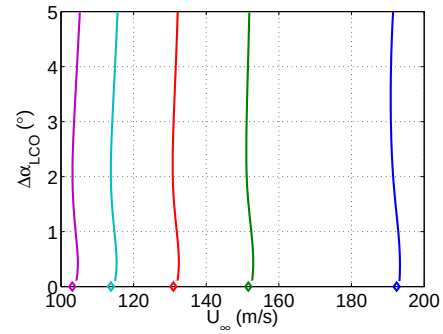

(a) Pitch amplitude

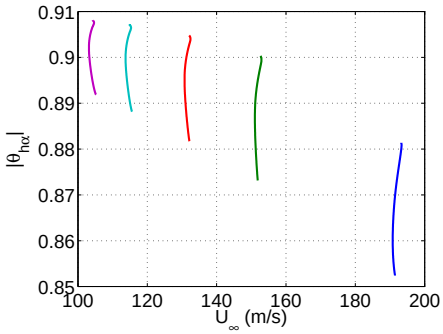

(b) Amplitude ratio

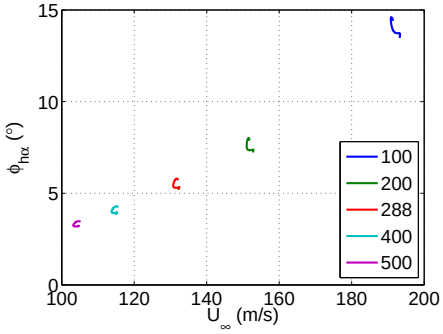

(c) Phase difference

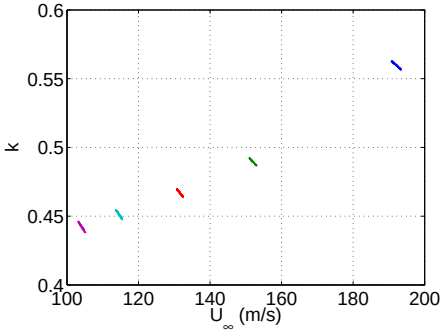

(d) Reduced frequency

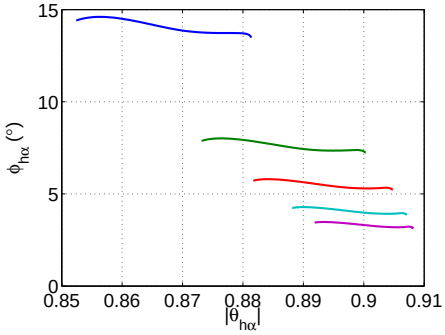

(e) Phase difference vs. amplitude ratio

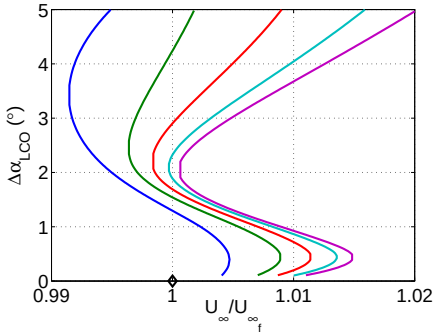

(f) Pitch amplitude

Figure D.1: LCO mode shape vs freestream velocity for a mass ratio variation at $M = 0.74$, $\bar{\alpha} = 0°$ in inviscid flow

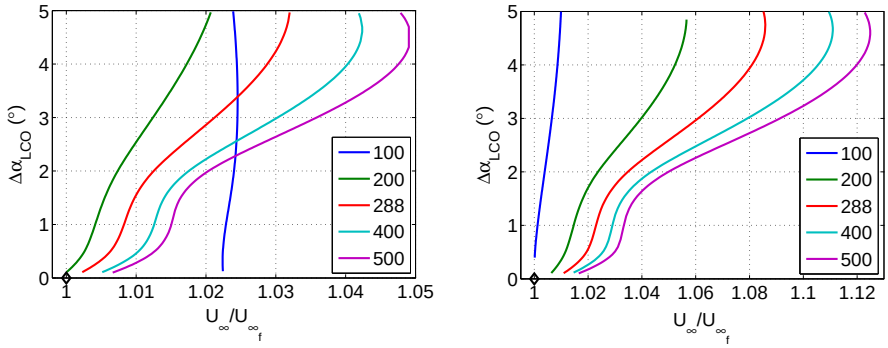

(a) $\omega_h/\omega_\alpha = 0.97$ (b) $\omega_h/\omega_\alpha = 1.21$

Figure D.2: LCO mode shape vs freestream velocity normalised by the linear flutter speed for a mass ratio variation at $M = 0.74$, $\bar{\alpha} = 0°$ and two different SFR

D

SUBSONIC FLOW WITH TRAILING-EDGE SEPARATION

Figure D.3 shows the bifurcation behaviour of the LCO mode shape versus the freestream speed under a variation of the mass ratio for the test case at $M = 0.3$, $\bar{\alpha} = 9.0°$. It is observed that the bifurcation becomes more supercritical when the mass ratio is increased. The mode shape tends to become pitch dominated for all mass ratios. The phase difference decreases with increasing mass ratio as for the test case in inviscid transonic flow. The same holds for the reduced frequency. The phase difference increases with increasing freestream velocity for all mass ratios. Figure D.4 shows the mass ratio variation for two other SFRs (0.97 and 1.21). At $\omega_h/\omega_\alpha = 0.97$ the bifurcation is subcritical, except at $\mu = 200$, where stable LCOs of large amplitude exist and hence the bifurcation is a saddle-node bifurcation of limit cycles, i.e. shows both stable and unstable LCOs. The slope of the bifurcation curves seems not to vary much with mass ratio for this SFR. At an SFR of 1.21 the bifurcation curves do not differ much from each other either, except at $\mu = 200$. For a mass ratio of 100 at $\omega_h/\omega_\alpha = 0.97$ and 1.21 extrapolation in the reduced frequency direction is again necessary. For a mass ratio of 150 no extrapolation is required at $\omega_h/\omega_\alpha = 0.97$. Therefore the bifurcation diagram for this mass ratio has been included in Figure D.4(a).

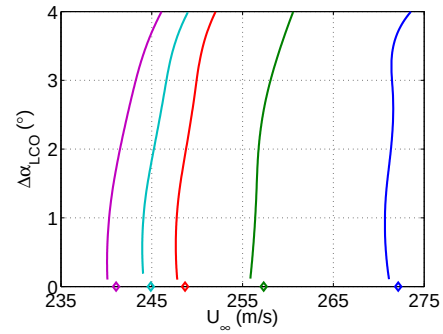

(a) Pitch amplitude

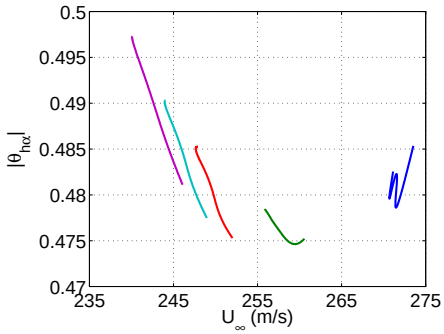

(b) Amplitude ratio

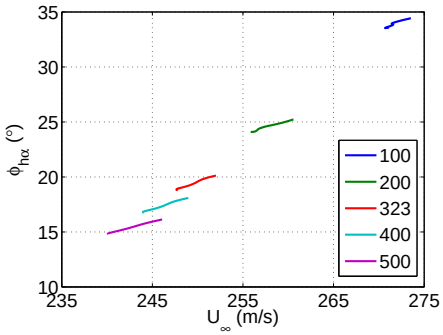

(c) Phase difference

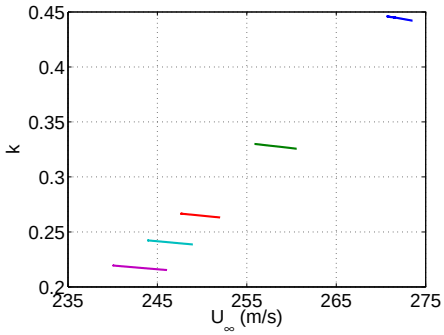

(d) Reduced frequency

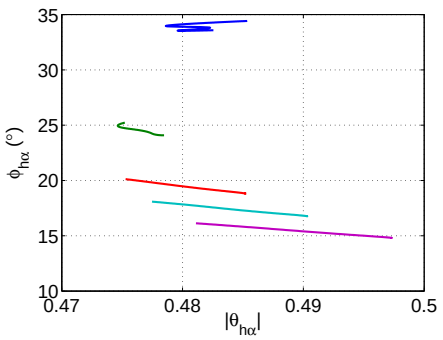

(e) Phase difference vs. amplitude ratio

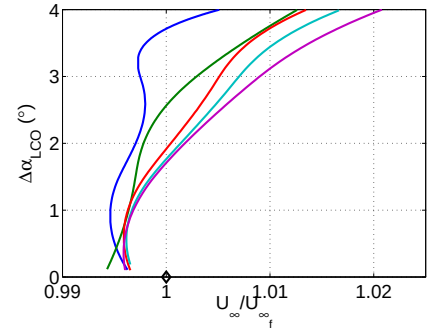

(f) Pitch amplitude

Figure D.3: LCO mode shape vs freestream velocity for a mass ratio variation at $M = 0.3$, $\bar{\alpha} = 9.0°$

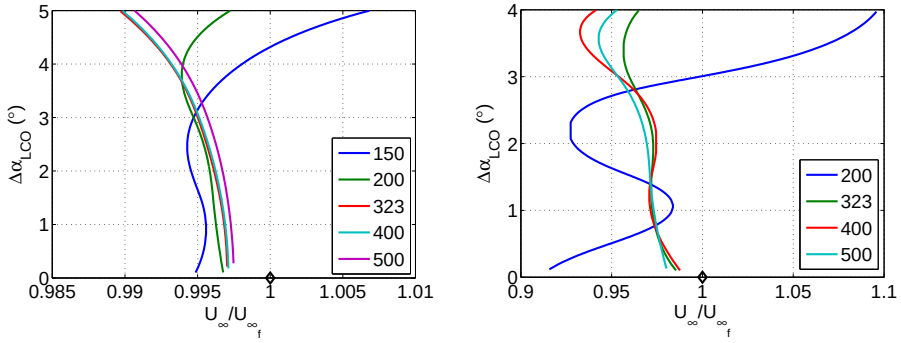

(a) $\omega_h/\omega_\alpha = 0.97$ (b) $\omega_h/\omega_\alpha = 1.21$

Figure D.4: LCO mode shape vs freestream velocity normalised by the linear flutter speed for a mass ratio variation at $M = 0.3$, $\bar{\alpha} = 9.0°$ and two different SFR

D

SUBSONIC FLOW WITH FREE BOUNDARY-LAYER TRANSITION

Figure D.5 shows the bifurcation behaviour of the NLR7301 airfoil in transitional flow at $M = 0.3$, $\bar{\alpha} = -1.3°$, $\mathrm{Re} = 5 \cdot 10^5$ and $\mathrm{Tu} = 0.05\%$ in case of a mass ratio variation from 100 to 1700. The SFR is 0.70. The bifurcation behaviour is seen to slightly change with decreasing mass ratio, i.e. at large LCO amplitudes the bifurcation diagrams become steeper when the mass ratio is decreased. Hence, the non-linearity becomes weaker. The LCO mode shape becomes more pitch dominated with decreasing mass ratio and with increasing freestream velocity for all mass ratios (after a slight initial increase with decreasing freestream velocity). The phase difference and the reduced frequency also decrease with decreasing mass ratio. However, during the bifurcation the phase difference first slightly decreases, but then increases for all mass ratios. When the structural frequency ratio is increased to 0.97, see Figure D.6(a), the bifurcation diagrams also become steeper with decreasing mass ratio. The same holds for $\omega_h/\omega_\alpha = 1.21$ as observed from Figure D.6(b).

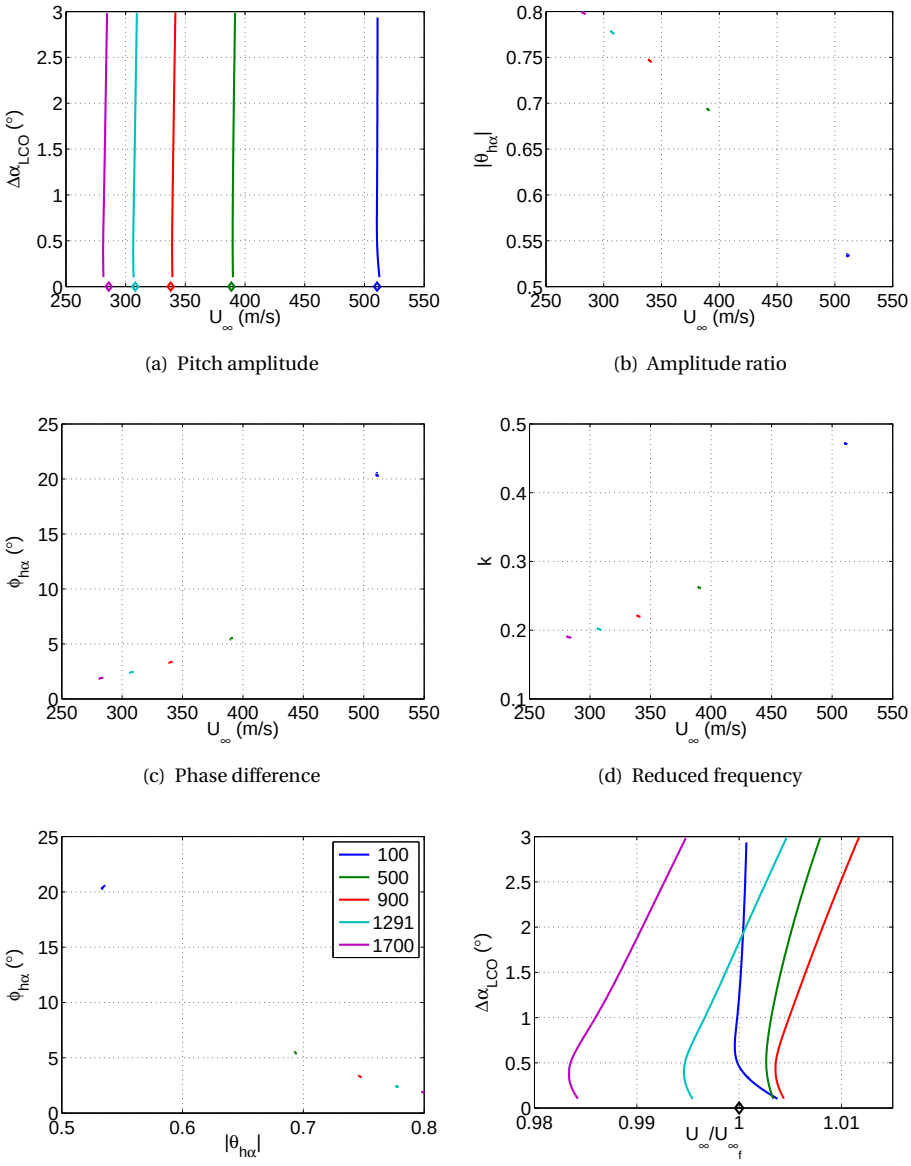

(a) Pitch amplitude

(b) Amplitude ratio

(c) Phase difference

(d) Reduced frequency

(e) Phase difference vs. amplitude ratio

(f) Pitch amplitude

Figure D.5: LCO mode shape vs freestream velocity for a mass ratio variation at $M = 0.3$, $\bar{\alpha} = -1.3°$, $\mathrm{Re} = 5 \cdot 10^5$ and Tu = 0.05% in transitional flow

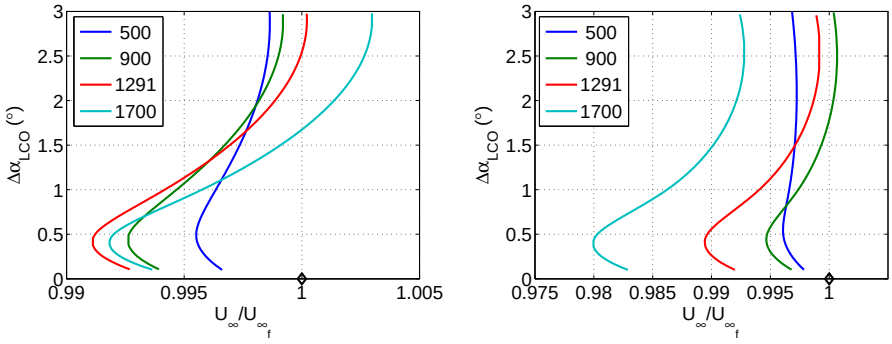

(a) $\omega_h/\omega_\alpha = 0.97$ (b) $\omega_h/\omega_\alpha = 1.21$

Figure D.6: LCO mode shape vs freestream velocity normalised by the linear flutter speed for a mass ratio variation at $M = 0.3$, $\bar{\alpha} = -1.3°$, $\mathrm{Re} = 5 \cdot 10^5$ and $\mathrm{Tu} = 0.05\%$ and two different SFR in transitional flow

D

D.1.2. STRUCTURAL DAMPING

Figures D.7, D.8 and D.9 show the bifurcation behaviour obtained when varying the structural damping for the test cases $M = 0.74$, $\bar{\alpha} = 0°$, $M = 0.3$, $\bar{\alpha} = 9.0°$ and $M = 0.3$, $\bar{\alpha} = -1.3°$. From these figures the same conclusions can be drawn as for the transonic viscous test case, see Section 5.4.3.

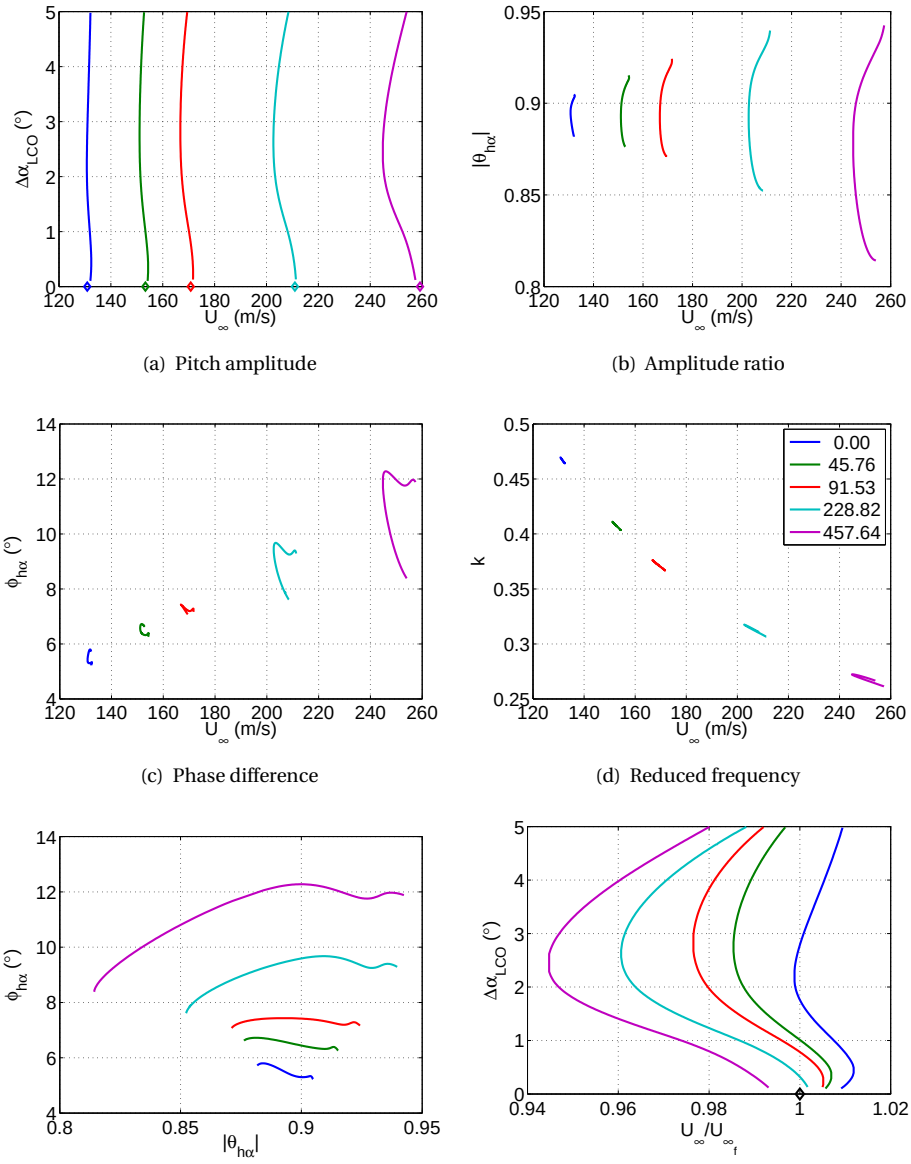

(a) Pitch amplitude

(b) Amplitude ratio

(c) Phase difference

(d) Reduced frequency

(e) Phase difference vs. amplitude ratio

(f) Pitch amplitude

Figure D.7: LCO mode shape vs freestream velocity for a damping variation at $M = 0.74$, $\bar{\alpha} = 0°$ (value of D_h is shown in the legend)

D

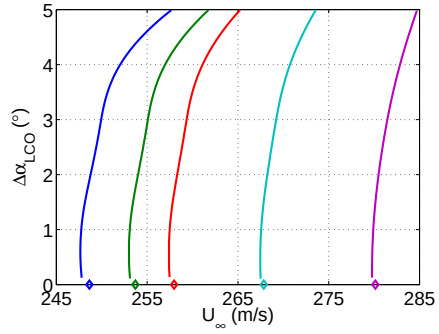

(a) Pitch amplitude

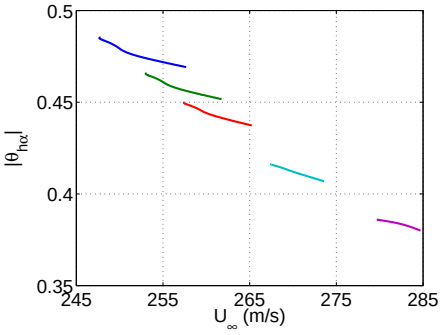

(b) Amplitude ratio

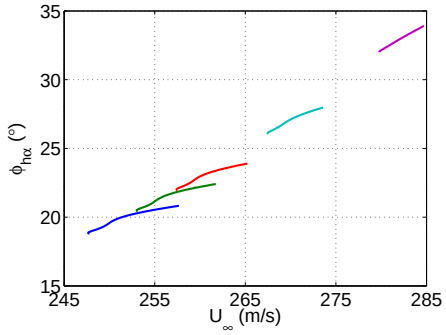

(c) Phase difference

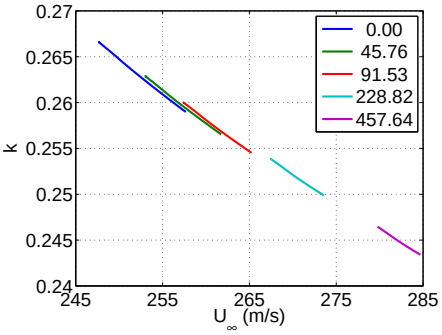

(d) Reduced frequency

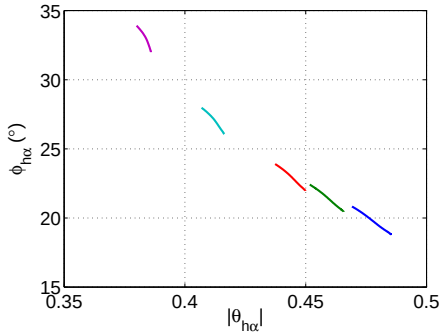

(e) Phase difference vs. amplitude ratio

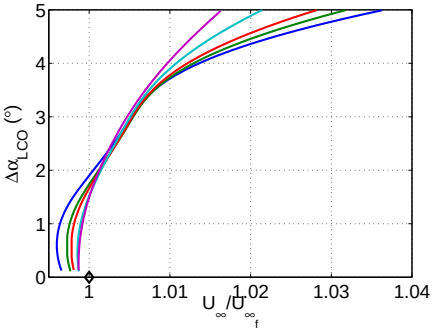

(f) Pitch amplitude

Figure D.8: LCO mode shape vs freestream velocity for a damping variation at $M = 0.3$, $\bar{\alpha} = 9.0°$ (value of D_h is shown in the legend)

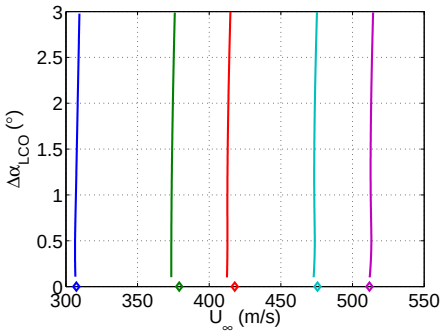

(a) Pitch amplitude

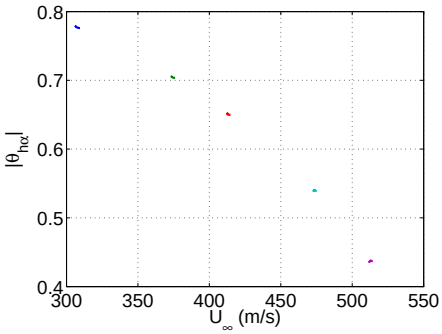

(b) Amplitude ratio

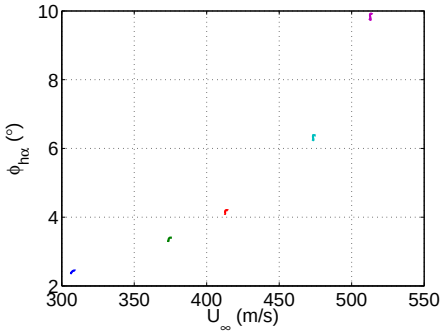

(c) Phase difference

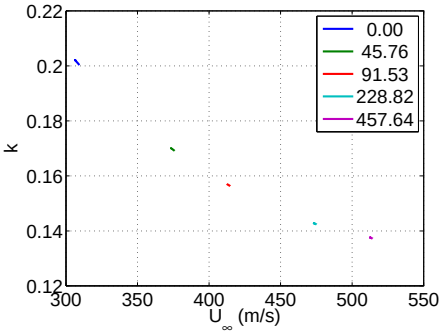

(d) Reduced frequency

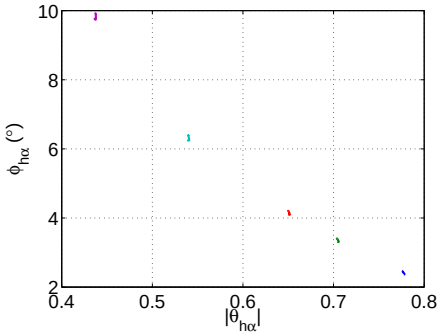

(e) Phase difference vs. amplitude ratio

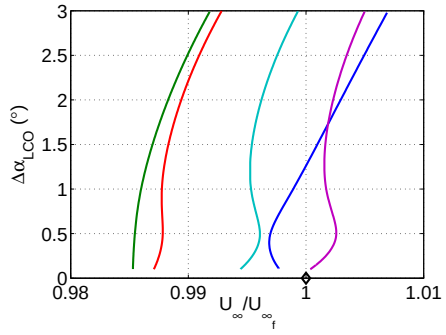

(f) Pitch amplitude

Figure D.9: LCO mode shape vs freestream velocity for a damping variation at $M = 0.3$, $\bar{\alpha} = -1.3°$, Re $= 5 \cdot 10^5$ and Tu $= 0.05\%$ in transitional flow (value of D_h is shown in the legend)

D.1.3. ELASTIC AXIS LOCATION

Figures D.10, D.11 and D.12 show the effect of an elastic axis location variation on the bifurcation behaviour of the LCO amplitude for the various sources of aerodynamic nonlinearity. The elastic axis location is depicted as percentage of the chord length and taken positive when located aft of the quarter-chord point. Not that for the subsonic flow case at $M = 0.3$ and $\bar{\alpha} = 9.0°$ the elastic axis location that is the most aft is at 35%c of the quarter-chord point, since no flutter was found for elastic axis locations further aft. Figure D.10 shows a change in bifurcation behaviour from subcritical to supercritical with increasing aft location of the elastic axis for the test case in inviscid transonic flow. As noted in Section 5.4.4, in subsonic flow with trailing-edge separation, the bifurcation changes from supercritical to subcritical when the elastic axis is displaced to further aft positions. In subsonic transitional flow the bifurcation type is not affected by the change of the elastic axis location. From the figures shown in this section, the same conclusions can be drawn as for the transonic viscous flow test case with regard to the LCO mode shape, i.e. the mode shape becomes more pitch dominated and the reduced frequency variation shifts to larger frequencies with increasing x_{ea}.

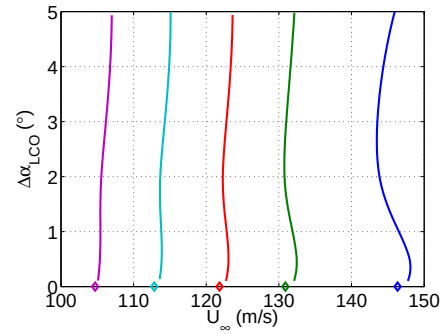

(a) Pitch amplitude

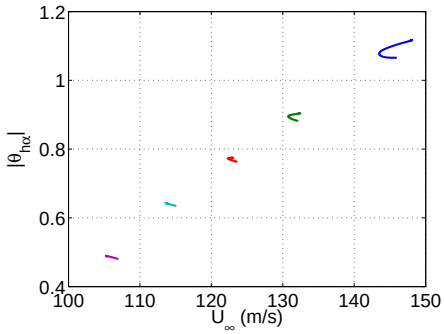

(b) Amplitude ratio

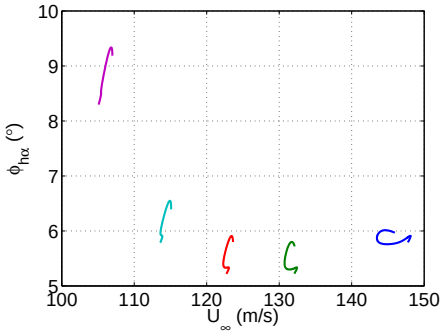

(c) Phase difference

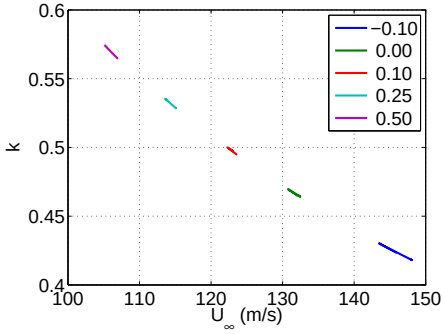

(d) Reduced frequency

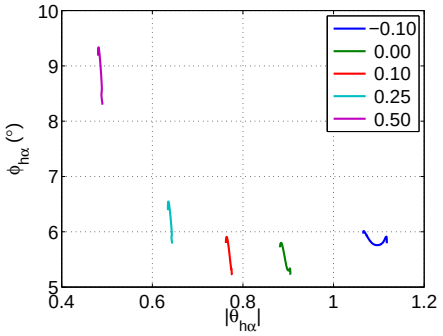

(e) Phase difference vs. amplitude ratio

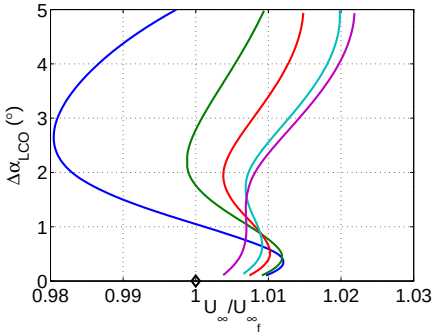

(f) Pitch amplitude

Figure D.10: LCO mode shape vs freestream velocity for a variation of the non-dimensional elastic axis location at $M = 0.74$, $\bar{\alpha} = 0°$

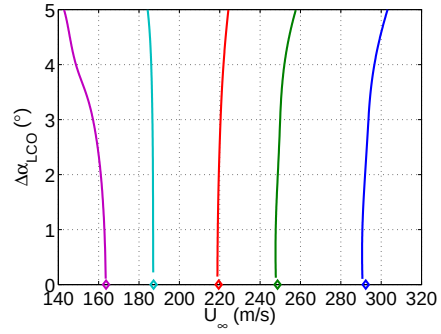

(a) Pitch amplitude

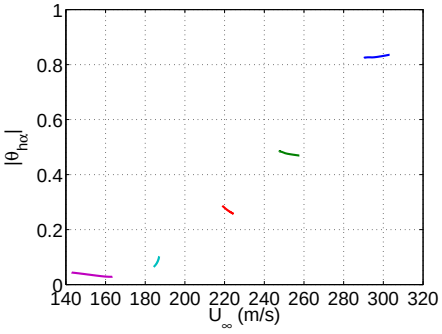

(b) Amplitude ratio

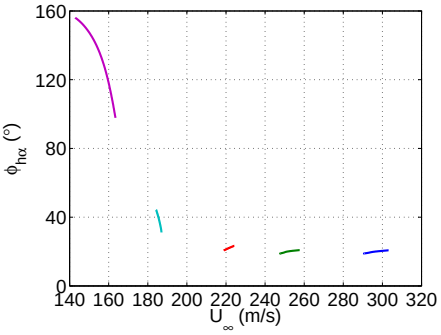

(c) Phase difference

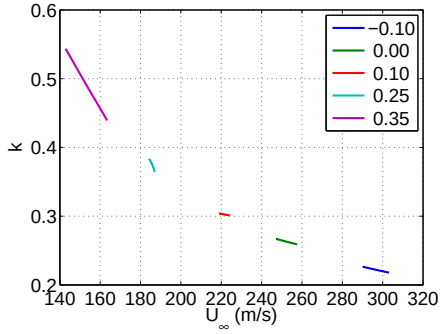

(d) Reduced frequency

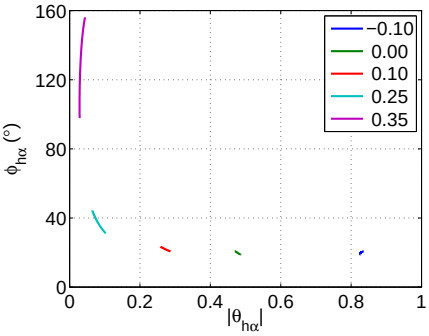

(e) Phase difference vs. amplitude ratio

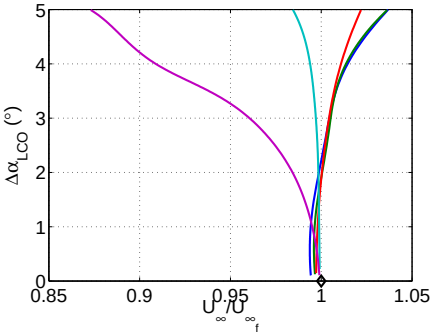

(f) Pitch amplitude

Figure D.11: LCO mode shape vs freestream velocity for a variation of the non-dimensional elastic axis location at $M = 0.3$, $\bar{\alpha} = 9.0°$

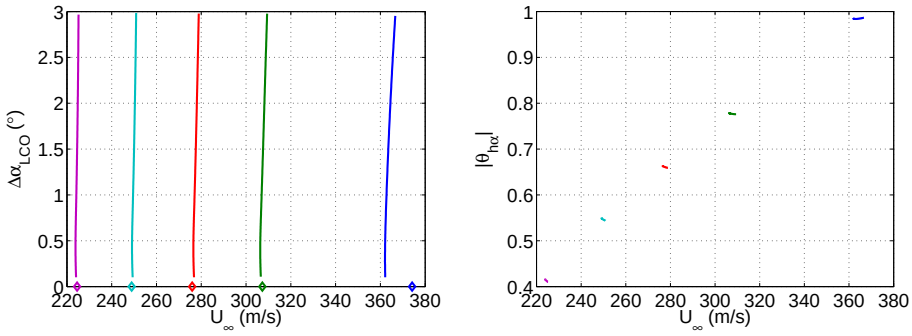

(a) Pitch amplitude

(b) Amplitude ratio

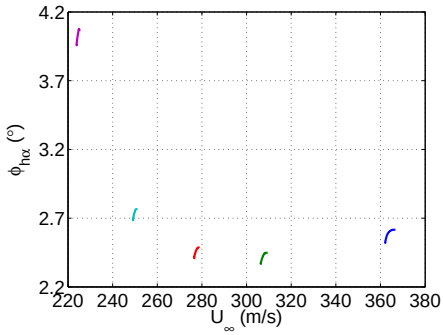

(c) Phase difference

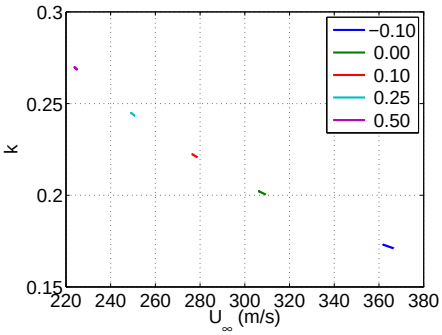

(d) Reduced frequency

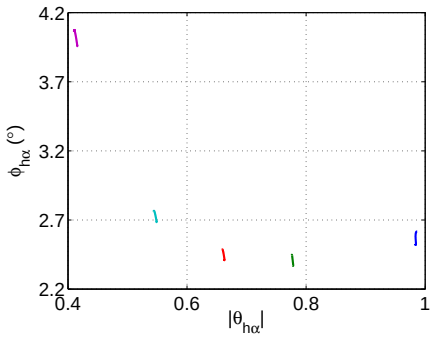

(e) Phase difference vs. amplitude ratio

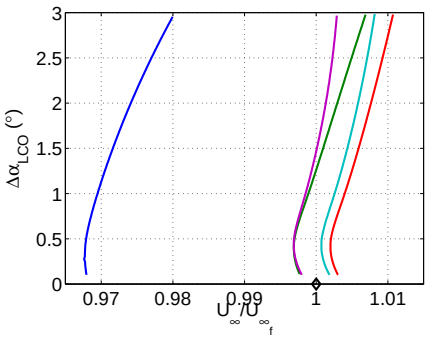

(f) Pitch amplitude

Figure D.12: LCO mode shape vs freestream velocity for a variation of the non-dimensional elastic axis location at $M = 0.3$, $\bar{\alpha} = -1.3°$, $\mathrm{Re} = 5 \cdot 10^5$ and Tu = 0.05% in transitional flow

D

D.2. RESPONSE SURFACE ANALYSIS

This section shows the results of a response surface analysis for the subsonic test cases. Figure D.13 depicts the bifurcation behaviour applying one-at-a-time constant aerodynamic forces for both test cases. Similar to the transonic test cases, see Section 5.5.3, the bifurcation behaviour for the subsonic cases deviates the most from the actual nonlinear case when the phase of the lift is held constant with pitch amplitude. When comparing the shape of the phase of the lift-slice of the response surface at the flutter and $\Delta\alpha_{LCO} = 5°$-mode, which are shown in Figures D.14 and D.15, very similar shapes are obtained, as for the transonic test cases (see Section 5.5.3).

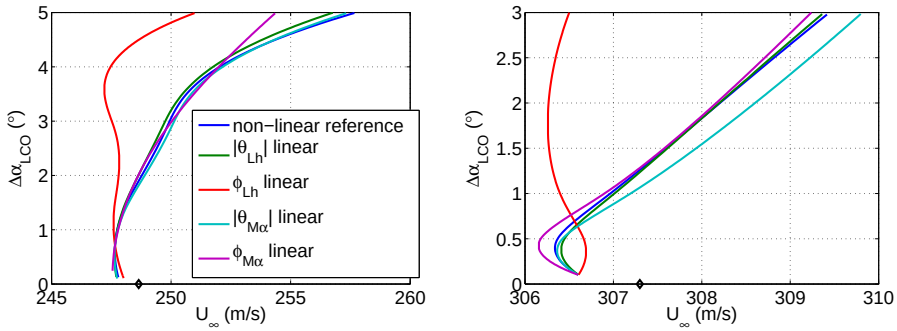

(a) $M = 0.3$, $\bar{\alpha} = 9.0°$ (b) $M = 0.3$, $\bar{\alpha} = -1.3°$, free trans.

Figure D.13: LCO amplitude vs freestream velocity for various viscous flow test cases applying one-at-a-time constant aerodynamic forces

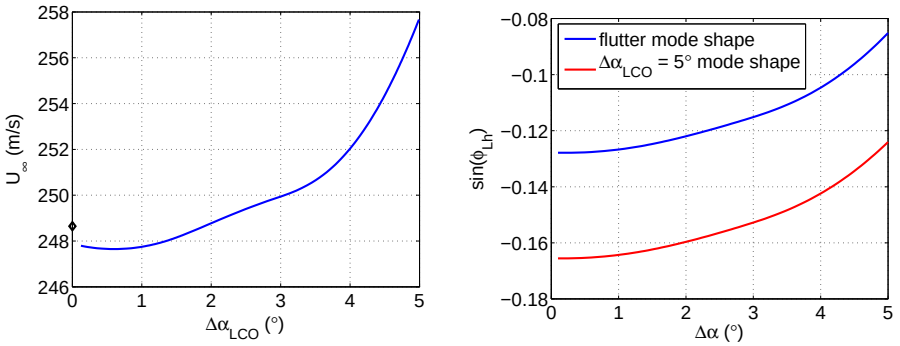

(a) U_∞ vs. $\Delta\alpha_{LCO}$ (b) ϕ_{Lh} vs. $\Delta\alpha$

Figure D.14: Freestream velocity versus LCO amplitude and ϕ_{Lh} versus pitch amplitude for RANS simulations at $M = 0.3$, $\bar{\alpha} = 9.0°$ at flutter mode shape and $\Delta\alpha_{LCO} = 5°$-mode shape

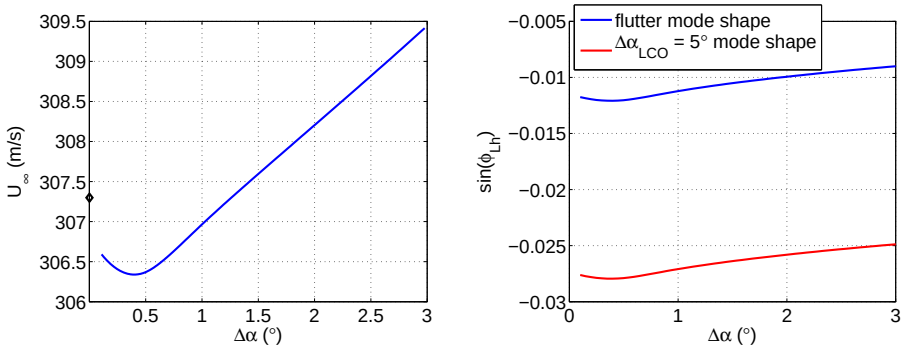

(a) U_∞ vs. $\Delta\alpha_{LCO}$ (b) ϕ_{Lh} vs. $\Delta\alpha$

Figure D.15: Freestream velocity versus LCO amplitude and ϕ_{Lh} versus pitch amplitude for RANS simulations at $M = 0.3$, $\bar{\alpha} = -1.3°$ in transitional flow at flutter mode shape and $\Delta\alpha_{LCO} = 5°$-mode shape

D

CURRICULUM VITÆ

Anna Catharina Leonarda Maria VAN ROOIJ

07-04-1988 Born in Berkel-Enschot, the Netherlands.

EDUCATION

2000–2006 Secondary School (VWO),
Bisschoppelijk College Echt, Echt, The Netherlands.

2006–2009 Bachelor of Science in Aerospace Engineering,
Faculty of Aerospace Engineering,
Delft Universtity of Technology, Delft, The Netherlands.

2009–2012 Master of Science in Aerospace Engineering,
Faculty of Aerospace Engineering,
Delft Universtity of Techonology, Delft, The Netherlands.
Master thesis research conducted at the Institute of
Aeroelasticity, German Aerospace Center (DLR),
Göttingen, Germany.
Topic: Flutter Behaviour of a Laminar Supercritical Airfoil - A Numerical Investigation into the Influence of Boundary Layer Transition.

2012–present PhD research,
Faculty of Aerospace Engineering,
Delft University of Techonology, Delft, The Netherlands.
PhD research conducted at the Institute of Aeroelasticity,
German Aerospace Center (DLR), Göttingen, Germany.
Topic: Aeroelastic Limit-Cycle Oscillations Resulting from Aerodynamic Non-Linearities.

LIST OF PUBLICATIONS

1. **A.C.L.M. van Rooij**, W. Wegner, *Numerical Investigation of the Flutter Behaviour of a Laminar Supercritical Airfoil*, Proceedings of the 18th DGLR-Fach-Symposium der STAB, 2012.

2. **A.C.L.M. van Rooij**, J. Nitzsche, H. Bijl, L. Tichy, *LIMIT-CYCLE OSCILLATIONS OF A SUPERCRITICAL AIRFOIL*, Proceedings of the International Forum on Aeroelasticity and Structural Dynamics (IFASD), 2013.

3. **A.C.L.M. van Rooij**, W. Wegner, *Numerical Investigation of the Flutter Behaviour of a Laminar Supercritical Airfoil*, New Results in Numerical and Experimental Fluid Mechanics IX, Notes on Numerical Fluid Mechanics and Multidisciplinary Design, p. 33-41, **124**, 2014.

4. M. Fehrs, **A.C.L.M. van Rooij**, J. Nitzsche, *FLUTTER PREDICTION IN THE TRANSONIC FLIGHT REGIME WITH THE γ-RE_θ TRANSITION MODEL*, Proceedings of the 6th European Conference on Computational Fluid Dynamics (ECFD VI), 2014.

5. M. Fehrs, **A.C.L.M. van Rooij**, J. Nitzsche, *Influence of boundary layer transition on the flutter behavior of a supercritical airfoil*, CEAS Aeronautical Journal, p. 291-303, **6**, 2015.

6. **A.C.L.M. van Rooij**, J. Nitzsche, R.P. Dwight, *PREDICTION OF AEROELASTIC LIMIT-CYCLE OSCILLATIONS BASED ON HARMONIC FORCED MOTION OSCILLATIONS*, Proceedings of the International Forum on Aeroelasticity and Structural Dynamics (IFASD), 2015.

7. **A.C.L.M. van Rooij**, J. Nitzsche, R.P. Dwight, *Energy budget analysis of aeroelastic limit-cycle oscillations*, Journal of Fluids and Structures, p. 174-186, **69**, 2017.

8. **A.C.L.M. van Rooij** J. Nitzsche, R.P. Dwight, *Prediction of aeroelastic limit-cycle oscillations based on harmonic forced motion oscillations*, AIAA Journal, submitted, 2016.

9. **A.C.L.M. van Rooij** J. Nitzsche, R.P. Dwight, *Bifurcations of limit-cycle oscillations of a two degree-of-freedom airfoil caused by aerodynamic non-linearities*, Proceedings of the 58th AIAA/ASCE/AHS/ASC Structures, Structural Dynamics, and Materials Conference, AIAA Science and Technology Forum and Exposition (SciTech), 2017.